

DESIGN AND CONTROL OF A SPHERICAL VTOL VEHICLE

by

(Ben) LOH WENG KHEONG

Bachelor of Science in Aerospace Engineering
Oklahoma State University
Stillwater, Oklahoma
2006

Master of Science in Mechanical Engineering
Oklahoma State University
Stillwater, Oklahoma
2009

Submitted to the Faculty of the
Oklahoma State University Mechanical and Aerospace Department
in partial fulfillment of the requirements for the degree of

DOCTOR OF PHILOSOPHY

December 2019

DESIGN AND CONTROL OF A SPHERICAL VTOL VEHICLE

Dissertation Approved:

Dr. Jamey Jacob

Dissertation Advisor

Dr. Andy Arena

Dr. Ronald Delahoussaye

Dr. Chuck Bunting

Name: (BEN) LOH WENG KHEONG

Date of Degree: DECEMBER, 2019

Title of Study: DESIGN AND CONTROL OF A VTOL SPHERICAL VEHICLE

Major Field: MECHANICAL AND AEROSPACE ENGINEERING

Abstract: This research presents the design of a spherically shaped Unmanned Aircraft System (UAS) called the All Terrain Land and Air Sphere (ATLASTM). ATLAS is designed to include competing design requirements necessary for operating in an indoor cluttered environment for emergency response and inspection applications, particularly around people, including the ability to hover, execute coordinated maneuvers with translational flight, land on uneven terrain, and return to flight. The spherical frame can interact with the environment and land without the need for coordinated vertical landing maneuverability such as other rotary winged devices, including multi-rotors or helicopters. One of the features that sets ATLAS apart from other similarly sized drones is the capability to roll on the ground to maneuver to a new location and avoid obstacles before executing an upright maneuver for recovery to flight. These features make ATLAS suitable as a search and rescue platform in supporting both aerial and ground operations. The diameter and payload capability of the ATLAS is scalable depending on the mission requirements. While multiple sizes have been developed, the primary system presented herein has a diameter of 40 cm (16 inch) and weighs about 900 grams (2 lbs).

The first part of this study investigates the characteristic of a passive flight control mechanism made up of eight movable hinged arc vanes positioned radially around the propeller tips. Such passive devices are not presented in any open propeller platform. Each vane is hinged and mechanically restricted to rotate between 0 to 90 degrees. A series of bench testing results show that these passive control surfaces generate an upward or downward force depending on the proximity and strength of the airflow interaction coming toward the propeller during flight conditions. These passive vanes can also help stabilize the vehicle in contrast to an open propeller setup.

The second part of this study evaluates control schemes for a single propeller with multiple control surfaces. Unlike ducted fans and multi-rotor platforms, the control vanes are strongly coupled to provide stability and control along all principal axes while counteracting the induced torque effects generated by a single pitch propeller. ATLAS has demonstrated stable flight tests by using a Proportional-Integrator-Derivative (PID) control based on the proposed control scheme and can successfully perform flight recovery from in-flight disturbances through the implementation of a non-linear model using the Newton-Euler formulation. Ground maneuvers are made possible by reversing the propeller direction to provide sufficient reverse thrust without the need for a variable pitch propeller.

ACKNOWLEDGEMENTS

I want to acknowledge everyone who played a role in throughout my academic accomplishments. I want to express my special thanks of gratitude to my mentor, Dr. Jamey Jacob who gave me the golden opportunity to become his student and to do this excellent research, which also helped me in doing a lot of research and I came to know about many new things I am thankful to them. I am also grateful for my committee members, Dr. Andy Arena and Dr. Delahousseya, each of whom has been my committee members since my master thesis, thank you for your patience throughout my research process and thank you for your teaching throughout my academic life in OSU. I am very much thankful to Dr. Chuck Bunting for his keen interest to be my outside committee member.

Secondly, thanks to my parents and siblings for giving encouragement, patient, and invaluable assistance to me. I want to thank Dave and Margaret Carroll, for their generous support and help. Without all them during my toughest time, I might not be able to complete this.

This research would not have been possible without the kind support and help of many individuals and organizations throughout the research time frame. I would like to extend my sincere thanks to these people in Mechanical and Aerospace Department (MAE) and Unmanned System Research Institute (USRI) : Fred Keating, Dillon Nelson, Taylor Mitchell, Dane Johnson, William Carroll, Rakshit Allamraju, John Gage, Dr. Joe Connor, Michael Puopolo, Taro Tsukada, Kathleen McNamara, Alyssa Avery, Shea Fehrenbach, Jared Allison, Victoria Natalie, Jackson Moore, Ryan Anderson, Seabrook Whyte, and Kedar Pai.

I am fortunate that the OSU Technology and Business Development Program (TBDP) funded the initial development of ATLAS in December 2012. I am also indebted to Daniel Will, the director of Cowboy Technology for introducing my research to the board of director of Cowboy Technology that resulted in a seed fund of \$350,000 for commercialization in November 2014 throughout November 2014 to December 2015.

Acknowledgements reflect the views of the author and are not endorsed by committee members or Oklahoma State University.

TABLE OF CONTENTS

Chapter	Page
I. INTRODUCTION	1
Goal and Objectives	3
II. LITERATURE REVIEW	6
Existing VTOL UAV with Protective Frame and Related Work	6
Fixed Frame Spherical Shape UAVs	8
Freely Rotating Spherical Frame UAVs	21
Existing Patents With Spherical Shape or Caged Design	23
Other Non-spherical Caged UAVs	27
Existing Movable Hinged Vanes	32
Preliminary Aerodynamic Theory	39
III. DESIGN AND CONSTRUCTION	44
Design Overview	44
Spherical Frame	44
Sizing of the Control Vanes	44
Other Structural/3D Components	46

Chapter	Page
Servo	47
Top and Bottom Vanes Attachment Method	48
Passive Movable Guide Vanes and Setup	48
Brushless Motor	49
Single Pitch Proeller	49
Battery	49
Electronic Speed Controller (ESC)	50
Mechanical and Electronic Thrust Reversal System)	50
Battery Eliminator Circuit (BEC)	51
Fuselage and Payload Compartment	52
Onboard Flight Controller	52
Android-based- app and Bluetooth	54
Computer based Graphical User Interface (GUI)	55
System Total Weight Distributions	56
 IV. GROUND TESTING SETUP AND RESULTS	 67
Facility and Equipment	67
Experimental Setup	71
Movable Vanes Assessment	71
Active Control and Propulsion System Assessment	80
Propulsion System Assessment	85
Experimental Result	87

Chapter	Page
Movable Vane Assessment Result	87
Active Control Assessment Result	99
Propulsion System Assessment Result	104
Behaviour of the Movable Vanes in Various Flight Conditions	107
Upward Vertical Take-Off	107
Hovering	107
Fast Descent - Downward Vertical Flight	110
Slow Descent and Vortex Condition - Downward Vertical Flight	111
V. DYNAMICS AND FLIGHT CONTROL	113
Impact of Center of Gravity Location on Flight and Ground Recovery Maneuvering	113
Propeller Placement and Center of Gravity	115
Different Control Vanes Configurations on Vehicle	118
4+ Configuration	119
8X (same) Configuration	121
8X (opposite) Configuration	122
4X Configuration	123
8+ (same) Configuration	124
8+ (opposite) Configuration	125
System Composition of ATLAS	126
Passive Movable Guide Vanes	128
Propeller Thrust	132

Chapter	Page
Motor Torque	133
Gyroscopic Moment	133
Gravitational Force	134
Side Panels	134
Control Surfaces Lift	135
Control Surfaces Drag	135
Moment of Inertia	136
Active Control Surfaces	136
Summary of Forces and Moments for ATLAS	136
Transformation Matrix	142
Linearization of Equations of Motion	143
Controllability and Observability	146
Preliminary Studies on the Dynamic for Hovering Stability	147
No Gyroscopic Precession Terms or Aerodynamic Forces and Moments	148
Gyroscopic Precession Terms Exist, No Aerodynamic Forces and Moments	149
Control System Design	149
Simulink Linearized Model for Hovering stability	151
Dimension measured by Solidwork	151
VI. FLIGHT TESTING AND VALIDATION	157
Flight Testing and Evaluations	157
Take off and Hovering Stability	157

Chapter	Page
Heading Hold	158
External Disturbance	158
Upright maneuvering	158
Altitude Hold	163
Sudden Descent Flight Test with Movable Vanes	165
VII. CONCLUSIONS AND FUTURE WORK	167
Conclusions	167
Dynamic Upright Maneuvering	167
Passive Control Movable Vanes	167
Coupled Active Control Configuration	168
Endurance and Vehicle Weight	169
Future Work	171
Alternative Flight Controller and Control Algorithm for Outdoor Navigation	171
Measurement of Aerodynamic Characteristic for Modeling Validation	171
ATLAS with Rover Mechanism	171
ATLAS with Foldable Frames	172
BIBLIOGRAPHY	176
Appendix A: Patent Detail for ATLAS	180
Appendix B: ATLAS with Coaxial Contra-Rotating Motor	182

LIST OF TABLES

Table		Page
1	Characteristic for each vane design	75
2	Design specifications of the Series 1580 Dynamometer	85
3	Testing results of the propulsion system.	107
4	Propulsion Dynamic Parameters.	107
5	Aerodynamic Parameters of ATLAS	153

LIST OF FIGURES

Figure	Page
1 VTOL vehicle tipping over due to pilot error or wind gust.	2
2 All Terrain, Land and Air Sphere (ATLAS).	2
3 Hover, forward flight, and dynamic upright before flight recovery.	3
4 Induced power vs. forward velocity needed by an UAV transistion from hover to forward flight [2].	7
5 Types of power generation for small UAVs.	8
6 Summary of Unmanned Aerial Vehicles with spherical shaped frame in respect to power gen- eration and control schemes.	9
7 Japanese Flying Sphere [3] [4].	11
8 Japanese Flying Sphere [3].	11
9 JFS rolls on the ground using the control surfaces [5].	12
10 Japanese Flying Sphere with conceptual wing section [5].	12
11 JFS with reversal thrust concept by using a variable pitch propeller [5].	13
12 National University of Singapore flying sphere [6].	14
13 Hawk Eye - Single propeller with Thrust Vector and four control vanes [7].	15
14 Korea’s Spherical Flying Vehicle (SFV) - Singlecopter with four control Vanes [8].	16
15 UNi-Copter by Chonbuk National University of Korea [9].	17

Figure	Page
16 UNi-Copter by Chonbuk National University of Korea with easy-to-essembly and flexible frame [9].	18
17 Spherical UAV with output ducts and shift-able C.G. mechanism [10].	19
18 Fleye - Selfies Drone [11].	20
19 Contra rotating propeller with 4 control vanes [12].	20
20 Contra-rotating rotors RC toy.	21
21 ELIOS by Flyability [13].	22
22 ELIOS's earlier prototype by Flyability [14].	22
23 Patent on different cage designs (2010.09.09).	23
24 Flying sphere with pendulum and gimbal system [15].	24
25 Spherical UAV frame with a cycloidal propeller.	25
26 Flying sphere as inspection platform (2013.04.22).	26
27 Flying Toy - Air Hogs Atmosphere.	27
28 Self-Righting Frame and Aeronautical Vehicle (2014.01.16).	28
29 HyTAQ quadrotor with a cylindrical cage with single rotating axis [16].	28
30 AirBurr and concept of operation [17].	29
31 Convertible UAV by ILS.	29
32 Most Spherical UAVs are not able to perform upright menuever.	30
33 Robot by University of Minnesota [18], [19].	31
34 B concept [20].	32
35 Movable vanes behaviour on JFS during forward flight.	33

Figure	Page
36 Asymmetric lift [21].	34
37 Ducted Fan with four Box Vanes and Stabilizer Vanes with Auxiliary Control Effector installed on the windward side of the ducted section [22].	34
38 HoverEye, iStar, GoldenEye, and T-Hawk.	35
39 Cutaway view showing Allied Aerospace iSTAR control vanes [25].	35
40 Methods to overcome asymmetric lift of the ducted fan due to crosswind [32].	37
41 Duct deflectors place near the duct lip and [34].	38
42 Flow through a duct.	39
43 Open Propeller.	40
44 ATLAS - All Terrain, Land and Air Sphere.	45
45 Structures and System of ATLAS.	45
46 Dimension of the main flate panel frame.	46
47 Dimension of a side flate panel.	47
48 Sizing and location of the control vanes.	48
49 Dimension of the top and bottom control surface.	49
50 1 of 8 sidepanel.	50
51 3D Components - Collars and Joints	51
52 HK15178 analog 9 grams servo.	52
53 Servo connected to top and Bottom control surfaces.	52
54 Hinged movable vanes position at 0 deg vs. 90 degs.	53
55 Passive movable vane setup.	54

Figure	Page
56 3D components - 1 of 8 movable hinged vane.	55
57 Dimension of a 3D printed movable vanes for a 11" prop.	56
58 T-motor MT2814-10, 770kv motor	56
59 Specifications of the T-motor MT2814-10, 770kv motor.	57
60 APC slow flyer electric 11x7 propeller.	58
61 4s Lipo 1550 mAh battery.	58
62 5V BEC.	58
63 Mechanical thrust reversal system with DPDT switch plus servo.	59
64 Electronic thrust reversal system removed the needs of servo and DPDT switch between motor and ESC.	59
65 3D components - top collar.	60
66 A GoPro Session 4 mounted ontop of the top collar for indoor rooftop inspection.	60
67 Multiwii ATmega 2560.	61
68 Multiwii setup for ATLAS.	62
69 Bluetooth module.	62
70 EZ-GUI Android based App.	63
71 Android app to tune the PID controller via Bluetooth.	64
72 GUI customized for ATLAS using Multiwii controller.	65
73 Component breakdown and weight contributions.	65
74 Detail components breakdown and weight contributions.	66

Figure	Page
75 Oklahoma State University’s Flotek Wind Tunnel.	68
76 Wind tunnel calibration to obtain the relationship between the tachometer value vs. wind speed at test section.	68
77 Flex 3 motion capture camera by OptiTrack.	69
78 OSU Indoor flight chamber with motion capture system.	69
79 An example of vehicle’s flight motion was captured by OptiTrack using the Motive software. .	70
80 ATLAS with multiple reflective markers. A virtual representative of the markers in the motion capture software.	70
81 Lift force of a single vane with 12x6 prop.	72
82 Setup to measure the lift force of a single vane.	72
83 The dimension of a single passive vane for force measurement.	73
84 The dimension of a single vane.	74
85 Seven vane designs and the drag measurement setup.	74
86 Setup with an annular plate.	75
87 Experimental setup using a fixed circular plate.	76
88 Annular plate setup for drop test.	77
89 Experimental arrangement for PIV measurement.	79
90 Experimental arrangement for thrust measurement.	80
91 Custom gimbal.	81
92 3D printed clamp.	81
93 4 movable vanes installed at the front of the vehicle.	82

Figure	Page
94 Custom balance to measure lift and drag.	83
95 TAL220 10kg load cell.	83
96 Measured load and residue load obtained from each load cells.	84
97 RC Benchmark's dynamometer.	85
98 Propulsion testing system by using the 1580 Dynamometer.	86
99 lift force of a single vane with 11x7 prop.	88
100 lift force of a single vane with 12x4.7 prop.	88
101 lift force of a single vane with 12x7 prop.	89
102 Vane's deflection angle versus air speed with uncertainty.	89
103 Movable vane deflection from vertical to horizontal position as the propeller RPM increases.	90
104 RPM vs. vane deflection angle.	91
105 Drag coefficient versus Reynold number.	92
106 Change of thrust with and without Annular Plate, $c = 2.5$ inches.	93
107 Force measurement by varying h.	93
108 Force measurement by varying h and c.	94
109 Change of displacement with and without annular plate.	95
110 Change of velocity with and without annular plate.	96
111 Annular plate provides stability during descending.	96
112 The air flow near the propeller (A) without and (B) with the annular fixed vane at 6500 RPM.	97
113 Flow characteristic around the propeller tip with and without a vane.	97
114 Efficiency and Thrust of the motor using 11x4.7 and 11x7 propeller.	98
115 Vehicle's attitude without any movable vanes installed.	99

Figure	Page
116 Vehicle's attitude with all 8 movable vanes installed.	100
117 Vehicle's attitude with 4 movable vanes at the front of the vehicle.	100
118 Lift and drag coefficient measurement by deflecting the top vanes ranging from 0 to 35 degrees with 5 degrees interval. Stall occurs after 20 degrees.	101
119 Lift and drag coefficient measurement by deflecting the bottom vanes ranging from 0 to 35 degrees with 5 degrees interval. Stall occurs after 20 degrees.	102
120 Lift and Drag coefficient at linear region.	103
121 Thrust measurement using MT2814-11 710 Kv motor.	104
122 Reverse thrust measurement using MT2814-11 710 Kv motor.	105
123 Torque measurement using MT2814-11 710 Kv motor.	105
124 11x7 propeller.	106
125 11x7 propeller reversing spinning direction.	106
126 Gyroscopic effect when roll command input was introduced.	108
127 The vehicle is pitching forward or backward when roll left or right command input was introduced, respectively.	108
128 Upward vertical Take-off.	109
129 Hovering condition.	110
130 Downward Vertical Flight - Fast Descent.	111
131 Downward Vertical Flight - Slow Descent.	112
132 The placement of control surface in relative to the center of gravity.	114
133 The effect of C.G. on flight and ground control	115
134 Effect of shifting C.G. above C.O.S (neg z-dir) on upright maneuver.	116
135 Hover, forward flight, and rolling on the ground.	117

Figure	Page
136 Top view of the propeller spinning in counter-clockwise direction.	118
137 Impact of the center of gravity location during (a) forwards flight and (b) wind gust.	119
138 Known Spherical Shape UAV with their control configurations.	120
139 4+ coinfiguration.	120
140 8Xsame configuration.	121
141 8X opposite configuration.	122
142 4X configuration.	123
143 8+same configuration.	124
144 8+ opposite configuration.	125
145 Pitching restoring moment for different control types.	126
146 Estimated drag force in the z-direction for 4 versus 8 control vanes for deflection angle ranges from 0 to 20 degrees.	127
147 Hinged movable vanes on the top half of the ATLAS.	129
148 Free body diagram of the hinged movable vanes while hovering and descending.	130
149 Free body diagram of the hinged movable vanes during translational flight.	132
150 Schematic of ATLAS's control vanes.	137
151 Resultant force due to vane deflections for decouple roll, pitch and yaw.	138
152 ATLAS with 8 vanes in body frame coordinate.	139
153 ATLAS's longitudinal axes.	140
154 ATLAS lateral axes.	140
155 Instability without gyroscopic and aerodynamic terms exist.	148
156 Neutral stability when gyroscopic term exists.	150

Figure	Page
157 ATLAS's control schematic.	152
158 Coding to implement PD controller to the microcontroller.	152
159 Per axis PD structure.	154
160 ATLAS	154
161 Linearized model using Simulink for pitching stability using PD controller.	155
162 ATLAS System.	156
163 Respond with step input on to reach a desired theta using PD controller for both rate and angle controller in the linerized model.	156
164 Hovering stability - 3 minutes flight with Heading Hold activated.	159
165 RPM, Watt and motor temperature at hovering flight.	160
166 Heading Hold test.	160
167 Throttle input to manually maintain the flight altitude.	161
168 Flight recovery and stability after the pilot executed multiple disturbances.	161
169 IMU data when performing upright maneuver.	162
170 Recorded power and amperage consumption when performing upright maneuver.	162
171 Foam ontop of the board to protect the barometer from light and direct airflow.	163
172 Change of elevation after altitude hold was enabled.	164
173 Vehicle's attitude after enabled altitude hold.	164
174 Recorded acceleration on the Z-axis with and without the movable vane.	165
175 Recorded change of altitude from the OptiTrack cameras. Displacement vs. frame.	166
176 Descending velocity for each test.	166
177 A GoPro session4 mounted ontop of the ATLAS for ceiling inspection.	169

Figure	Page
178 ATLAS in comparison with other spherical UAVs with control vanes and single or coaxial propeller.	170
179 The overview of ATLAS concept with rover mechanism in 2011.	172
180 Straight wheel and tilted Wheel.	173
181 Rover design mockup.	174
182 ATLAS with foldable frame.	175
183 Foldable frame prototype for compact ATLAS design.	175
184 International Patent of ATLAS, page 1 of 41.	181
185 Types of COTS coaxial contra-rotating motor.	183
186 RPM vs. reversed thrust by reversing the motor spinning direction force using one of the single propeller of AEO-RC CR28M.	184
187 Thrust and torque measurement produced by AEO-RC CR28M.	184

CHAPTER I

INTRODUCTION

The interest in Unmanned Aerial Vehicle (UAV) has been increasing as their becoming immense importance in various applications such as military, security, emergency response, and disaster monitoring. The majority of the UAV, like fixed wing and quadcopter design, has some limitations when operating within a confined space. Semi or fully autonomous helicopter and quadcopter have the potential to operate in very confined spaces like urban environments or even indoors, with minimal operator interaction. However, such platform with the expose blades that can easily get damaged upon contact with an object or the surrounding environment. This demand has led to the development of several of these shrouded fan vehicles, such as the GoldenEyes, HoverEye, Kestrel, and iSTAR. Although these vehicles can be protected by duct or guard ring, the orientation vehicle about the terrain is still critical for autonomous vertical take-off and landing (VTOL) and recovery. Figure 1 depicts the scenario when aircraft tipping over due to wind gust or accidentally bump onto an object during a flight. In addition, self-recoverability is not a typical feature in these aerial vehicles design. The self-recoverability here means the ability for the vehicle to re-orientate itself into a proper orientation before returns to flight. An aerial vehicle without such ability means the termination of a mission if such an incident occurs. In another word, a flipped vehicle has no further operation value if it cannot be recoverable to continue a mission. A protective frame with the flexibility to recover from any terrain could be beneficial.

The objective of this research is to investigate, design, and validate the active and passive control system of a spherical shape UAV for indoor operation with dynamic upright capability for flight recovery. The vechile is called the All Terrain Land and Airsphere (ATLAS) as shown in figure 3. The spherical frame of ATLAS, as shown in figure 2, is designed to protect the propeller, avionics, and control surfaces. By using only a single pitch propeller-motor configuration and eight control vanes, the vehicle can perform VTOL and transit into translation flight, in which similar to that of a helicopter. Apart from that, the ATLAS demonstrate the capability to land in any orientations and rolls onto the ground until it comes to a standstill.

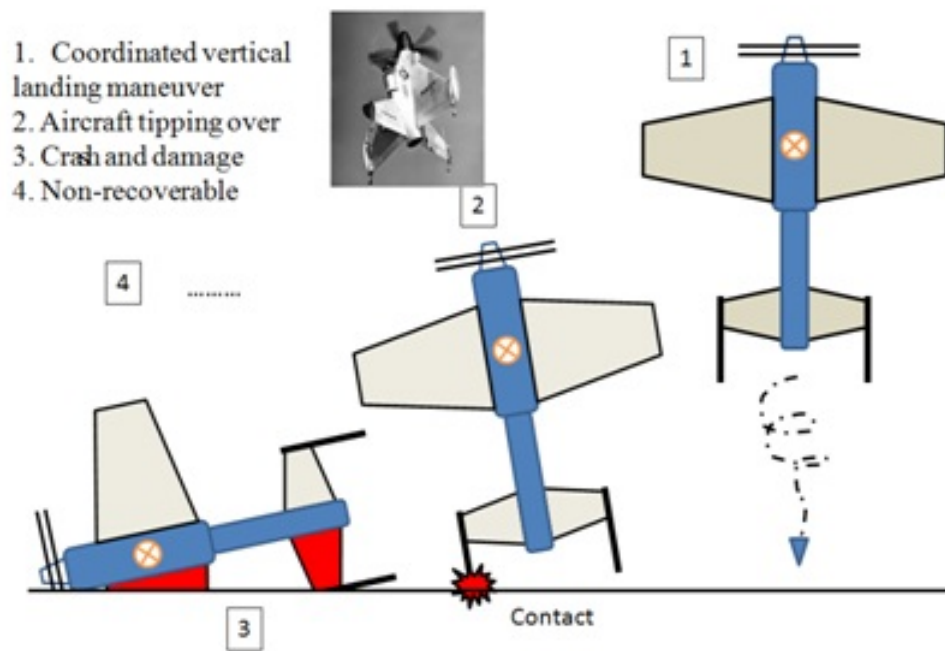


Figure 1: VTOL vehicle tipping over due to pilot error or wind gust.



Figure 2: All Terrain, Land and Air Sphere (ATLAS).

It can then be piloted to an upright orientation before taking off again. All these features make ATLAS a versatile UAV suitable for search and rescue mission in supporting both aerial and ground operations. This dissertation presents the control scheme, aerodynamic components, structural design, and control system of ATLAS. The aerodynamic components are to identify the components on the vehicle that produces forces and moments acting on the vehicle center of gravity located at the center of the sphere. The structural component is mainly presenting the structural material needed to ensure the spherical frame of the vehicle can withstand impact loads. The control system components present the investigation of the control scheme of the couple control surfaces, microcontrollers, and electronics needed to provide stability and control to operate the vehicle in both aerial and ground operation indoor.

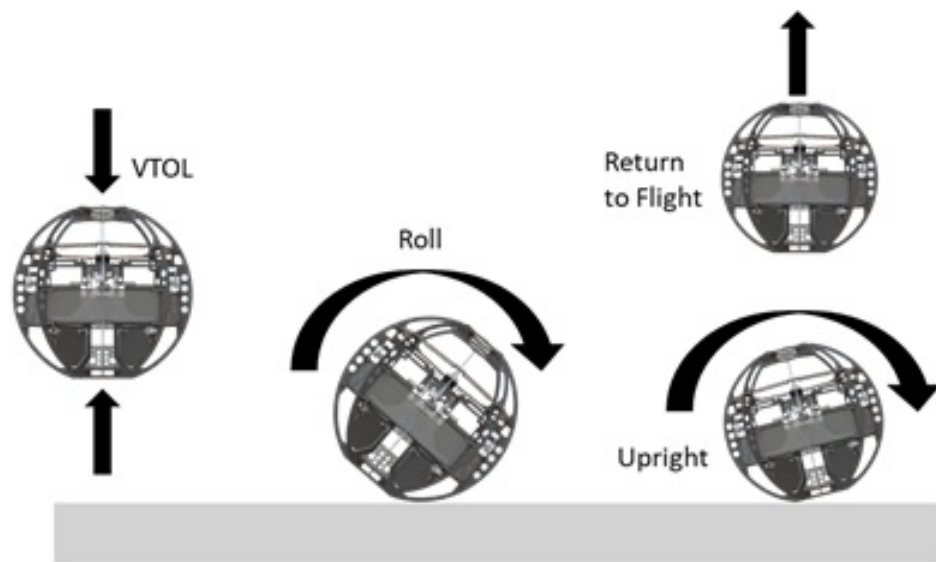


Figure 3: Hover, forward flight, and dynamic upright before flight recovery.

Goal and Objectives

The goal of this research is to investigate, design, and validate the active and passive control system of a spherical shape UAV for indoor operation with dynamic upright capability for flight recovery.

OBJECTIVE 1: LITERATURE REVIEW

This aim to research existing spherical shaped UAV with/or similar characteristic on control configuration and movable vane mechanism.

- 1.1 Summarize UAV concepts with spherical shape frame and relevant platforms with passive vanes.
- 1.2 Identify the challenges of JFS and other Vertical Take Off and landing (VTOL) platforms.

OBJECTIVE 2: PASSIVE Control - Movable Guide Vane

The goal is to understand the active and passive control that works within the spherical frame.

- 2.1 Study the characteristic of passive vanes on JFS versus similar auxiliary control in other UAVs.
- 2.2 Identify parameters that affect the performance of the passive vanes to develop testing methodologies that quantify the impact on the UAV performances.
- 2.3 Summarize the performance of the passive vanes in various flight conditions.

OBJECTIVE 3: ACTIVE CONTROL - Control Vanes and Avionic system

This purpose is to identify and select from potential flight control scheme along with the avionic components needed to fit into the spherical frame.

- 3.1 Identify and compare potential or existing control scheme using control surfaces and a single propeller.
- 3.2 Select the control scheme and develop the equation of motion of the vehicle. Modeling and analyzing the linearized conditions.

OBJECTIVE 4: FLIGHT TESTINGS AND VALIDATIONS

The purpose is to validate the control scheme in flight, the function of the spherical shape frame and ground recovery mechanism for flight recovery.

- 4.1 Design and build an ATLAS by using COTS PID controller and implement the proposed control scheme

developed in Objective 3.

4.2 Identify and validate the propulsion system that satisfies the desired flight conditions and flight recovery.

4.3 Perform flight performance analysis thru a series of flight testing.

CHAPTER II

LITERATURE REVIEW

This chapter consists of two parts. Part 1 of this chapter presents existing spherical shape Vertical-Take-Off-and-Landing (VTOL) vehicles that consists of some degrees of protective element and/or ground mobility capability. Part 2 presents findings related to the passive movable vanes.

2.0 Existing VTOL UAV with Protective Frame and Related Work

The flight of an aerial vehicle requires the generation of forces for lift, propulsion, and control. The method to create these forces is to generate momentum, which produces a reacting force by following Newtons Second Law of Motion. The kinetic energy increases whenever the momentum of a mass of fluid increases. Thus, to produce a continuous force, energy must be continuously generated and transferred to the fluid. The power required to do this is referred to as induced power. For a VTOL platform, the two fundamental techniques to produce force are control surfaces and actuator disks (propeller). Recall [1] that induced power for a finite wing section is proportional to the square of the lift and inversely proportional to the airspeed, and actuator disc power is proportional to the 3/2 power of lift, the total induced power required for level flight is

$$P_i = AL_A^{\frac{3}{2}} + \frac{B}{V}(W - L_A)^2 \quad (1)$$

where A and B is constant that depend on the configuration and density altitude. Minimum induced power can be found by differentiating equation with respect to L_A yields

$$\frac{\partial P_i}{\partial L_A} = \frac{3}{2}AL_A^{\frac{1}{2}} - \frac{2B}{V}(W - L_A) = 0 \quad (2)$$

Rearranging,

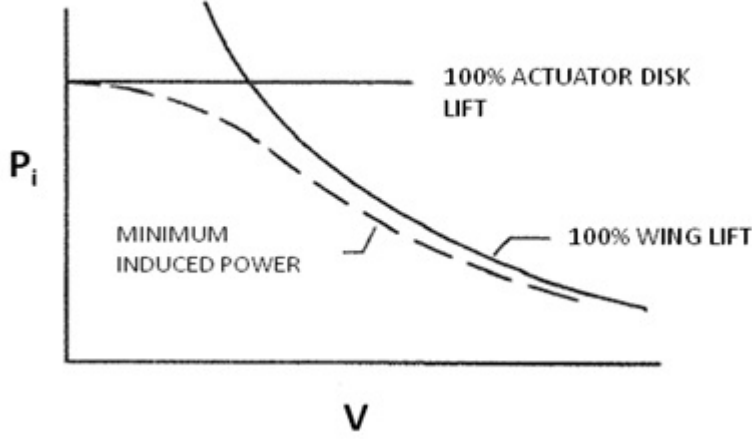


Figure 4: Induced power vs. forward velocity needed by an UAV transition from hover to forward flight [2].

$$L_A^2 - 2W\left[1 + \frac{9}{32}\left(\frac{AV}{B}\right)^2 \frac{1}{W}\right]L_A + W^2 = 0 \quad (3)$$

The equation above can be solved for the actuator disk lift, L_A , which results in the minimum induced power at any forward airspeed. Note that as $V \rightarrow 0$, $L_A \rightarrow W$ and as $V \rightarrow \infty$, $L_A \rightarrow 0$. This means that at hover the actuator disk must generate sufficient lift to overcome the weight of the vehicle; at forward flight, the lift should be generated entirely by the wing or control surfaces; in between is an optimum combination. Figure 4 illustrates that properly distributing the lift load, the total induced power will be less than that required by either control surfaces or actuator disc acting alone. Figure 5 show the types of power generations using actuator disc (propeller) for small UAVs in comparison to a helicopter.

A wide variety of spherical shape platforms emerges since the appearance of the Japanese Flying Sphere in 2011. This research tabulates the known commercial product, research platforms, and patents that are spherical shape in figure 6. The variety of platform is classified primarily in term of frame types, propulsion systems, primary and secondary control system. Overall the spherical platform can be identified into two kinds of frames: Freely-Rotating-Frame versus Fixed-Frame structure. The next category is differentiated based on three types of the propulsion system presented in figure 5, mainly single fixed propeller, counter-rotating propellers, and multi-propeller system. The active control surface can be broken down from no




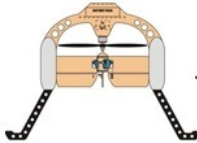
Type of Powered Lift Generator				
Types	Helicopter	Multi-copter	Coax-copter	Single-copter
# of Propeller	1 main rotor 1 tail rotor	> 3	2	1
Propeller type	Variable Pitch	Fixed Pitch	Fixed Pitch	Fixed Pitch
Efficiency (4 is the best)	2	1	3	4
Mechanical Complexity	1	3	2	4
Indoor flight capability	1	2	3	4
Control	<ul style="list-style-type: none"> ➤ Constant RPM with variable pitch ➤ Tail rotor ➤ Or Dual coaxial Duo Rotors 	<ul style="list-style-type: none"> ➤ Variable RPM controller 	<ul style="list-style-type: none"> ➤ Control flaps ➤ Variable RPM control for yaw control ➤ Flv bar 	<ul style="list-style-type: none"> ➤ Control flaps ➤ Stators
				

Figure 5: Types of power generation for small UAVs.

control vanes up to 8 control vanes. Other control surfaces or methods were introduced in some platforms and identify separately like movable vanes, thrust vectoring, cycloidal propeller, etc. The chapter will introduce the presented platforms/research in detail.

2.1 Fixed Frame Spherical Shape UAVs

Japanese Flying Sphere

The Japanese Flying Sphere (JFS) was first introduced in 2011 by Sato Humiyuki, a member of the Japan Technical Research and Development Institute (TRDI) as the world first spherical shape UAV [4]. As shown in figure 7, the JFS has a diameter of 42 cm (16 in) and weighs only 350 grams (0.77 lbs). Maximum of 8 minutes is the reported flight endurance. This prototype is carrying a penny size camera as its only payload.

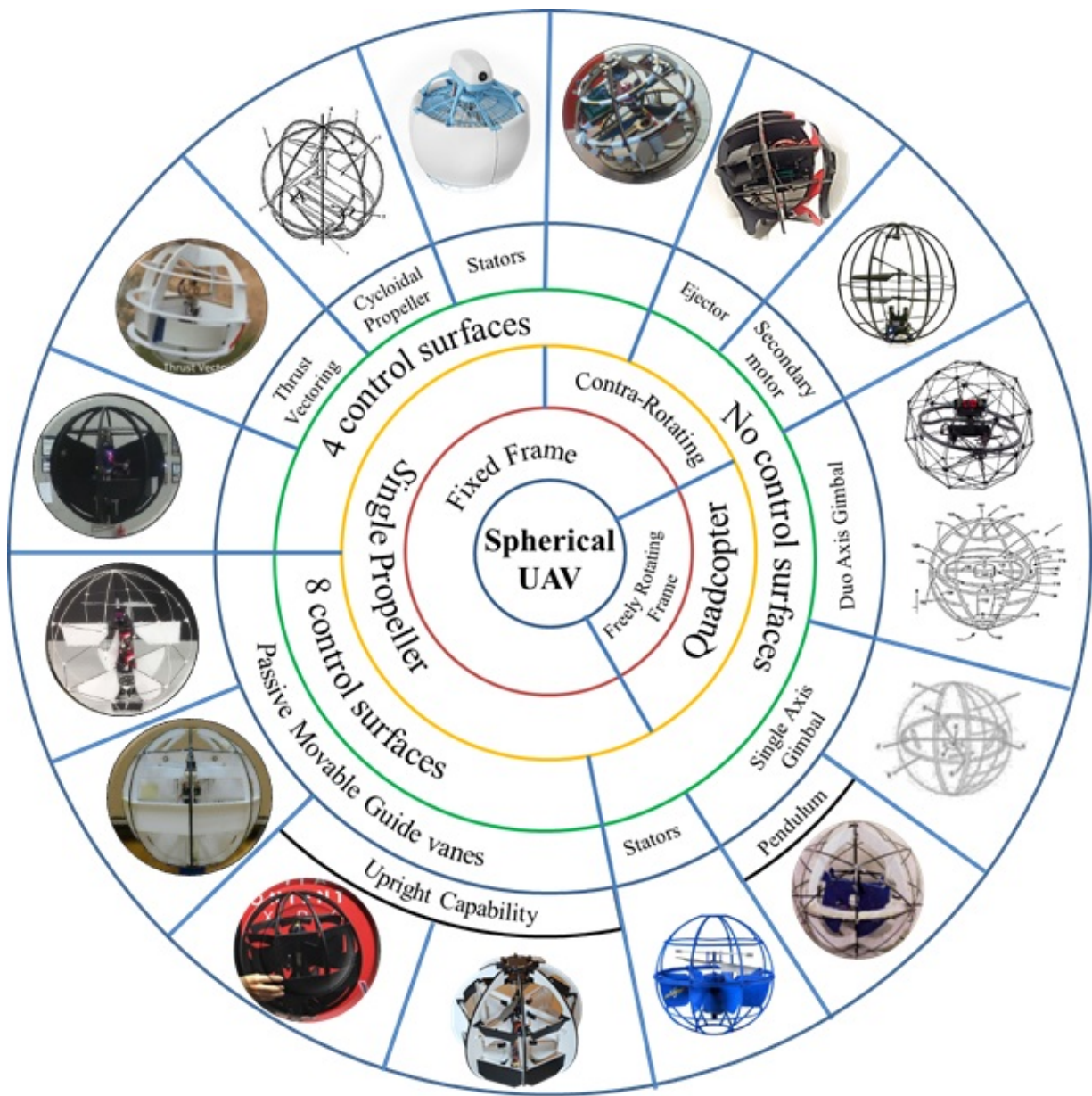


Figure 6: Summary of Unmanned Aerial Vehicles with spherical shaped frame in respect to power generation and control schemes.

JFS can perform both hover and forward flight characteristic similar to a quadcopter or helicopter by using the control surfaces fitted within the frame. Unlike traditional helicopter with an exposed propeller, the JFS has its single propeller located within the frame. Its spherical shape frame allows the vehicle to land and rolls freely on the ground until a full stop when the battery power is critically low. Landing the JFS requires no coordinated maneuverability and can even drop close to the ground as the thrust gradually decreases. The vehicle is susceptible to bouncing on the ground during landing because of its lightweight structure.

The demonstrated JFS uses a single fixed pitch propeller and consists of eight control surfaces within the frame to manipulate the attitude of the vehicle in flight and ground mobility[?]. When on the ground, deflecting all eight control surfaces simultaneously under the propeller slipstream can easily create a rotating moment to roll the vehicle back and forth to roll away from any obstacles due to its lightweight structure. Such features are presented in figure 9. Return to flight is possible after re-orientate the vehicle into the upright position on the ground before taking off again.

The uniqueness of the JFS design and mixture of multiple functionalities leads to the research and the development of the All-Terrain, Land and Air Sphere (ATLAS). The interests come not only from the unconventional configuration with coupled control surfaces but also from the design standpoint in comparison to well-established aerial platforms like a ducted fan. Integrating the coupled actuators and flight control is not trivial as only limited literature is available about the JFS other than the Japanese patent document found online.

The Japanese patent document illustrates alternative JFS conceptual designs [5]. Figure 10 shows a flying sphere concept with body cover and two pieces of foldable bowl-shaped that claim to act as a lifting surface to provide lift in flight. The propeller with three blades can vary their pitch angle and attached to a dual rotational motor. Figure 11 shows the JFS with the ability to recover from a hole by reversing the propeller slipstream using the propeller with an adjustable pitch angle. The concept also depicts a shiftable center of gravity (C.G.) mechanism in the fuselage to change the C.G. between hover and forward flight. Figure 9 depicts the sphere rolling to the left by directing the airflow using the control vanes.

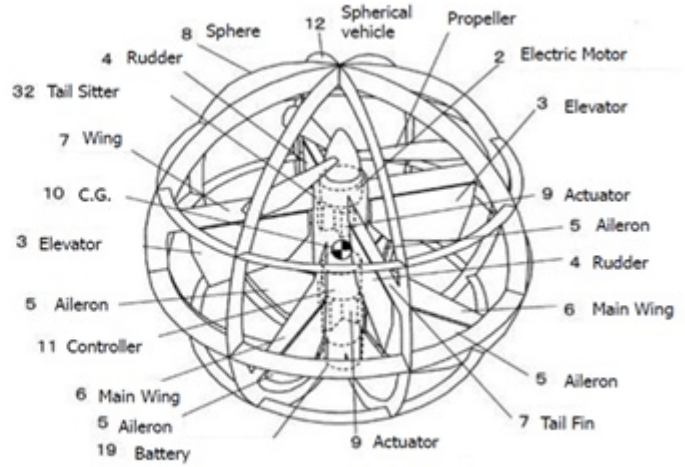


Figure 7: Japanese Flying Sphere [3] [4].

Flying spy-camera

Japanese scientists create a remote-controlled surveillance device the size of a beach ball

Spherical Air Vehicle

Motor Contained in modified plastic bottle		Propeller			
Camera Transmits live video images		Control flap			
<table style="width: 100%; border-collapse: collapse;"> <tr> <td style="width: 50%;">Total weight: 350 g</td> <td style="width: 50%;">Material cost: \$1,400</td> </tr> <tr> <td>Flight time: 8 minutes</td> <td></td> </tr> </table>		Total weight: 350 g	Material cost: \$1,400	Flight time: 8 minutes	
Total weight: 350 g	Material cost: \$1,400				
Flight time: 8 minutes					

Diameter: 42 cm

Future development:

- ▶ Autopilot
- ▶ Turbulence control
- ▶ Poor weather function

Movements

Source: Japan Defense Technical Research and Development Institute

AFP

Figure 8: Japanese Flying Sphere [3].

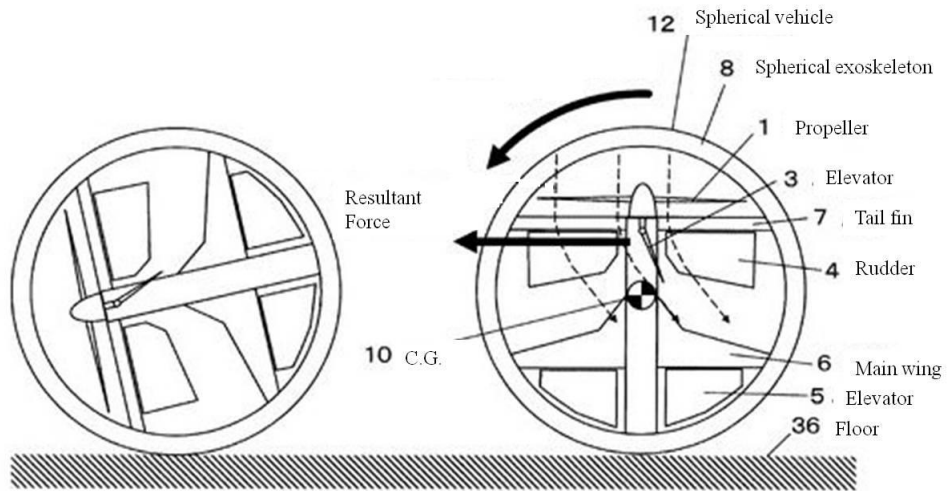


Figure 9: JFS rolls on the ground using the control surfaces [5].

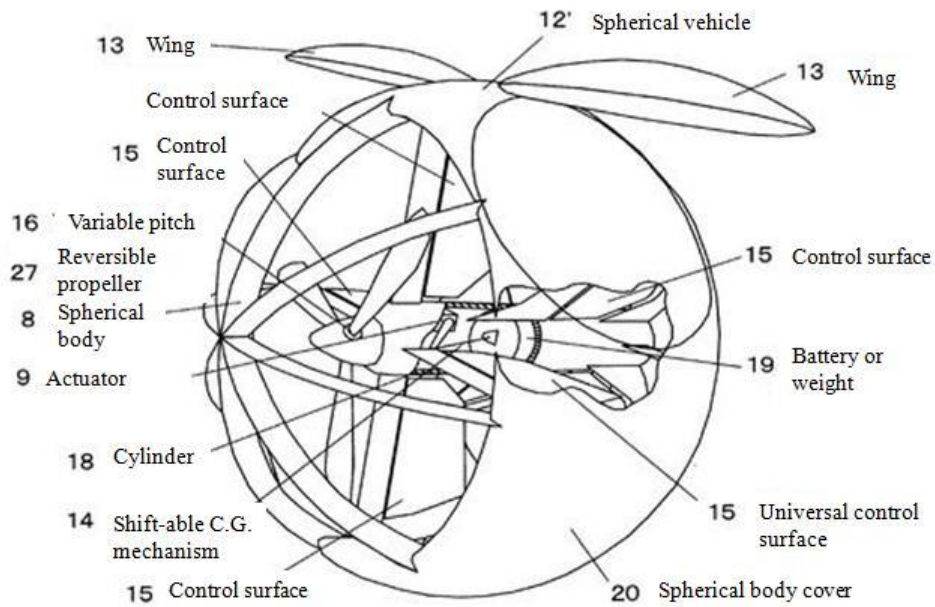


Figure 10: Japanese Flying Sphere with conceptual wing section [5].

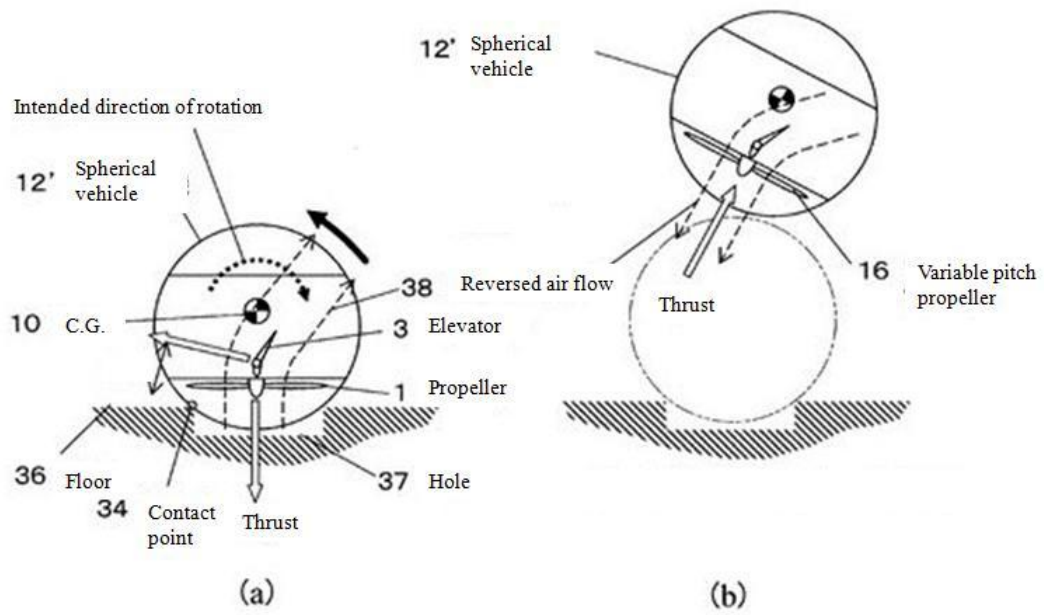


Figure 11: JFS with reversal thrust concept by using a variable pitch propeller [5].



Figure 12: National University of Singapore flying sphere [6].

University of Singapore Flying Sphere

After the first appearance of the Japanese Flying Sphere, The National University of Singapore (NUS) built and tested their own spherical shape in 2013. The researcher build their UAV based on the control system of a ducted fan UAV because of the limited knowledge of the specification of the JFS. [6]. Figure 12 is showing the design using 8 control vanes and movable vanes. However, no detail of the movable vanes was mentioned. The vehicle weighs about 551 grams with 42 cm diameter. The frame is made up of Depron foam sheet. The reported flight endurance was about 7 minutes. With limited literature available regarding the Japanese sphere, the NUS team come up control scheme eight control surface where the top four vanes are the pitch and roll control vanes, which the bottom four vanes are the yaw control vanes. The vehicle is not capable of upright maneuvering for flight recovery.

Flying Vehicle with Thrust Vectoring

Figure 13 shows the Hawk Eye flying sphere developed in Bombay, India for Tectfest 2012. No literature detail was found, and only online video was available to demonstrate its flight capability [7]. The Hawkeye is with thrust vectoring mechanism with four control surfaces under the slipstream of the propeller located at the bottom of the sphere to provide stability and control. The vehicle is made of lightweight foam board



Figure 13: Hawk Eye - Single propeller with Thrust Vector and four control vanes [7].

and has three annular plates around the spherical structure to provide structural rigidity. The vehicle is not designed to roll on the ground and not intended for flight recovery capability. Their flight video shows that the vehicle has a high center of gravity above the center of the sphere that causes the vehicle to tilt upside down after landing on the ground.

Korea Spherical Flight Vehicle (SFV)

The Korea Aerospace University Flight Control Lab has built and tested a spherical flight vehicle with a single rotor and four control surface in 2013. The vehicle called the Spherical Flight Vehicle (SFV), as shown in figure 14 weighs about 562 grams and has a diameter of 44 cm (17 in). The recorded flight time was about 6 minutes. The researcher claims that the vehicle can also land or move on the ground by rolling but not demonstration on recovering to flight. This sphere design also equipped with movable vanes similar to those available in the JFS. However, similar to NUS's flying sphere, no detail on the movable vanes functions was mentioned. Both attitude and altitude controller is achieved by using the Kalman Filter and PID controller. No further development was reported as it was only designed for an engineering competition.

Korea Uni-Copter

The Chonbuk National University of Korea has designed and tested a spherical frame made of flexible frame structure called the Uni-Copter in 2017 [9]. Figure 15 is showing two prototype Uni-copters with eight



Figure 14: Korea's Spherical Flying Vehicle (SFV) - Singlecopter with four control Vanes [8].

control surfaces in which similar to the JFS. However, no movable vanes were installed. The Uni-copter shown in the picture has a diameter of 480 mm and 200mm with the respective masses of these vehicles of 430 grams and 160 gram. Their goal is to design an easy-to-assemble and flexible frame UAV made of foam board and fiberglass reinforced polymer (FRP) bars and carbon fiber bars. The bars were connected by using 3D printed nylon linkages as shown in figure 16. In comparison to the NUS flying sphere control, the bottom vanes are coupled to provide roll, pitch, and yaw control. The top vanes, however, perform similar to those of NUS where two of the top are providing roll, while the others are to provide the pitch. Their flight test result shows that such a control scheme is underperforming for yaw control to overcome induced torque generated by the single propeller. No presentation on the structural integrity of the flexible frame structure was reported. Furthermore, also like the NUS sphere, the UNI-copter is not capable of neither upright maneuvering or ground mobility.

Air duct Flying Sphere Concept

Figure 17 shows a spherical UAV concept without any conventional control surfaces. The concept uses four output duct sections to direct airflow to the side of the sphere to achieve flight stability [10]. The propulsion system consists of a contra-rotating propeller to control the yaw of the vehicle by adjusting the differential rotation speed of the propellers. Without any conventional control surfaces, the sphere uses a center of gravity (C.G.) shifting mechanism by adjusting the battery position within the center of the vehicle along

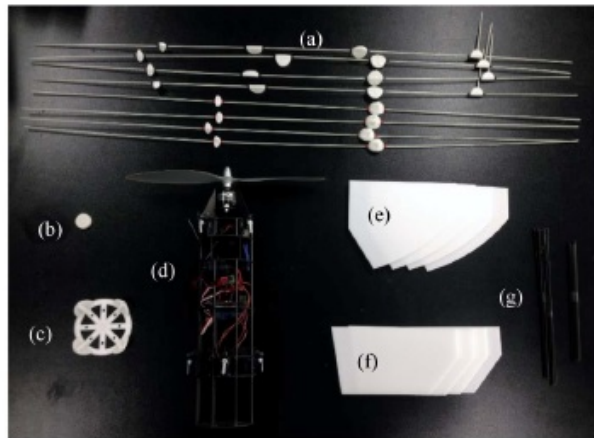


Figure 15: UNi-Copter by Chonbuk National University of Korea [9].

the X-Y axis. Figure 17 (d) shows the detail of such a mechanism. Thus, when the C.G. of the battery is in line with the line of thrust, the vehicle is in vertical flight or hover. Shifting the battery in one direction causes the vehicle to achieve translational flight. No mention on whether this concept has the capability to upright and return to flight. However, the inventor never tested and presented any flight results due to the time constraint of the project deadline.

Fleye

Figure 18 is a semi-spherical shaped drone that is based on a ducted-fan UAV concept. The initial idea for this design started in Nov 2013 and presented in Kickstarter in December 2015 promoted as a safe selfies drone. The ducted panel is made of a lightweight foam core. The attitude of the vehicle is controlled by using four control surface (boxes) and stators within the ducted panel and uses a single propeller. The stators are there to overcome the induced torque created by the single pitch propeller. The drone can be controlled using its custom smartphone app. Fleye is a 23cm (9 in) ball that weighs about 450g (16 oz). The top of the vehicle is where the onboard controller and camera were mounted. The vehicle has a sonar to measure



(a) Main bars for the sphere-shaped structure; (b) top and bottom connectors; (c) bottom of the central tower; (d) central tower with one rotor, one propeller, eight servomotors, batteries, one wireless transmitter, etc.; (e) control surfaces on the lower side; (f) control surfaces on the upper side; (g) sub-bars for the control surfaces and sphere-shaped structure.

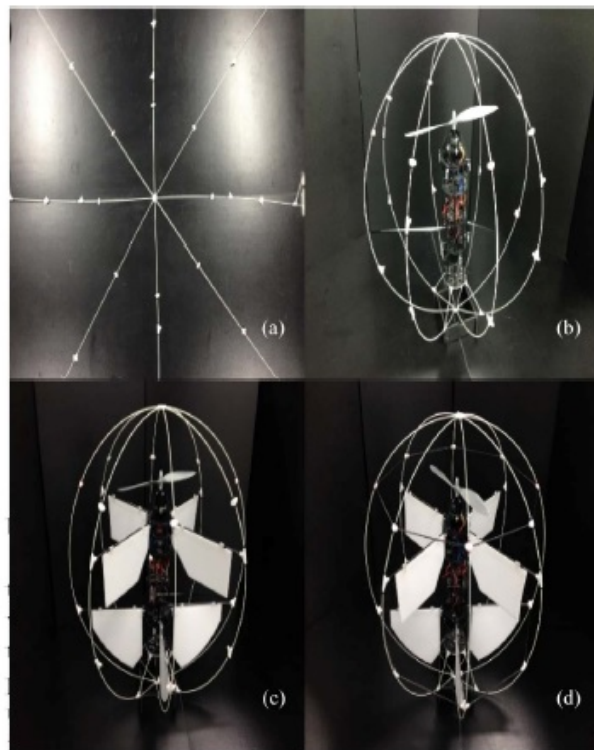


Figure 16: UNi-Copter by Chonbuk National University of Korea with easy-to-essembly and flexible frame [9].

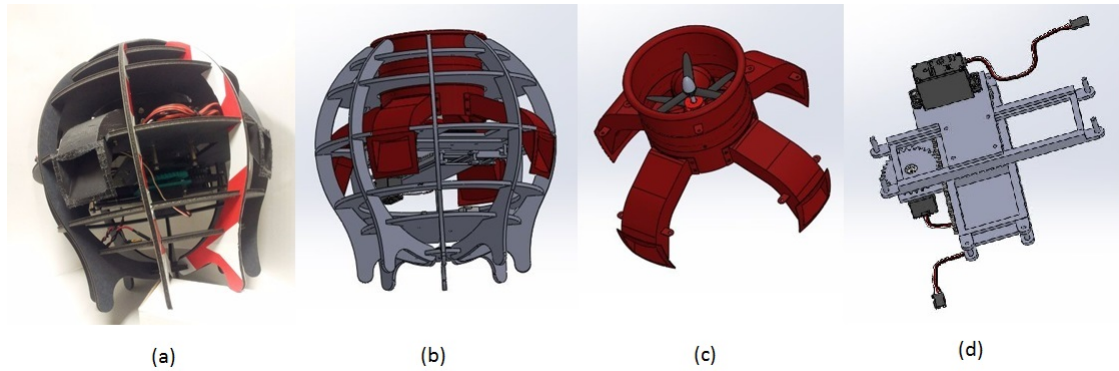


Figure 17: Spherical UAV with output ducts and shift-able C.G. mechanism [10].

ground distance up to 3 meters (10 ft), and an optical flow camera mounted at the bottom of the vehicle. It is powered by a 3s 1500mAh Lipo battery and claims to have a 10 minutes flight time. However, this selfies drone is not designed to roll on the ground and not capable of flight recovery from the ground. More detail about Fleye can be found in [11].

United Kingdom Contra Rotating Platform

Figure 19 presents a design of a coaxial with four control surfaces spherical UAV presented by School of Aerospace, Transport and Manufacturing of Cranfield University in United Kingdom [12]. The control surfaces at the base of the sphere will generate roll and pitch moments as opposed to conventional swap plate design while the coaxial setup provides yaw moments and an increase in thrust of the system. The yaw moment can be produced by the differential propeller speed. The vehicle is made of plywood and weighs about 0.59 kg. The propulsion uses two 3-blade 8 x 4.5 propellers and carries a 1300mAh Li-Po battery. The vehicle has an ultrasonic sensor mounted at the bottom and the top of the sphere to measure the distance from the floor and the roof. A Proportional Differential (PD) controller was designed for this vehicle lateral and longitudinal control. However, no successful controlled flight was reported.



Figure 18: Fleye - Selfies Drone [11].



Figure 19: Contra rotating propeller with 4 control vanes [12].



Figure 20: Contra-rotating rotors RC toy.

Toy with Contra-Rotating Propeller

Figure 20 shows a spherical toy vehicle using a coaxial contra-rotating propeller with a spherical cage mounted on the outside. Note that there is a flybar (or stabilizer bar) on top of the propellers to achieve hovering stability. A third propeller is needed to achieve translational flight. Since the center of gravity (C.G.) is located at the bottom of the sphere, the toy is expected to self upright after landed. No ground mobility is possible to avoid an obstacle while on the ground.

2.2 Freely Rotating Spherical Frame UAVs

ELIOS

Flyability, a Swiss company, designed and demonstrated ELIOS to operate in confined spaces and contact with people. Figure 21 shows that ELIOS consists of a quadcopter hinged within an external spherical cage. Early development of ELIOS in figure 22 shows prototype using four control vanes and contra-rotating propellers instead of a quadcopter platform. ELIOS has a take-off weight of 700 grams, including battery and camera as its integrated payload. ELIOS consists of a protective cage entirely decoupled from the drone itself so that the vehicle is not affected by collisions and only destabilizing the outer cage that allows the vehicle to continue flying after a contact. The company claims that the current beta version can hover for about 10 minutes with its default payloads. Detail of the ELIOS can be found in [13].



Figure 21: ELIOS by Flyability [13].



Figure 22: ELIOS's earlier prototype by Flyability [14].

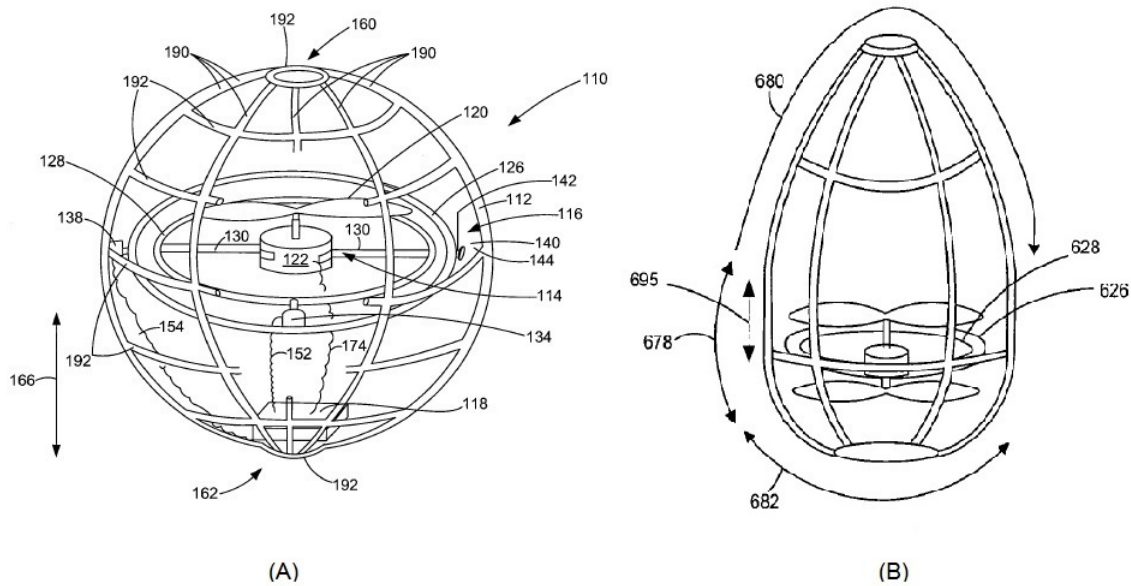


Figure 23: Patent on different cage designs (2010.09.09).

2.3 Existing Patents With Spherical Shape or Caged Design

This subsection presents patents or concepts related to UAV with a spherical shape or caged design. The finding is described chronologically.

Caged UAV with Gimball - US2010/0224723 A1, Sept 2010

This invention presented multiple designs of an aerial vehicle with the propulsion system and a protective frame. The propulsion system includes one or motor rotors or propellers. Figure 23 illustrates a motor mounted on a gimbal system to provide stability in flight. No control vanes are noted. The patent claims that the aerial vehicle is controlled by controlling the pitch and yaw angles of the rotors (item 138 and 134 in the figure), by controlling the angular positions of the gimbals.

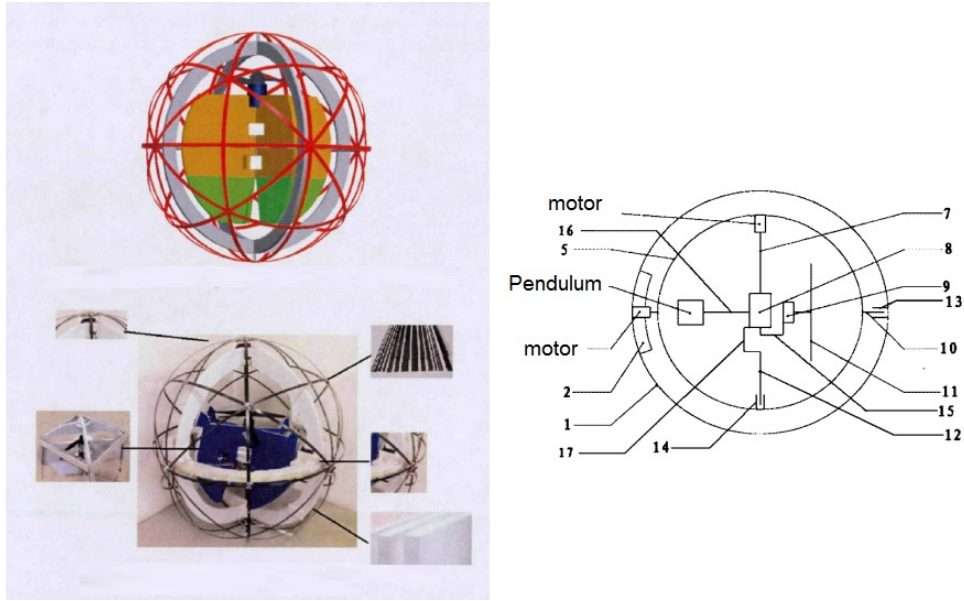


Figure 24: Flying sphere with pendulum and gimbal system [15].

Spherical UAV with Pendulum - CN102358421B, Sep 2011

This invention is designed by The School of Automation at the Beijing University of Posts and Telecommunications in China. As illustrated in figure 24, the top left part is the short axis motor, which makes a relative rotation of the spherical shell and inner frame around the short-axis to change the direction of rolling movement on the ground and swinging flight in the air. The bottom left part is the inner flying device, which can realize the flight function for the vehicle, and the control rudders are set at the bottom of this part; the top right part is the meshed spherical shell made from the carbon fiber. The middle right part is the long-axis motor, which makes the inner flying device rotates around the long axis like a pendulum and causing the vehicle to move forward on the ground or make the aerial vehicle fly forward in the flight motion; the bottom right part is the inner frame, which is a structure to connect the spherical shell to the inner flying device with the long-axis and short-axis motors. Despite their paper [15] has shown a successful take-off flight, no detail of flight attitude or vehicle characteristics were presented.

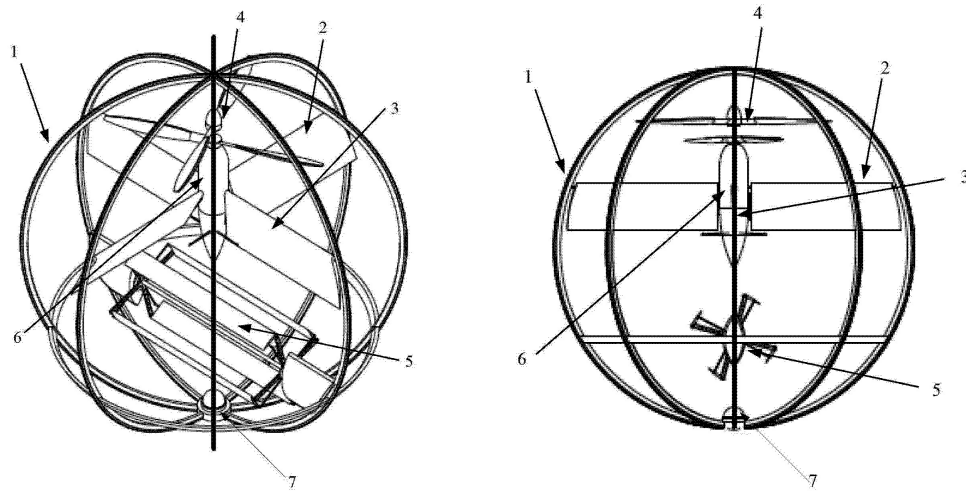


Figure 25: Spherical UAV frame with a cycloidal propeller.

Spherical Micro UAV with Cycloidal Propeller - CN202896880U, Oct 2012

Figure 25 shows that the invention relates to a propulsion mechanism with cycloidal propeller placed under the rear end of the longitudinal axis of the vehicle. The cycloidal propeller is to provide attitude stability and additional thrust. According to the invention, the mechanism uses two coaxial propellers with four control surfaces distributed on a plane vertical to the longitudinal axis where two marks as rudder and elevator, respectively. To realize a pitching moment to achieve forward flight when hovering, the elevator will deflect while simultaneously increasing the rotational rate of the cycloidal propeller to generate additional thrust. Since the cycloidal propeller is only available along the pitching axis of the vehicle, the vehicle needs to actuate the rudder to rotate the vehicle along the axis of the propeller before repeating the pitching maneuver as described before.

Spherical UAV with Steerable Struct Wheels - DE202013003774 U1, April 2013

This design concept has some similarity to the Japanese Flying Sphere except it comes with wheels. This flying sphere concept, as shown in figure 26, is designed as an inspection platform, preferably for wind

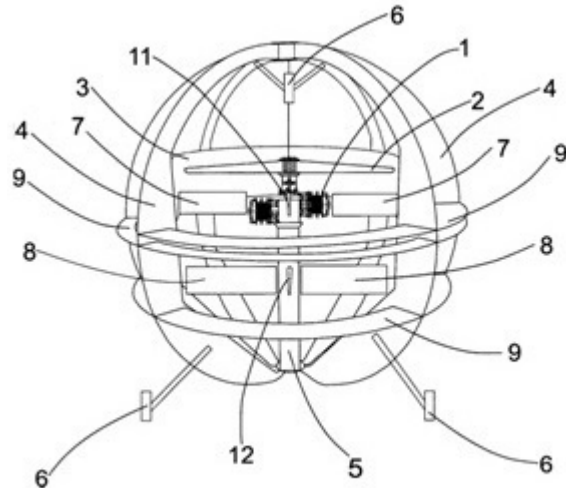


Figure 26: Flying sphere as inspection platform (2013.04.22).

turbines inspection. The frame padded with foam material to The concept is showing two strut wheels attached to the bottom half of the spherical frame as shown as item 6 in figure 26. However, it is not clear how many control surfaces are needed to control the attitude of the vehicle in flight.

Hovering Toy with Stators - USD697,145S, Jan 2014

Figure 27 shows a flying toy with eight fixed stators and a single propeller with a flybar installed inside a plastic cage. The fixed stators purpose is to counteract the yaw moment. This attitude of the toy is not controllable during hovering and has a sonic sensor underneath the toy. The detection of the hand of the user from the sonic sensor will cause the toy to "bounce" off the palm of the operator with an increasing rotational speed of the propeller.

Self-Upright Toy - US 2014/0014767 A1, Jan 2014

Figure 28 shows an aerial toy vehicle that can rights itself from an inverted state in an upright state has a self-righting frame assembly with an apex preferably at the top of a central vertical axis. A pair of contra-rotating propellers with fly bar is located within the central void of the frame assembly and orientated to



Figure 27: Flying Toy - Air Hogs Atmosphere.

provide a lifting force. The frame provides self-righting function and protection of plastic propeller therein. This apex provides initial instability to begin a self-righting process when the vehicle is inverted on a surface. A lift and stabilization panel extends across the upper portion of the frame to provide lift, drag, and stability.

2.4 Other Non-spherical Caged UAVs

HyTAQ

The Illinois Institute of Technology demonstrated a novel take on the roll-cage-wrapped flying vehicle called Hybrid Terrestrial and Aerial Quadrotor (HyTAQ) [16]. HyTAQ uses a spinning cylindrical cage that also allows it to roll along the ground to get around. The vehicle uses the quadrotor to propel the vehicle on the ground. The researcher claimed that rolling uses far less energy than flying because there is no extra weight from additional mechanical components needed to spin the cage; thus it can operate six times longer than a similarly-sized flying-only quadrotor.

AirBurr and Convertible UAV

Laboratory of Intelligent Systems (LIS) in Switzerland is developing a bio-inspired vehicles designed for both flight and ground mission. LIS developed Airburr in 2013, a flying robot that is not only flying indoors but

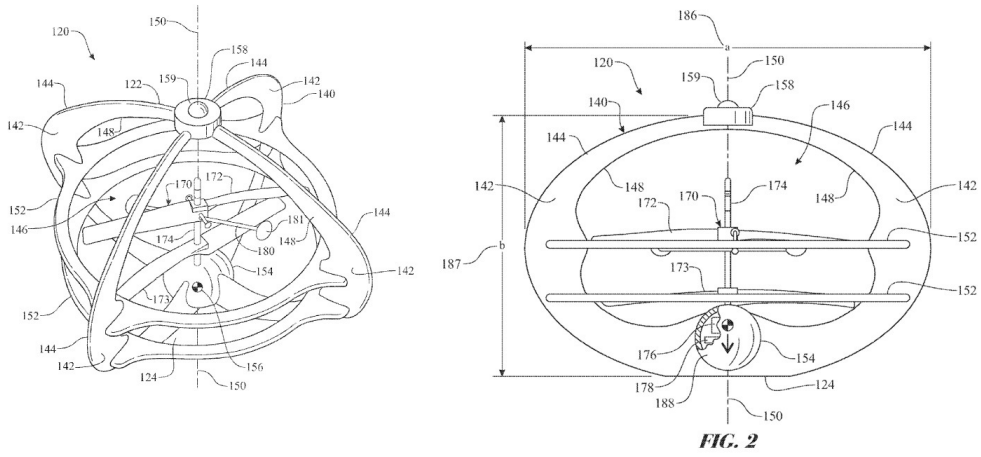


Figure 28: Self-Righting Frame and Aeronautical Vehicle (2014.01.16).

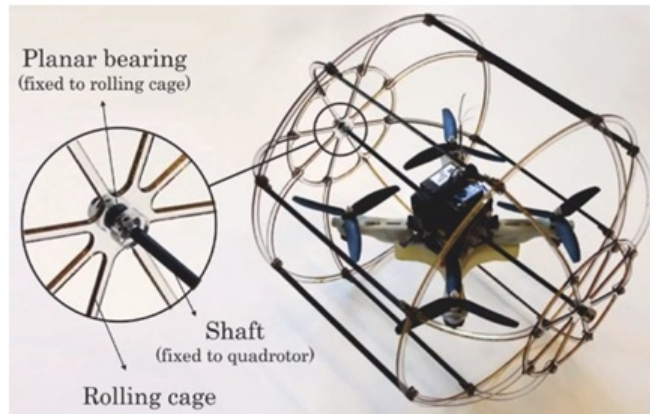


Figure 29: HyTAQ quadrotor with a cylindrical cage with single rotating axis [16].



Figure 30: AirBurr and concept of operation [17].



Figure 31: Convertible UAV by ILS.

can physically interact with its environment. The AirBurr as shown in figure 30 aims to resist collisions with obstacles and return to flight after a crash by using a system of spring-loaded carbon fiber legs to upright itself when on the ground [17]. The current prototype can autonomously stabilize using four control vanes and contra-rotating propellers but has not yet achieved any high-level directional attitude control in flight. Figure 31 shows another hybrid robot designed by LIS as a flying platform designed to hover, fly, roll on the ground, and upright itself by using deployable wings section. The goal of this robot is to enhance the ground locomotion using actuation mechanism to deploy the wings. The robot is expected to use its actuated wing sections to roll and to help steer the robot on the ground.



- 2011 JFS (350g) - No literature**
- 8 active vanes (Control unknown)
 - CG at the center ?
 - No explanation on movable vanes
 - Using slipstream and vanes to upright



- 2013 Korea Single Copter (550g)**
- 4 active vanes
 - No explanation on movable vanes
 - Cannot upright



- *2012 ATLAS Single Prop**
- 4 active vanes
 - No movable vanes
 - Cannot upright



- 2015 Single Prop with thrust vectoring**
- 4 active vanes
 - No movable vanes
 - Cannot upright



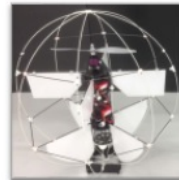
- *2011 ATLAS Contra Rotating**
- 8 active vanes (needs proper controller)
 - Cannot upright



- 2013 UK Contra Rotating**
- 4 active vanes
 - No movable vanes
 - Cannot upright, still have controlling issues.



- 2013 Singapore NUS**
- 8 active vanes
 - No explanation on movable vanes
 - Cannot upright



- 2017 Korean Uni-Copter (420g)**
- 8 active vanes
 - Flexible designed for rapid assembly
 - No movable vanes
 - Cannot upright, still have controlling issues.

* Earlier ATLAS Prototype

Figure 32: Most Spherical UAVs are not able to perform upright maneuver.

2.5 UAVs with Ground Mobility

Note that the majority of the UAVs discussed earlier in this chapter are only designed to hover and transition into forwarding flight and vice versa, but not for ground mobility. Figure 32 shows that most of the spherical shaped UAV with control surfaces are not design for ground mobility. These UAVs spend most of their surveillance mission in the air and can hardly physically intervene in the environment. Even if the UAV is designed to have decent hovering characteristic, with weak or non-existent wireless communication signals and densely populated obstacle fields, robust flight control system and proximity sensors are strongly emphasized to detect an imminent collision and maneuver the aircraft around them autonomously. Coordinated VTOL maneuvering is also needed to avoid the vehicle from tipping over.

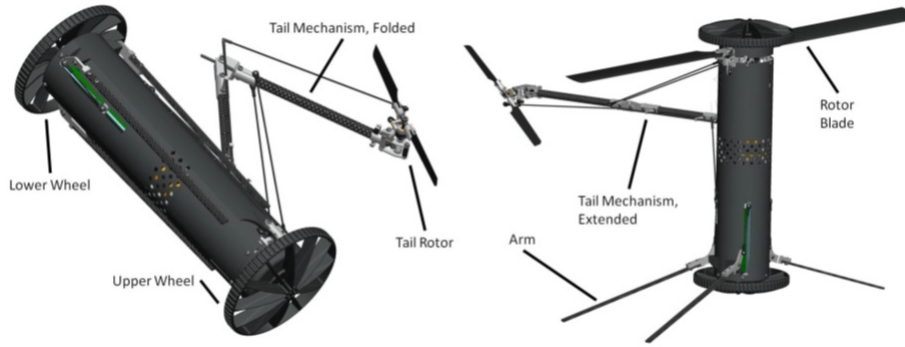


Figure 33: Robot by University of Minnesota [18], [19].

University of Minnesota

Center for Distributed Robotics at the University of Minnesota collaborated with the US Army to develop a robot that can operate on the ground using two wheels and deployable propeller [18], [19]. The prototype, as shown in Figure 33, weighs about 440 grams and has a thrust/weight ratio of 1.37. Such design is extremely fragile with its crucial components exposed to the environment, although they have in mind a successor that will be a whole lot more robust, relying on a non-coaxial system for flight instead. The transition from the ground to flight was successfully demonstrated.

”B”

In May 2013, Witold Mielniczek from University of Southampton announced a quadcopter with four wheels, called the ”B” as shown in figure 34 [20]. The features of the B include vertical take-off and landing, able to transition on the move between driving, flying and back again. The wheels naturally guard the blades around them. If an impact occurs on the side of the vehicle, the prop-saver will protect the blades. Despite the smooth transition from flying to ground mobility, the orientation of the B has to remain in an upright position like a typical quadcopter. A self-upright maneuver is not possible if the vehicle is tipped over or lost one of the exposed propellers.



Figure 34: B concept [20].

2.6 Existing Movable Hinged Vanes

The analysis of the JFS flight video shows that the deflection angle of these movable vanes is restricted within 0 degrees (vertical) to 90 degrees (horizontal) and are passively actuated depending on the RPM of the spinning propeller. A couple of remarks were made on the vanes behavior in-flight based on figure 35: (A) The vehicle is up against the wall, with no forward motion and the relative wind is coming directly towards the propeller, all eight vanes deflected into the horizontal position parallel to the propeller plane. The movable vanes behave similarly during stable hover and taking-off. (B) The vehicle is maneuvering to the left, and the left-hand spoilers are horizontal, the movable vanes on the right side of the sphere are drooped and trapped by the outer cage of the sphere. The right-hand movable vanes oppose the rotation to the sphere. (C) The vehicle tilted to the left, and the movable vanes drooped on the right side.

Related Work

The JFS consists of passively actuated movable hinged vanes that are positioned radially in proximity to the tip of a single rotating propeller. Such setup only available in JFS and not mentioned of such function anywhere. Similarly, the NUS's Spherical Vehicle [6] and the Spherical Flight Vehicle (SFV) [8] integrated passive vanes but no detail of their design or purpose was presented as well [6]. In 2017, Moon [9] presented a one of their prototype that integrated similar passive hinged vanes that claim to improve the flight stability, but no specifics were presented anywhere. Their current flexible structure UNI-copter design, however, shows no passive vanes being integrated. Unlike JFS with passive vanes near the propeller tip, some ducted fan

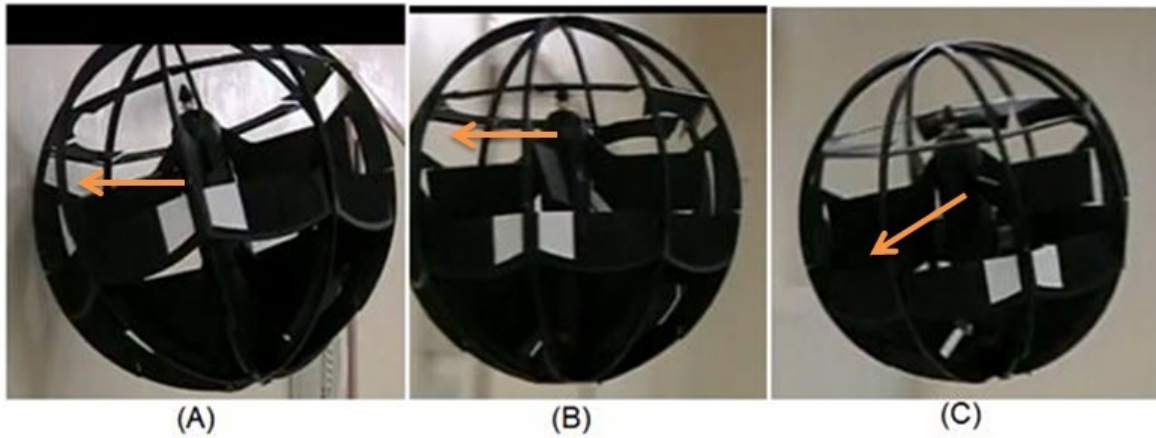


Figure 35: Movable vanes behaviour on JFS during forward flight.

platforms have presented similar feature that produces lift at the inlet lips of the ducted section as shown in figure 37.

Ducted Fan and Auxiliary Controller

Ducted fan or shrouded-rotor is a propulsion arrangement where a fan, which is a type of propeller, is mounted within a cylindrical shroud or duct. Some of the prominent ducted fans platforms are the HoverEye, iSTAR; GoldenEye, and T-Hawk [23] shown in figure 38. The ducted fan is selected as one of the preferred platforms because it produces more thrust than an open propeller with the same diameter and of equivalent power [24]. This enhanced efficiency is a result of the duct producing thrust and eliminating propeller tip losses. The platform has a plurality of control vanes located within the air duct or below the propeller slipstream as depicted in an example in figure 39 and 37.

Overall, the ducted fan is a compact and complex aerial system. It is essential for a ducted fan UAV to remain stable in gusting cross-winds, to be able to transition quickly to translational flight and to have adequate forward-flight performance characteristics. A primary disadvantage of the ducted fan is the asymmetric lift. Studies have shown that the ducted fans experience significant nose-up pitching moment when the vehicle is transitioning from hover to forward flight, as shown in figure 36. A similar situation is also present while hovering in a crosswind condition. Significant research has been focusing on providing a robust

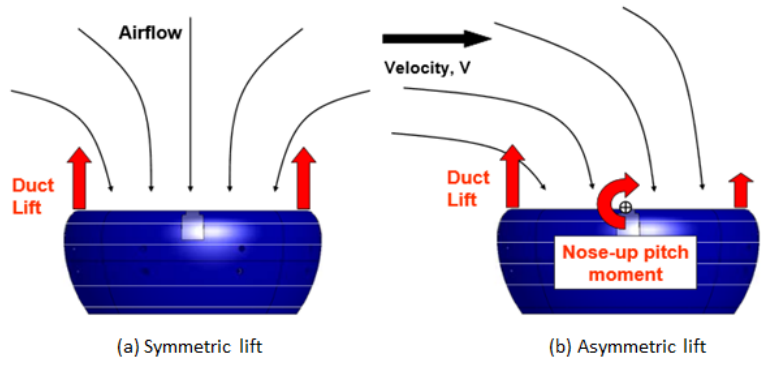


Figure 36: Asymmetric lift [21].

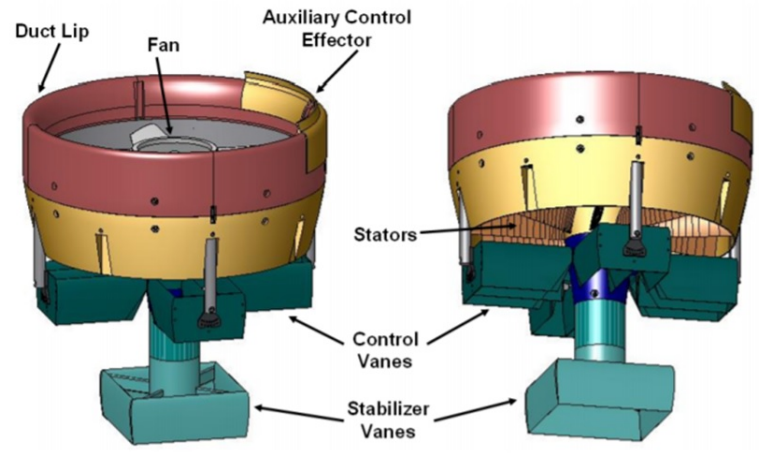


Figure 37: Ducted Fan with four Box Vanes and Stabilizer Vanes with Auxiliary Control Effector installed on the windward side of the ducted section [22].



Figure 38: HoverEye, iStar, GoldenEye, and T-Hawk.

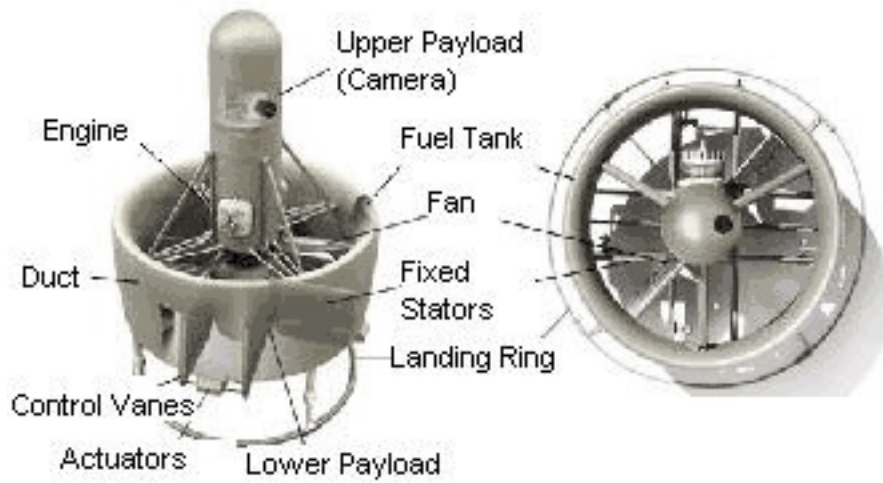


Figure 39: Cutaway view showing Allied Aerospace iSTAR control vanes [25].

control system to operate under crosswind conditions [26, 27, 28, 29].

The pressure on the duct surface created by the air flows induced by the fan significantly affecting the overall forces and moments on the ducted fan platform. According to Kruger[30], the duct lip geometry is very influential in the overall ducted fan aerodynamic characteristic as high-speed air flow into the duct and causes a low-pressure region on the lip of the duct section. In particular, the rapid flow into the duct causes a low-pressure region on the lip of the duct section. Such condition results in a net force in the thrust direction while hovering and can produce lift and pitching moment in translational flight [31]. During the transition from hover to translational flight, which occurs at low speed and high angle of attack, ducted fans experience nose-up pitching moments. This same condition is also present while hovering in a crosswind condition. The destabilizing pitching moment is one of the critical challenges in designing and controlling the ducted fan platform.

Duct lip shaping alone cannot adequately alleviate the destabilizing pitching moment due to asymmetric lift. As a result, some control devices were tested to alleviate the load placed on the control vanes and provide the vehicle with other means of attitude control. Fleming et al. [32] have tested five different types of auxiliary control devices, as shown in figure 40, to either produce more lift or spoil the lift already being generated by the duct lip in a crosswind. These control devices are 40 (A) an internal duct vane and thrust reversal that are adapted from Moller's control devices [33], a "duct deflector" on the windward side of the internal duct wall; 40 (B) a trailing edge flap on the leeward side of the duct, which increases the effective camber of the duct profile; 40 (C) an inlet lip spoiler at the windward side; 40 (D) "leading edge slat" on the leeward side of the inlet; 40 (E) and lip flow control using normal and tangential flow blowing at the lip. According to Fleming's observation, these control vanes perform better than other methods at low crosswind speeds. However, as the crosswind speed increased, the authors observed that these control vanes are stalled.

Duct deflector is another control device to disrupt the flow inside the duct lip, namely to reduce the lift produced by the fan and the duct lip on the windward side [34]. The duct deflector is securely attached to the windward strut and had small flaps that extended outward into the flow. While the ducted fan enhances efficiency on thrust, adding such auxiliary control devices, as well as its control system, are significantly impacting the overall vehicle weight.

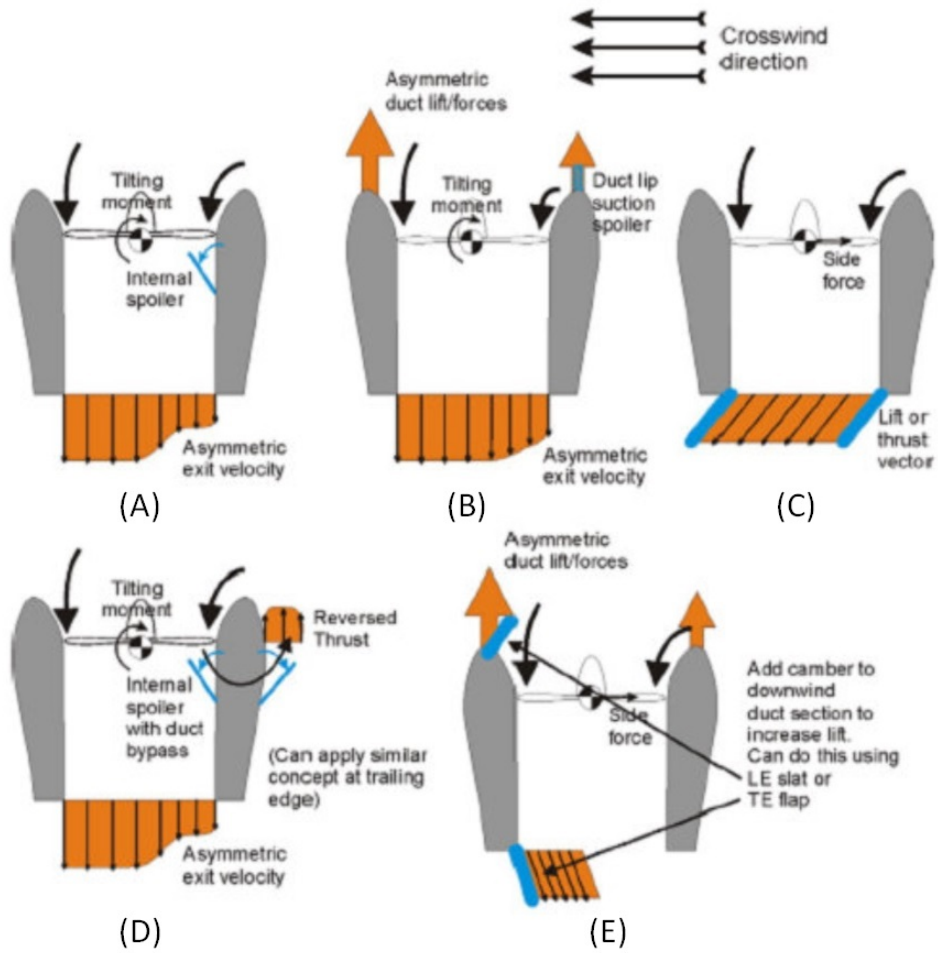


Figure 40: Methods to overcome asymmetric lift of the ducted fan due to crosswind [32].

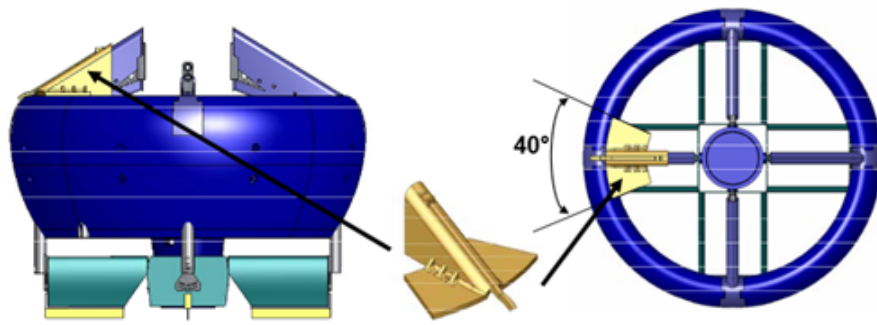


Figure 41: Duct deflectors place near the duct lip and [34].

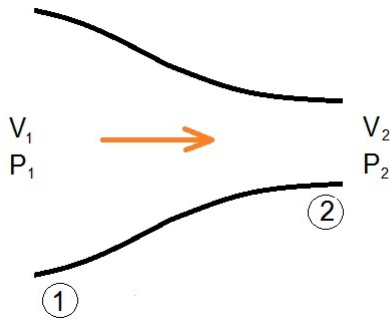


Figure 42: Flow through a duct.

2.7 Preliminary Aerodynamic Theory

Bernoulli's Principle

For an incompressible, steady flow of an ideal fluid free of internal friction, there are three kinds of energy: kinetic energy due to motion, potential energy associated with pressure, and gravitational potential energy. Thus, Bernoulli's equation states that

$$P_1 + \frac{1}{2}\rho V_1^2 + \rho g h_1 = P_2 + \frac{1}{2}\rho V_2^2 + \rho g h_2 \quad (4)$$

Where p is the pressure, ρ is the density, h is the elevation, g is the gravitational acceleration, and V is the velocity. The term, $\frac{1}{2}\rho V^2$ is also known as dynamic pressure. The differences in elevation usually can be ignored and only considering the change of energy of the flow through a duct. It means that static pressure plus dynamic pressure of every point is equal to constant value through a duct or a tube.

Open Rotor Theory

According to the Newton's law of motion, the thrust force is the result of accelerating a mass of air. Figure 43 illustrates the airflow through an open propeller. There are several regions specified by a number within a circle. Region 0 is located at distance sufficiently far above the rotor that the air is not affected by the

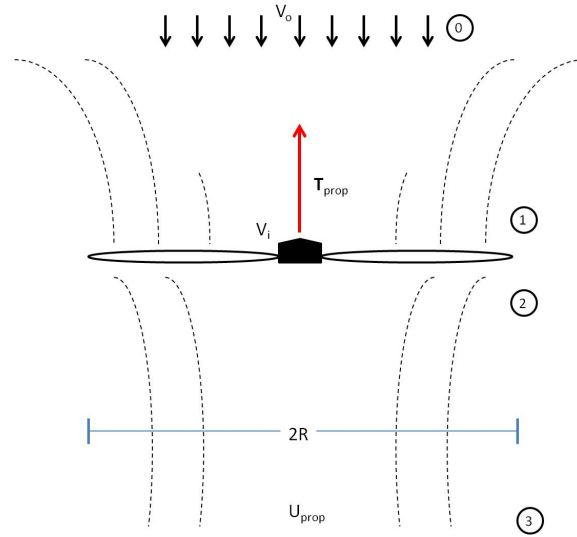


Figure 43: Open Propeller.

propeller. In region 0, the air can be modeled to have a downward velocity of v which is used to model vertical movement. In hover and in the absence of wind, v_0 can be assumed to have zero velocity, or $v_0 = 0$.

Below this region, air flows in the disk perpendicular to the rotating propeller and is accelerated through the propeller until it reaches the fully developed wake region. The velocity of the airflow just above the rotor is known as the induced velocity, v_i . In the wake region, the velocity of the airflow is known as the exit velocity, U_{prop} . The region of moving air is called the *slipstream* which is identified by the dashed line. For a system in equilibrium, like in hover, the slipstream is assumed to be constant with no external disturbance. The propeller is modeled as a thin disc where a pressure differential occurs. An expression for the mass flow rate is given by

$$\dot{m} = \rho A v_i = \rho A_e U_{prop} \quad (5)$$

where v_i and U_{prop} are the induced and exit airflow velocity, respectively. Assuming the induced velocity is uniform, irrotational, and the system is in equilibrium, the mass flow rate for the air moving through the rotor is constant. The force or thrust produced is equal to the mass flow rate times the total change in velocity, which for a state of hover is equal to the exit velocity.

$$T = \dot{m}(U_{prop} - v_0) = \dot{m} U_{prop} \quad (6)$$

The velocity of the airflow can be determined using the change of kinetic energy over time, which is also the power supplied to the airflow. Since power is given as force time velocity, the power supplied to the air is the product of the rotor thrust and the induced velocity,

$$P = T v_i \quad (7)$$

If the system losses are assumed to be negligible, the power supplied by the system is also equal to the change in kinetic energy ΔKE , of the airflow over time t , as shown by,

$$P = \frac{\Delta KE}{t} = \frac{1}{2} \dot{m}(U_{prop} - v_0) = \frac{1}{2} \dot{m} U_{prop} \quad (8)$$

Since the power supplied to the system must be same for Equation 7 and 8, this yields a relationship between the induced velocity and the exit velocity given by

$$U_{prop} = 2v_i \quad (9)$$

From the definition of the mass flow rate in 5, this leads to a relationship between the propeller area and the exit wake area. Also, from 6, a relationship between the thrust and the induced velocity is obtained, given by

$$A_e = \frac{A}{2} \quad (10)$$

$$T = \dot{m} v_i = 2\rho A v_i^2 \quad (11)$$

Bernoulli's equation can be used to determine an expression for the thrust. Since the propeller is modeled as a thin disk, the generated thrust can be given as the product of the pressure distribution over the disk and the disk area. Bernoulli's equation is applied for region 0 to 1, and 2 to 3, but cannot be applied for

region 1 to 2 since the propeller adds energy to the slip stream. This application of Bernoulli's equation leads to

$$p_0 = p_1 + \frac{1}{2}\rho v_i^2 \quad (12)$$

$$p_2 + \frac{1}{2}\rho v_i^2 = p_0 + \frac{1}{2}\rho U_{prop}^2 \quad (13)$$

$$T = (p_2 - p_1)A = \frac{1}{2}\rho A U_{prop}^2 \quad (14)$$

Comparison of Equation 11 and 14 leads the same conclusions given by Equation 9 and 10. The area reduction of the wake is known as wake contraction which can be observed for real helicopter. The theory exaggerates the wake contraction since friction, non-uniform and rotational flow, which all consume power, are not accounted for.

Dimensionless Coefficients

Often dimensionless coefficients are used to describe the aerodynamic forces. Since the lift and drag can change with respect to the direction of the free stream, or the airfoil angle of attack, these coefficients are also a function of the angle fo attack. Expressions for lift and drag coefficients for an airfoil are given by

$$C_L = \frac{L}{\frac{1}{2}\rho S v_\infty^2} \quad (15)$$

$$C_D = \frac{D}{\frac{1}{2}\rho S v_\infty^2} \quad (16)$$

where S is the airfoil surface area, and v_∞ is the free stream velocity. Another commonly used aerodynamic force is thrust. The convention shown for the thrust coefficient by

$$C_T = \frac{T}{\frac{1}{2}\rho A (\omega R)^2} \quad (17)$$

where ω is the rotor speed and R is the radius of the propeller. The Reynold number, which is given by

$$Re = \frac{\rho vx}{\mu} \quad (18)$$

is used to estimate the quality or properties of an airflow over some airfoil or surface, where x is the length of the airfoil parallel to the flow stream, ρ is the fluid density, v is the airflow velocity, and μ is the fluid viscosity. Higher Re values are attributed to turbulent flows or when the flow stream becomes separated.

Aerodynamic Forces on a Flat Plate

The lift coefficient for the case of a thin or symmetric airfoil at low angle of attack is given by

$$C_l = \frac{L}{\frac{1}{2}\rho SV^2} = 2\pi\alpha \quad (19)$$

where the lift curve slope, a is given as the change of the lift coefficient with respect to the change in the angle of attack,

$$a = \frac{\delta C_l}{\delta \alpha} = 2\pi \quad (20)$$

Note that this is an ideal case since lift coefficient is affected by the Reynolds numbers. The lift curve slope for a cambered and symmetric airfoils are both equal to 2π . The difference of a cambered airfoil is that lift is produced even at zero angle of attack as well as differences in the stall characteristics. If α_0 is the angle of attack at which the airfoil produces zero lift, then the lift coefficient is given by

$$C_l = a(\alpha - \alpha_0) \quad (21)$$

CHAPTER III

DESIGN AND CONSTRUCTION

This chapter describes the design features of the ATLAS vehicle to establish the framework for the flight test and validations of the proposed active and passive control scheme for a spherical shape UAV.

3.0 Design Overview

The ATLAS is composed of three parts, which are the propulsion system, the attitude control system, and the airframe system, as shown in fig. 44. The propulsion system includes the brushless DC motor, the microcontroller, battery, and a fixed pitch propeller. The attitude control is composed of two layers of control vanes within the rotational flow field generated by a single propeller. These control vanes produce a certain amount of aerodynamic forces by which the vehicle dynamics are controlled. The vehicle airframe system includes eight flat plates panels, carbon rods, and side panels. The carbon rods and side panels serve as the supporting structure among the plate frames.

3.1 Spherical Frame

The spherical frame is made up of flate foam plate. Four Plate 1 is designed to hold top vanes, and another four Plate 2 is designed to hold bottom vanes. Each panel is cut out from a single piece of 5mm thick paper reinforced foam board using a CNC machine. The surface of the cutout panel is later reinforced with clear tape to strengthen the foam panel. The total weight of these reinforced panels is 123 grams.

3.2 Sizing of the Control Vanes

The effectiveness of the control surfaces and the length of the arm of the acting force of the control surfaces need to be confirmed. These are the design variables of the design of the active control surfaces. The

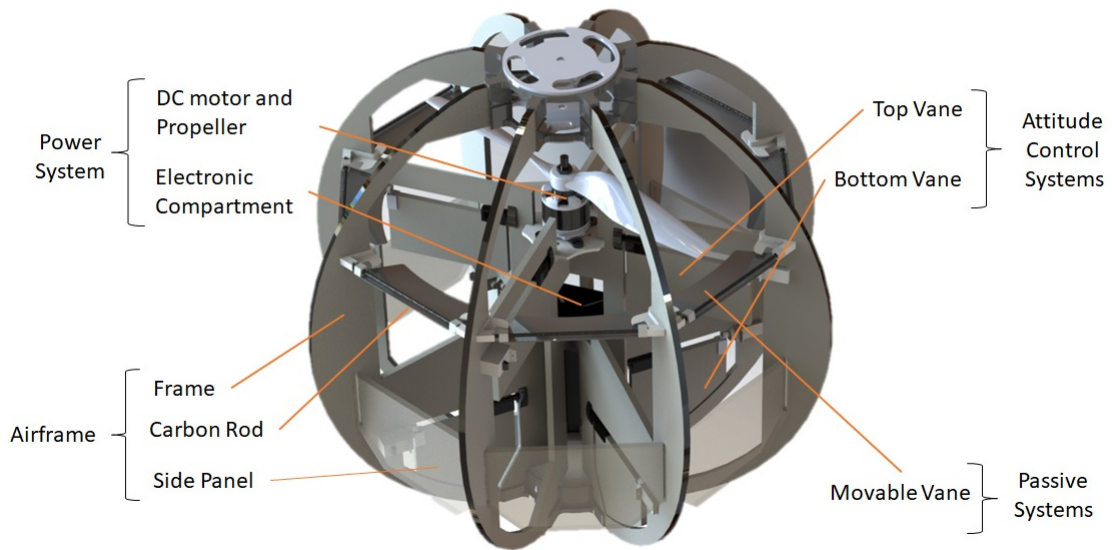


Figure 44: ATLAS - All Terrain, Land and Air Sphere.

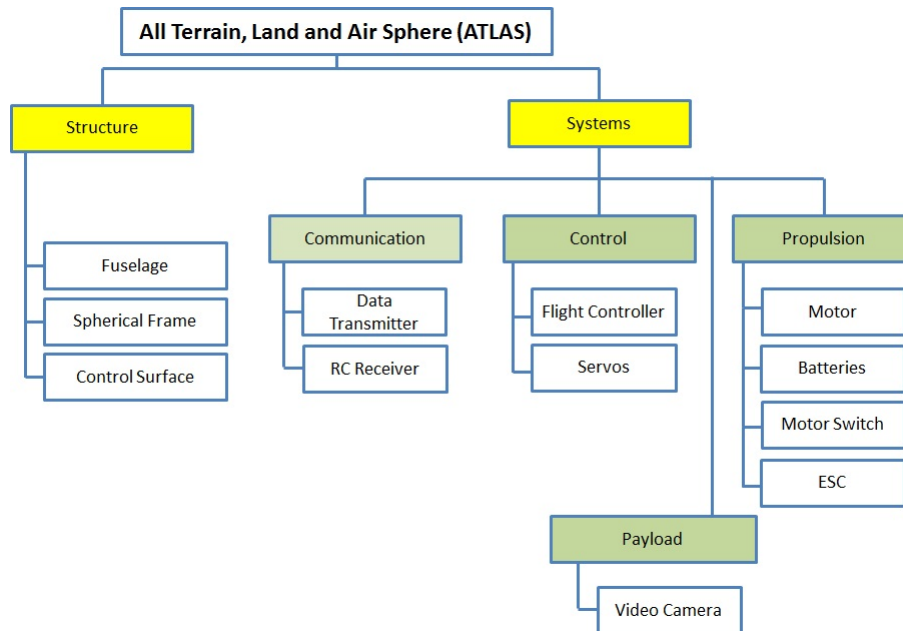


Figure 45: Structures and System of ATLAS.

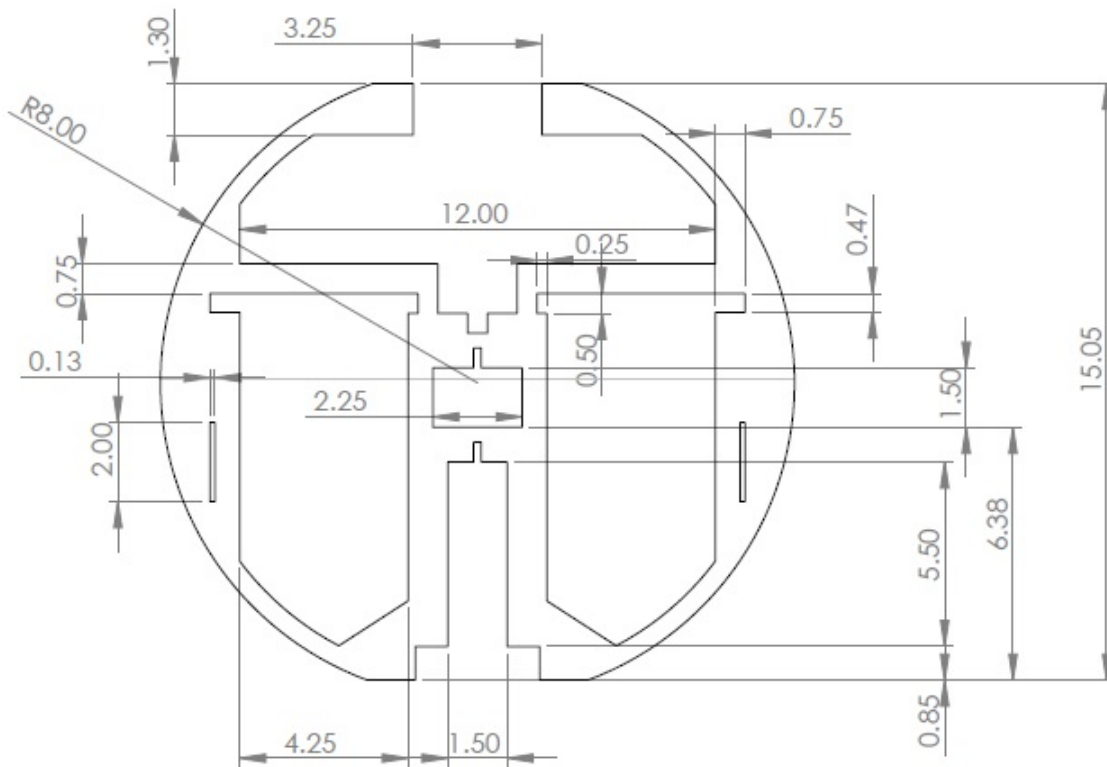


Figure 46: Dimension of the main flate panel frame.

maximum size of the control surface area is restricted by the inner diameter of the spherical frame. The control vanes sizing was determined by quarterly divided the sphere into four segments, as shown in fig. 48. The propeller is fitted within the top half of the circle, h_1 and h_2 depending on the height of the motor. The top vanes and bottom vanes are placed within the third segment, h_3 and fourth segment, h_4 , respectively. The control vanes are made of 5mm thick paper reinforced foam board. Figure 49 shows the dimension of each top and bottom control vanes for a 16" diameter ATLAS.

3.3 Other Structural/3D Components

These are 3D printed parts made of ABS plastic to hold the airframe components together. Fig. 51 shows the detail for each parts. Both top collar and Bottom collar are designed to hold the foam panels together.

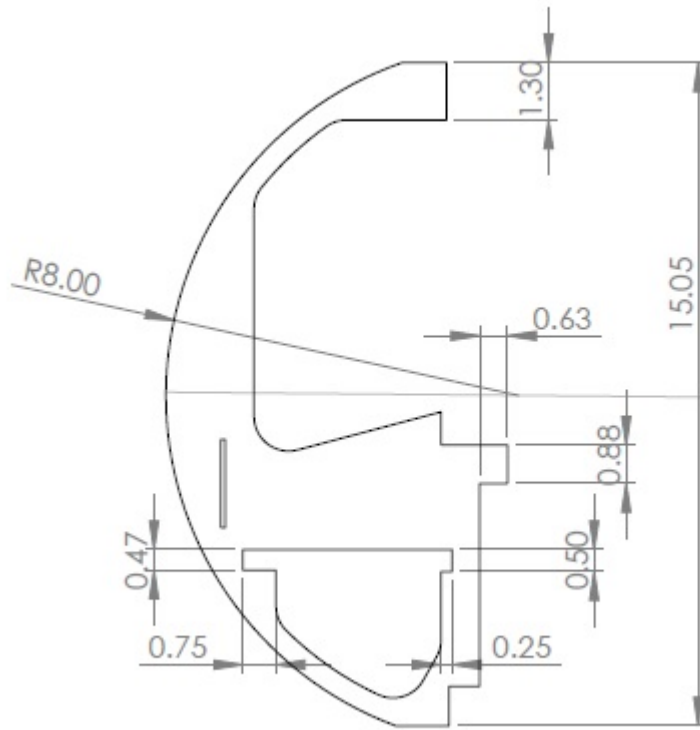


Figure 47: Dimension of a side flate panel.

Both ends of a 0.01” diameter carbon fiber rods can insert into the slots on both sides of the Joint part. The carbon fiber rod helps support the gap between the foam panels radially.

3.4 Servo

ATLAS uses Hobbyking HK15178 analog servo to actuate each control vanes. The selected servo has a torque of 1.2 kg/cm at 4.8 V or 1.4 kg/m at 6V, with speed of 0.10/60 Deg at 4.8V or 0.09/60 Deg at 6V, respectively. The plug type is JR type. To translate the rotational motion of the servo to actuate the control vanes and reduce moving parts, the servo arm is attached directly onto the side of the vanes along the vane’s hinge line.

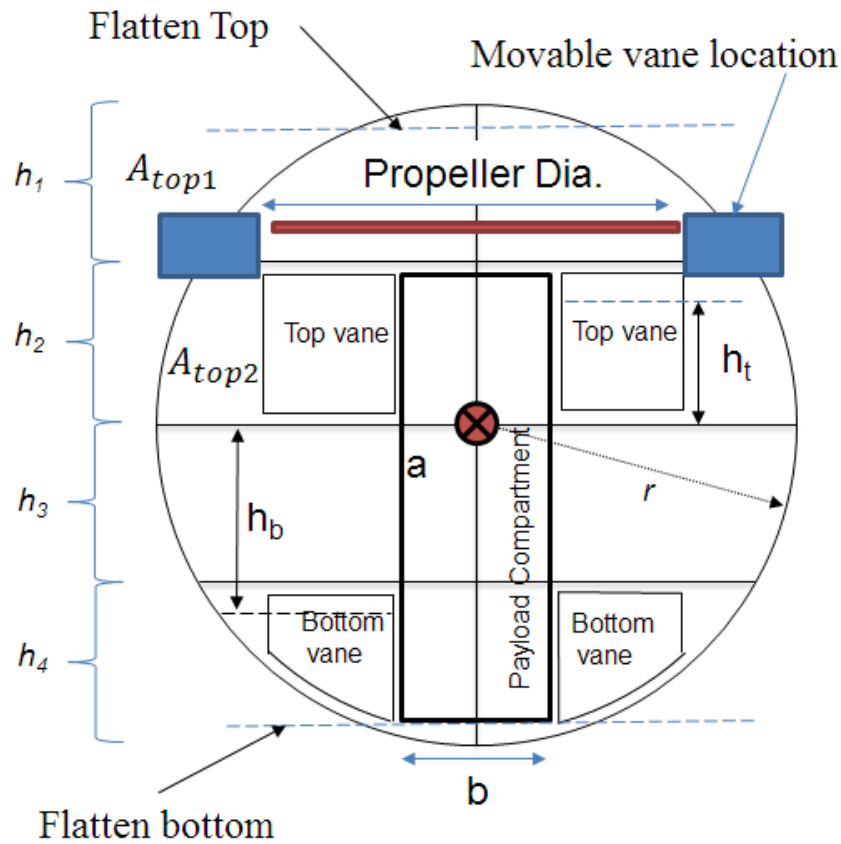


Figure 48: Sizing and location of the control vanes.

3.5 Top and Bottom Vanes Attachment Method

Figure 53 shows the 9 grams servo are attached directly to the control vane without any linkages. A 3D printed part was made to hold the servo horn and attached permanently using epoxy to the side of the control vane.

3.6 Passive Movable Guide Vanes and Setup

Figure 54 shows ATLAS consists of eight passively actuated movable vanes that are positioned radially in the proximity to the tip of the propeller. Fig. 55 shows the parameters of the movable vanes within the

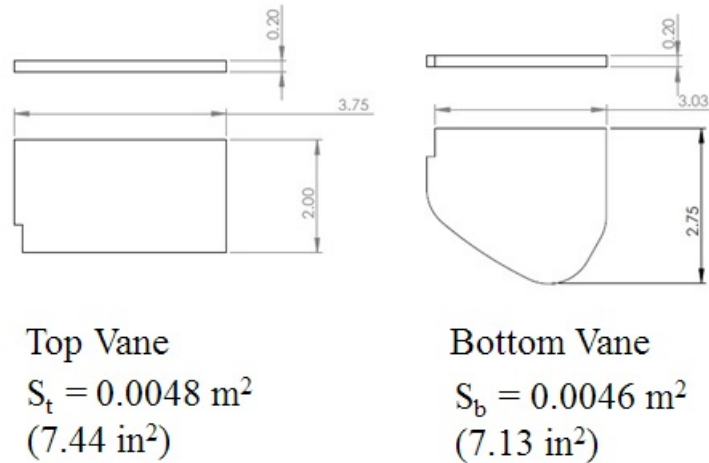


Figure 49: Dimension of the top and bottom control surface.

spherical frame. Note that the rotation for each vane is mechanically restricted between 0 to 90 degrees. 90 degrees is when the movable vane is fully deflated and remaining horizontal or parallel with the propeller plane. 0 degree is vertical or perpendicular to the propeller plane.

3.7 Brushless Motor

The latest ATLAS vehicle uses a T-motor MT2814-10, with 770kv as shown in figure 58. It weighs about 120 grams with its specifications shown in figure 59. Earlier prototypes using coaxial propellers is presented in Appendix B.

3.8 Single Pitch Propeller

The propeller is a APC slow flyer electric 11x7 propeller as shown in figure 60

3.9 Battery

The battery is a 14.8V 4 cell lithium-polymer (Li-Po) with 1550mAh capacity, as shown in figure 61. The weight of the battery is about 177grams with a dimension of 72 x 36 x 35mm. The battery has an XT60



Figure 50: 1 of 8 sidepanel.

connector type. It has a discharge rate of 75C and a max burst discharge rate of 150C.

3.10 Electronic Speed Controller (ESC)

The ATLAS equipped with the Phoenix Edge Lite 50-Amp, as shown in figure 64. The weight of the ESC is about 28 grams (1.0oz) without wires. The ESC has a dimension of 25.4 x 50.8 x 23.2 mm. This ESC can support battery size ranging from 2 to 8 cells lithium polymer battery with a maximum of 50amp continuous amperage at full throttle. The user can program the Battery Eliminator Circuit (BEC) voltage between 5 to 8.4 V. The ESC can produce a 5 amp peak BEC output. The function with the data logging capability allows the user to record the performance of the motor during flight test. The Edge series introduces a user programmable auxiliary wire can be used for helicopter governor gain input adjustments mid-flight, serve as an audible beacon after an unexpected landing, act as an RPM output for three-axis gyros that support RPM sensors, be used as an ESC arming lock or as a receiver arming lock. The reverse throttle program is the key function that allows ATLAS to reverse the thrust for upright maneuver. This program is only available in 2017 as part of their 4.24 version firmware update.

3.11 Mechanical and Electronic Thrust Reversal System

Figure 63 shows a Double Poles Double Throw (DPDT) switch used to reverse the motor polarity that provides the up-right maneuverability in the earlier prototyping stage of ATLAS. The switch is actuated

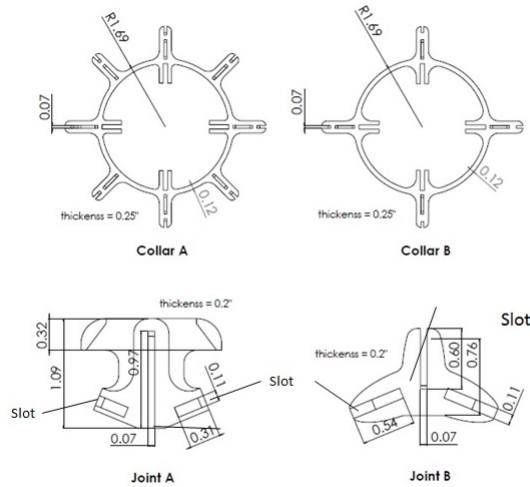


Figure 51: 3D Components - Collars and Joints

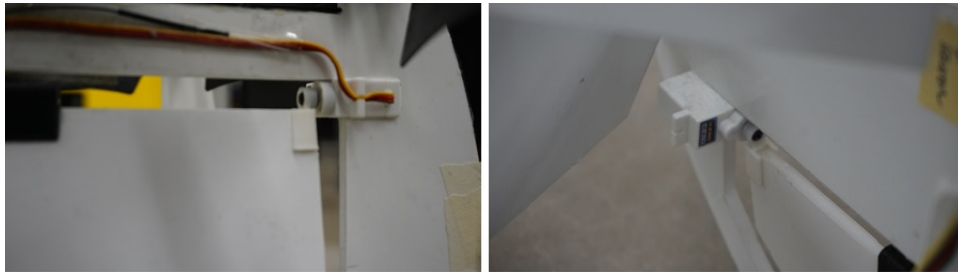
using a 9-gram servo. The mechanical actuation switch was later replaced and directly controlled by using an EDGE 50 amp Creative Castle ESC as seen in fig. 64, as described previously. The controller will use the AUX LINE to reverse the motor direction. When the AUX LINE receives a signal below 20% ($< 1.2ms$) the motor will spin in the direction specified by the Motor Direction setting. When a signal above 80% ($> 1.8ms$) is received, the motor will spin in the opposite direction. Signals between 20% and 80% do not affect the motor direction. If the motor is rotating when the AUX LINE indicates a change in direction, the controller will stop applying power to the motor until it has stopped before reversing the motor in the opposite direction.

3.12 Battery Eliminator Circuit (BEC)

Despite the Phoenix Edge ESC has an integrated BEC, an additional BEC is required to provide sufficient power to energize the eight servos. The Creative Castle BEC, as shown in figure 62, is designed to operate at up to 6S LiPo with a 10A peak servo load. The weight of the BEC is about 10 grams.



Figure 52: HK15178 analog 9 grams servo.



Top Control Vane Servo

Bottom Control Vane Servo

Figure 53: Servo connected to top and Bottom control surfaces.

3.13 Fuselage and Payload Compartment

The top of the ATLAS is a 3D part collar designed to have a compartment, as shown in figure 65 to integrate payloads like camera and sensors. Figure 66 is an example that shows a Session 4 Gopro being mounted to face the upward for indoor roof inspection purpose.

3.14 Onboard Flight Controller

Various types of flight controllers were tested throughout the research, that includes APM by Ardupilot, KKboard by Hobbyking, and Piwhawk. Due to the size restriction, power, and programming experience needed to customize a flight controller, Multiwii Crius by Hobbyking was selected as the main controller board to developed ATLAS. Figure 68 shows the Multiwii board that features multiple series interfaces as

Passively movable vanes

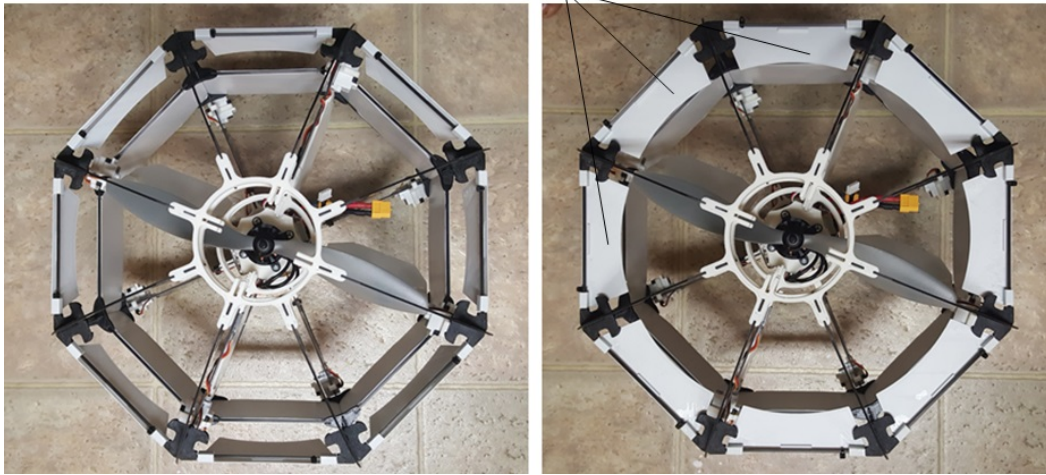


Figure 54: Hinged movable vanes position at 0 deg vs. 90 degs.

well as a dedicated I2C interface using an ATmega 2560 microcontroller. It has the dimension of 50 mm x 50 mm and weighs about 14.2 grams. The motion sensing side features a MEMS gyro, an MPU6050 by IvenSense, which has the gyro and accelerometer sensor on a single chip. There is also an HMC5883L 3-axis digital magnetometer and a barometer sensor with a resolution of 10 cm height different. The board has eight input channels for a standard radio receiver and supports up to eight motor or servo outputs, two servo output for pitch and roll gimbal system and one servo output to trigger a camera button. The board also features six analog outputs and an I2C port for extending devices. The board is programmable using Arduino software by using a MicroUSB connection. Additional sensors can be integrated into the board, such as 10 Hz GPS, sonar sensors, Bluetooth. A 5V BEC is needed to provide additional power to energize the board and the eight servos. Below are some listed features about the Multiwii board :

- Supported MegaPiratedNg and Multiwii Firmware
- Up to 8-axis motor output
- 8 input channels for standard receiver
- 4 serial ports for debug/Bluetooth Module/OSD/GPS/telemetry
- 2 servos output for PITCH and ROLL gimbal system
- 6 analog output

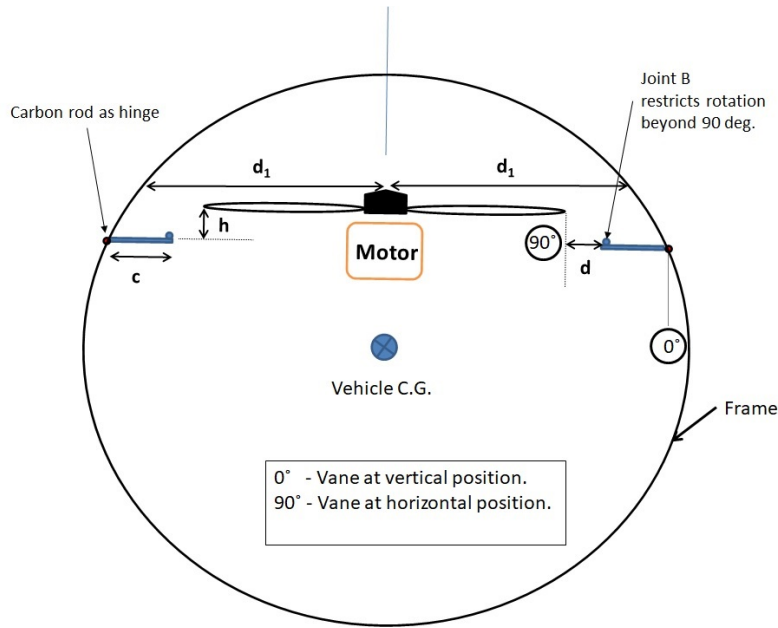


Figure 55: Passive movable vane setup.

- A I2C port for extend sensor or device
- Separate 3.3V and 5V LDO voltage regulator
- ATMEGA 2250 controller
- MPU6050 6 axis gyro/accel with motion processing unit
- HMC5883L 3-axis digital magnetometer, MS5611-01BA01 high precision altimeter, FT232RQ USB-UART chip and micro USB receptacle
- On Board logic level converter
- Match the standard RoHS

3.15 Android- base- app and Bluetooth

Another option for field configuration without a computer is to use an Android smartphone and a Bluetooth module. For recording flight data, only Bluetooth module or FTDI communication can active at a time.

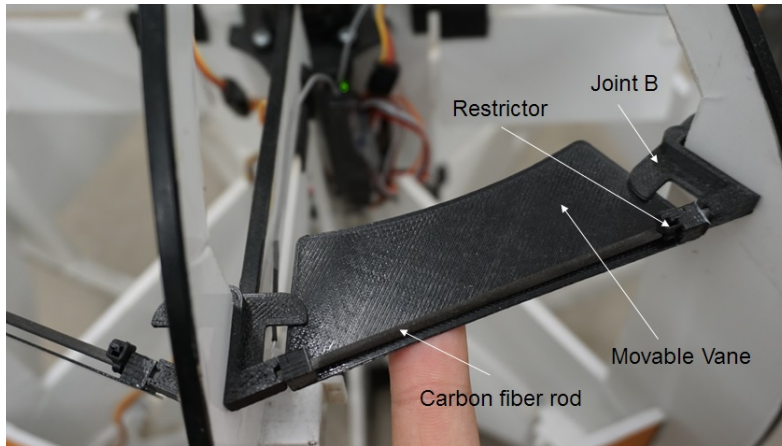


Figure 56: 3D components - 1 of 8 movable hinged vane.

For an Android smartphone, EZ-GUI Multiwii v4.5.450 app is used to allow a user to tune the PID gains and all parameters in the flight controller. The app converts the flight data into an Excel file for post-flight analysis. Figure 70 shows a screenshot of some of the EZ-GUI smartphone app functions. However, since the app was designed for multirotor, this app is only being used for flight data collection and PID tuning for ATLAS. Figure 71 showing the detail tab to tune the PID gains of the controller during a flight.

3.16 Computer based Graphical User Interface (GUI)

Figures 72 show the GUI interface tailored for the ATLAS flight controller. The interface of the GUI is customizable using the Processing 2 software. The GUI also displays sensor data and vehicle attitude from the flight controller thru Bluetooth communication at a baud rate of 57600. This GUI allows the user to modify operational mode options, parameters and trimming or limit the servo travel. List below is showing the functions shown in the GUI.

- A - Communication port to connect Multiwii over USB
- B & C - Filtered reading from onboard sensors
- D & F - Visualization of the vehicle's attitude
- E - Reading from Magnetometer and GPS Module
- G - PWM value - Input from transmitter controller and output from servo(s) and motor(s)

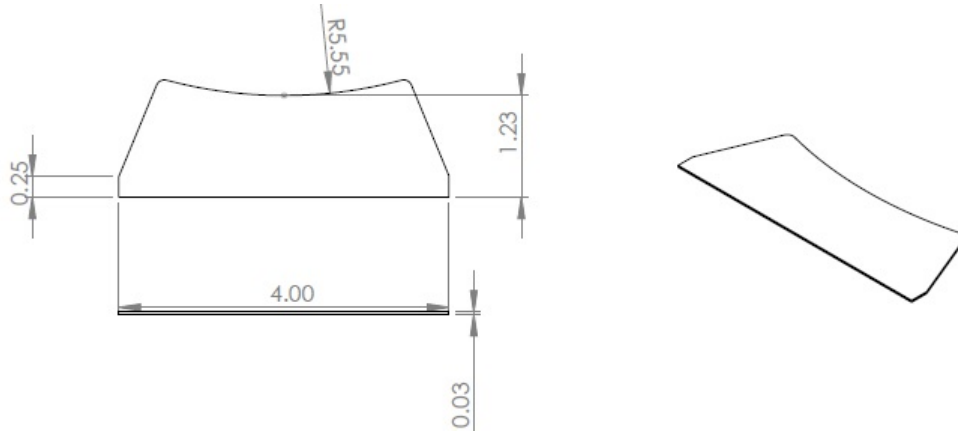


Figure 57: Dimension of a 3D printed movable vanes for a 11” prop.



Figure 58: T-motor MT2814-10, 770kv motor

- H - Modes Option
 - I - Parameters /Settings to set the Global and Altitude PID
- Expo settings set the Expo and Rate settings for throttle, or Pitch/Roll
- J - Servo trimming, max and min travel limit

3.17 System Total Weight Distributions

The pie chart below shows the distribution of the components for a 900 gram ATLAS introduced in figure 73. Table 74 shows the detailed breakdown for each major components.

KV	770
Configu-ration	12N14P
Stator Diameter	28mm
Stator Length	14mm
Shaft Diameter	4mm
Motor Dimension(Dia.*Len)	Φ35×36mm
Weight(g)	120g
Idle current(10)@10v(A)	0.5A
No.of Cells(Lipo)	3-4S
Max Continuous current(A)180S	29A
Max Continuous Power(W)180S	500W
Max. efficiency current	(6-19A)>81%
internal resistance	100mΩ

Figure 59: Specifications of the T-motor MT2814-10, 770kv motor.



Figure 60: APC slow flyer electric 11x7 propeller.



Figure 61: 4s Lipo 1550 mAh battery.



Figure 62: 5V BEC.

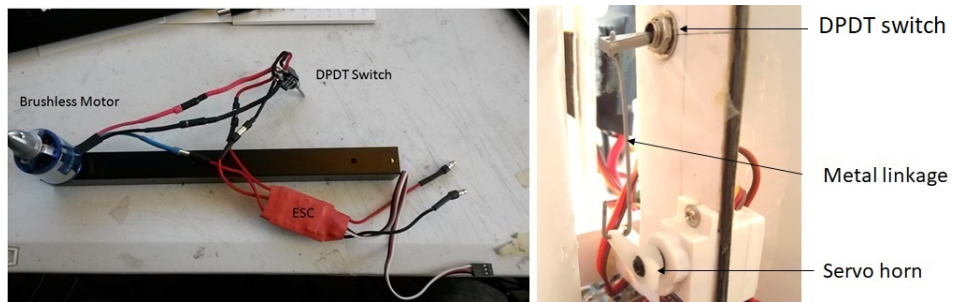


Figure 63: Mechanical thrust reversal system with DPDT switch plus servo.

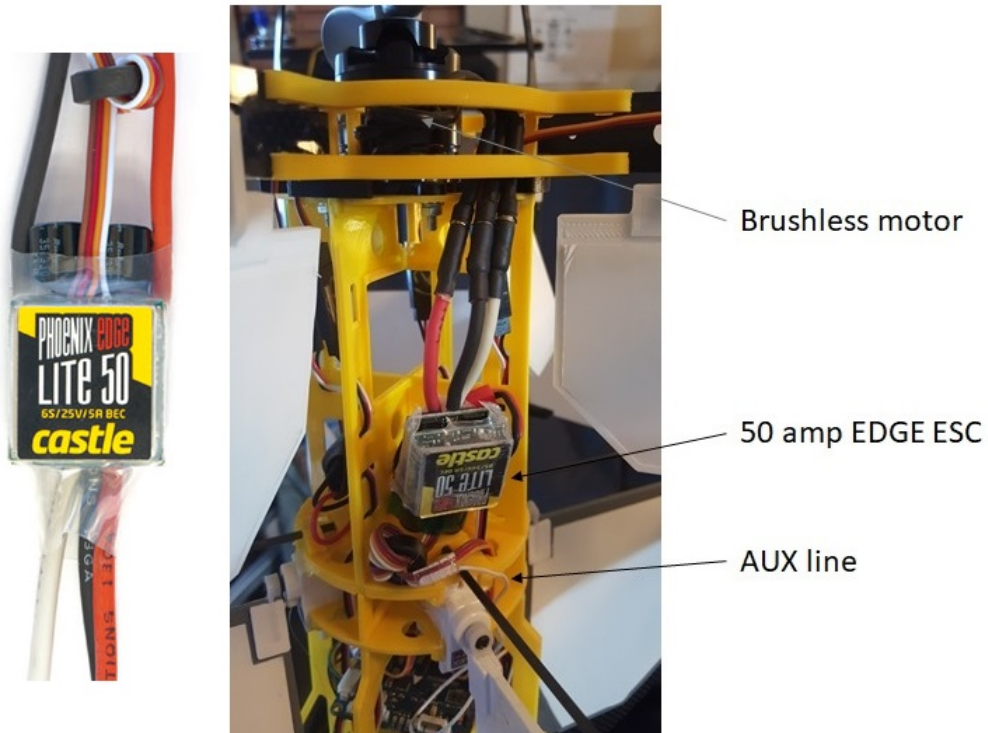


Figure 64: Electronic thrust reversal system removed the needs of servo and DPDT switch between motor and ESC.

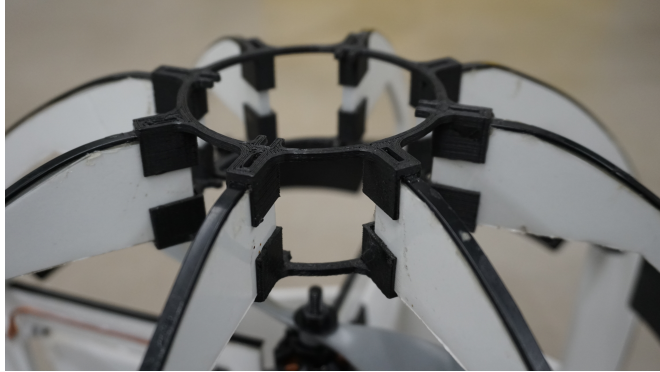


Figure 65: 3D components - top collar.



Figure 66: A GoPro Session 4 mounted on top of the top collar for indoor rooftop inspection.

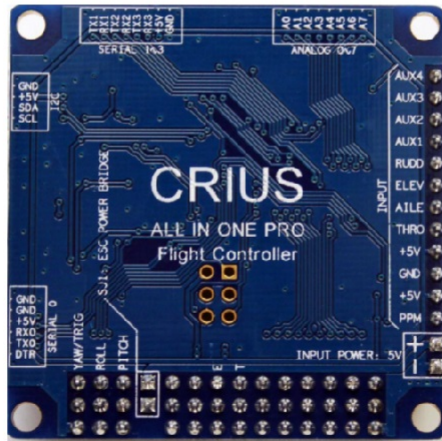
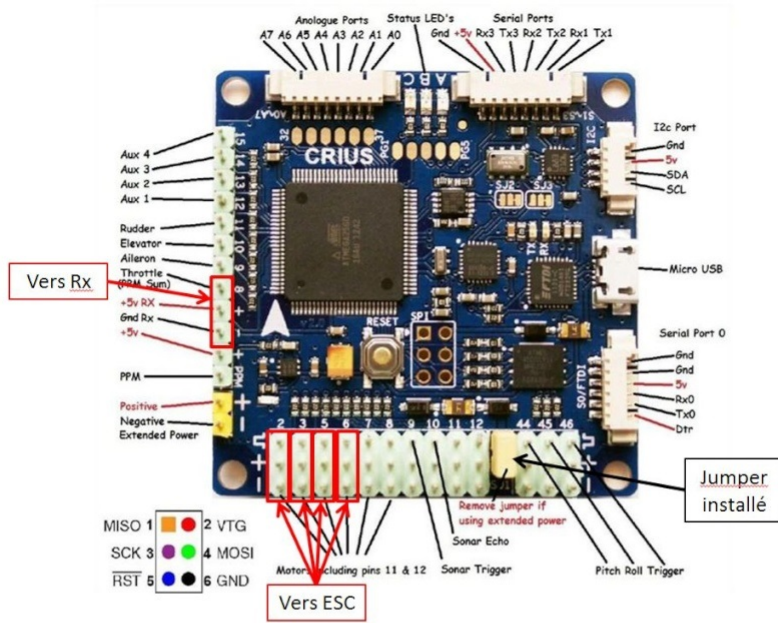


Figure 67: Multiwii ATmega 2560.

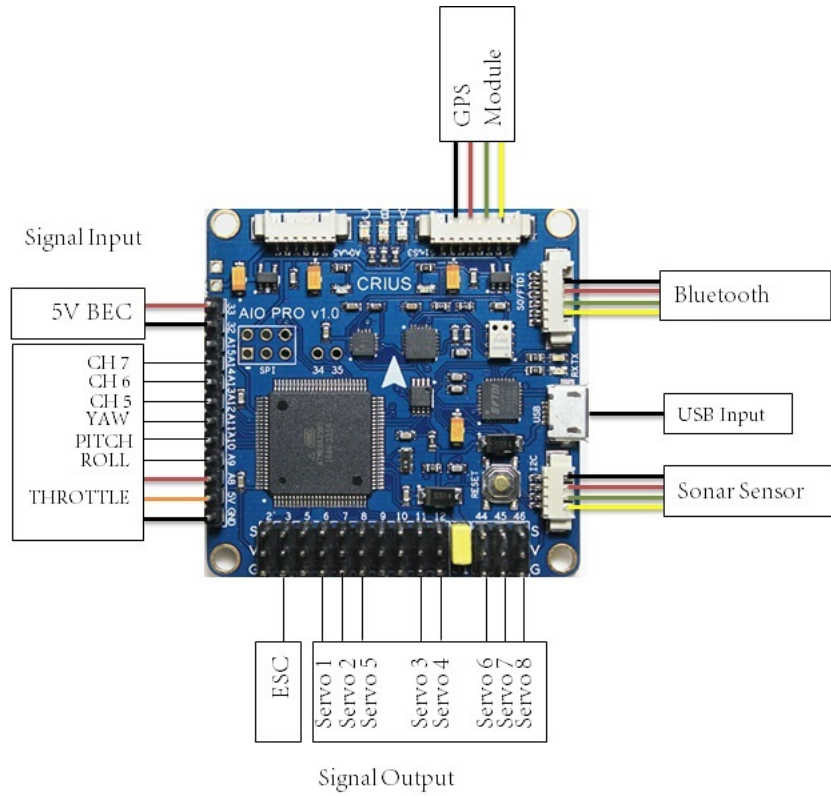


Figure 68: Multiwii setup for ATLAS.

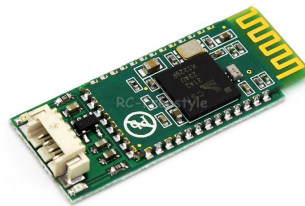


Figure 69: Bluetooth module.

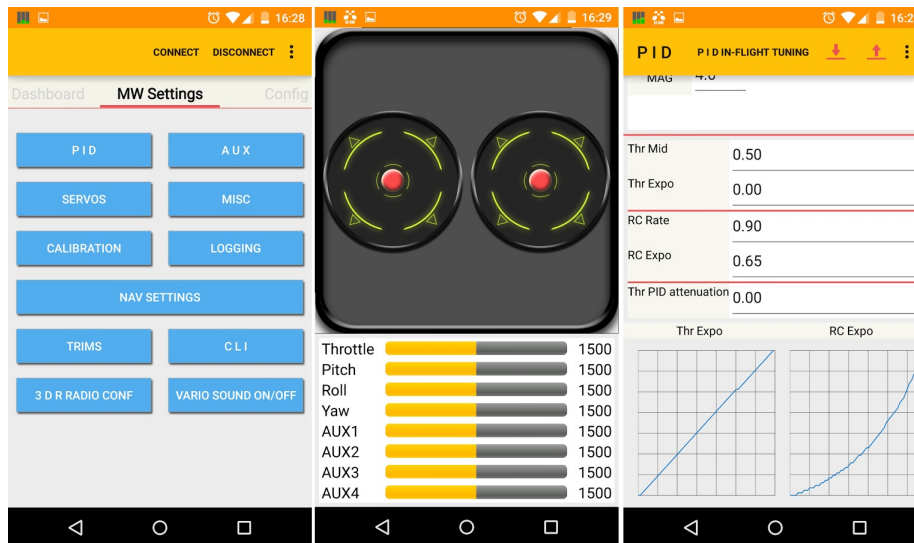


Figure 70: EZ-GUI Android based App.

PID				
PID IN-FLIGHT TUNING				
	P	I	D	RATE
ROLL	3.3	0.030	23	0.00
PITCH	3.3	0.030	23	
YAW	6.8	0.045	0	0.00
ALT	6.4	0.025	24	
Pos	0.11	0.0		
PosR	2.0	0.08	0.045	
NavR	1.4	0.20	0.080	
LEVEL	9.0	0.010	100	
MAG	4.0			
Thr Mid	0.50			
Thr Exp				

Figure 71: Android app to tune the PID controller via Bluetooth.

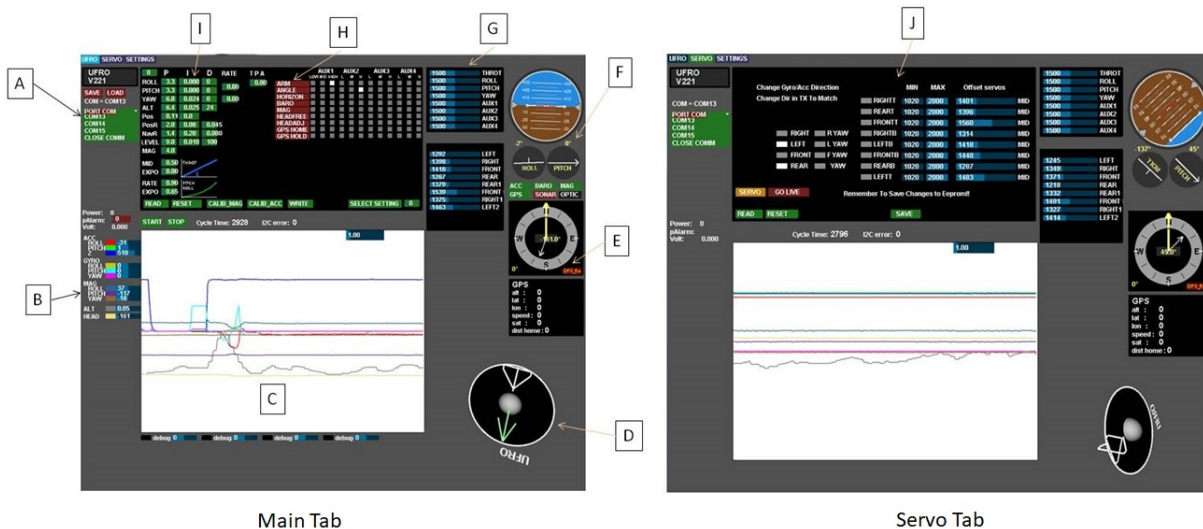


Figure 72: GUI customized for ATLAS using Multiwii controller.

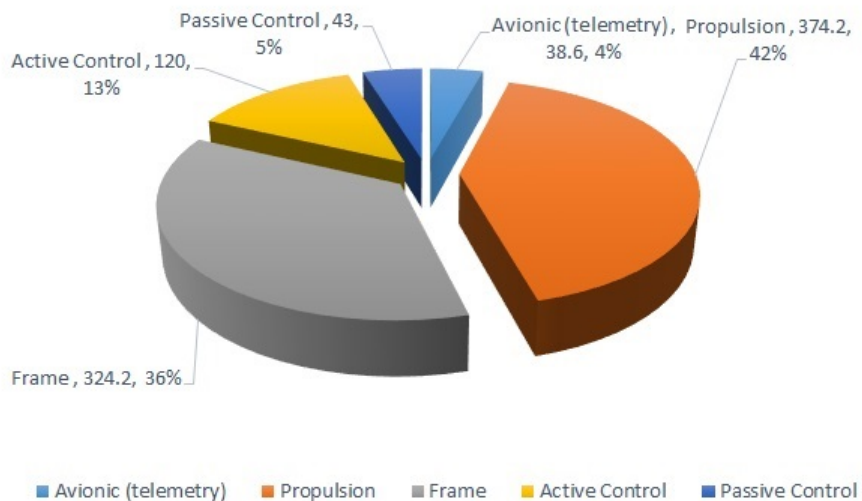


Figure 73: Component breakdown and weight contributions.

	Items	Grams	%
Avionic	Controller Board	13	1%
	RX	10.6	1%
	BEC	10	1%
	Bluetooth	5	1%
Passive Control	Movable vanes clip	11	1%
	Movable vanes + carbon rod+ plastic	32	4%
Active Control	Control vanes and parts	40	4%
	Servos	80	9%
Propulsion	ESC + cable	54.4	6%
	Motor MT-2814-10 770kv	120	13%
	Propeller 11x7	14.8	2%
	Lipo 1550 mAh Battery	185	21%
Frame	motor abs mount	6	1%
	bottom abs and cap	24	3%
	Foam Panel and Reinforce stripe	123.2	14%
	Side Panels	60	7%
	Adhesive and others	111	12%
Total Weight (grams)		900	100%

Figure 74: Detail components breakdown and weight contributions.

CHAPTER IV

GROUND TESTING SETUP AND RESULTS

This chapter presents the ground experimental setups, testing, and results.

4.0 Facility and Equipments

Wind Tunnel

The Oklahoma State University FLOTEK 1440 wind tunnel is an open loop Eiffel tunnel with a contraction ratio of 12:1, down to a test section measuring 12" x 12" x 36" (305mm x 305mm x 914mm) long. The air velocity through the test section is variable up to 132 fps (40m/s). The test section has clear acrylic side walls and top to give a clear observation of the test in progress. Figure 76 shows the relationship between the tachometer value vs. the average wind speed in the test section of the wind tunnel. The wind speed was measured using a Pro-vernier anemometer placed at the middle of the wind tunnel test section.

Flight Test Chamber and Motion Tracking System

OSU Indoor flight chamber with a motion capture system was used to investigate the flight dynamics of the ATLAS. As shown in figure 78, Twelve Flex 3 cameras by OptiTrack was setup using six tripods to cover the flight area. Each camera has a resolution of 640 x 480 with 100 frames per second frame rate. To capture the entire flight trajectory, the vehicle should not fly beyond the field of view of the cameras. MOTIVE, a dedicated motion capture software for Flex 3, was used to playback and analyze the trajectory of each flight test. Figure 79 shows the flight trajectory of the vehicle in X, Y, and Z axis. Motion data can be converted to excel format for post-processing.



Figure 75: Oklahoma State University's Flotek Wind Tunnel.

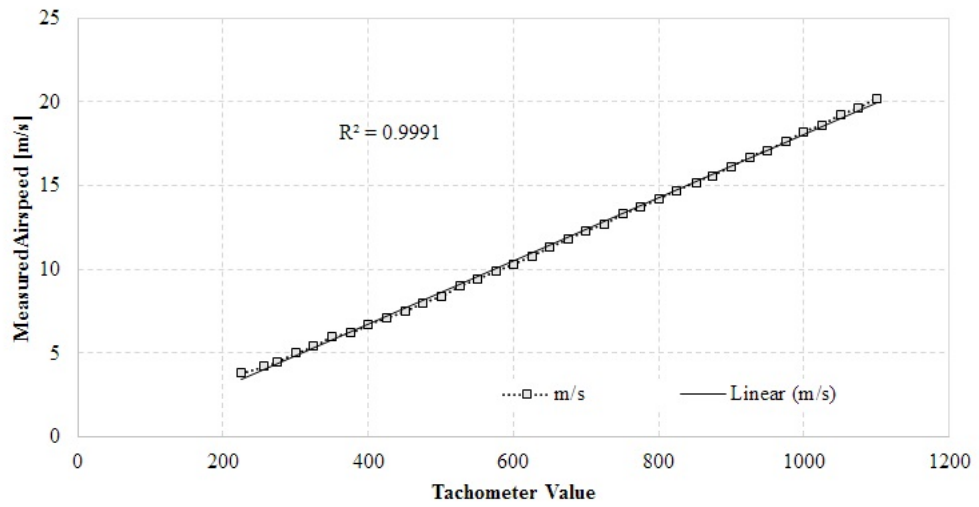


Figure 76: Wind tunnel calibration to obtain the relationship between the tachometer value vs. wind speed at test section.



Figure 77: Flex 3 motion capture camera by OptiTrack.

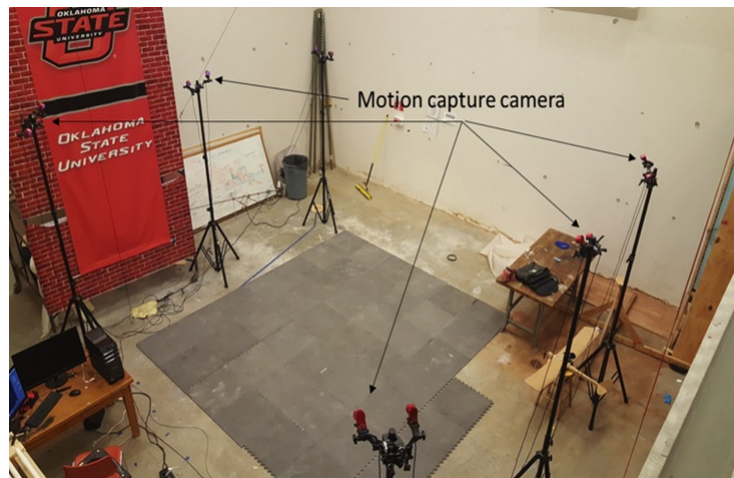


Figure 78: OSU Indoor flight chamber with motion capture system.

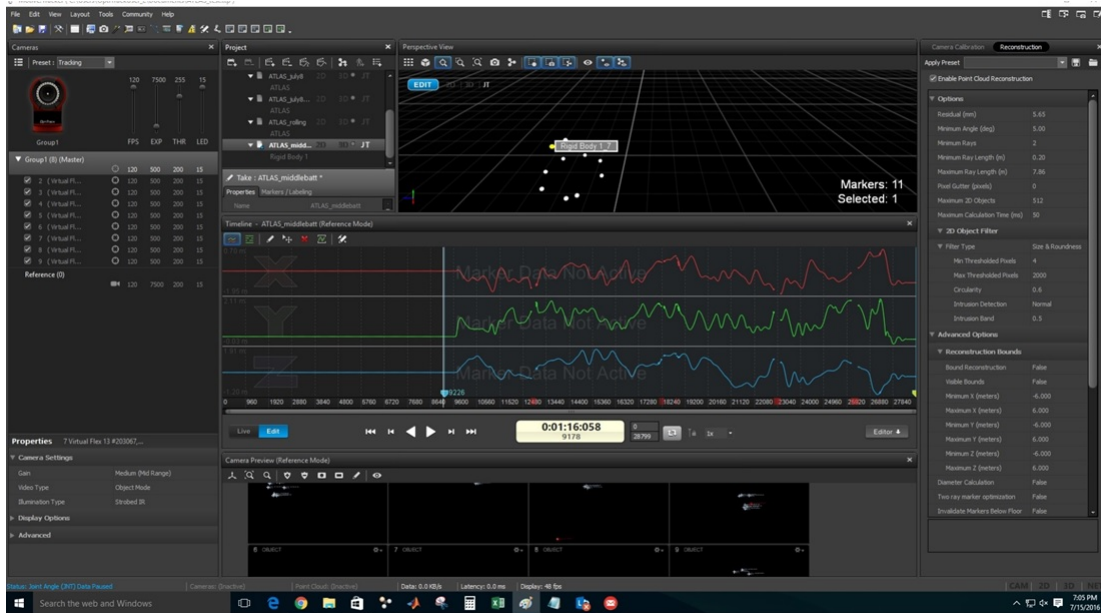


Figure 79: An example of vehicle's flight motion was captured by OptiTrack using the Motive software.

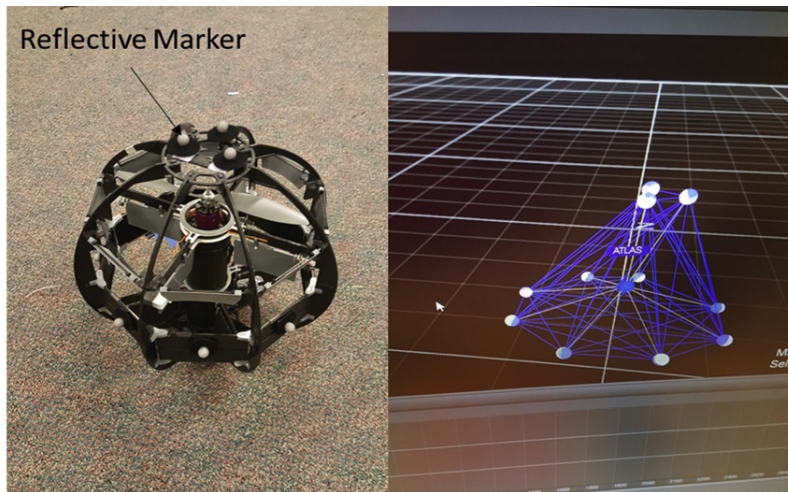


Figure 80: ATLAS with multiple reflective markers. A virtual representative of the markers in the motion capture software.

4.1 Experimental Setup

4.1.1 Movable Vanes Assessment

Single Vane - Force Measurement

The goal of this test is to measure the change of forces applied to a single vane using three different propellers. Figure 82 shows the mechanical setup to measure the force applied to a single horizontally fixed vane at different propeller RPM values. An anemometer was set up about 5" under the propeller slipstream to measure the wing speed. The propeller is 11x7, 12x4.7, and 12 x 7. An MT2814-10 700Kv motor is connected to a controller board that was pre-programmed to spins at different PWM from 1000 to 1400. Force measurement was made using a dual-range force sensor by Pro Vernier. This sensor can measure forces as small as 0.01 Newtons and as large as 50 Newtons. The dimension of a single fixed vane is shown in Figure 84. Figure 81 shows an example of the reading from the anemometer and the load cell. Each test was repeated three times to get the average, max, and min value from the load cell reading at the condition when the slipstream has reached a steady state velocity. Figure 83 shows the dimension of the passive vane for this test.

Single Vane - Equivalent Air Speed to Deflect a Vane

This test measures the equivalent wind speed needed to deflects the vane until it reaches a horizontal position. The vane weighs about 5 grams.

Single Vane - Smoke Visualization

Smoke visualization was conducted to exam the flow behavior near the propeller tip on both fixed and hinged vane configurations. The movable vane is only deflected between 0 to 90 degrees. The vane is made of foam board and weighs about four grams after attached with a metal washer. A washer is attached as a counter-weight to ensure that the flap can droop downward passively when reduces throttle, or else it will remain deflected as the propeller is spinning.

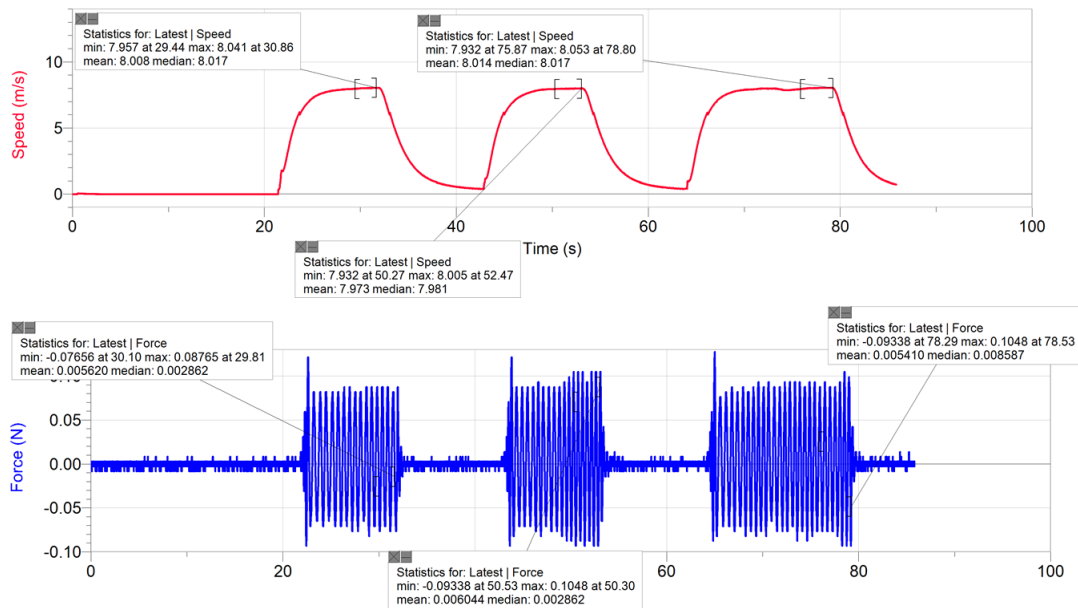


Figure 81: Lift force of a single vane with 12x6 prop.

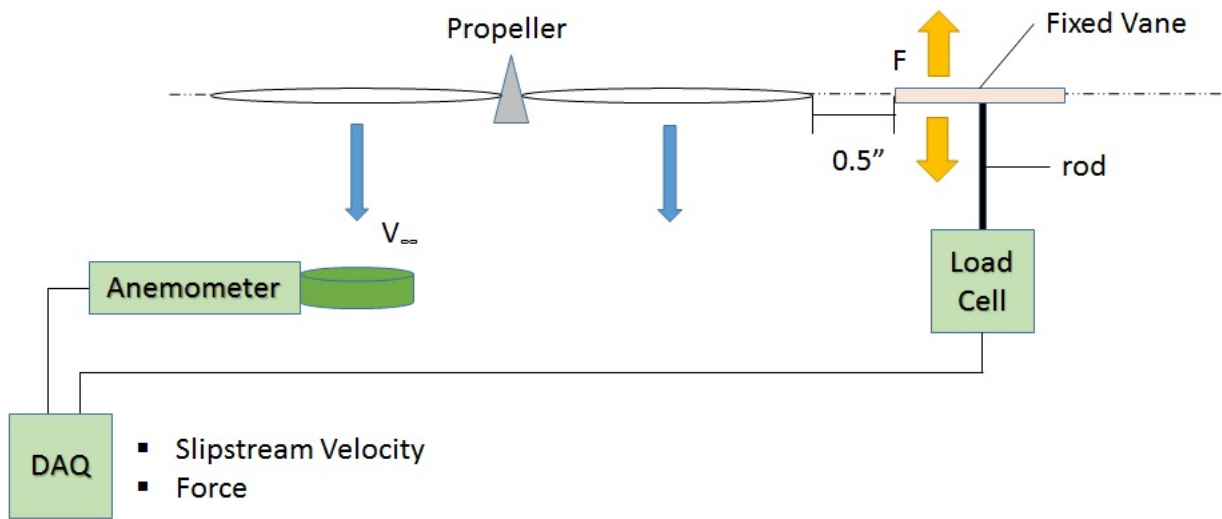


Figure 82: Setup to measure the lift force of a single vane.

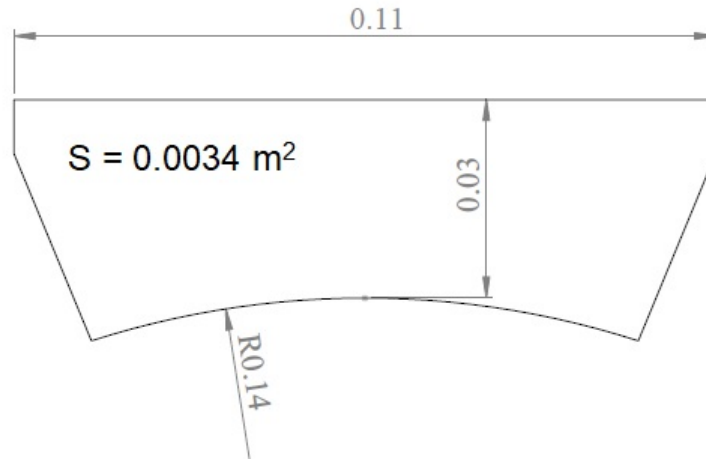


Figure 83: The dimension of a single passive vane for force measurement.

Single Vane - Design Impact on Drag Characteristic

This test is to study the vane design effect on the drag force. This test compared seven designs of passive vanes. Table 2 shows the defined dimension for each design in term of the chord length, thickness, frontal area, and radius based on the dimension definition in figure 84. All six vanes were 3D printed with ABS plastic except for the vane design number 7. The drag measurement was conducted by using the Flotek 1440 wind tunnel with a test section measuring 305 mm (W) x 305 mm (H) x 914 mm (L) (12 in x 12 in x 36 in). The entrance cone of the wind tunnel has a contraction ratio of 12:1. The air velocity through the test section is variable up to 25 m/s (82 ft/s). Each vane design was tested at the wind velocity ranging from 1.5 to 21.8 m/s.

Annular Plate - Change of Thrust With and Without Annular Plate at $h = 0$

The set up in figure 86 is to investigate the impact of an annular flat plate on the thrust produced by a 12x6 propeller. The annular flat plate has 16 inches outer diameter and 12.5 inches inner diameter that give a chord length of 2.5 inches.

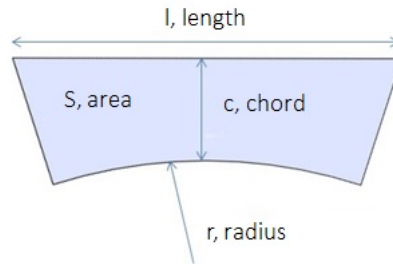


Figure 84: The dimension of a single vane.

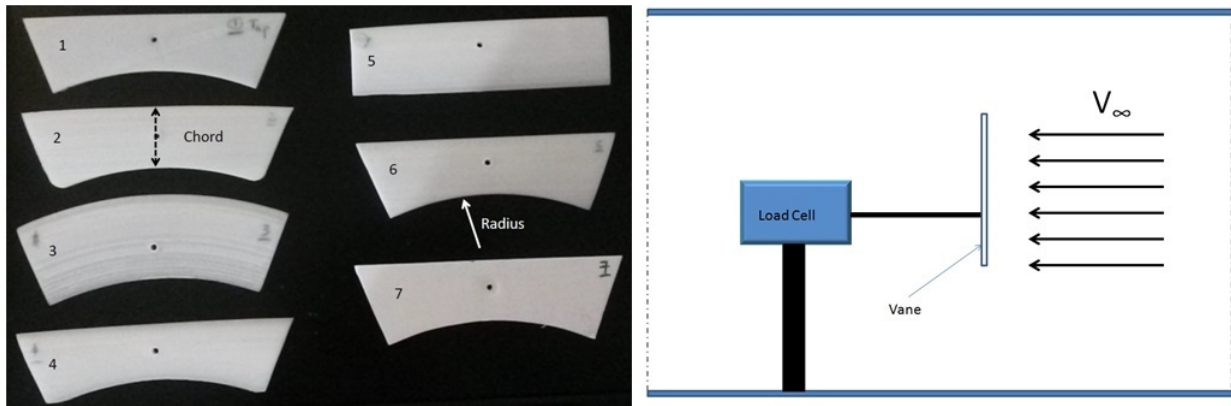


Figure 85: Seven vane designs and the drag measurement setup.

Vane Type	Chord, mm(in)	Area, mm ² (in ²)	Thickness, mm(in)	Radius, mm(in)	Profile
(1) Thin Flat Plate	0.035 (1.37)	5625.8 (8.72)	2.54 (0.10)	159 (6.25)	Flat
(2) Chamber	0.038 (1.50)	5625.8 (8.72)	6.35 (0.25)	159 (6.25)	Ellipse with semi minor axis = thickness
(3) Round Plate	0.051 (2.00)	7348.4 (11.39)	3.07 (0.12)	159 (6.25)	NACA 0012 (top side only)
(4) Symmetrical	0.032 (1.25)	4406.4 (6.83)	4.17 (0.16)	165 (6.5)	NACA 0012
(5) Rectangular	0.047 (1.85)	7535.5 (11.68)	5.72 (0.23)	N/A	NACA 0012
(6) Flat Bottom	0.035 (1.37)	5625.8 (8.72)	4.78 (0.19)	159 (6.25)	Ellipse with semi minor axis = thickness
(7) Foam Plate	0.035 (1.37)	5625.8 (8.72)	4.78 (0.19)	159 (6.25)	Flat.

Table 1: Characteristic for each vane design

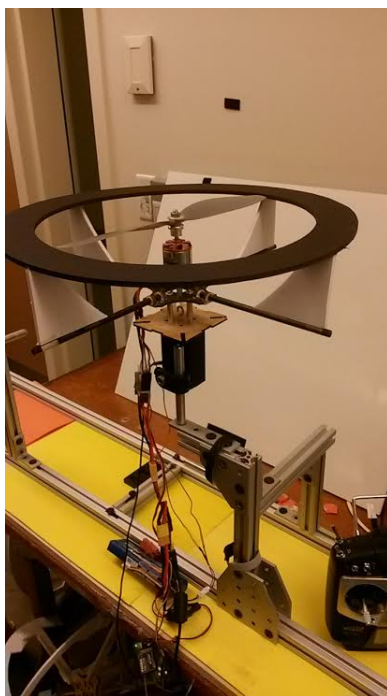


Figure 86: Setup with an annular plate.

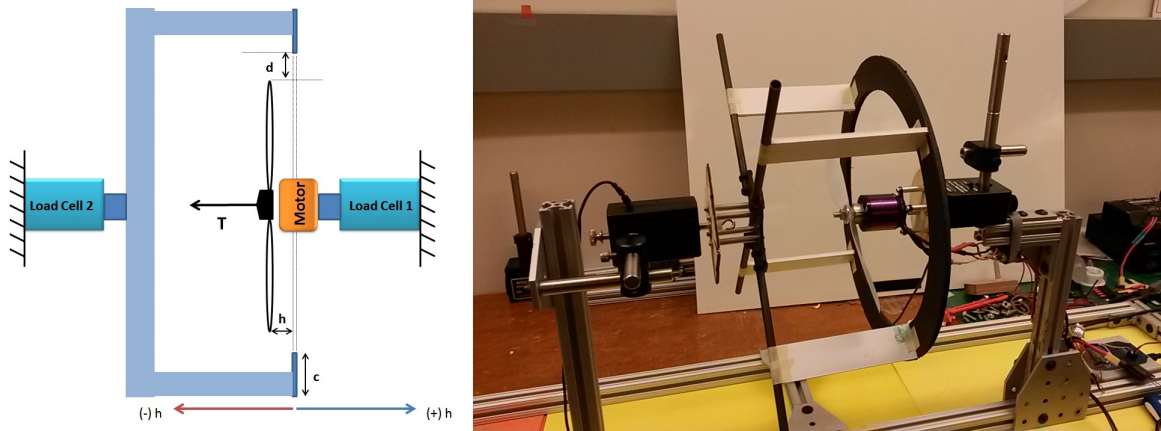


Figure 87: Experimental setup using a fixed circular plate.

Annular Plate - Change of Lift at Constant Rotor RPM

For the hover condition, a fixed annular plate was used to estimate the sum of forces generated when all eight vanes are fully deflected at a constant rotor RPM since direct measurement was not possible in flight. Figure 87 shows the bench test setup that can vary the height of the annular plate in relative to the propeller plane. Two annular plates made of 0.0048 m (3/8 in) thick foam board were tested. Both plates have the same inner diameter of 0.241 m (9.5 in). The difference is the outer diameter, where one is 0.273 m (10.75 in), and another is 0.279 m (11 in). Each gives a chord length of 0.32 m (1.25 in) and 0.38 m (1.5 in), respectively. The setup consists of two load cells where one measures the thrust generated by the propeller at constant RPM and the other measures the load applied on the annular plate. Each load measurement was repeated at three different RPMs at 5000, 6500, and 8400. The propulsion system consists of a 0.225 x 0.152 m (9 x 6 in) propeller mounted on an A30-10XL 900kV HACKER brand brushless motor. Figure 108 shows the force measurement at distance ranging between - 0.025 m to + 0.025 m (-1.0 in to +1.0 in) with a 0.013 m (0.5 in) interval.

Annular Plate - Effect on Descending Rate

This test evaluates the rate of descending affected by only a fixed annular disc to simulate the condition when all the 8 vanes are deflected upward as the vehicle rapidly descending. A typical in-flight condition has

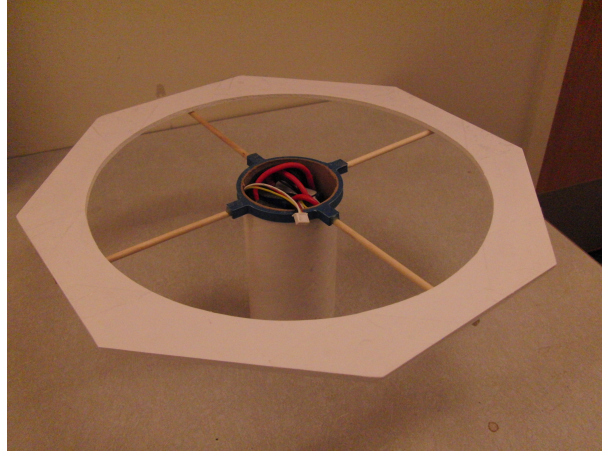


Figure 88: Annular plate setup for drop test.

the propeller spinning as the vehicle descending; however, this test model was simplified without having any motor and propeller. The setup consisted of a 0.0762 m (3 in) diameter cardboard tube attaches to a fixed annular disc, as shown in figure 88. The total frontal area of the disc is 0.05 m^2 (69.79 in^2). The weight of the setup is adjustable by putting ballast into the tube. This setup weighs about 772 g (1.7 lbs) with the annular disc itself weighs about 31g (0.07 lbs). Three setups were tested. The first two setups have a constant weight with and without the annular disc. The third setup has no disc and minus the added structural weight that needed to support the annular disc. This third setup is served as a baseline to compare the descent rate to the previous two setups. This test used a CASIO Exilim high-speed camera to capture each drop test at 300 frames per second. The video is then post-processed using the TRACKER software [36] to obtain the descending rate.

Annular Plate - Smoke Visualization

Particle Image Velocimetry (PIV) measurement was used to visualize the airflow interaction with the vane when the propeller is spinning. The PIV analysis was conducted using the Lavision System with a single Imager sCOMS camera. Figure 112 (A) and (B) shows the flow field with and without the vane. Figure 112 (A) shows that the flow above the propeller is coming toward the propeller tip at a steep angle. The placement of fixed vanes shows that the flow is attached to the top side of the vane and almost parallel to

the propeller plane. The airflow on top of the vanes introduces the low-pressure region and the pressure difference between the top, and bottom side of the vane causes the vane to deflect upward and toward the propeller tip.

Vanes Effect on Thrust and Motor Efficiency

The goal of this test is to quantify the effect of movable vanes on the total thrust and motor efficiency. Figure 90 shows the measurement setup. An RC dynamometer was modified to mount the ATLAS. A baseline measurement was collected without the movable vanes to quantify the change in force applied to the ATLAS frame when propeller spinning at different RPM. The test was only showing the results from 11x4.7 and 11x7 propeller because the spherical frame is designed for an 11 in diameter propeller. The efficiency value was obtained directly from the dynamometer result by divided Watt by Thrust values (N/W). The total weight of the movable vanes is measured.

Movable Vanes Impact on Hovering Stability

Control input from the active control surfaces needs to be isolated to investigate the impact of the movable vanes on the vehicle's stability. A gimbal fixture, as shown in figure 91 was constructed to clamp the ATLAS that only allows a single rotational axis through the center of gravity of the vehicle. The ball bearing on both sides was used to ensure the rotation is not affected by friction. Figure 92 shows the 3d printed clamp attached to one of the panels of the ATLAS with a stainless steel rod pivot along the ball bearing. There are three tests here: No vanes, with all eight blades and four partial vanes. The goal of this test is to investigate the impact of these vanes on pitching stability independent from active control surfaces. Figure 93 shows four movable vanes installed only at the front of the vehicle. The active control vanes are trimmed at 0 deg deflection, and the PD controller is turned off to prevent self stabilize due to active control vanes during test.

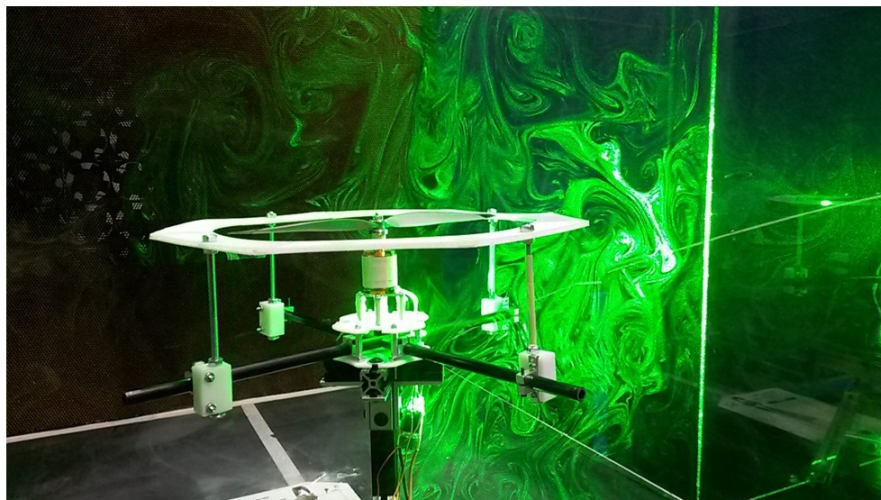
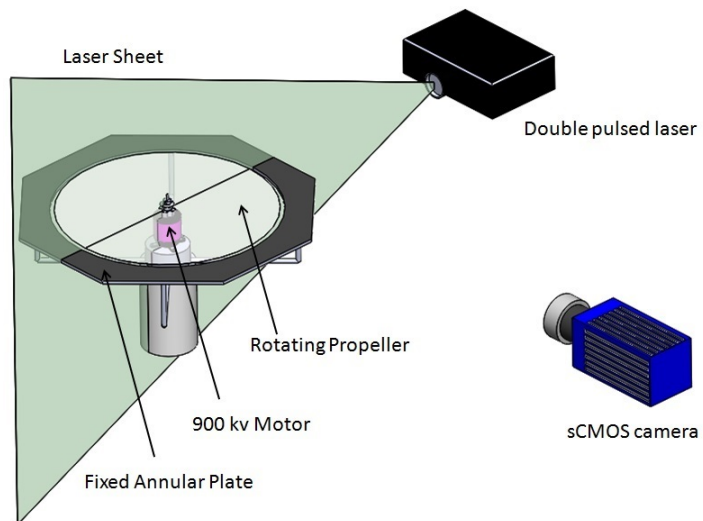


Figure 89: Experimental arrangement for PIV measurement.

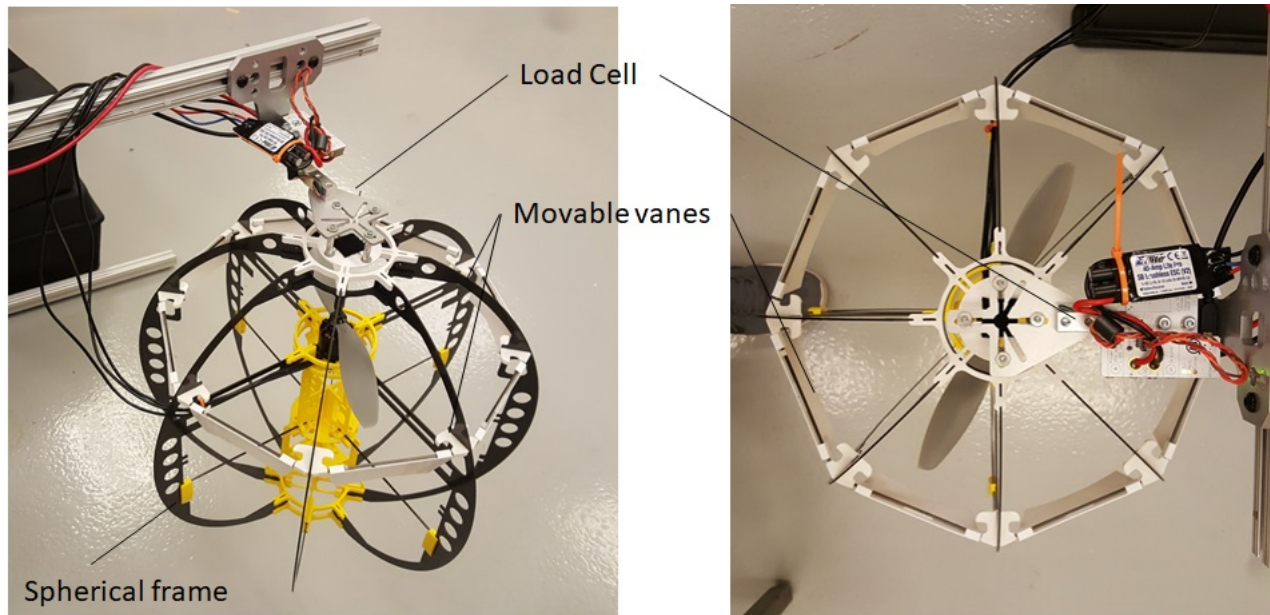


Figure 90: Experimental arrangement for thrust measurement.

4.1.2 Active Control and Propulsion System Assessment

Lift and Drag Coefficient Measurement of the Preliminary Control Vanes Design

Wind tunnel test was conducted to obtain lift and drag characteristic of the top and bottom vanes with the given size at different airspeed. The goal is to use these results to predict the aerodynamic behavior of different control vanes based on the configurations, as discussed earlier. The airspeed represents the slipstream generated by the propeller rotating at different RPM that ranges from 14.2 m/s to 18.2 m/s.

To measure the lift and drag of the vane, a balance was custom made using Arduino board as shown in figure94. The custom balance uses one 10kg S-type load cell and one 10kg straight bar load cells for lift and drags measurement, respectively. Figure 95 shows one of the straight bar load cells. Before conducting the wind tunnel test, a 2-D calibration is needed. Traditional calibration methods require an alignment of the balance and the load cells in such a way that every load cell reads only one component [37]. Therefore, a method using an interaction matrix is applied to calibrate the custom made balance. The graphs in 96 shows the measured and residue load obtained from each load cells by measuring four different weighs ranging from



Figure 91: Custom gimbal.



Figure 92: 3D printed clamp.

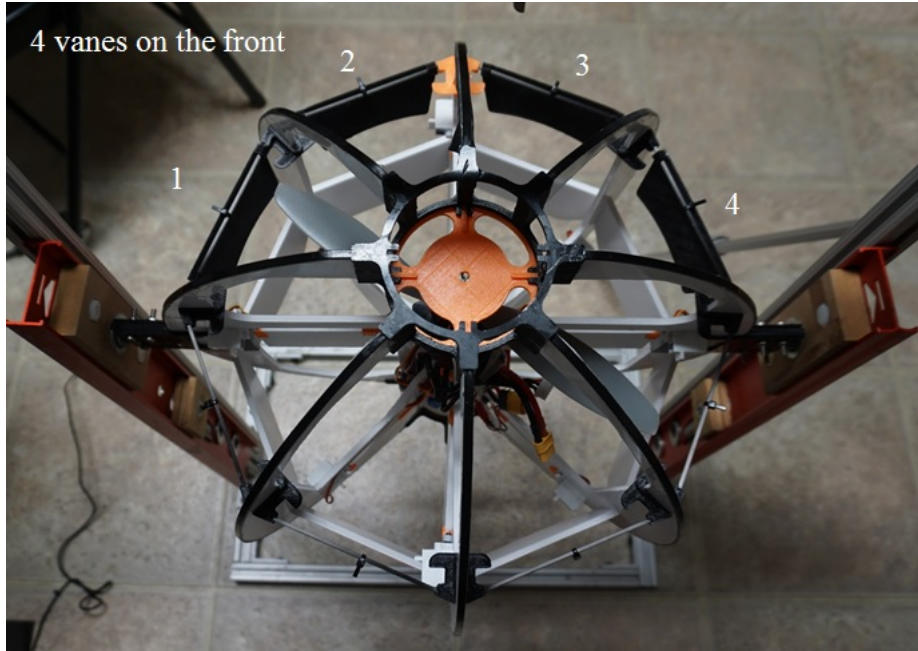


Figure 93: 4 movable vanes installed at the front of the vehicle.

25 grams to 100 grams with an interval of 25 grams increment. Each loading component is evaluated as a linear combination of the two interacting functions. The result is a linear approximation relating a known loading to the reading, where k_{ij} values represent interaction coefficients.

$$F_y = K_{11}F_{ya} + K_{12}F_{xa} \quad (22)$$

$$F_x = K_{12}F_{ya} + K_{22}F_{xa} \quad (23)$$

Or in matrix form,

$$\begin{bmatrix} F_y \\ F_x \end{bmatrix} = \begin{bmatrix} K_{11} & K_{12} \\ K_{12} & K_{22} \end{bmatrix} \begin{bmatrix} F_{ya} \\ F_{xa} \end{bmatrix} \quad (24)$$

where F represents a force. By inverting the $[K_{ij}]$ matrix, an expression for the actual loading corrected for interaction effects is derived.

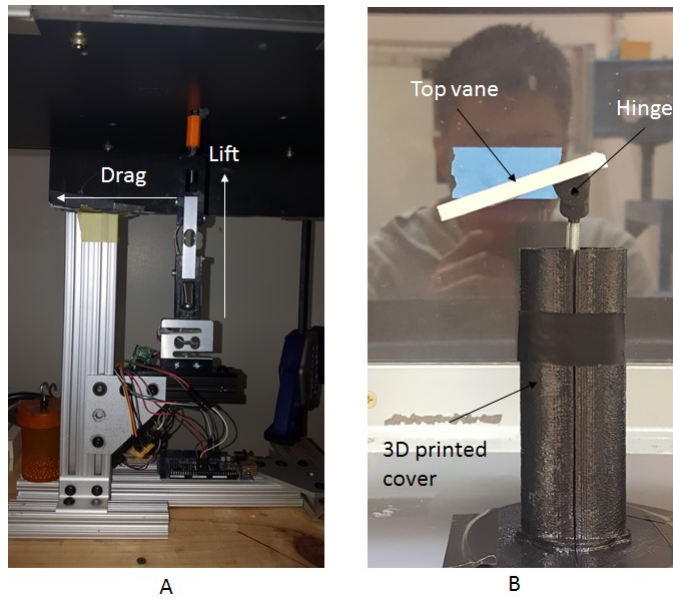


Figure 94: Custom balance to measure lift and drag.

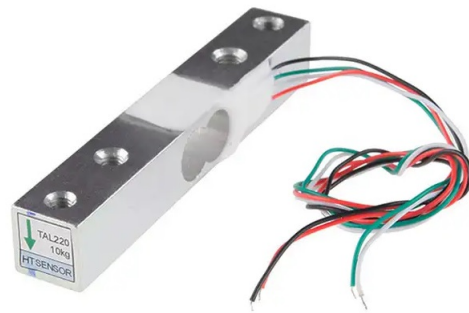


Figure 95: TAL220 10kg load cell.

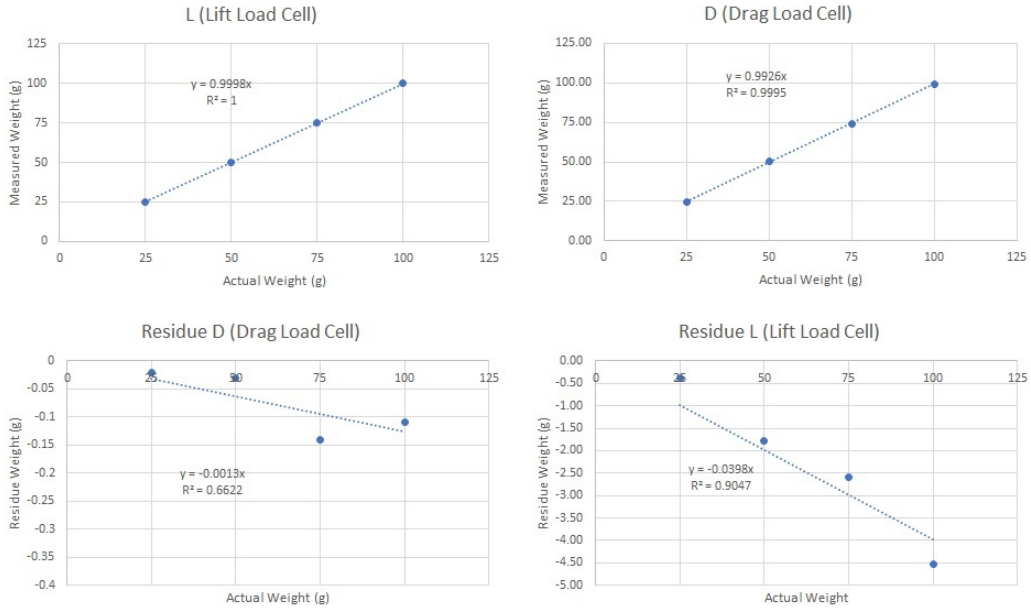


Figure 96: Measured load and residue load obtained from each load cells.

$$\begin{bmatrix} F_{ya} \\ F_{xa} \end{bmatrix} = \begin{bmatrix} K_{11} & K_{12} \\ K_{12} & K_{22} \end{bmatrix}^{-1} \begin{bmatrix} F_y \\ F_x \end{bmatrix} \quad (25)$$

where F_y and F_x is the uncalibrated readings of lift and drag, respectively with the derived interaction matrix $[K_{ij}]^{-1}$, the desired calibrated loading F_{xa} and F_{ya} can be obtained. Therefore, the calibration test result from graph 96 give the following interaction matrix,

$$\begin{bmatrix} K_{11} & K_{12} \\ K_{12} & K_{22} \end{bmatrix} = \begin{bmatrix} 0.9998 & -0.0013 \\ 0.9926 & -0.0398 \end{bmatrix} \quad (26)$$



Figure 97: RC Benchmark’s dynamometer.

Specification	Min.	Max.	Tolerance	Unit
Thrust	-5	5	0.5 %	kgf
Torque	1.5	1.5	0.5 %	Nm
Voltage	0	35	0.5 %	V
Current	0	40	1 %	A
Angular Speed*	0	190K	1	eRPM
Coil Resistance	0.003	240	0.5 %	ohm
Digital scale	0	3	0.5 %	kgf

*Electrical RPM, divide by the number of motor poles to obtain true mechanical RPM.

Table 2: Design specifications of the Series 1580 Dynamometer

4.1.3 Propulsion System Assessment

Thrust, Reverse Thrust, and Torque Measurement

Fig. 98 shows the setup to measure propulsion characteristics. A dynamometer made by RC Benchmark, as shown in figure 97, was used to measure the thrust, torque, voltage, and current to calculate the parameter K_T , K_M , and K_v . Curve fitting is conducted to obtain the desired parameters. An anemometer was set up separately from the dynamometer to measure the slipstream velocity five inches behind the propeller.

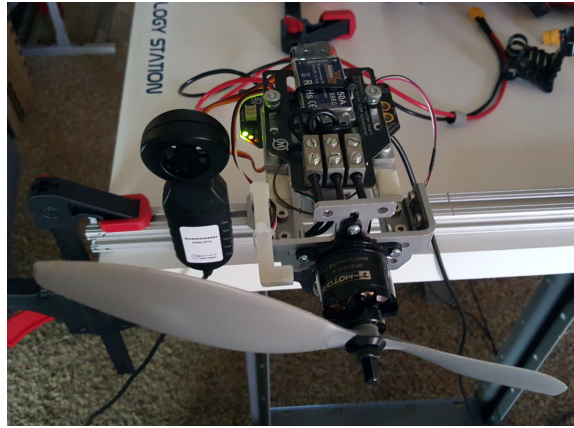


Figure 98: Propulsion testing system by using the 1580 Dynamometer.

Gyroscopic Precession

With a single prop rotating for thrust there will be a gyroscopic effect. The single axis gimbal, as described in figure 91, was used to measure the rotational rate when executing a roll input command.

Challenges with Single Propeller Propulsion

In general, a single-propeller-driven UAV is vulnerable to multiple propulsion related issues: propeller induced torque, gyroscopic moment, P-factor, and swirling slipstream. Such issues should be of concerned and mitigated in this research.

Gyroscopic precession or torque-induced precession is the phenomenon in which the axis of a spinning object describes a cone in space when an external torque is applied to it. When viewed from behind a propeller, most clockwise turning propeller causes the rest of the plane to have the tendency to rotate clockwise, which is a drawback in a single-propeller-driven UAV. Therefore, helicopters vehicles waste some power to feed a tail-rotor; meanwhile, a fixed-wing aircraft, in hover flight, use differential control surfaces like elevon and ailerons.

Typically, aerobatic airplanes have a wingspan of greater than 1 m, which limits the maximum torque-roll rate by about 180 degrees per second, allowing an inexperienced pilot to control the airplane easily [35]. For a MAV size that is 3 - 5 times smaller, it is assuming that the torque-roll rate is inversely proportional to the

cube of the wingspan. If the wingspan decreases by a factor of 2, the torque-roll rate increases by a factor of 8, therefore, the induced torque may become a driving factor in designing the VTOL control system for MAVs [35].

The P-factor, also known as asymmetric blade effect and asymmetric disc effect is another adverse effect in the single-propeller-driven aircraft. This factor is responsible for asymmetrical relocation of the propeller's center of thrust when the aircraft is at a high angle of attack. As viewed from the cockpit, the aircraft tends to yaw to the left for using a clockwise turning propeller. Deflecting of the rudder helps to maintain level straight flight; however, as a penalty, the aircraft drag increases.

The effect of rotational airflow is inherent in a single-propeller propulsion system. The air passes the propeller rotates into a twisting helix around the fuselage and presses against the vertical tail, causing induced yaw and roll effect to the aircraft. These results in energy losses and reducing overall thrust efficiency of the propulsion.

4.2 Experimental Result

4.2.1 Movable Vane Assessment Result

Single Vane - Force Measurement

Figure 99, 100, and 101 is the results of force measurement. These results show that the 12-inch propeller fluctuates significantly at lower RPM. However, at higher RPM or PWM value of 1400, propeller 11x7 yields the highest lift force, followed by 12x6 and 12x4.7 propeller. The 11x7 propeller produces 20 % more lift than the 12x6 propeller. The test indicates that the smaller propeller diameter with higher pitch might yield the best results in this test setup where $h = 0$.

Single Vane - Equivalent Air Speed to Deflect a Vane

Figure 102 is the plot shows the wind speed versus the deflection angle. The result indicates that the incoming airflow toward the tip of propeller needs to reach about 7 m/s (10.27 ft/s) to fully deflect the vane

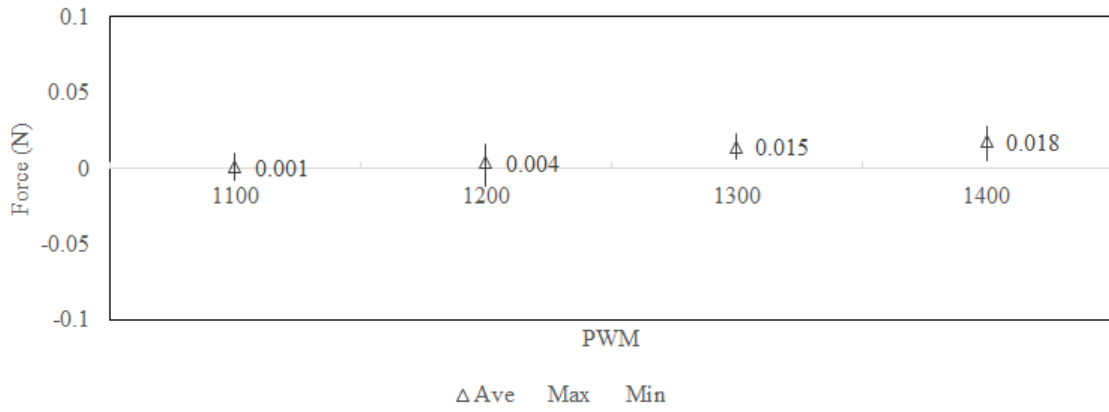


Figure 99: lift force of a single vane with 11x7 prop.

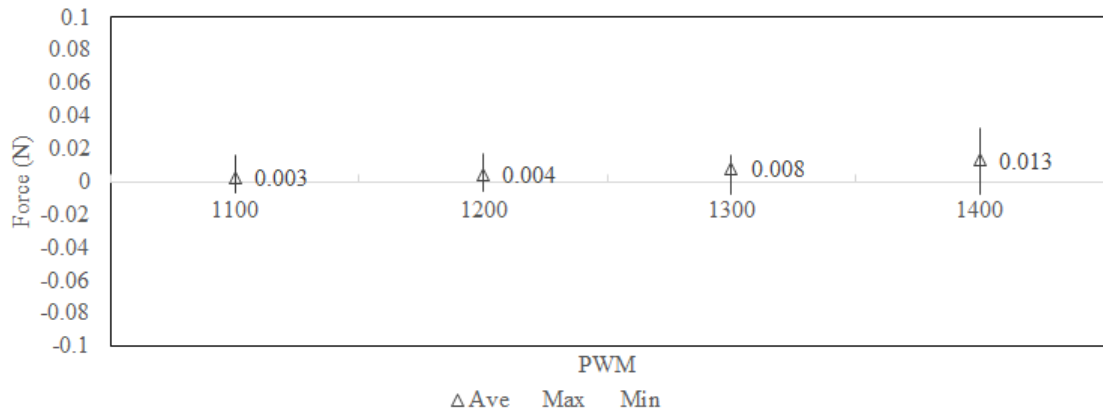


Figure 100: lift force of a single vane with 12x4.7 prop.

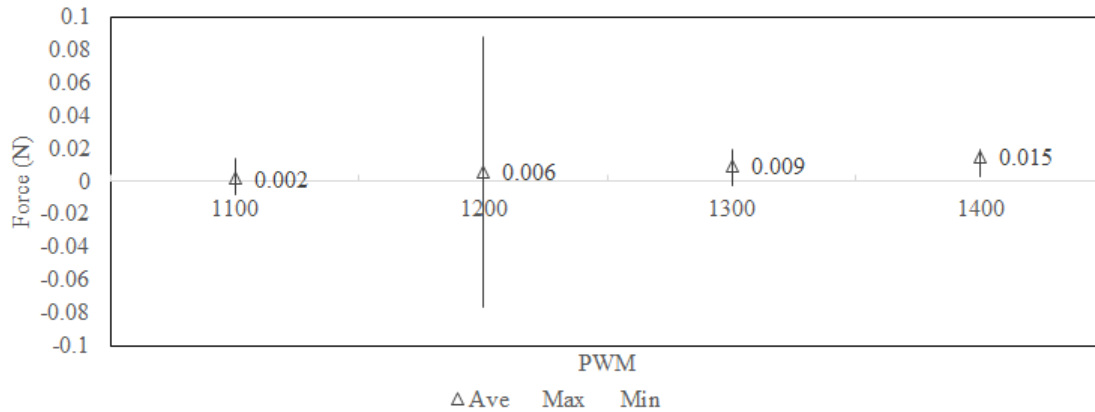


Figure 101: lift force of a single vane with 12x7 prop.

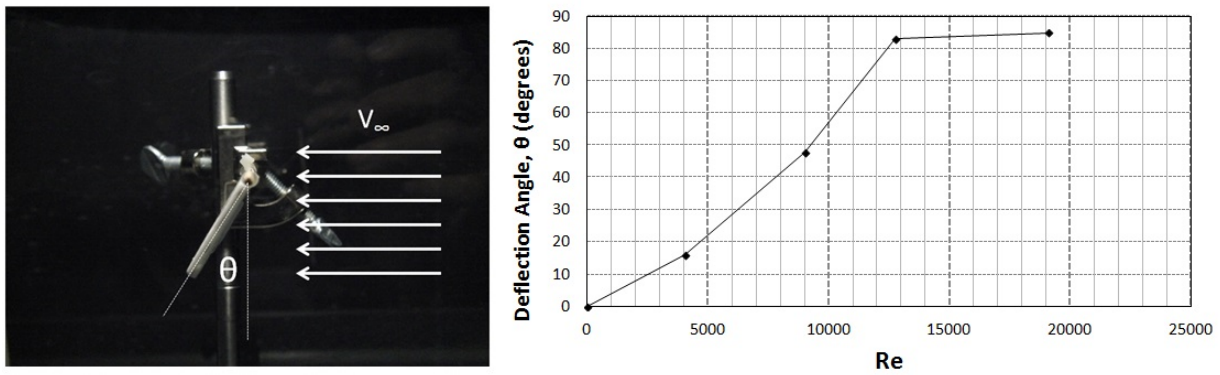


Figure 102: Vane's deflection angle versus air speed with uncertainty.

upward. The Reynold number is about 19,000. Further increasing the wind velocity will not deflect the vane further since it is mechanically restricted near 90 degrees. The calculated lift coefficient is 0.23.

Single Vane - Smoke Visualization

Figure 103 shows the sequence of the movable vane deflecting upward as the propeller RPM increases to 4200 RPM. Figure 104 shows the relationship of the propeller RPM with respect to the deflection angle of the movable vanes. The maximum and minimum values show the range of fluctuation in the deflection angle when tested under a fixed RPM value. There are 50 data points for each RPM. The graph shows that

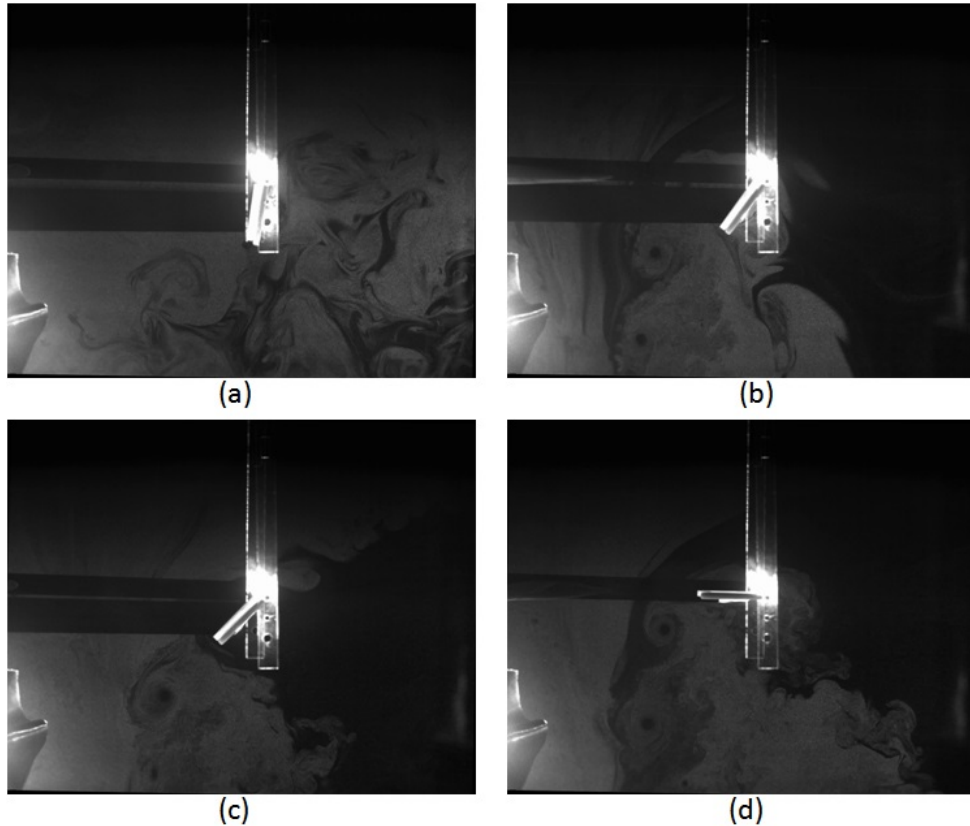


Figure 103: Movable vane deflection from vertical to horizontal position as the propeller RPM increases.

at higher RPM, which is equivalent to take-off or hovering mode, the movable vane remains horizontal (90 degrees). However, the vanes fluctuate significantly, and the flow is highly unsteady during the intermediate stages. As the illustration in figure 113 shows, when the vane is present, the flow is significantly directed horizontally into the plan of the propeller, decreasing the pressure on the top side of the vane and creating an upward force.

Single Vane - Design Impact on Drag Characteristic

Figure 105 shows the test result for all the vane design when tested at Reynold (Re) number ranging from 4,000 to 80,000. The arrow in the figure 105 represents the deflection of the vane (design number 7) when it has reached a horizontal position at minimum free stream velocity at Reynold number of 19,000. Reynold

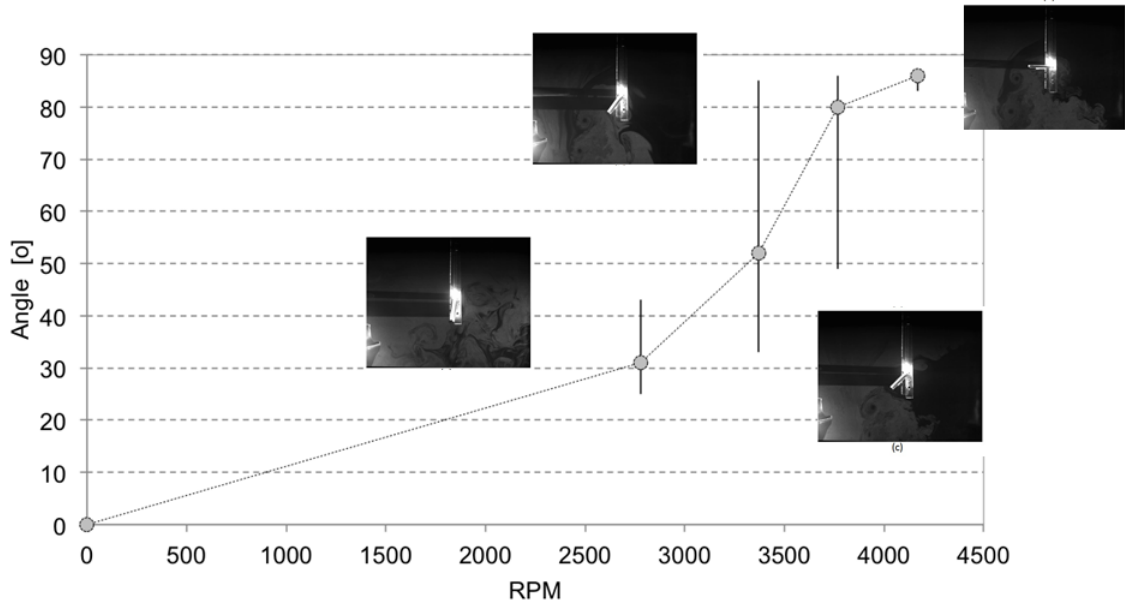


Figure 104: RPM vs. vane deflection angle.

number below the 19,000 is a transitional stage when the propeller starts spinning, and airflow is gradually increasing to deflect the vanes. The result in figure 105 shows that plate 2 with chamber design provide the highest drag coefficient. In contrast, Plate 5 as the rectangular wing design with a NACA 0012 profile, has the lowest drag coefficient among all vane designs. With the assumption that each vane design will be having the same structural weight of 5 grams, plate 1, 6 and 7 exhibit similar performance when operating at $Re=19,000$. Plate 6 yields the highest value of the three designs. Note that all three plates have a flat surface on either one side or both sides of the plate. All plate 2, 4, and 3 has close coefficient at $Re = 19,000$. Plate 2 and 4 exhibit a similar reduction in drag coefficient as Re number increases. However, the drag coefficient for plate 3 performed the worse as the Re number increases in comparison to both plate 2 and plate 4. Overall, the result shows that the drag coefficient is not significantly affected as the Re number increases up to 60,000. Therefore, a flat plate is the preferred design for ATLAS because of its simplest structural design.

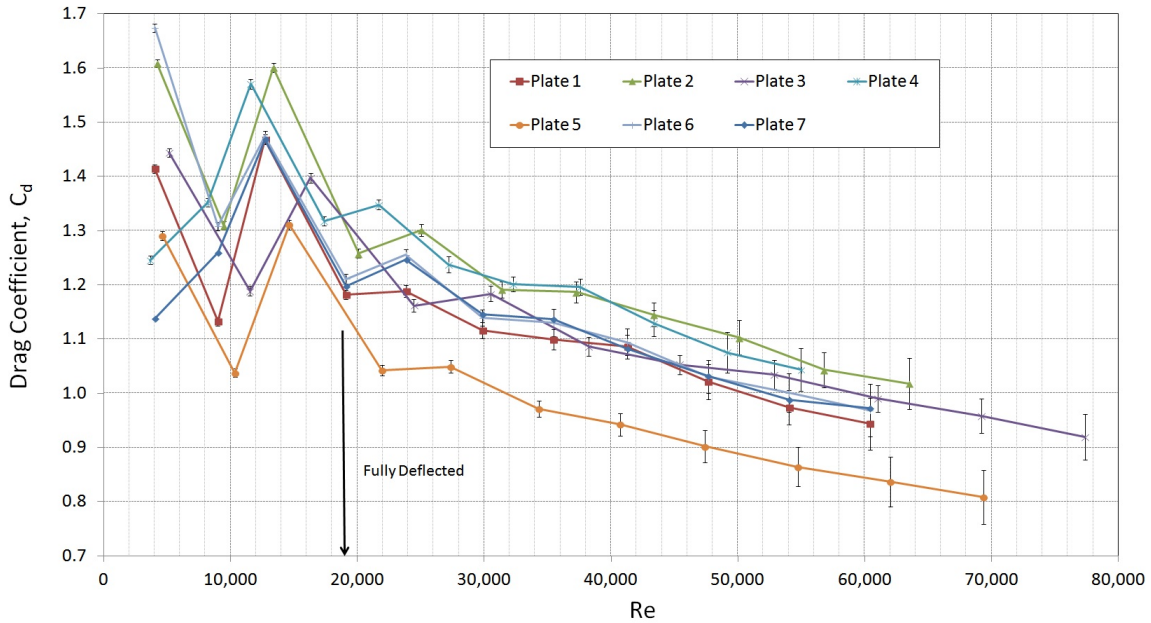


Figure 105: Drag coefficient versus Reynold number.

Annular Plate - Change of Thrust With and Without Annular Plate at $h = 0$

Figure 106 shows two tests results with and without out the annular plate with $c = 2.5$ inches.

Annular Plate - Change of Lift at Constant Rotor RPM

The result shows that placing the plate at $h = 0$ m yields the highest net force, in the same direction as the thrust force. The result indicates that place the plate ahead of the propeller ($-h$ direction) above 0.013 m (0.5 in) can invert the direction of the load applies to the annular plate.

Annular Plate - Effect on Descending Rate

The result in both figure 109 and 110 show a reduction in the rate of descending with the use of an annular plate. The drop test reviewed that the annular plate can provide pitching/rolling stability while descending. Figure 111 shows that the setup without the annular plate roll significantly, as demonstrated in figure 111

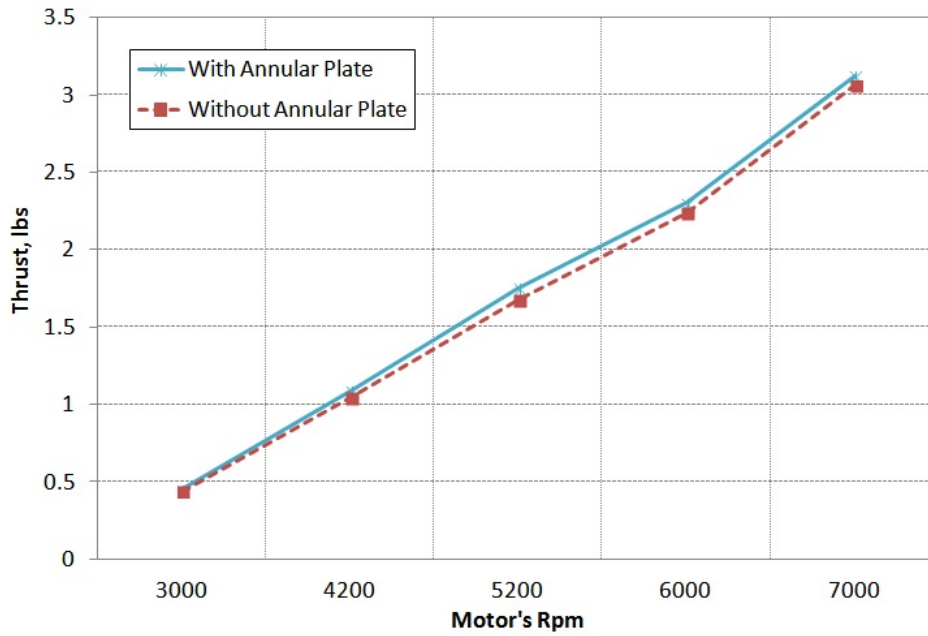


Figure 106: Change of thrust with and without Annular Plate, $c = 2.5$ inches.

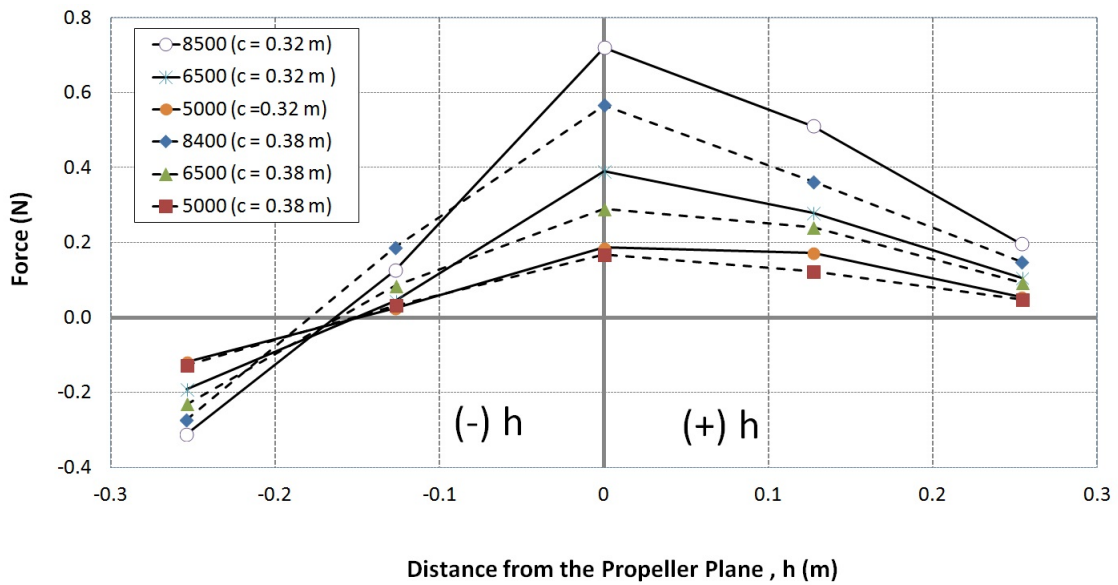


Figure 107: Force measurement by varying h .

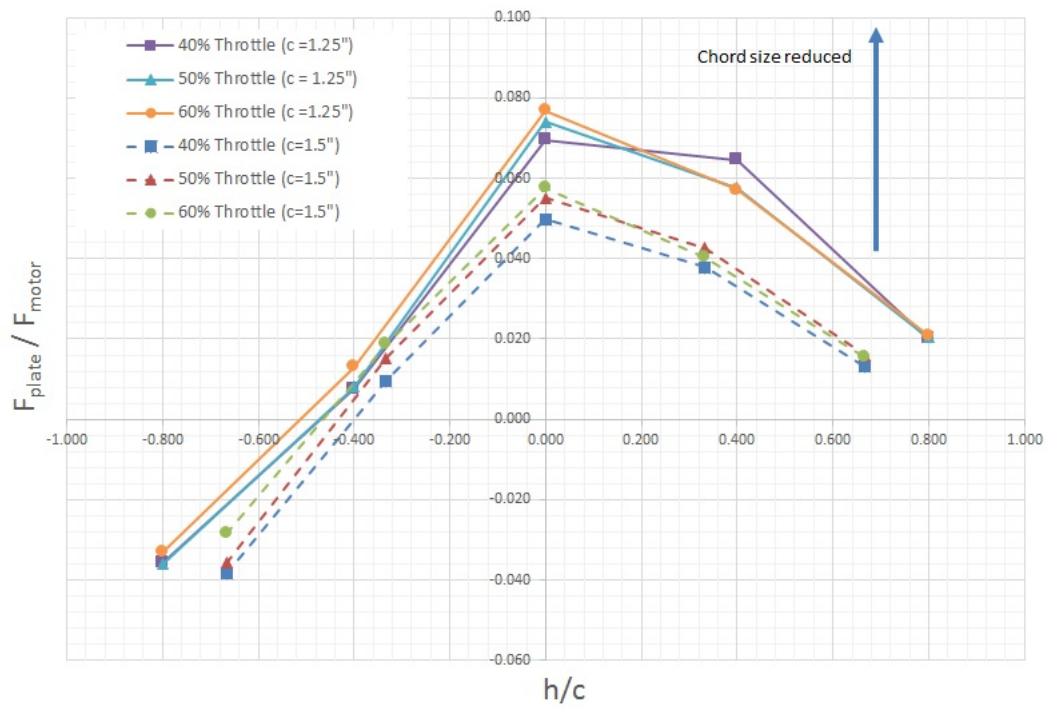


Figure 108: Force measurement by varying h and c .

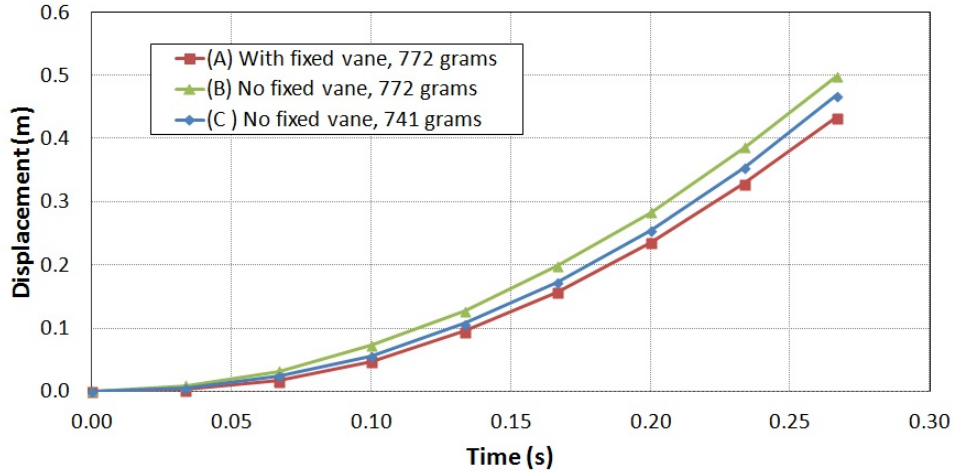


Figure 109: Change of displacement with and without annular plate.

(B) since the C.G. of the setup was not perfectly aligned laterally. Equation 27 calculate the amount of drag coefficient for this particular annular plate during descending and yield $C_d = 1.6$.

$$W = D = C_D \frac{1}{2} \rho V^2 A_c \quad (27)$$

Annular Plate - Smoke Visualization

Figure 112 (a) and (b) shows the results without and with the annular plate. The test shows that the flow above the propeller is coming toward the propeller tip at a steep angle in comparison to Figure 112(b). The placement of a fixed vane shows that the flow is attached to the top side of the vane and almost parallel to the propeller plane.

Movable Vanes effect on Thrust and Motor Efficiency

Figure. 114 shows the result by using two 11 inches propeller with different pitches: 11 x 4.7 and 11 x 7. The results show that the movable vane helps increase the overall thrust for both propellers. On the other hand, the 11x7 propeller yields higher motor efficiency when operating with the movable vanes. The pitch

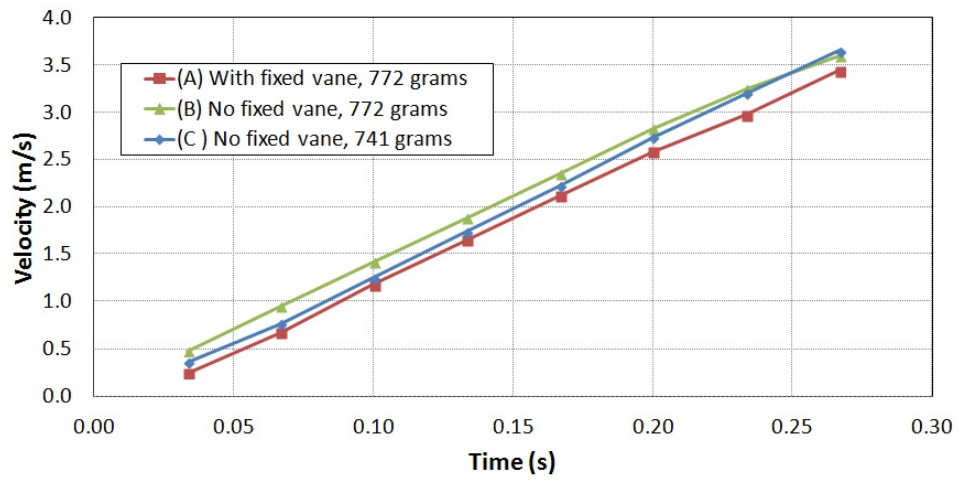


Figure 110: Change of velocity with and without annular plate.

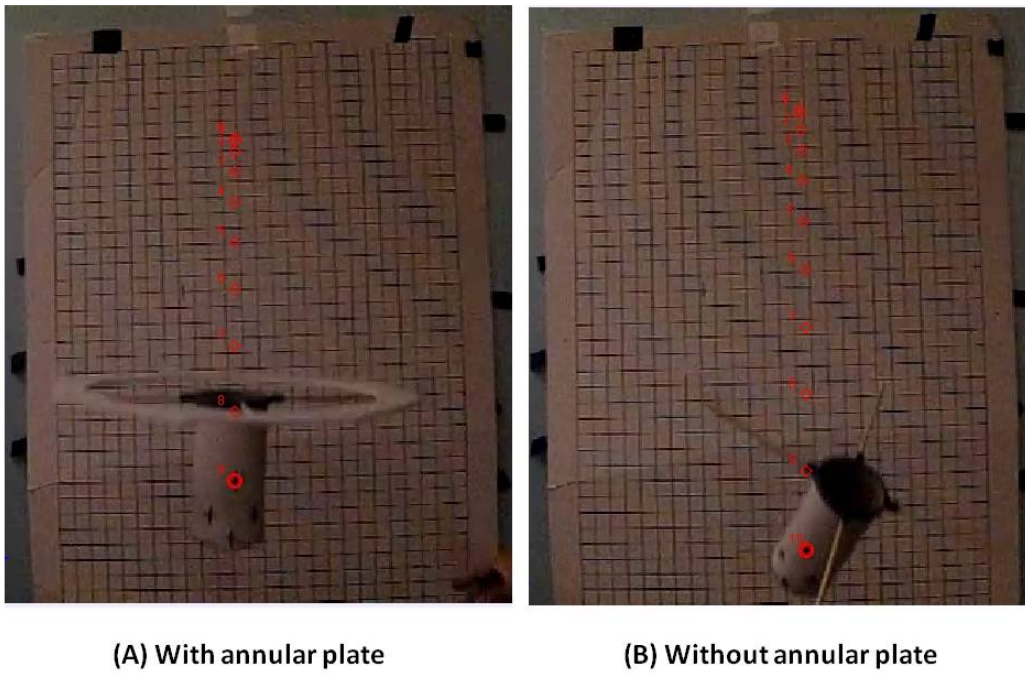


Figure 111: Annular plate provides stability during descending.

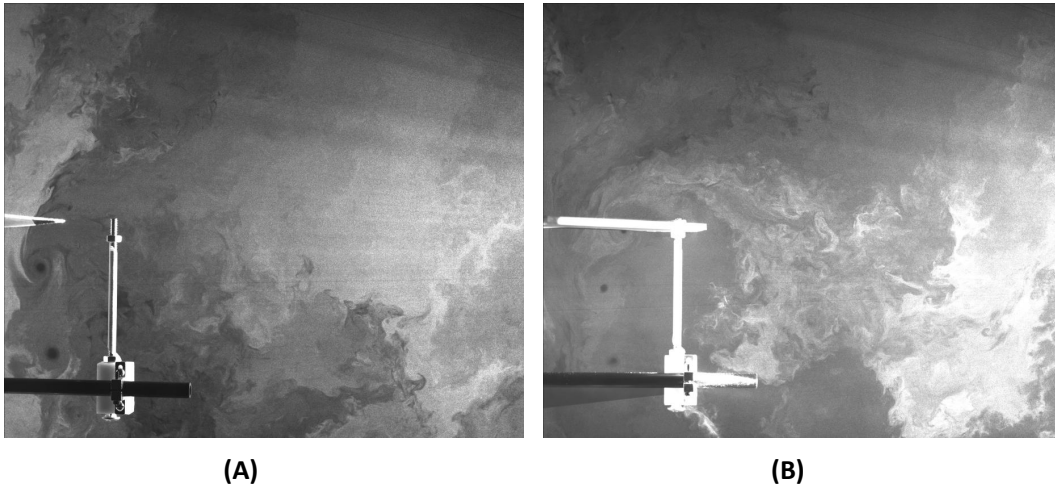


Figure 112: The air flow near the propeller (A) without and (B) with the annular fixed vane at 6500 RPM.

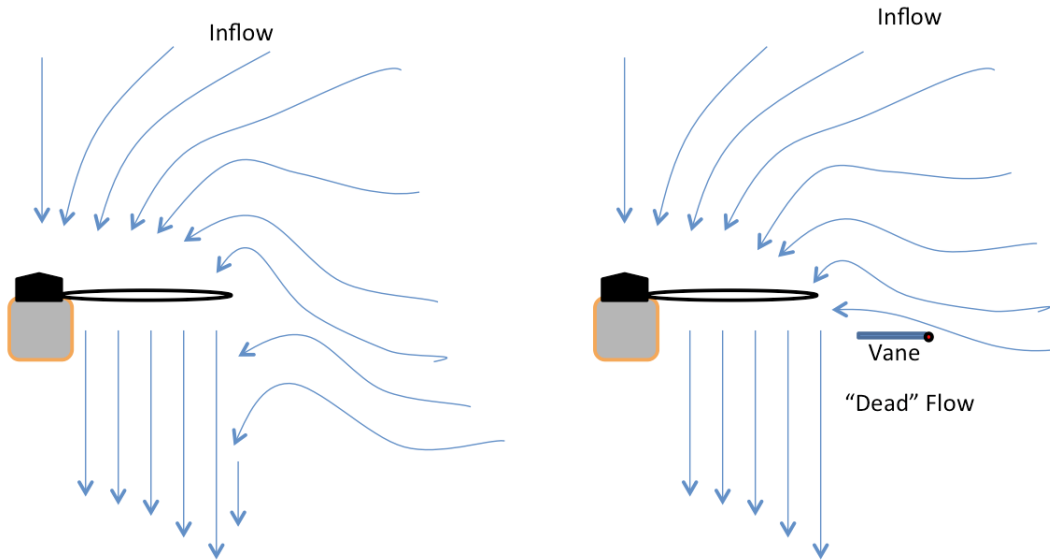


Figure 113: Flow characteristic around the propeller tip with and without a vane.

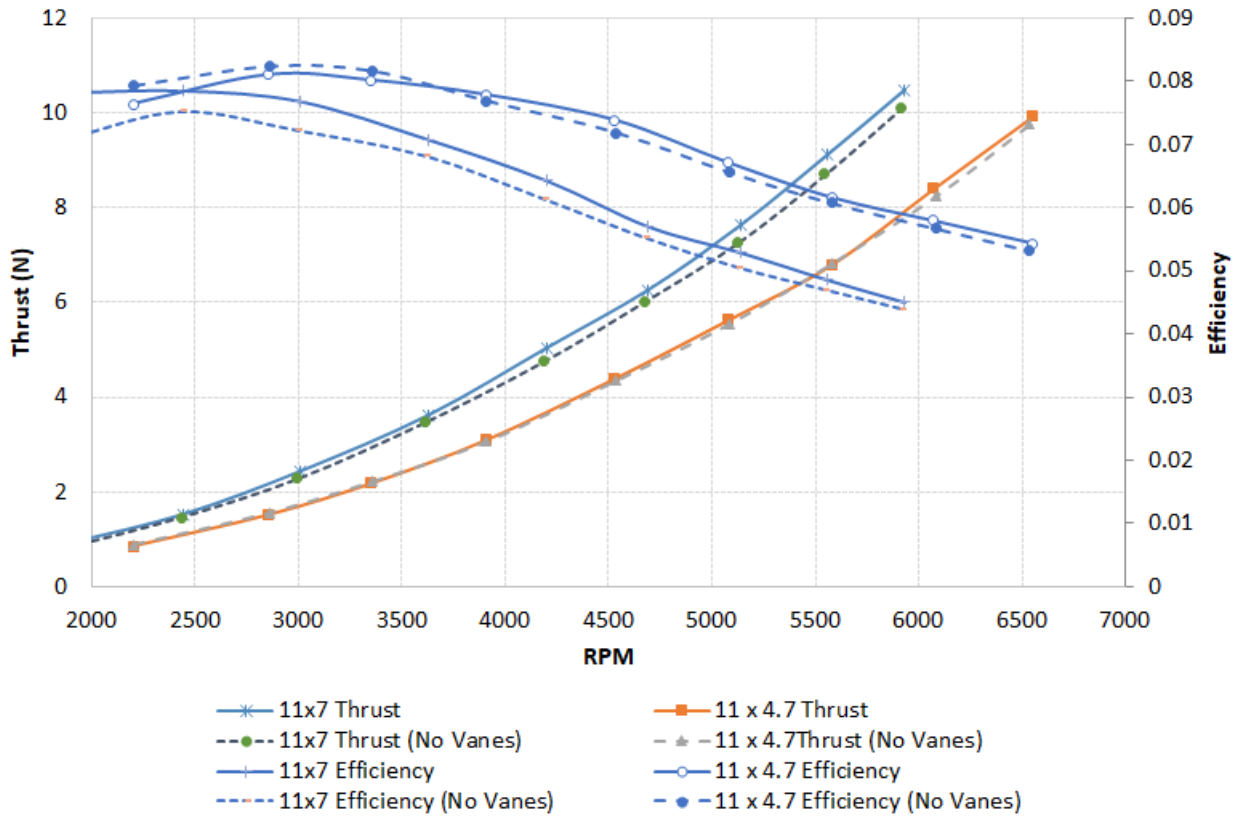


Figure 114: Efficiency and Thrust of the motor using 11x4.7 and 11x7 propeller.

of the propeller produces different results from this bench test. The 11x7 yields 4% higher thrust when the propeller is spinning at rpm near hovering condition around () rpm. However, the 11x 4.7 propeller is not showing significant improvement in thrust when operating with movable guide vanes. In term of efficiency, the higher pitch propeller shows a consistent increase in efficiency throughout the recorded rpm range. On the other hand, the 11x 4.7 prop show increase in efficiency below 3800 rpm without the movable guide vane. However, both propeller when operating in hovering or take off condition, it still produces better efficiency as RPM increases. Propeller with higher pitch yield higher thrust and motor efficiency compare to the lower pitch propeller that has the same diameter. This shows that propeller selection can impact the performance of the thrust and motor efficiency.

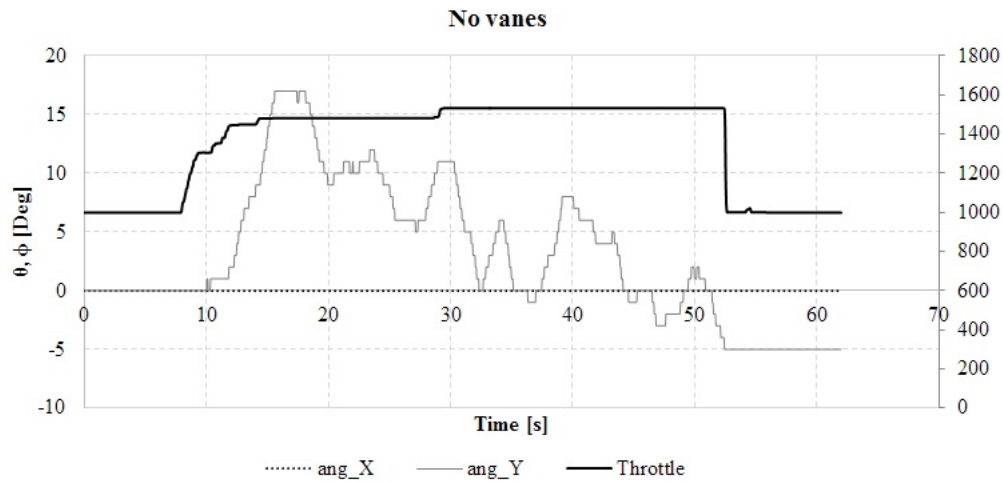


Figure 115: Vehicle's attitude without any movable vanes installed.

Movable Vanes Impact on Vehicle's Stability

Figure 115, 116 and 117 shows that the movable vanes can impact the vehicle stability. The usage of 8 movable vanes shows that vehicle reduce the pitching oscillation within 5 degree angle when roll is restricted using the gimbal setup. Figure 117 shows that that 4 movable vanes installed on the front of the vehicle can produce additional pitching movement at a constant throttle value.

4.2.2 Active Control Assessment Result

Lift and Drag Coefficient Measurement of the Preliminary Control Vanes Design

Wind tunnel test was conducted to obtain lift and drag characteristic of the top and bottom vanes with the given size at different airspeed. The goal is to use these results to predict the aerodynamic behavior of different control vanes based on the configurations, as discussed earlier. The airspeed represents the slipstream generated by the propeller rotating at different RPM. The wind speeds ranging from 14.2 m/s to 18.2 m/s.

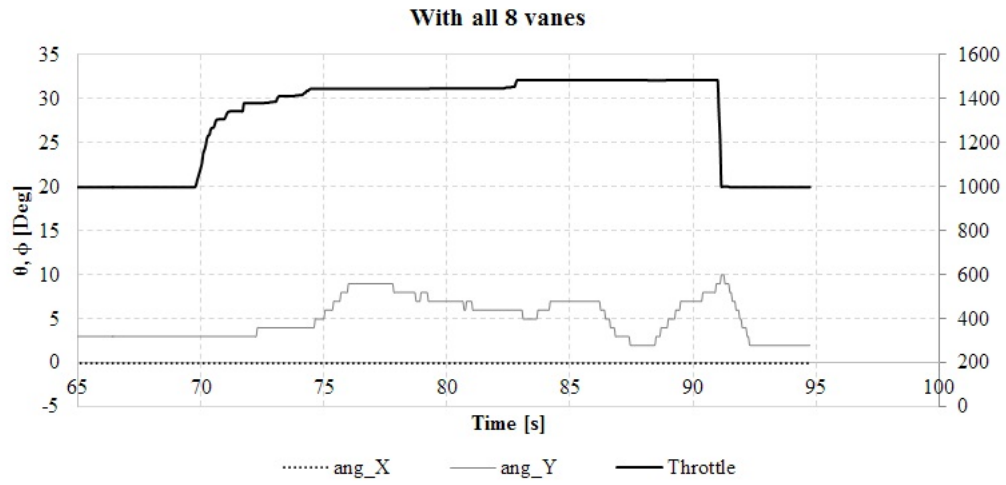


Figure 116: Vehicle's attitude with all 8 movable vanes installed.

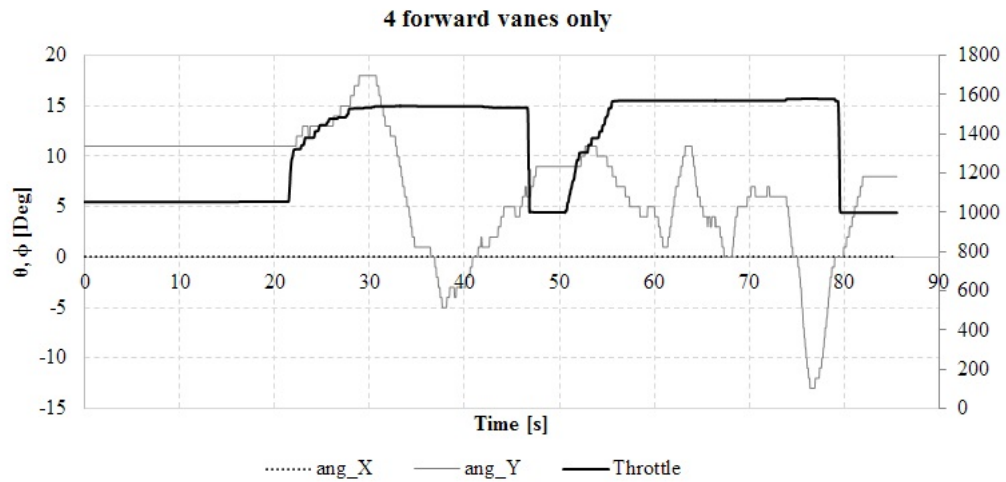


Figure 117: Vehicle's attitude with 4 movable vanes at the front of the vehicle.

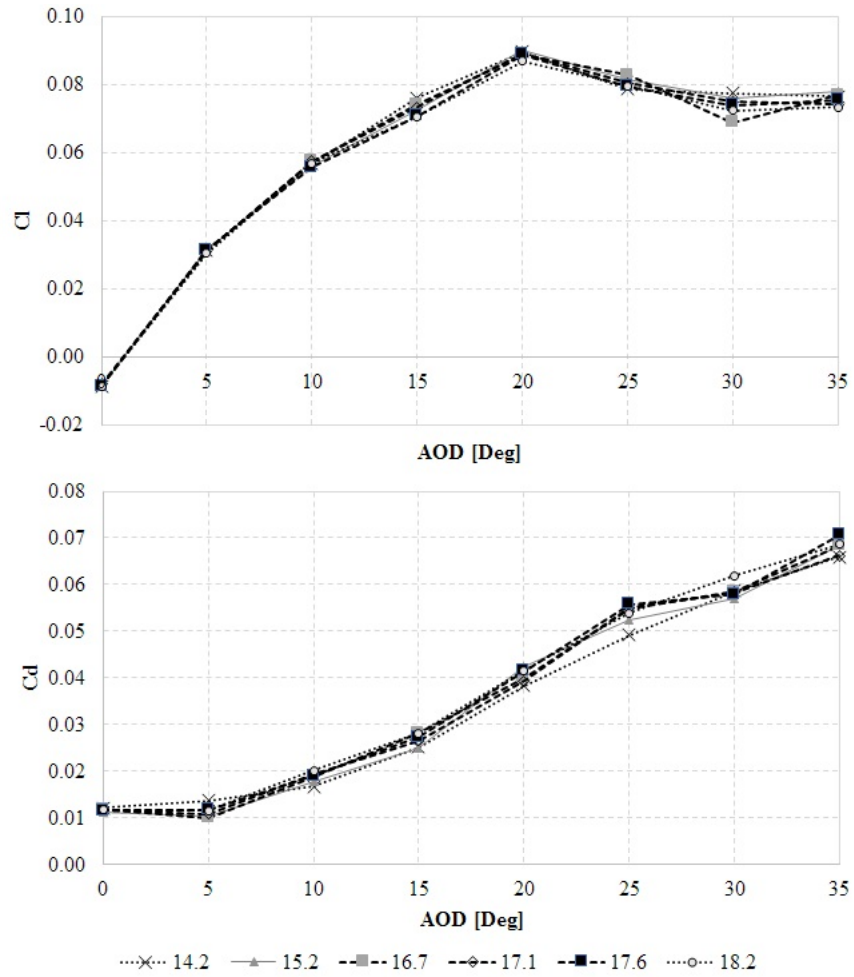


Figure 118: Lift and drag coefficient measurement by deflecting the top vanes ranging from 0 to 35 degrees with 5 degrees interval. Stall occurs after 20 degrees.

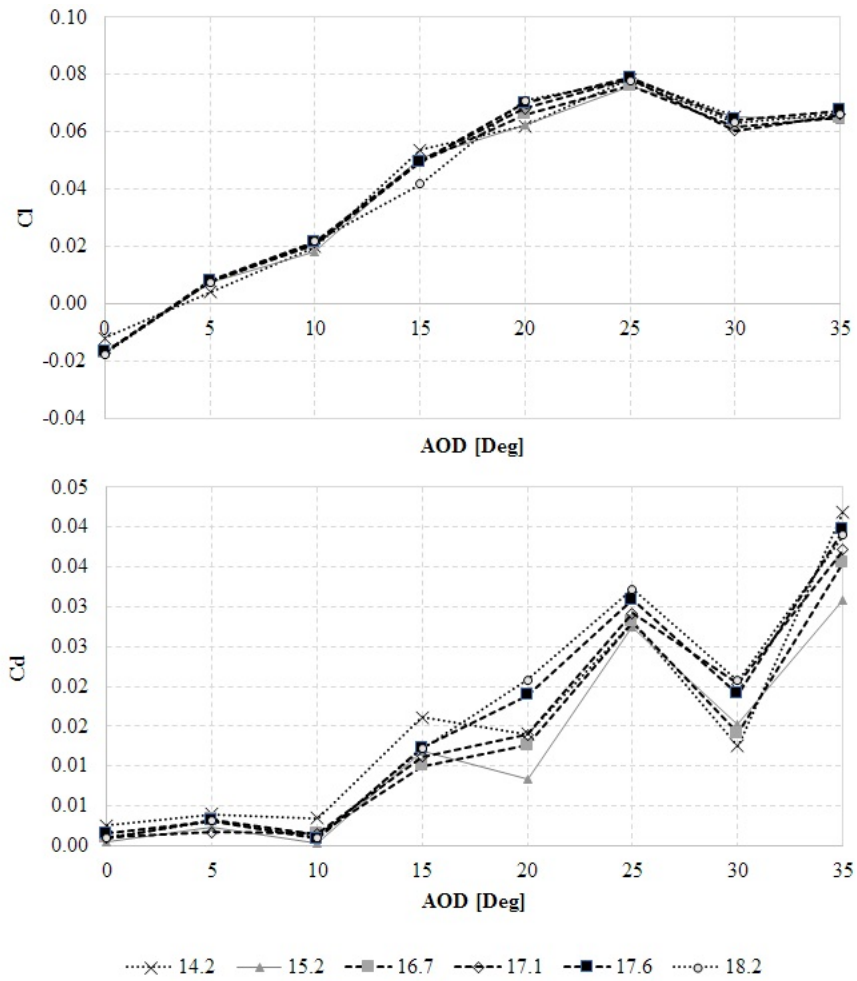


Figure 119: Lift and drag coefficient measurement by deflecting the bottom vanes ranging from 0 to 35 degrees with 5 degrees interval. Stall occurs after 20 degrees.

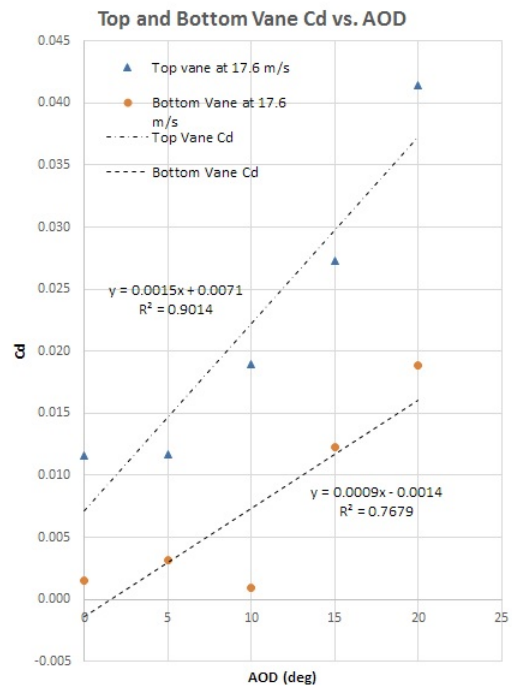
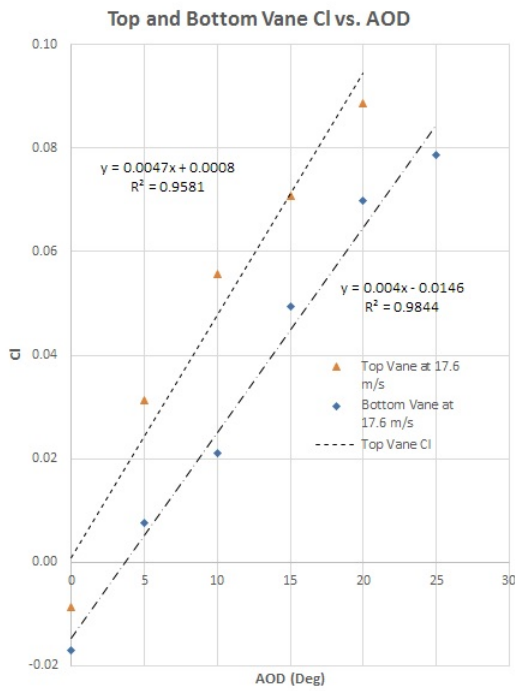


Figure 120: Lift and Drag coefficient at linear region.

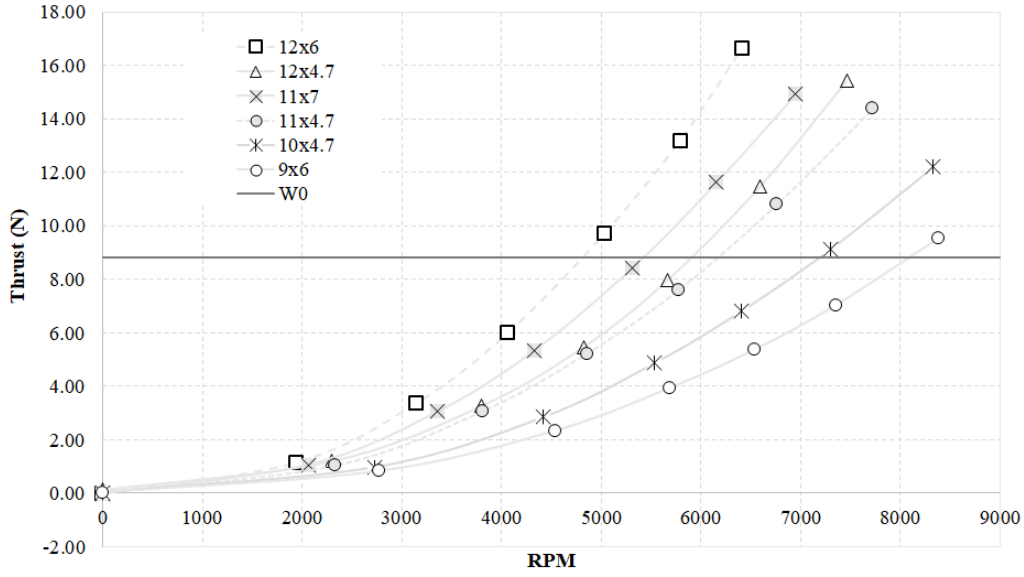


Figure 121: Thrust measurement using MT2814-11 710 Kv motor.

4.2.3 Propulsion System Assessment Result

Thrust, Reverse Thrust and Torque Measurement

Table 3 shows the testing results of the propulsion system using different propellers from 9 inches to 12 inches at different fixed pitch propeller. The test uses a MT2814-11 710kv brushless motor powered by a 14.8 V 1550 mAh lipo 75C battery. Figure 121 and 122 shows the amount of thrust and reverse thrust. Figure 122 shows that the reverse propeller slipstream provides sufficient thrust to push the ATLAS for upright maneuvers before returning to flight. Figure 123 shows the torque measurement.

Gyroscopic Precession

Figure 126 shows that the vehicle pitching angle is slowly increasing in time when deflecting the control vanes to execute a left roll command. The first roll command input produces a 3.1 deg/s pitching rate between the 12.4 s to 17.4 s time frame. The following right roll command was executed and similar pitching motion, but in the opposite direction was observed. A backward pitch command is simultaneously needed when

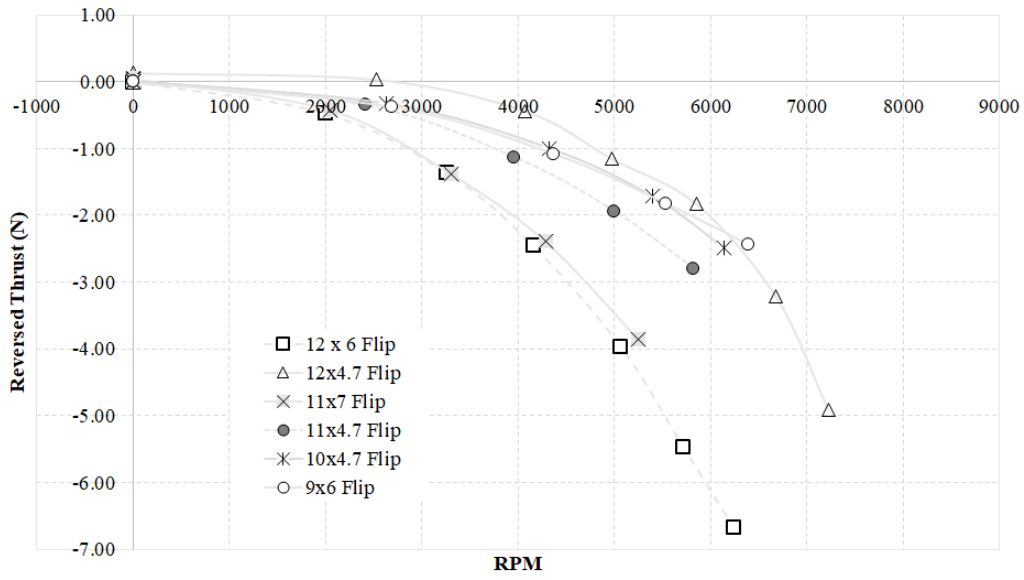


Figure 122: Reverse thrust measurement using MT2814-11 710 Kv motor.

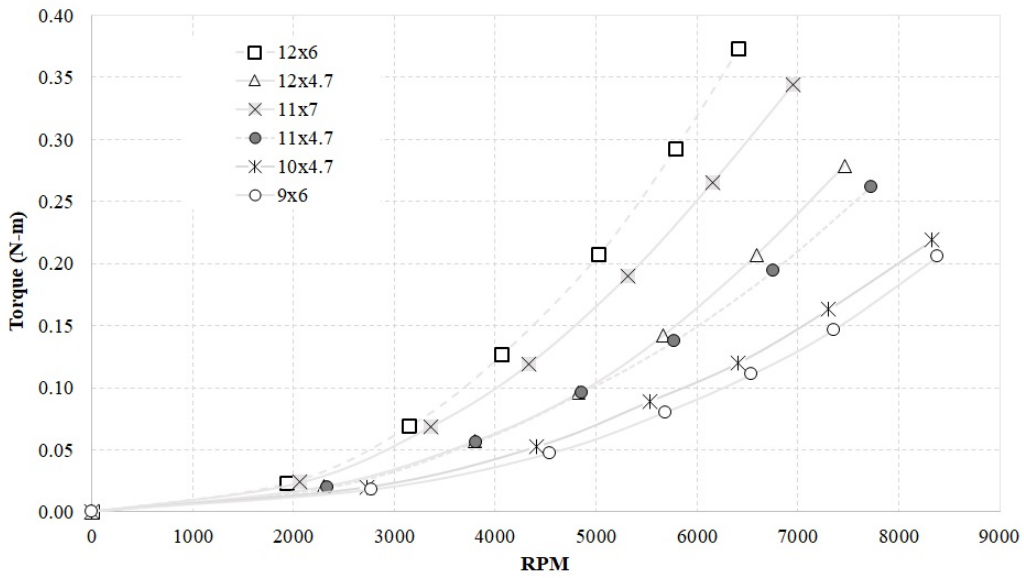


Figure 123: Torque measurement using MT2814-11 710 Kv motor.

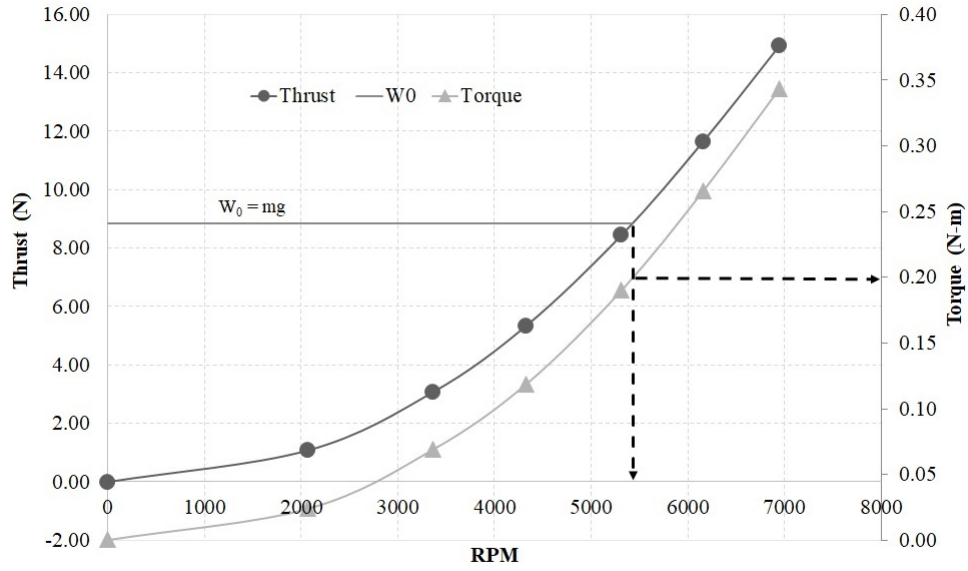


Figure 124: 11x7 propeller.

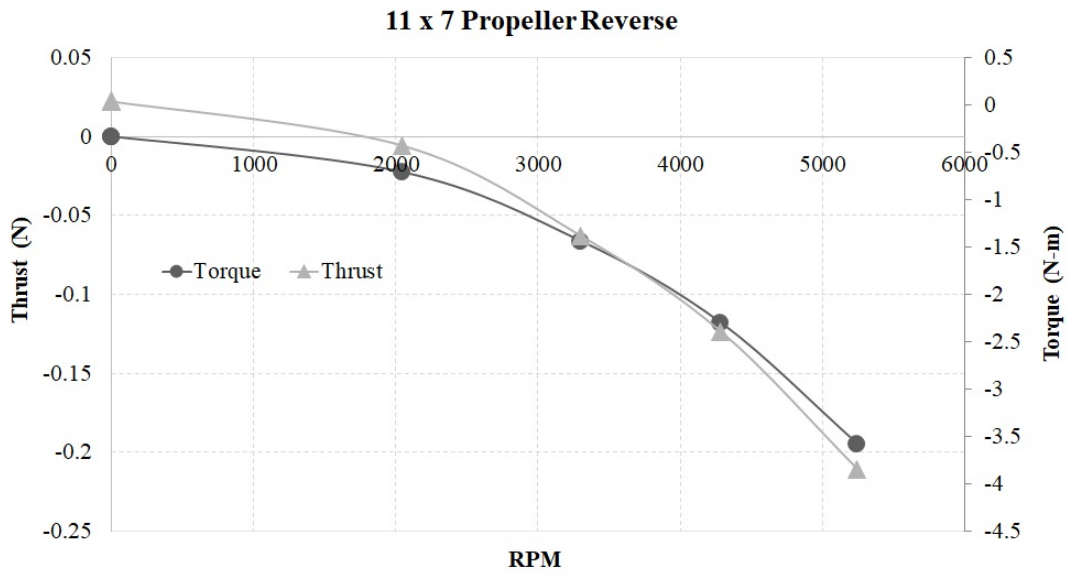


Figure 125: 11x7 propeller reversing spinning direction.

Table 3: Testing results of the propulsion system.

Time (ms)	RPM	Thurst (N)	Torque (N m)	Wind Speed (m/s)
1.1	2322	1.09	0.02	4.8
1.2	3807	3.12	0.06	8.6
1.3	4821	5.29	0.01	11.4
1.4	5727	7.78	0.15	14.2
1.5	6750	10.96	0.21	17.3
1.6	7694	14.51	0.28	19.9

Table 4: Propulsion Dynamic Parameters.

Parameter	Value
Thrust coefficient, K_T	2.43e-7
Torque coefficient, K_M	4.70e-9
Coefficient of the slipstream velocity, K_V	2.50e-3

executing a left rolling command in order to cancel out the gyroscopic precession effect. This execution can be done by mixing the roll and pitch radio signals via the radio channel mixing features.

4.3 Behaviour of the Movable Vanes in Various Flight Conditions

Observation from the ATLAS flight test shows that the movable vanes are responding depending on the flight conditions. This subsection introduces five theoretical flight conditions can be seen by the propeller, namely: Hovering, Upward Vertical Flight, Downward Vertical Flight in Fast, Moderate, and Slow Descent.

Upward Vertical Take-Off

This is a condition when a vehicle is climbing vertically during take-off at a constant rate of V_z . At upstream infinite, the speed V_0 of air flow in front of the rotor is equal and opposite to the rate of climb rate, where $V_0 = V_z$. Note that V_z and U_{prop} have the same direction. The rate of climb is added to the induced velocity.

Hovering

Hovering is the condition when the vehicle is immobile relative to the air when $V_0 = 0$. In the rotor disc plane, the air flows at the induced speed, where $V_1 = U_{prop}$. During hover, the movable flap is deflected

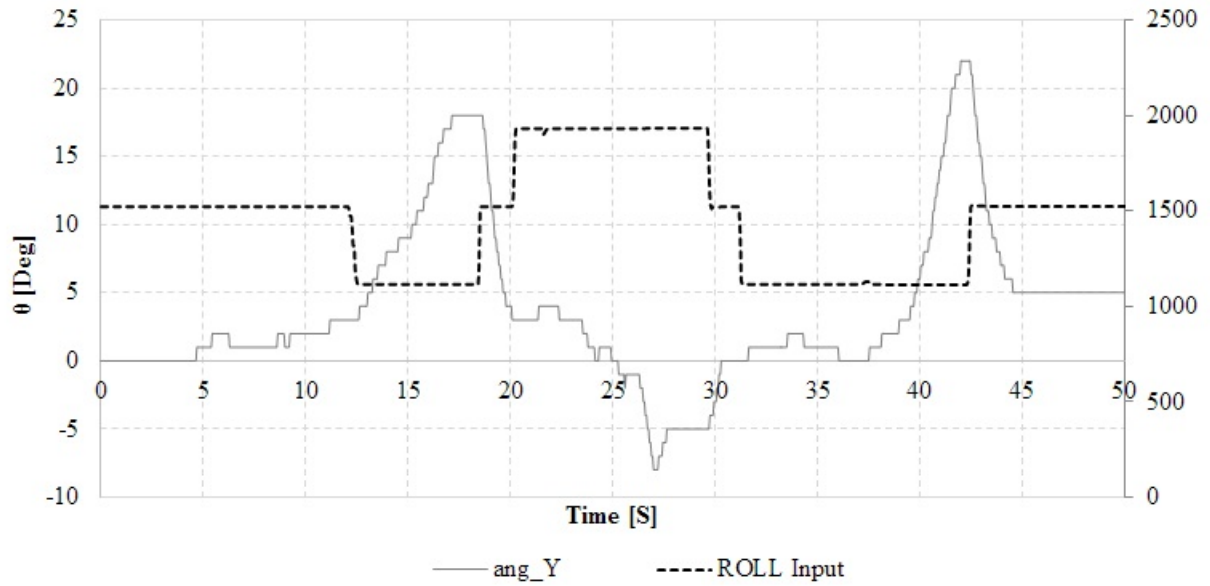


Figure 126: Gyroscopic effect when roll command input was introduced.



Figure 127: The vehicle is pitching forward or backward when roll left or right command input was introduced, respectively.

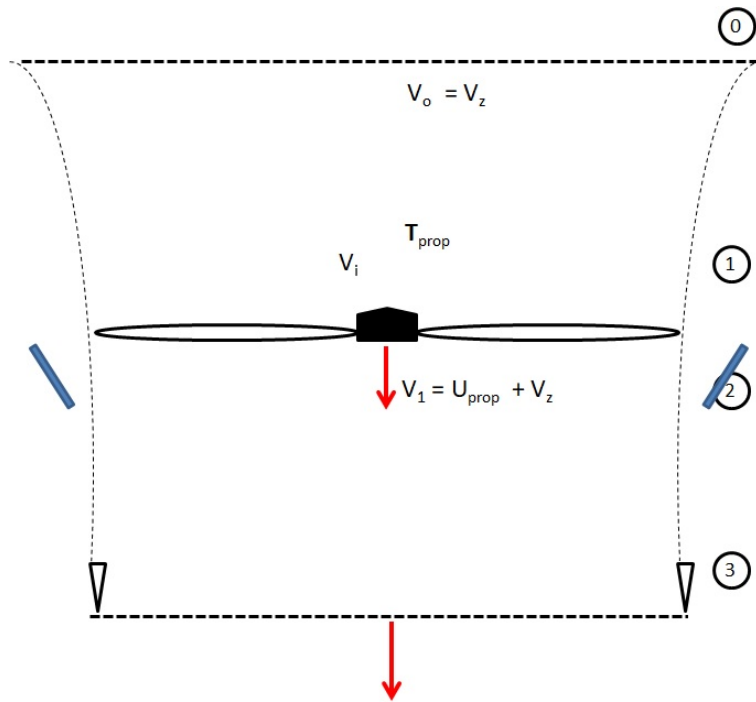


Figure 128: Upward vertical Take-off.

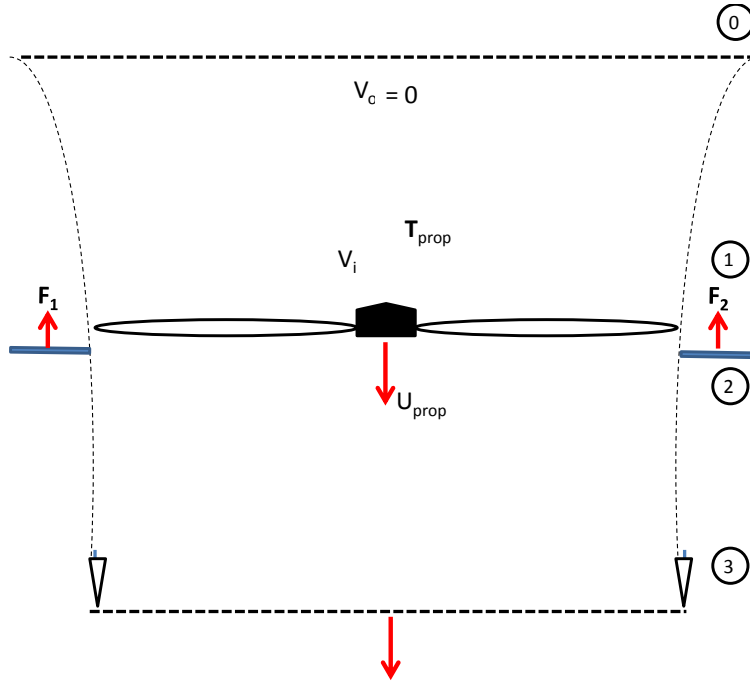


Figure 129: Hovering condition.

passively due to the inflow toward the tip of the propeller. The movable vane remains horizontal at 90 degrees in parallel with the propeller plane as depicted in figure 129. The amount of lift generated by these movable vanes will create a force that produces a moment that opposite to each other. Such moment arm due to the movable vanes can be seen as an aerodynamic balance to counter-act any minor perturbation within the spherical frame.

Fast Descent - Downward Vertical Flight

When the vehicle is descending, the air flow is inverted and passes upwards through the rotor. At the downstream infinite, velocity V_z of air flow is equal and opposite to the downward velocity of the vehicle. The rotor-induced speed, U_{prop} is still directed downwards and opposite to V_z , and this results in velocity decreases. At the rotor level, it is equal to $V_z - U_{prop}$ and reaches $V_z - 2U_{prop}$ at the upstream infinite. As

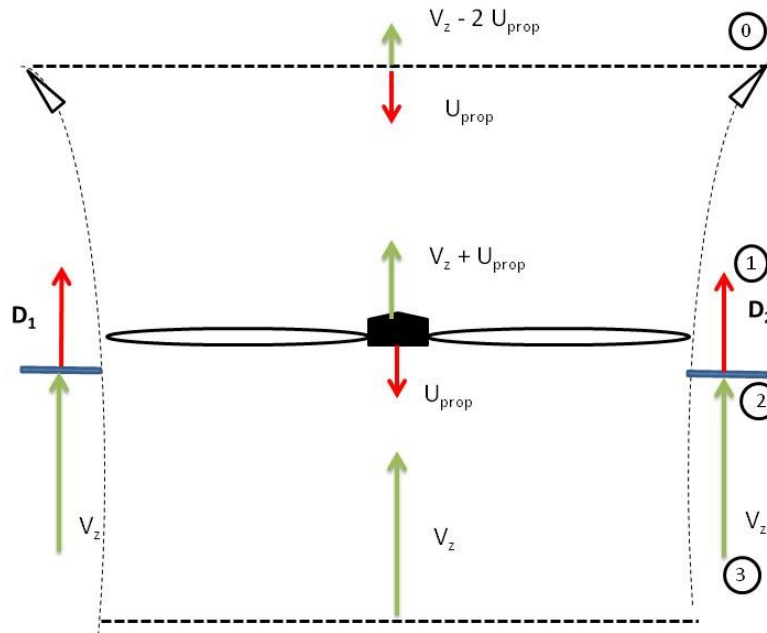


Figure 130: Downward Vertical Flight - Fast Descent.

$V_z - 2U_{prop}$, this speed remains positive i.e., it is always directed in the same direction. Note that these flow conditions, the rotor is Windmilling.

Slow Descent and Vortex Condition - Downward Vertical Flight

While fast and moderate rates of descent correspond to unpowered flight conditions Figure 131 shows that as the vertical velocity of air flow at the downstream infinite, V_z , is lower than the induced speed, U_{prop} , the inversion of the air flow velocity occurs under the rotor. As at the rotor level, $V_z - U_{prop} < 0$, a occurs under the rotor, and the air flow is turned down. The upper air flow forms a vortex near the blade tips. The upward and downward air flows concur on the rotor disc. The blades now rotate in their wash while the air forms a vortex ring insulating the rotor that is no longer traversed by the air flow. This phenomenon is called Vortex Condition. Such condition is dangerous as the rotor (or control vanes), in the stall area, cannot be

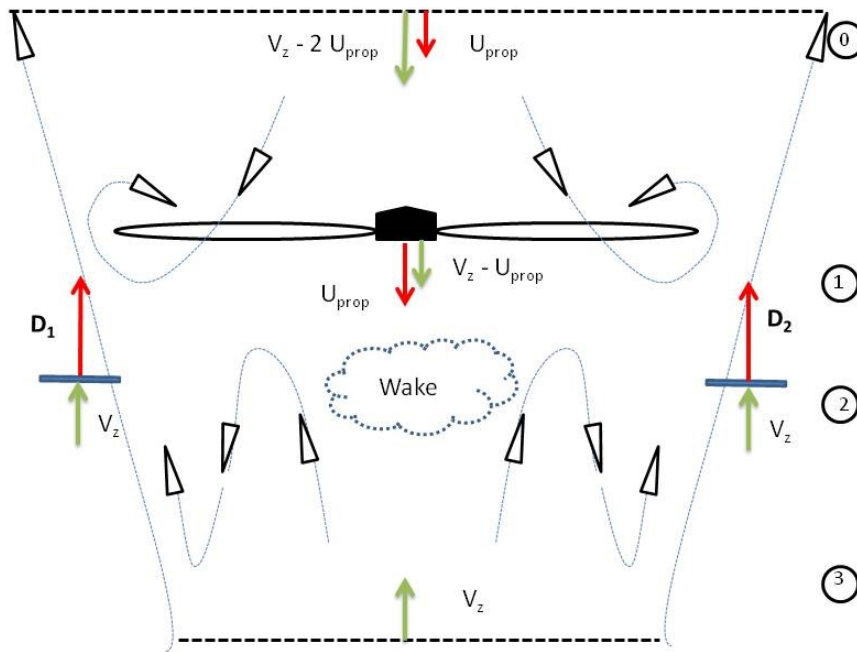


Figure 131: Downward Vertical Flight - Slow Descent.

controlled anymore. It is easy for the vehicle to come out from this situation, either by flying forward or by increasing thrust to increase V_z . Omker [40] has shown that propeller operating at low Reynold number can experience a decrease in thrust when operating at VRS conditions. VRS is an unsteady, turbulent condition characterized by a loss of collective control and thrust fluctuations.

CHAPTER V

DYNAMICS AND FLIGHT CONTROL

This chapter discusses the active and passive control system of ATLAS. The vehicle is modeled as a rigid body influenced by aerodynamic, propulsion, gravitational forces, and moment acting on the vehicle's center of gravity. Six degrees of freedom rigid body equations of motion are utilized with Euler angles for attitude parameterization.

5.0 Impact of Center of Gravity Location on Flight and Ground Recovery Maneuvering

The placement of the C.G. along the thrust line can influence the performance of the flying sphere in flight and ground. For a typical airplane system with fixed wing and horizontal tail, the C.G. is typically ahead of the center of pressure to achieve stable longitudinal stability to restore the vehicle after being perturbed in flight. On the other hand, shifting the C.G. slightly toward the aft, provide better hovering stability and maneuverability, as demonstrated by most hovering 3D acrobatic plane. The C.G. of the flying sphere has to be located below than the C.O.S when considering ground operation to execute self-upright position and prevent the sphere from automatically tip over wherever the vehicle is landed on the ground. However, moving the C.G. further downward from the C.O.S will then penalize the longitudinal/lateral stability in flight and become less controllable in flight. Due to these effects, the JFS design as shown in figure 10 claims to use a mechanism to shift the C.G. of the vehicle depending on the operational modes. Figure 132 shows that the spherical UAV with the capability of ground recovering needs to have a C.G. location that can satisfy both in flight and ground operation. On the other hand, figure 133 depicts the effect on pitching moment by varying the C.G. location assuming the placement of the control vanes is fixed under the C.O.S of the vehicle.

When the vehicle is on the ground, the propeller spinning direction was reversed to tilt the vehicle upright, as shown in figure 134. The figure shows a contact point when the vehicle is on the ground, assuming no

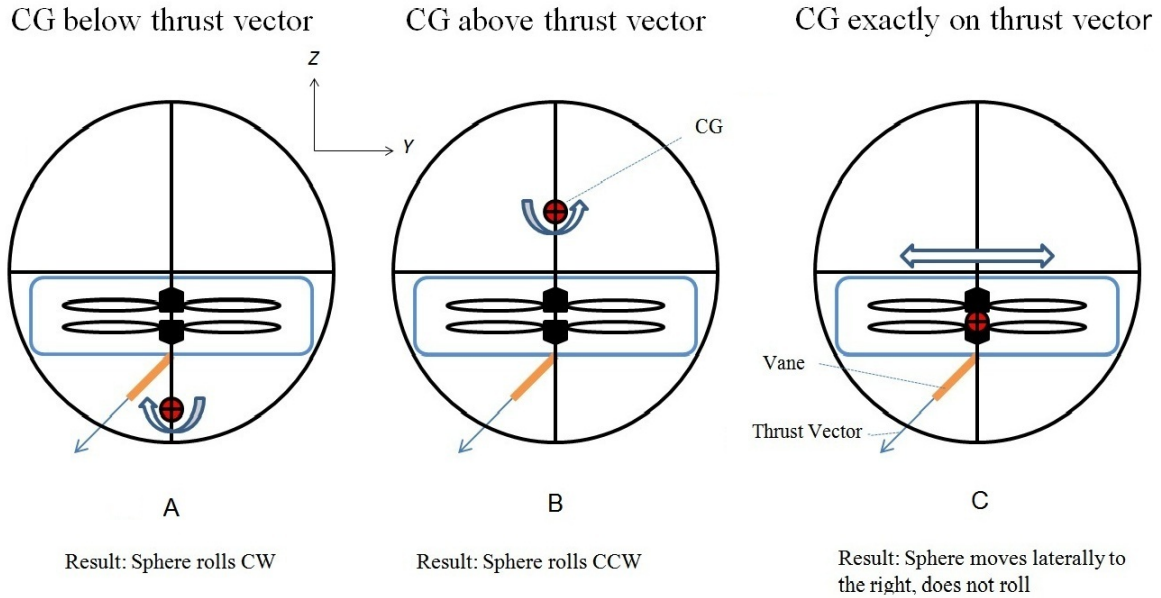


Figure 132: The placement of control surface in relative to the center of gravity.

slip condition. The l_w is the distance of the location of C.G in respect fo the center of the sphere (C.O.S).

The sum of pitching moment in counter-clockwise wise direction is:

$$M_y = Tr - mg \cos \theta l_w \quad (28)$$

For equilibrium state, the sum of moment is 0, that makes

$$Tr = mg \cos \theta l_w \quad (29)$$

The equation above shows that if the vehicle's C.G. is above the C.O.S, where $l_w > 0$, the vehicle is top-heavy and will tilt in a clockwise direction. The C.G. is located at the C.O.S if $l_w = 0$. If the $l_w < 0$ in the z-direction, the center of the gravity will cause the vehicle to tilt forward further after landed on the ground. In order to tilt upright, sufficient reversed thrust is needed to produce rotational moment to overcome the moment due to the weight. To simplify the ATLAS design in this research and avoid additional weight penalty to have adjustable C.G mechanism like the JFS, the center of gravity of the vehicle is set at

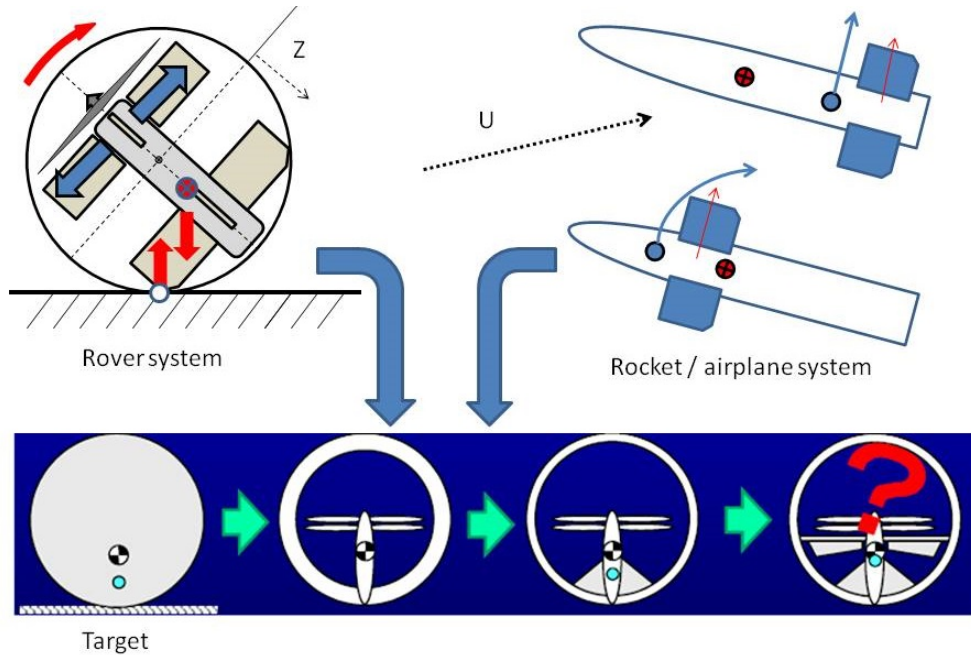


Figure 133: The effect of C.G. on flight and ground control

the C.O.S. where $(x, y, z) = (0,0,0)$.

5.1 Propeller Placement and Center of Gravity

As the propeller is spinning in a circular pattern, the velocity of the airflow across the propeller can vary depending on the position of the blade in the plane of rotation relative to the incoming airflow direction. Therefore, the airflow meeting each blade varies as the propeller rotates. Looking from the top of the propeller plane as shown in Figure 2, assuming the headwind is coming direction from the front, the highest velocity of airflow occurs over the right blade with the propeller spinning in the counter-clockwise direction. As the relative wind speed of the advancing propeller blade increases, the right propeller blade develops more lift. On the other hand, slow relative wind is acting on the retracting left blade of the propeller. The phenomenon is known as the P-factor, also known as asymmetric blade effect.

Which way the propeller moves against the direction of the relative headwind is determined by which part of the propeller blade has higher lift. Since a spinning motor with a single propeller is essentially a gyroscope,

C.O.S – Center of Sphere
C.G. – Center of Gravity

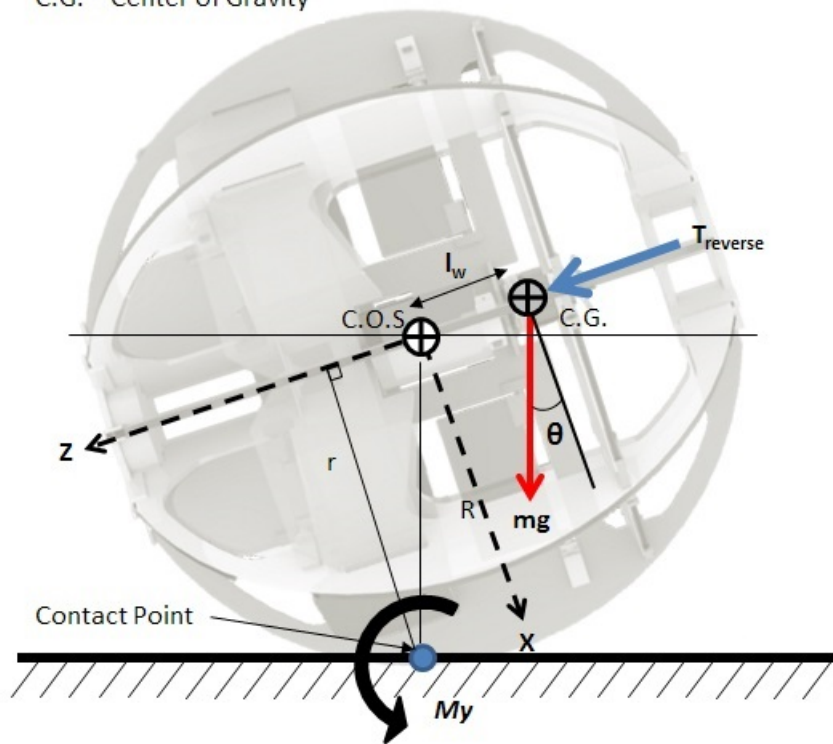


Figure 134: Effect of shifting C.G. above C.O.S (neg z-dir) on upright maneuver.

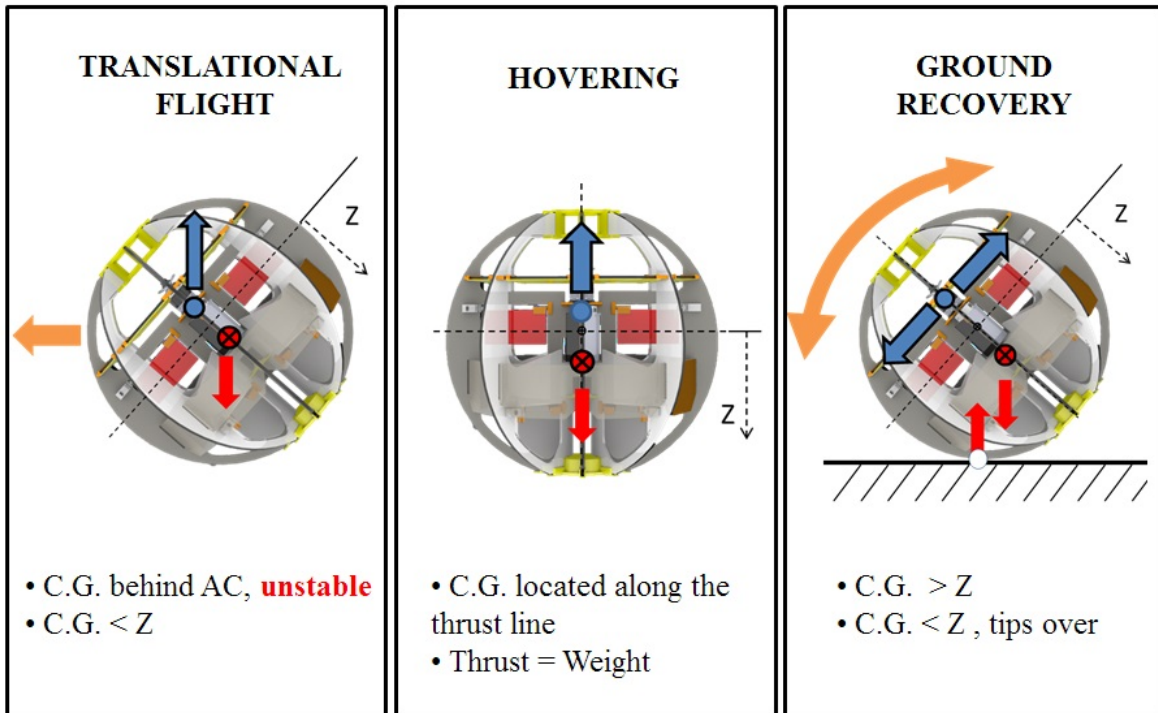


Figure 135: Hover, forward flight, and rolling on the ground.

the resultant force with more lift from the advancing propeller blade is felt 90 degrees in the direction of rotational. Assuming the center of gravity is below the propeller, the combined effect of dissymmetry of lift and torque induced precession can cause the nose to rise or pitch up.

Depending on the vertical placement of the center of gravity along the thrust line of the vehicle, the net torque can impact the translational speed of the vehicle [41, 42]. Two flight conditions considered here are: transitioning from hover flight to forward flight and wind gust disturbance from hover flight. Figure 137a shows the vehicle is tilting left or torque counter-clockwise to execute forward flight. If the center of gravity is located above the propeller plane, the induced drag from the propeller could cause the vehicle to torque in clockwise to increase pitch angle and become unstable as the forward speed increases. If the center of gravity is below the propeller plane, the resultant pitch angle can decrease to damp the system. Surprisingly, the effect is similar when the vehicle is experiencing wind gust disturbance from hovering conditions. Figure

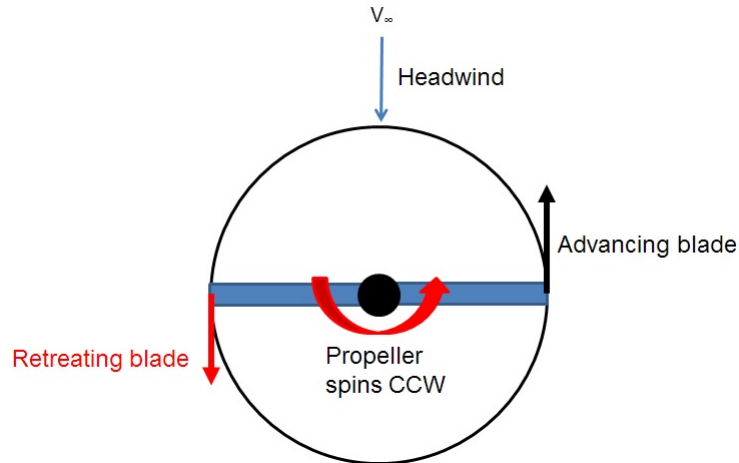


Figure 136: Top view of the propeller spinning in counter-clockwise direction.

137b shows such a situation. The vehicle with the center of gravity placed above the propeller should be able to pitch in counter-clockwise to counteract the gust disturbance. The vehicle would be drifting with the wind if the center of gravity placed below the propeller plane. Such a phenomenon was observed when ATLAS was experiencing some headwind or gust. Perhaps the ideal position to achieve stability for both forward flight and gust rejection conditions is to place the propeller close to the center of gravity of the vehicle. Furthermore, the pitching authority from the control surfaces must be sufficient to counteract this induced pitching moment tendency from the propeller.

5.2 Different Control Vanes Configurations on Vehicle

Figure 138 shows the known type of control scheme configurations presented by some spherical shaped UAVs presented in the literature review. Note that the Japanese Flying Sphere control is still unknown. The previous section has set the center of gravity at the center of the spherical frame. With this assumption, a total of six types of control configurations were investigated before deciding the proper control scheme for ATLAS design. The goal here is to estimate the restoring moment each control scheme can produce. The highest restoring moment due to control surface deflection will be selected as the control scheme for ATLAS. This subsection derives the forces and moments for all three major axes along with a top view and side view of control vanes for each control scheme configurations. There 6 types of control configurations

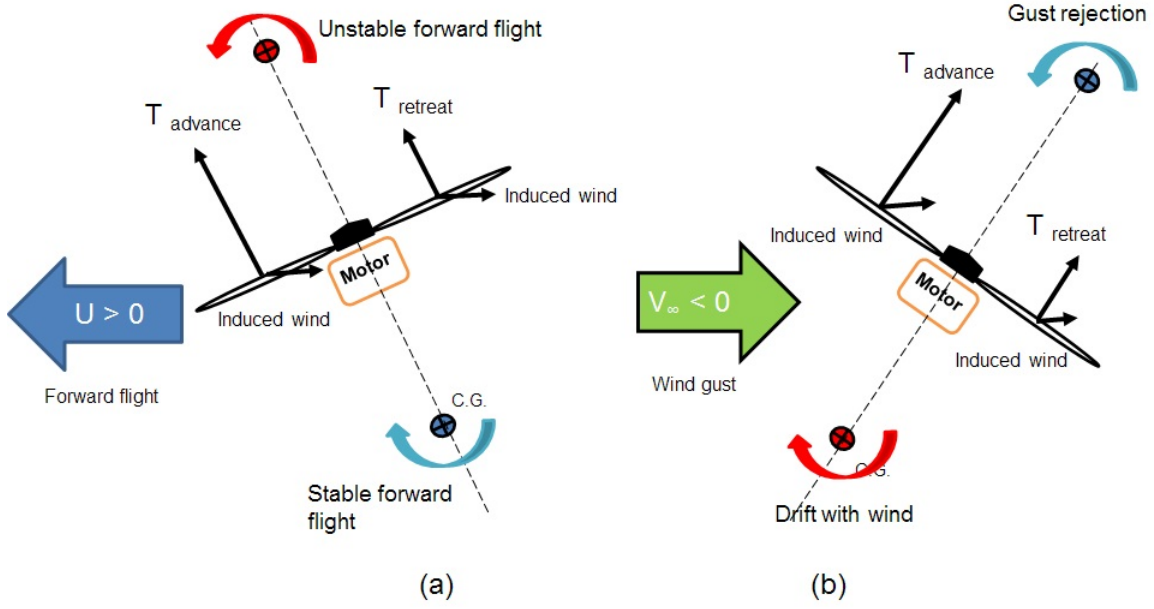


Figure 137: Impact of the center of gravity location during (a) forwards flight and (b) wind gust.

are 4+, 8X (same), 8X(oppo), 4X, 8+(same), and 8+(oppo). Note that the L_t and L_b is the lift for top and bottom vane, respectively. D_t and D_b is the drag for the top and bottom vane, respectively. h_t and h_b is the longitudinal distance of the quarter chord of the top and bottom vane from the center of gravity of the vehicle. d_t and d_b is the lateral distance of the top and bottom vanes from the center of gravity of the vehicle. θ_n is the deflection angle where n represents the control vane number 1 to 4 is the top vanes, and number 5 to 8 is the bottom vanes.

4+ Configuration

This configuration consists of four control vanes, where the primary axes for roll and pitch is aligned with the body frame.

$$Fx_{(4+)} = -L_t(\delta_7 - \delta_5) \quad (30)$$

$$Fy_{(4+)} = L_t(\delta_6 - \delta_8) \quad (31)$$

TYPES	ROLL	PITCH	YAW	UAV
Type 1 (4+)	6,8	5,7	5,6,7,8	
Type 2 (8+0) (8 vanes, non-coupled)	1,3	2,4	5,6,7,8	
Type 3 (8+0) (8 vanes, top and bottom are non-coupled)	1,3	2,4	1,2,3,4,5,6,7,8	 
Type 4 (8+0) (8 vanes, coupled)	1,3,5,6,7,8	2,4,5,6,7,8	1,2,3,4,5,6,7,8	 

□ Top Vanes = 1,2,3,4 □ Bottom Vanes = 5,6,7,8

Figure 138: Known Spherical Shape UAV with their control configurations.

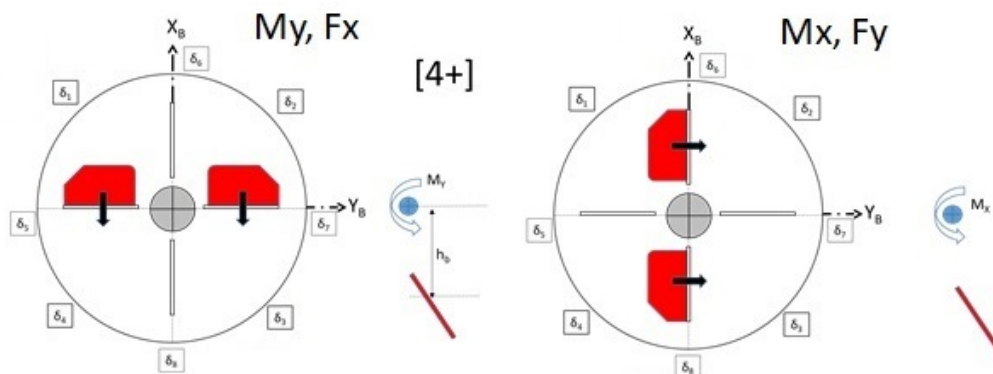


Figure 139: 4+ configuration.

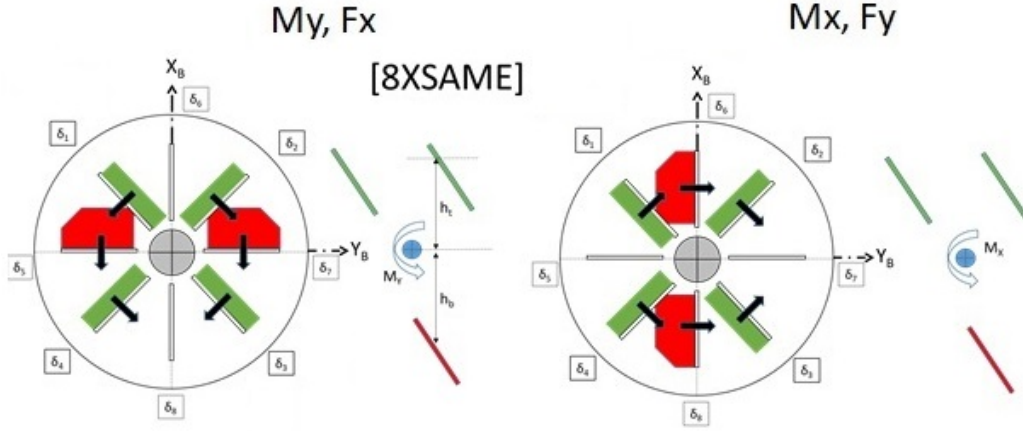


Figure 140: 8Xsame configuration.

$$Fz_{(4+)} = D_b(\delta_5 + \delta_6 + \delta_7 + \delta_8) \quad (32)$$

$$Mx_{(4+)} = -L_t(\delta_6 - \delta_8)h_b \quad (33)$$

$$My_{(4+)} = -L_t(\delta_7 - \delta_5)h_b \quad (34)$$

$$Mz_{(4+)} = L_t(\delta_5 + \delta_6 + \delta_7 + \delta_8)d_b \quad (35)$$

8X (same) Configuration

Note that the bottom vanes configuration is similar to the 4+ configuration and the top vanes configuration are similar to the 4X configurations. Both top and bottom vanes are deflecting in the same direction to each other.

$$Fx_{(8X_s)} = -L_t(-\delta_1 + \delta_2 + \delta_3 - \delta_4)h_t \cos \frac{\pi}{4} - L_b(\delta_7 - \delta_5) \quad (36)$$

$$Fy_{(8X_s)} = L_t(\delta_1 + \delta_2 - \delta_3 - \delta_4)h_t \cos \frac{\pi}{4} + L_b(\delta_6 - \delta_8) \quad (37)$$

$$Fz_{(8X_s)} = D_t(\delta_1 + \delta_2 + \delta_3 + \delta_4) + D_b(\delta_5 + \delta_6 + \delta_7 + \delta_8) \quad (38)$$

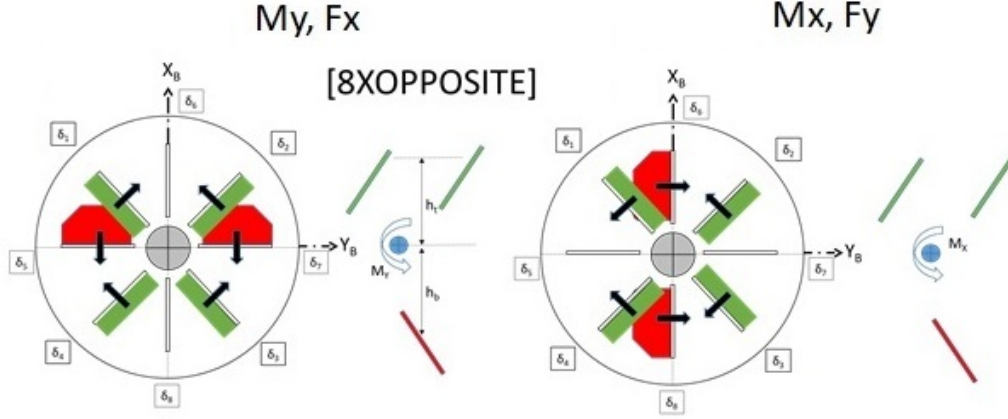


Figure 141: 8X opposite configuration.

$$Mx_{(8X_s)} = L_t(\delta_1 + \delta_2 - \delta_3 - \delta_4)h_t \cos \frac{\pi}{4} - L_b(\delta_6 - \delta_8)h_b \quad (39)$$

$$My_{(8X_s)} = L_t(-\delta_1 + \delta_2 + \delta_3 - \delta_4)h_t \cos \frac{\pi}{4} - L_b(\delta_7 - \delta_5)h_b \quad (40)$$

$$Mz_{(8X_s)} = L_t(\delta_1 + \delta_2 + \delta_3 + \delta_4)d_t + L_b(\delta_5 + \delta_6 + \delta_7 + \delta_8)d_b \quad (41)$$

8X (opposite) Configuration

Note that the bottom vanes configuration is similar to the 4+ configuration and the configuration of the top vanes are similar to the 4X configurations. Both top and bottom vanes are deflecting in the opposite direction to each other.

$$Fx_{(8X_o)} = L_t(\delta_1 - \delta_2 - \delta_3 + \delta_4) \cos \frac{\pi}{4} - L_b(\delta_7 - \delta_5) \quad (42)$$

$$Fy_{(8X_o)} = -L_t(-\delta_1 - \delta_2 + \delta_3 + \delta_4) \cos \frac{\pi}{4} - (\delta_6 - \delta_8) \quad (43)$$

$$Fz_{(8X_o)} = D_t(\delta_1 + \delta_2 + \delta_3 + \delta_4) + D_b(\delta_5 + \delta_6 + \delta_7 + \delta_8) \quad (44)$$

$$Mx_{(8X_o)} = -L_t(-\delta_1 - \delta_2 + \delta_3 + \delta_4)h_t \cos \frac{\pi}{4} - (\delta_6 - \delta_8)h_b \quad (45)$$

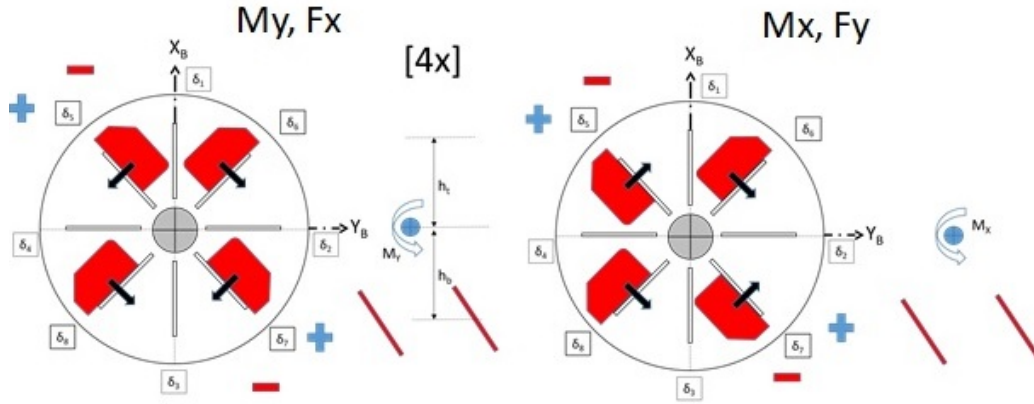


Figure 142: 4X configuration.

$$My_{(8Xo)} = -L_t(\delta_1 - \delta_2 - \delta_3 + \delta_4)h_t \cos \frac{\pi}{4} - L_b(\delta_7 - \delta_5)h_b \quad (46)$$

$$Mz_{(8Xo)} = L_t(\delta_1 + \delta_2 + \delta_3 + \delta_4)d_t + L_b(\delta_5 + \delta_6 + \delta_7 + \delta_8)d_b \quad (47)$$

4X Configuration

This configuration consists of four control vanes that is 45 degrees offset in comparison to the 4+ configuration.

$$Fx_{(4X)} = L_t(\delta_5 - \delta_6 + \delta_7 - \delta_8) \cos \frac{\pi}{4} \quad (48)$$

$$Fy_{(4X)} = L_t(\delta_5 + \delta_6 - \delta_7 - \delta_8) \cos \frac{\pi}{4} \quad (49)$$

$$Fz_{(4X)} = D_b(\delta_5 + \delta_6 + \delta_7 + \delta_8) \quad (50)$$

$$Mx_{(4X)} = -L_b(\delta_5 + \delta_6 - \delta_7 - \delta_8)h_b \cos \frac{\pi}{4} \quad (51)$$

$$My_{(4X)} = -L_b(-\delta_5 + \delta_6 + \delta_7 - \delta_8)h_b \cos \frac{\pi}{4} \quad (52)$$

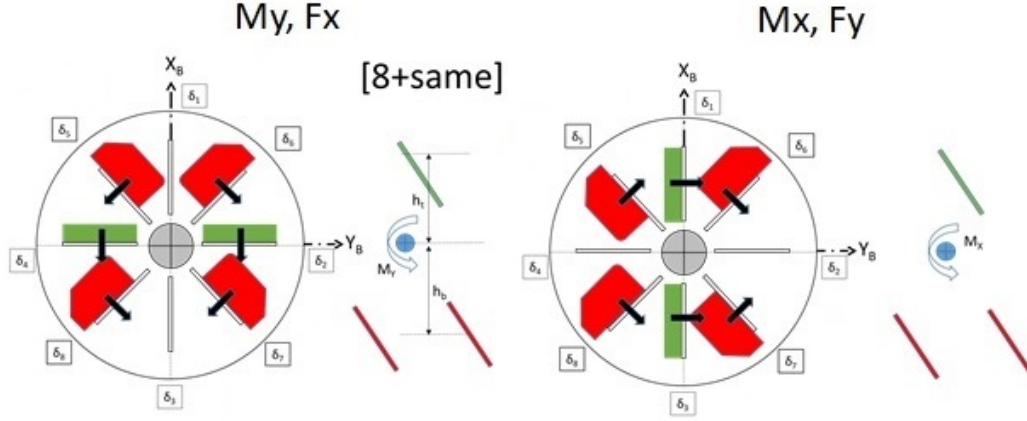


Figure 143: 8+same configuration.

$$Mz_{(4X)} = L_b(\delta_5 + \delta_6 + \delta_7 + \delta_8)d_b \quad (53)$$

8+ (same) Configuration

Note that the bottom vanes configuration is similar to the 4x configuration and the top vanes configuration are similar to the 4+ configurations. Both top and bottom vanes are deflecting in the same direction.

$$Fx_{(8+s)} = -(\delta_4 - \delta_2) - (-\delta_5 + \delta_6 + \delta_7 - \delta_8)\frac{\pi}{4} \quad (54)$$

$$Fy_{(8+s)} = -(\delta_1 - \delta_3) + (\delta_5 + \delta_6 - \delta_7 - \delta_8)\cos\frac{\pi}{4} \quad (55)$$

$$Fz_{(8+s)} = D_t(\delta_1 + \delta_2 + \delta_3 + \delta_4) + D_b(\delta_5 + \delta_6 + \delta_7 + \delta_8) \quad (56)$$

$$Mx_{(8+s)} = -L_t(\delta_1 - \delta_3)h_t - (\delta_5 + \delta_6 - \delta_7 - \delta_8)h_b\cos\frac{\pi}{4} \quad (57)$$

$$My_{(8+s)} = -L_t(\delta_2 - \delta_4)h_t - L_b(-\delta_5 + \delta_6 + \delta_7 - \delta_8)h_b\cos\frac{\pi}{4} \quad (58)$$

$$Mz_{(8+s)} = L_t(\delta_1 + \delta_2 + \delta_3 + \delta_4)d_t + L_b(\delta_5 + \delta_6 + \delta_7 + \delta_8)d_b \quad (59)$$

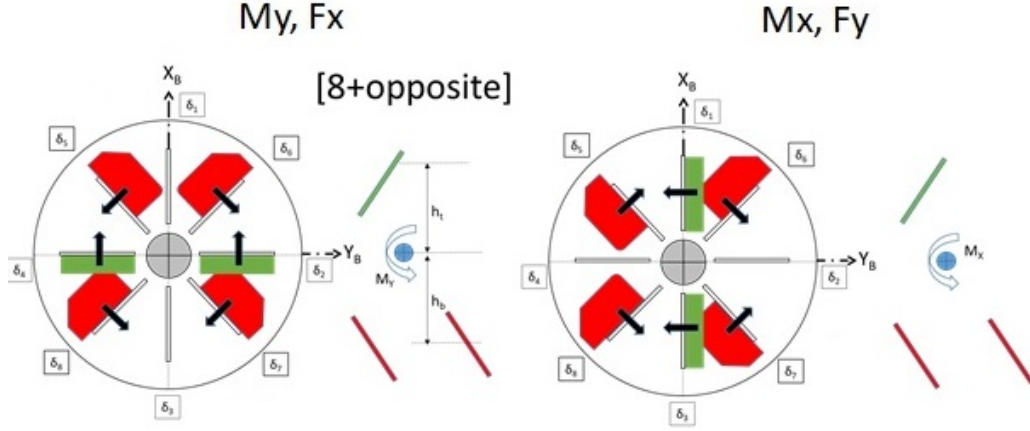


Figure 144: 8+ opposite configuration.

8+ (opposite) Configuration

Note that the bottom vanes configuration is similar to the 4x configuration and the configuration of the top vanes are similar to the 4+ configurations. Both top and bottom vanes are deflecting in the opposite direction to each other.

$$Fx_{(8+o)} = (\delta_4 - \delta_2) - (-\delta_5 + \delta_6 + \delta_7 - \delta_8) \frac{\pi}{4} \quad (60)$$

$$Fy_{(8+o)} = (\delta_1 - \delta_3) + (\delta_5 + \delta_6 - \delta_7 - \delta_8) \cos \frac{\pi}{4} \quad (61)$$

$$Fz_{(8+o)} = D_t(\delta_1 + \delta_2 + \delta_3 + \delta_4) + D_b(\delta_5 + \delta_6 + \delta_7 + \delta_8) \quad (62)$$

$$Mx_{(8+o)} = L_t(\delta_1 - \delta_3)h_t - L_b(\delta_5 + \delta_6 - \delta_7 - \delta_8)h_b \cos \frac{\pi}{4} \quad (63)$$

$$My_{(8+o)} = L_t(\delta_2 - \delta_4)h_t - L_b(-\delta_5 + \delta_6 + \delta_7 - \delta_8)h_b \cos \frac{\pi}{4} \quad (64)$$

$$Mz_{(8+o)} = L_t(\delta_1 + \delta_2 + \delta_3 + \delta_4)d_t + L_b(\delta_5 + \delta_6 + \delta_7 + \delta_8)d_b \quad (65)$$

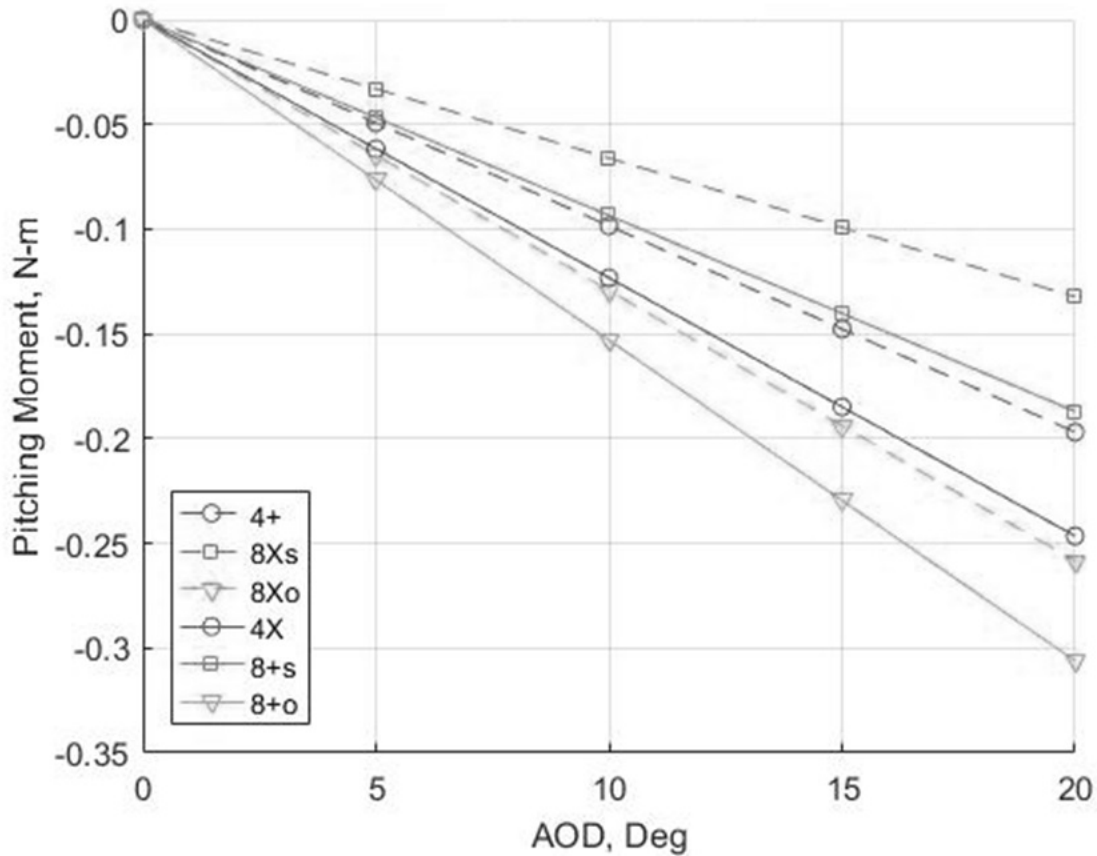


Figure 145: Pitching restoring moment for different control types.

The graph 145 shows the restoring moment from all the potential active control configuration can product by using the lift and drag coefficient for the top and bottom vanes obtained from the wind tunnel test described in Chapter 3. The graph shows that the 8+oppo configuration has the steepest slope of the moment with respect to the deflection angle of the control vanes that can quickly restore the moment. Note that more control vanes mean more drag will be generated, as shown in figure 146.

5.3 System Composition of ATLAS

In the case of hovering, low-speed flight and level flight, the main forces of the vehicle include gravitation forces, thrust, and moment caused by the power system, the controlling forces and moment caused by

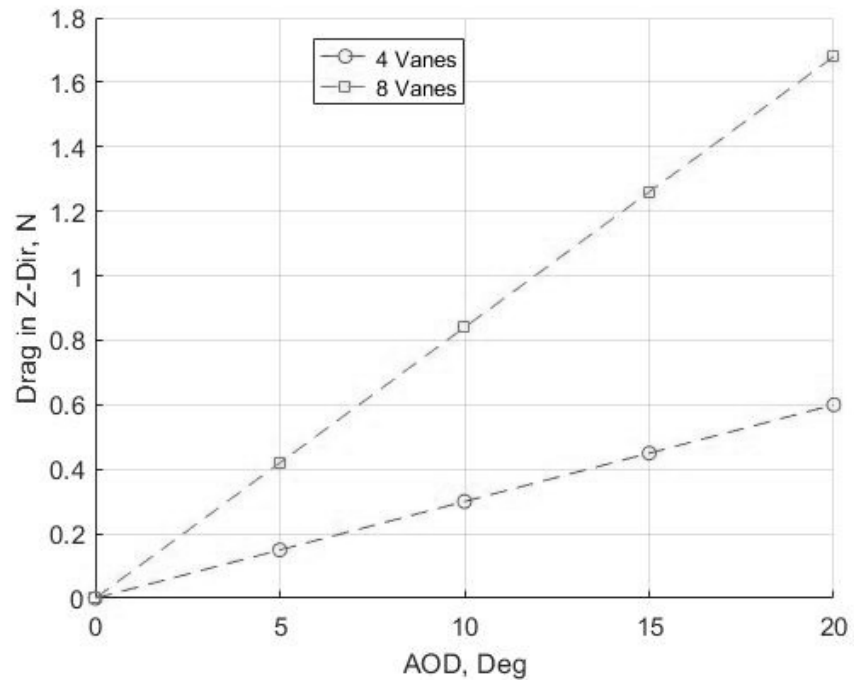


Figure 146: Estimated drag force in the z-direction for 4 versus 8 control vanes for deflection angle ranges from 0 to 20 degrees.

the passive and active control flaps, and the spinning moment caused by a high-speed rotating propeller. Therefore, the resultant force and moment of the vehicle are given, respectively, by

$$F_{vehicle} = F_{passive} + F_{active} + F_{gravity} + F_{motor} \quad (66)$$

$$M_{vehicle} = M_{passive} + M_{active} + M_{gyro} + M_{motor} \quad (67)$$

where F_{active} , $F_{passive}$, $F_{gravity}$ and F_{motor} are active surfaces, passive surfaces, gravity, and thrust control. M_{active} , $M_{passive}$, M_{gyro} and M_{motor} are active and passive surfaces moment, gyroscopic precession moment, and thrust moment.

Passive Movable Guide Vanes

Figure 147 shows the schematic of the vane's position in relative to the propeller tips. Figure 148 and 149 represents the free body diagram of the movable vanes behavior while in hovering, translational flight, and descending conditions. Note that these figures excluded the forces and moments produced by the active control surfaces of the vehicle. Figure 148 shows the movable vanes deflects upward while hovering and descending. Figure 149 depicts the conditions of the vanes when pitching/rolling for translational flight. F_1 and F_2 represents the lift force of the vanes caused by the incoming airflow while the propeller is spinning at a constant RPM. D_1 and D_2 represents the drag forces seen by each movable. The subscript 1 represents all the vanes on the left-hand side, and 2 represents all the right-hand side vanes in the 2D diagram. There are four movable vanes on each side. θ is the deflection angle of the vanes, in which $\theta = 90$ degrees when the vanes fully deflected and remain in a horizontal position due to the mechanical restriction. Combining with the drop test result in the previous section, the annular plate can provide pitching/rolling stability when the vehicle is descending; it can assume that drag forces are being applied as the vehicle falling vertically or experiencing a momentary drop when throttle decreases during flight. These equations below represent the forces along the Z-axis and the pitching/rolling moments acting on the center of gravity of the vehicle.

$$F_{z(passive)} = T_{motor} + 4D_1 \sin \theta + 4D_2 \sin \theta + 4F_1 \sin \theta + 4F_2 \sin \theta - W_{total} \quad (68)$$

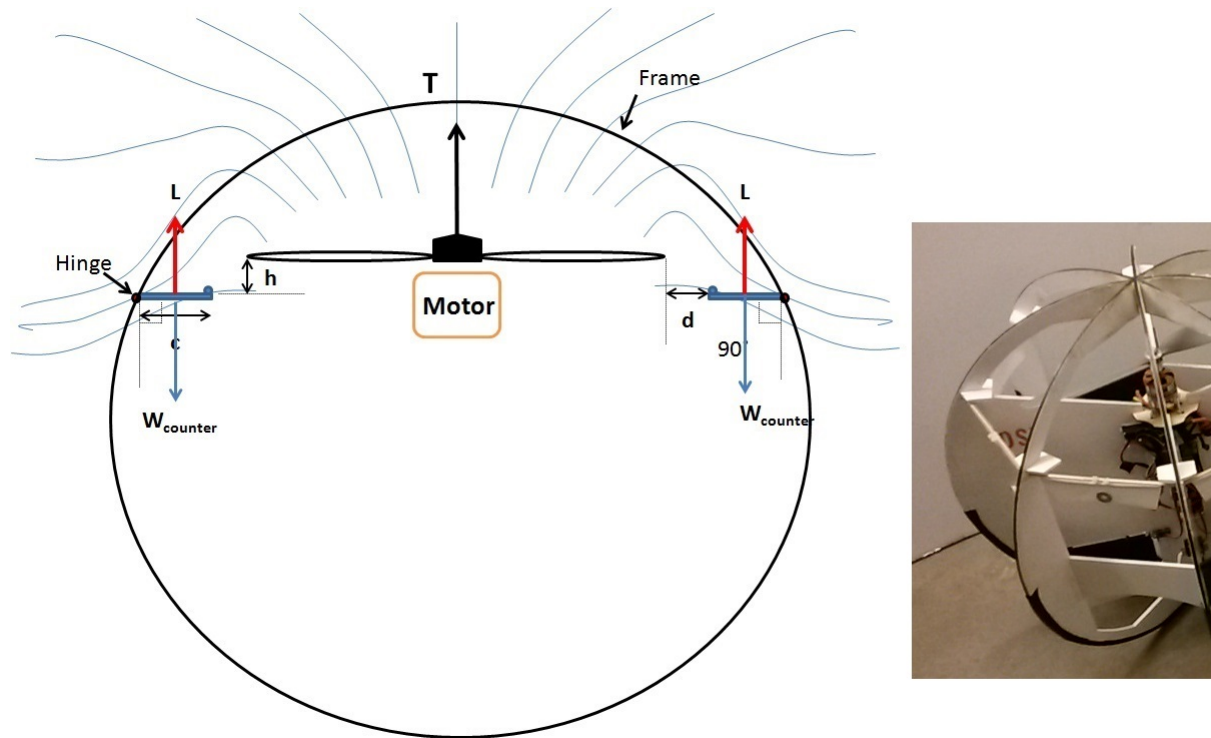


Figure 147: Hinged movable vanes on the top half of the ATLAS.

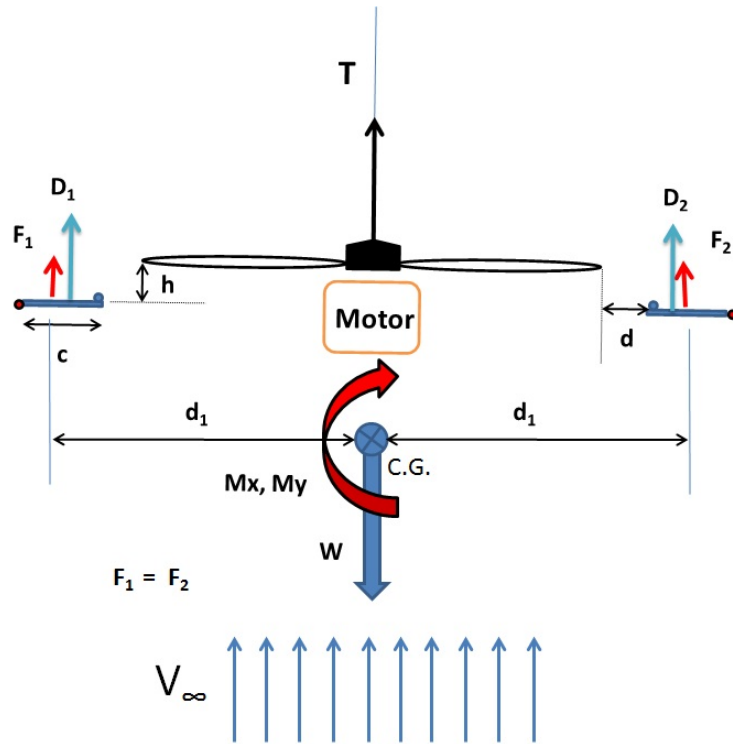


Figure 148: Free body diagram of the hinged movable vanes while hovering and descending.

$$M_{y(\text{passive})} = M_{x(\text{mv})} = 4d_1(F_1 + D_1) + 4d_2(F_2 + D_2) \quad (69)$$

During take-off, the top of all the vanes experiences incoming airflow. The dynamic pressure at this moment temporarily overcome the weight of the movable vanes and causes them to deflects and remains vertical, where $\theta = 0$ as long as the dynamic pressure is higher than the weight. This makes equation 68 and 69 becomes

$$F_{z(\text{passive})} = T_{\text{motor}} - W_{\text{total}} \quad (70)$$

$$M_{y(\text{passive})} = M_{x(\text{passive})} = 0 \quad (71)$$

While hovering, both F and D forces are acting simultaneously to provide hovering stability when $\theta = 90$. The spinning propeller at a constant RPM will keep the vanes fully deflected horizontally as air is flowing into the propeller plane.

$$F_{z(\text{passive})} = T_{\text{motor}} + 4D_1 + 4D_2 + 4F_1 + 4F_2 - W_{\text{total}} \quad (72)$$

$$M_{y(\text{passive})} = M_{x(\text{passive})} = 4d_1(F_1 + D_1) + 4d_2(F_2 + D_2) \quad (73)$$

While the vehicle is descending, free steam is coming up from the bottom of the vehicle and causes all the vanes to deflected upward. The vanes produce a drag force to reduces the descending velocity. Equation 74, 75 and figure 148 show that the moment created by the D_1 (counter-clockwise moment) and D_2 (clockwise moment) can also help stabilizes the longitudinal or lateral axis.

$$F_{z(\text{passive})} = T_{\text{motor}} + 4F_1 + 4F_2 - W_{\text{total}} \quad (74)$$

$$M_{y(\text{passive})} = M_{x(\text{passive})} = 4d_2D_1 - 4d_2D_2 \quad (75)$$

where D_1 and $D_2 \ll F_1$ and F_2 should be considered small when the propeller is slowing down for descending.

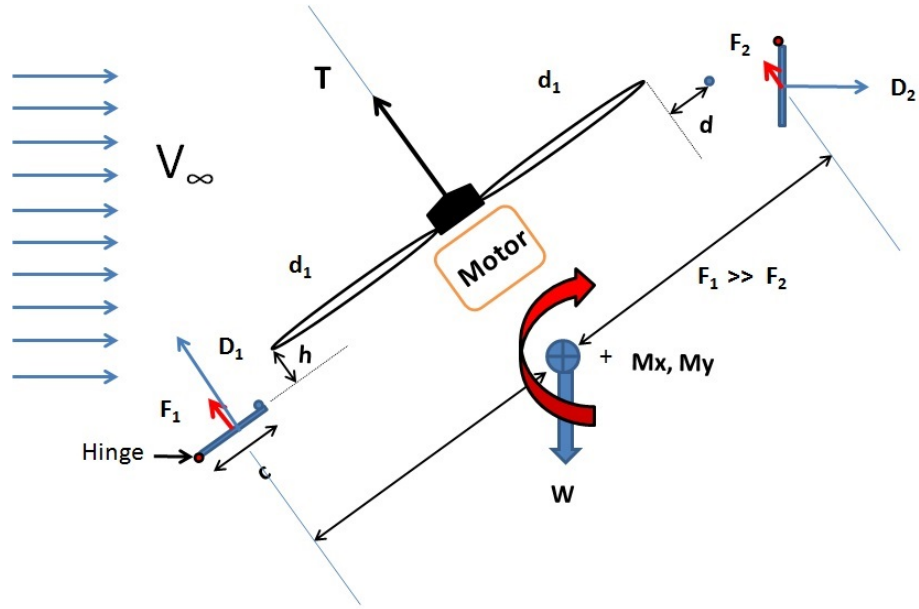


Figure 149: Free body diagram of the hinged movable vanes during translational flight.

Furthermore, when the vehicle is suddenly tilting from stable hovering as depicted in figure 149, the vanes on the left side remain horizontal as the sudden increase of D_1 as well as F_1 . The increase of force is due to a combination of free stream velocity and air flowing into the propeller plane. On the other hand, the vanes on the right side will drop down. The vanes on both sides create a counter-clockwise moment on pitching moment,

$$M_{y(\text{passive})} = 4D_1d_2 - 4D_2d_2 \quad (76)$$

Propeller Thrust

According to Equation 14, an expression of the total thrust, T_{motor} , as a function of slipstream velocity U_{prop} is given by

$$\begin{aligned} T_{motor} &= \dot{m}(U_{prop} + V_{\infty}) - \dot{m}V_{\infty} \\ &= \rho S_{prop}(U_{prop} + V_{\infty}) \end{aligned} \quad (77)$$

where ρ is the air density, U_{prop} is the slipstream velocity created by the propeller, and S_{prop} is the propeller area. The propeller slipstream can be estimated based on the thrust when $V_\infty = 0$,

$$U_{prop} = \sqrt{\frac{T_{motor}}{2\rho S_{prop}}} \quad (78)$$

Motor Torque

A single motor-wing aircraft always generate an induced torque due to the rotation of the motor. The thrust, T_{motor} and the moment, M_{motor} created by a single propeller are proportional to the squared angular velocity of the propeller, as shown below:

$$T_{motor} = \omega^2 K_T \quad (79)$$

$$M_{motor} = \omega^2 K_M \quad (80)$$

where K_T is the constant which relates the thrust to the square of the angular velocity of the propeller; K_M is the constant which relates the moment to the square of the angular velocity of the propeller. These two constants can be written as

$$K_T = c_T \frac{\rho D^4}{4\pi^2} \quad (81)$$

$$K_M = c_p \frac{\rho D^5}{8\pi^2} \quad (82)$$

Gyroscopic Moment

Precession is the resultant action, or deflection, of a spinning motor when a deflecting force is applied to its rim [38]. A rotating propeller inside the spherical frame produces a similar effect like a gyroscope. When a force is applied to deflect the propeller out of its plane of rotation, this causes a resulting force of 90

deg ahead of and in the direction of the rotation propeller. This resulting pitching or rolling moment or a combination of the two depending on the control surfaces at which the force was applied [39].

Since the rotating speed of motor Ω is very high during the UAV flight, another angular velocity, ω is generated.

$$M_{gyro} = \times I_p \omega_p \begin{bmatrix} -p \\ q \\ 0 \end{bmatrix} \quad (83)$$

where I_p is the rotating inertia of the propeller, ω_p as the angular velocity.

Gravitational Force

The current ATLAS designed to operate at low attitude. Therefore, the body force of the vehicle is considered a constant without the need to consider the variation of gravity acceleration with the different latitude. Hence, g is constant at 9.81 m/s^2 and the body force of the vehicle is computed by,

$$W = mg = W_{total} \quad (84)$$

Side Panels

At low flight speed, the presence of the side panels contributes a reaction force called ram drag force, D_p .

$$D_x = D_y = QS_{panel} \frac{\partial D_{panel}}{\partial \delta_\alpha} \alpha \quad (85)$$

In the inertial frame of ATLAS, the ram drag is neglected when assuming no crosswind is present as the vehicle operating indoor.

$$D_x = D_y = 0 \quad (86)$$

Control Surfaces Lift

Compare to the control surfaces contributions, the lift acting on the spherical cage is considered small when operating indoor and assume that the spherical frame is not affected by the propeller slipstream. The total lift generated by the ATLAS controls surfaces during flight mode can be expressed as follows,

$$L = L_t + L_b \quad (87)$$

where each term on the right hand side of the equation is given by,

$$L_t = QS_t C_{L_t} \quad (88a)$$

$$L_b = QS_b C_{L_b} \quad (88b)$$

$$Q = \frac{1}{2} \rho V_{prop}^2 \quad (88c)$$

$$C_{L_t} = C_{l_\delta} \delta_{(1,2,3,4)} \quad (88d)$$

$$C_{L_b} = C_{l_\delta} \delta_{(5,6,7,8)} \quad (88e)$$

Control Surfaces Drag

In the similar way, the total drag generated by the ATLAS control surface can be expressed as following,

$$D = D_t + D_b \quad (89)$$

where each term on the right-hand side of the equation is given by,

$$D_t = QS_t C_{D_t} \quad (90a)$$

$$D_b = QS_b C_{D_b} \quad (90b)$$

$$Q = \frac{1}{2} \rho V_{prop}^2 \quad (90c)$$

$$C_{D_t} = C_{D_t} \delta_{1,2,3,4} \quad (90d)$$

$$C_{D_b} = C_{D_b} \delta_{5,6,7,8} \quad (90e)$$

Moment of Inertia

The ATLAS is a spherical shape with axis-symmetric in both XZ and YZ plane, the product of inertia moment is

$$I_{xy} = I_{xz} = I_{yz} = 0 \quad (91)$$

Active Control Surfaces

Figure 150 shows the setup of the eight control surfaces on ATLAS. The C.G. is located at the C.O.S. The body-fixed frame is established using the right-hand rule by directing the z-axis pointing downward to the direction of the thrust line and y-axis towards the right side of the vehicle. Vane 1 to 4 is identified as top vanes. Vane 2 and 4 are identified as elevator, to provide forward/backward motion, and vane 1 and three are identified as the aileron, to provide left/right translation motion. All top vanes are responding to yaw commands as well. The bottom vanes are identified as vane 5 to 8, and there are couple with roll, pitch, and yaw commands as shown in figure 151. The bottom vanes are 45° offset relative to the top vanes. O_B is the C.G. of the vehicle.

5.4 Summary of Forces and Moments for ATLAS

The deflection angles for every eight vanes are denoted by the symbols δ_1 to δ_8 . A positive vane deflection defines as one that results in blockage of the airflow viewing from the top of the sphere, as illustrated in figure 150. The pitching motion is provided by deflecting vane 2, 4, and all bottom vanes. Similarly, the rolling motion of the vehicle is provided by deflecting vane 1, 3, and all bottom vanes. The yawing motion is provided by deflecting all eight vanes. Therefore, a positive pitching motion can be created by rotating the control surfaces where $\delta_4 = \delta_6 = \delta_7 = +\delta_\theta$ and $\delta_2 = \delta_5 = \delta_8 = -\delta_\theta$. As a result, the vehicle can tilt in a positive pitch direction. In a similar way, a positive rolling motion can be created by moving the top control surface $\delta_1 = \delta_7 = \delta_8 = -\delta_\phi$ and $\delta_3 = \delta_5 = \delta_6 = +\delta_\phi$. For a positive yawing motion, both top and bottom control surfaces $\delta_1 = \delta_2 = \delta_3 = \delta_4 = \delta_5 = \delta_6 = \delta_7 = \delta_8 = +\delta_\psi$ as shown in fig. 151. Following are

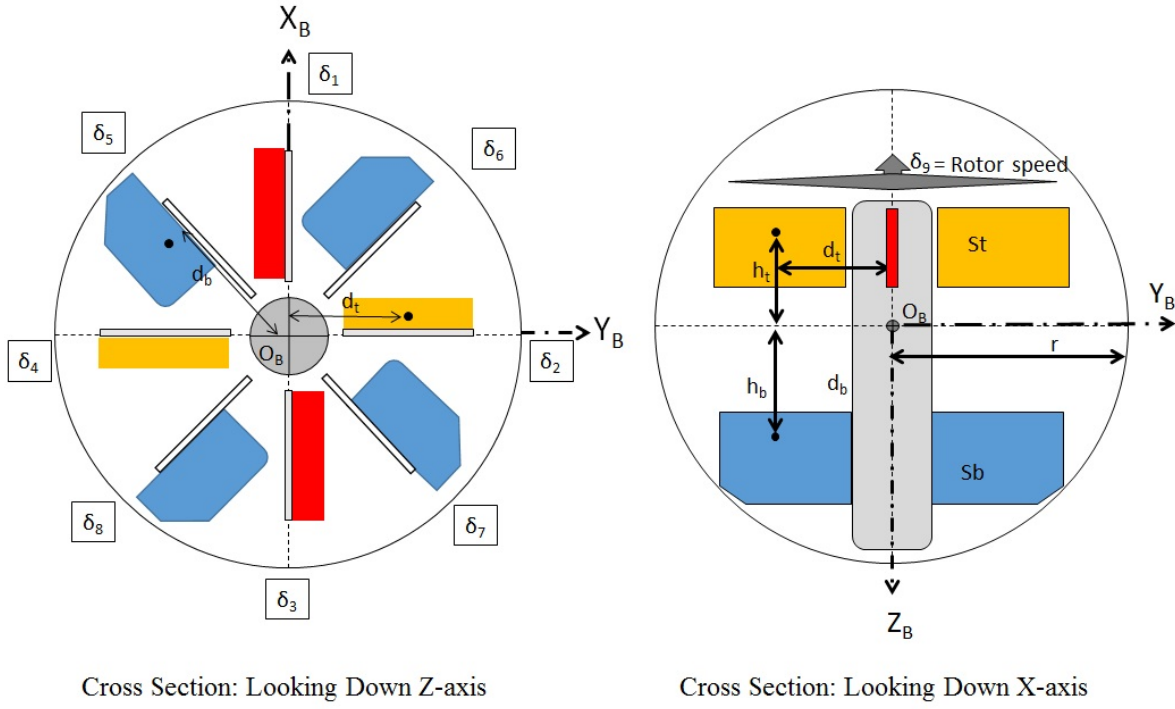


Figure 150: Schematic of ATLAS's control vanes.

the full set of nonlinear equations describing the motion for an airframe having a rotation in a body-frame coordinate system:

$$F_x = \frac{\partial L_t}{\partial \delta_t} (\delta_4 - \delta_2) + \frac{\partial L_b}{\partial \delta_b} \cos \frac{\pi}{4} (-\delta_5 + \delta_6 + \delta_7 - \delta_8) - mg \sin \theta - D_x \quad (92)$$

$$F_y = \frac{\partial L_t}{\partial \delta_t} (\delta_1 - \delta_3) + \frac{\partial L_b}{\partial \delta_b} \cos \frac{\pi}{4} (\delta_5 + \delta_6 - \delta_7 - \delta_8) + mg \cos \theta \sin \phi - D_y \quad (93)$$

$$F_z = \frac{\partial D_t}{\partial \delta_t} (|\delta_1| + |\delta_2| + |\delta_3| + |\delta_4|) + \frac{\partial D_b}{\partial \delta_b} (|\delta_5| + |\delta_6| + |\delta_7| + |\delta_8|) + mg \cos \theta \cos \phi - T_{motor} - F_{z_{passive}} \quad (94)$$

$$M_x = \frac{\partial L_t}{\partial \delta_t} (\delta_1 - \delta_3) h_t - \frac{\partial L_b}{\partial \delta_b} \cos \frac{\pi}{4} (\delta_5 + \delta_6 - \delta_7 - \delta_8) h_b + \frac{\partial D_t}{\partial \delta_t} (|\delta_2| - |\delta_4|) d_t + \frac{\partial D_b}{\partial \delta_b} \cos \frac{\pi}{4} (-|\delta_5| + |\delta_6| + |\delta_7| - |\delta_8|) d_b + M_{x(passive)} + D_y l_p - I_p \omega_p q \quad (95)$$

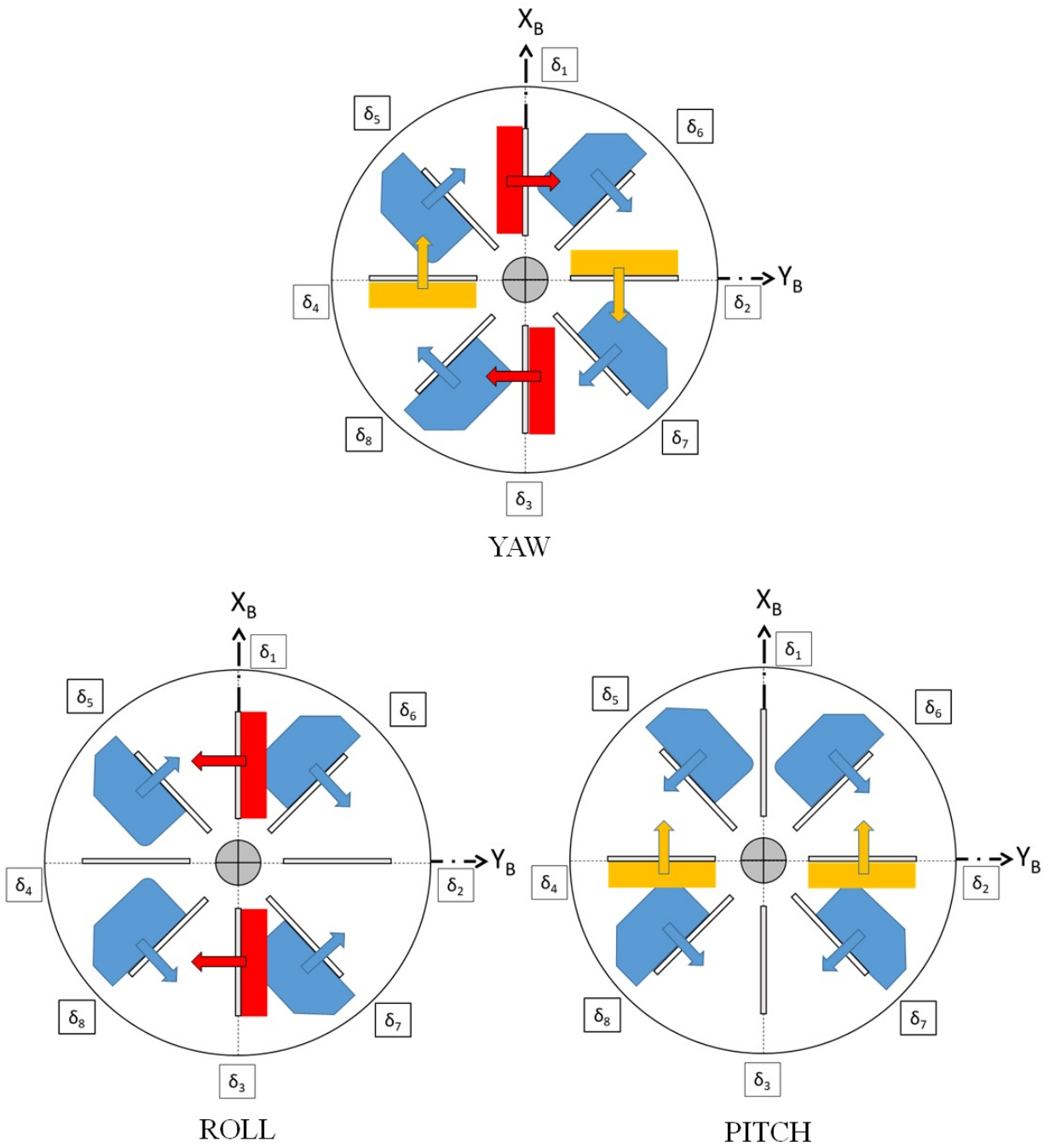


Figure 151: Resultant force due to vane deflections for decouple roll, pitch and yaw.

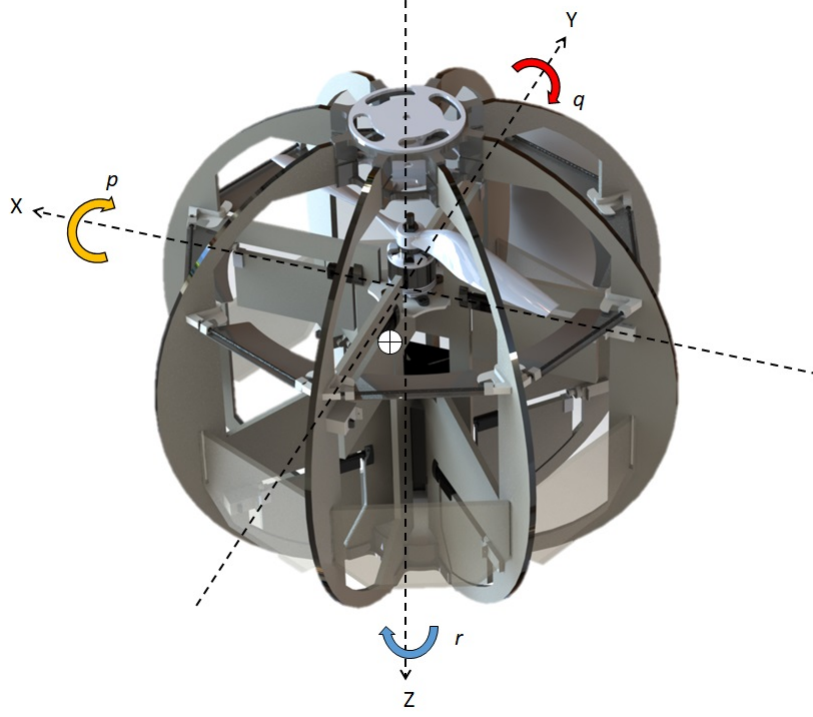


Figure 152: ATLAS with 8 vanes in body frame coordinate.

$$\begin{aligned}
 M_y = & \frac{\partial L_t}{\partial \delta_t} (\delta_2 - \delta_4) h_t - \frac{\partial L_b}{\partial \delta_b} \cos \frac{\pi}{4} (-\delta_5 + \delta_6 + \delta_7 - \delta_8) h_b + \frac{\partial D_t}{\partial \delta_t} (|\delta_3| - |\delta_1|) d_t \\
 & + \frac{\partial D_b}{\partial \delta_t} \cos \frac{\pi}{4} (-|\delta_5| - |\delta_6| + |\delta_7| + |\delta_8|) d_b + M_{y(\text{passive})} + D_x l_p + I_p w_p p
 \end{aligned} \tag{96}$$

$$M_z = \frac{\partial L_t}{\partial \delta_t} (\delta_1 + \delta_2 + \delta_3 + \delta_4) d_t + \frac{\partial L_b}{\partial \delta_b} (\delta_5 + \delta_6 + \delta_7 + \delta_8) d_b + M_{\text{motor}} \tag{97}$$

$$\dot{u} = \ddot{x} = \frac{F_x}{m} = \frac{1}{m} \frac{\partial L_t}{\partial \delta_t} (\delta_4 - \delta_2) + \frac{1}{m} \frac{\partial L_b}{\partial \delta_b} \cos \frac{\pi}{4} (-\delta_5 + \delta_6 + \delta_7 - \delta_8) - g \sin \theta - \frac{D_x}{m} \tag{98}$$

$$\dot{v} = \ddot{y} = \frac{F_y}{m} = \frac{1}{m} \frac{\partial L_t}{\partial \delta_t} (\delta_1 - \delta_3) + \frac{1}{m} \frac{\partial L_b}{\partial \delta_b} \cos \frac{\pi}{4} (\delta_5 + \delta_6 - \delta_7 - \delta_8) + g \cos \theta \sin \phi - \frac{D_y}{m} \tag{99}$$

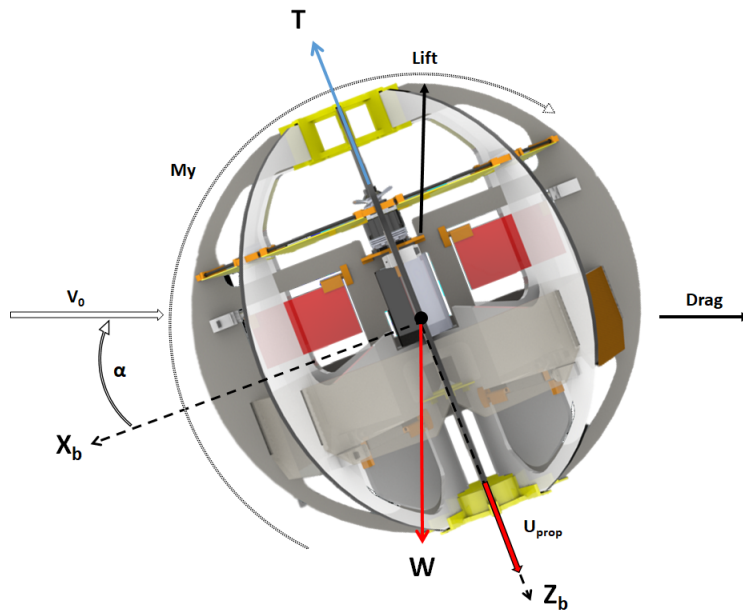


Figure 153: ATLAS's longitudinal axes.

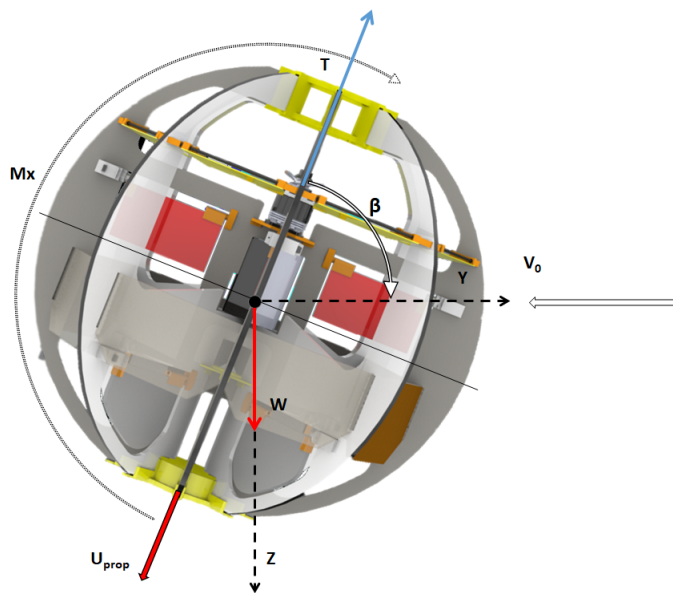


Figure 154: ATLAS lateral axes.

$$\begin{aligned}\dot{w} = \ddot{z} = \frac{F_z}{m} &= \frac{1}{m} \frac{\partial D_t}{\partial \delta_t} (|\delta_1| + |\delta_2| + |\delta_3| + |\delta_4|) + \frac{1}{m} \frac{\partial D_b}{\partial \delta_b} (|\delta_5| + |\delta_6| + |\delta_7| + |\delta_8|) \\ &+ g \cos \theta \cos \phi - \frac{T_{motor}}{m} - \frac{F_{z_{passive}}}{m}\end{aligned}\quad (100)$$

$$\begin{aligned}\dot{p} = \ddot{\phi} = \frac{M_x}{I_{xx}} &= \frac{h_t}{I_{xx}} \frac{\partial L_t}{\partial \delta_t} (\delta_1 - \delta_3) - \frac{h_b}{I_{xx}} \frac{\partial L_b}{\partial \delta_b} (\delta_5 + \delta_6 - \delta_7 - \delta_8) \cos \frac{\pi}{4} \\ &+ \frac{d_t}{I_{xx}} \frac{\partial D_t}{\partial \delta_t} (|\delta_2| - |\delta_4|) \\ &+ \frac{d_b}{I_{xx}} \frac{\partial D_b}{\partial \delta_b} (-|\delta_5| + |\delta_6| + |\delta_7| - |\delta_8|) \cos \frac{\pi}{4} + \frac{M_{x(passive)}}{I_{xx}} + \frac{Dy l_p}{I_{xx}} - \frac{I_p w_p q}{I_{xx}}\end{aligned}\quad (101)$$

$$\begin{aligned}\dot{q} = \ddot{\theta} = \frac{M_y}{I_{yy}} &= \frac{h_t}{I_{yy}} \frac{\partial L_t}{\partial \delta_t} (\delta_2 - \delta_4) - \frac{h_b}{I_{yy}} \frac{\partial L_b}{\partial \delta_b} (-\delta_5 + \delta_6 + \delta_7 - \delta_8) \cos \frac{\pi}{4} \\ &+ \frac{d_t}{I_{yy}} \frac{\partial D_t}{\partial \delta_t} (|\delta_1| - |\delta_3|) \\ &+ \frac{d_b}{I_{yy}} \frac{\partial D_b}{\partial \delta_b} (-|\delta_5| - |\delta_6| + |\delta_7| + |\delta_8|) \cos \frac{\pi}{4} + \frac{M_{y(passive)}}{I_{yy}} + \frac{Dx l_p}{I_{xx}} + \frac{I_p w_p p}{I_{yy}}\end{aligned}\quad (102)$$

$$\begin{aligned}\dot{r} = \ddot{\psi} = \frac{M_z}{I_{zz}} &= \frac{d_t}{I_{zz}} \frac{\partial L_t}{\partial \delta_t} (\delta_1 + \delta_2 + \delta_3 + \delta_4) + \frac{d_b}{I_{zz}} \frac{\partial L_b}{\partial \delta_b} (\delta_5 + \delta_6 + \delta_7 + \delta_8) \\ &+ \frac{M_{motor}}{I_{zz}}\end{aligned}\quad (103)$$

For control system implementation purposes, the following virtual vanes that corresponding to coupled roll, pitch and yaw input defined as:

$$\begin{bmatrix} \delta_1 \\ \delta_2 \\ \delta_3 \\ \delta_4 \\ \delta_5 \\ \delta_6 \\ \delta_7 \\ \delta_8 \end{bmatrix} = \begin{bmatrix} 1 & 0 & 1 \\ 0 & -1 & 1 \\ -1 & 0 & 1 \\ 0 & 1 & 1 \\ 1 & -1 & 1 \\ 1 & 1 & 1 \\ -1 & 1 & 1 \\ -1 & -1 & 1 \end{bmatrix} \begin{bmatrix} \delta_r \\ \delta_p \\ \delta_y \end{bmatrix}\quad (104)$$

Substitutes the control terms in 104 into the forces and moments equations from 92 to 97 yields:

$$F_x = \delta_\theta \left[2 \frac{\partial L_t}{\partial \delta_t} + 4 \frac{\partial L_b}{\partial \delta_b} \cos \frac{\pi}{4} \right] - mg\theta \quad (105)$$

$$F_y = \delta_\phi \left[2 \frac{\partial L_t}{\partial \delta_t} + 4 \frac{\partial L_b}{\partial \delta_b} \cos \frac{\pi}{4} \right] + mg\phi \quad (106)$$

$$F_z = mg - k_T u_t \quad (107)$$

$$M_x = \delta_\theta \left[2 \frac{\partial L_t}{\partial \delta_t} h_t + 4 \frac{\partial L_b}{\partial \delta_b} h_b \cos \frac{\pi}{4} \right] - I_p w_p q \quad (108)$$

$$M_y = \delta_\phi \left[-2 \frac{\partial L_t}{\partial \delta_t} h_t - 4 \frac{\partial L_b}{\partial \delta_b} h_b \cos \frac{\pi}{4} \right] + I_p w_p p \quad (109)$$

$$M_z = \delta_\psi \left[4 \frac{\partial L_t}{\partial \delta_t} d_t + 4 \frac{\partial L_b}{\partial \delta_b} d_b \right] + K_M u_t \quad (110)$$

5.5 Transformation Matrix

$$\begin{aligned} p &= \dot{\phi} - \dot{\psi} \sin \theta \\ q &= \dot{\theta} \cos \theta + \psi \cos \theta \sin \phi \\ r &= \dot{\psi} \cos \theta \cos \phi - \dot{\theta} \sin \phi \end{aligned} \quad (111)$$

$$\begin{aligned} \dot{\theta} &= q \cos \theta - r \sin \phi \\ \dot{\phi} &= p + q \sin \phi \tan \theta + r \cos \phi \tan \theta \\ \dot{\psi} &= (q \sin \phi + r \cos \phi) \left(\frac{1}{\cos \theta} \right) \end{aligned} \quad (112)$$

5.6 Linearization of Equations of Motion

Although aircraft can change its flight path quite rapidly, the linearization process will be considered relative to a fixed flight condition. The linearization of the equation of motions will allow a determination of an airframe's small amplitude dynamic behavior about a trim point. The following assumptions were made for perturbation analysis: 1) Small motion dynamics will be initiated from hover stable flight with the aircraft controls and thrust set for a trim, static equilibrium flight condition. 2) The body axes will be aligned with the initial velocity vector, and as such, will become known as the airframe's stability axes.

The forces acting on the airframe due to both aerodynamic and gravitational terms may be expressed as

$$\begin{aligned}
 F_x &= X_0 + \Delta X - mg \sin \theta \\
 F_y &= Y_0 + \Delta Y - mg \cos \theta \sin \phi \\
 F_z &= Z_0 + \Delta Z - mg \cos \theta \cos \phi
 \end{aligned}
 \tag{113}$$

where the mg related terms are due to body-weight components and the Euler angles θ and ϕ . Terms such as X_0 represents the equilibrium value of the corresponding force component whereas ΔX is the force term due to the time-varying aerodynamic forces caused by aircraft attitude, motion, and control deflections from trim condition. The moment's components acting on the aircraft relative to the center of gravity are defined as

$$\begin{aligned}
 M_x &= L = L_0 + \Delta L \\
 M_y &= M = M_0 + \Delta M \\
 M_z &= N = N_0 + \Delta N
 \end{aligned}
 \tag{114}$$

where the 0 subscript refers to initial trim conditions whereas the typical ΔL term will correspond to the time-varying aerodynamic moments that arise due to the aircraft attitude, motion, and control deflection from the trim condition. Suppose $f(X)$ is a non-linear function. Here, X is the state of the system, where it contains several state variables. To linearize $f(X)$, a multi-dimensional Taylor expansion can be used to get

$$f(X) \approx f(X_0) + f_{x_1}(X_0)\Delta X_1 + f_{x_2}(X_0)\Delta X_2 + \dots + f_{x_n}(X_0)\Delta X_n + H.O.T
 \tag{115}$$

where X_0 is the initial point. The linearization will only be valid close to this point. Also, the term ΔX_i is the deviation of variable X_i from the initial point X_0 . The Higher Order terms (H.O.T) will be neglected when applying linearization to simplify the equation. Before linearization, the set of six coupled equations of motion appear as

$$\begin{aligned}
X_0 + \Delta X - mg \sin \theta &= m(\dot{u} + qw - rv) \\
Y_0 + \Delta Y + mg \cos \theta \sin \phi &= m(\dot{v} + ru - pw) \\
Z_0 + \Delta Z + mg \cos \theta \cos \phi &= m(\dot{w} + pv - qu)
\end{aligned} \tag{116}$$

$$\begin{aligned}
L_0 + \Delta L &= I_{xx}\dot{p} + qh_z - I_{xz}pq - I_{xz}\dot{r} \\
M_0 + \Delta M &= I_{xx}\dot{q} + rq(I_{xx} - I_{zz}) + I_{xz}(p^2 - r^2) \\
N_0 + \Delta N &= I_{zz}\dot{r} + pq(I_{yy} - I_{xx}) + I_{xz}(qr - \dot{p})
\end{aligned} \tag{117}$$

The equation assume that $I_{xy} = I_{yz} = 0$. Now introduce the perturbation substitutions, in which each variable consists of an equilibrium steady-state term (subscript 1) plus a perturbation terms, e.g.,

$$\begin{aligned}
U &= U_1 + u \\
P &= P_1 + p
\end{aligned} \tag{118}$$

Next assume that all steady-state motion variables except U_1 and θ_1 are zero, i.e., $P_1 = Q_1 = R_1 = V_1 = W_1 = \phi_1 = 0$. This corresponds to the case of hovering with a small forward velocity components, or hovering with a weak headwind. Crosswind components are usually avoided when hovering to prevent the necessity of constant trimming moment that reduces the thrust available and maximum control authority in one direction. The thrust perturbation also considered negligible where $K_t = K_m = 0$. The small perturbation assumption is also considered; thus all products of perturbation terms can be neglected. Also, $\sin \theta = 0$ and $\cos \theta = 1$. Then the linearized dynamic equations becomes

$$\dot{u} = \ddot{x} = \frac{F_x}{m} = \delta_\theta \left[2 \frac{1}{m} \frac{\partial L_t}{\partial \delta_t} + 4 \frac{1}{m} \frac{\partial L_b}{\partial \delta_b} \cos \frac{\pi}{4} \right] - g\theta \tag{119}$$

$$\dot{v} = \ddot{y} = \frac{F_y}{m} = \delta_\phi \left[2 \frac{1}{m} \frac{\partial L_t}{\partial \delta_t} + 4 \frac{1}{m} \frac{\partial L_b}{\partial \delta_b} \cos \frac{\pi}{4} \right] + g\phi \tag{120}$$

$$\dot{w} = \ddot{z} = \frac{F_z}{m} = g \quad (121)$$

$$\dot{p} = \ddot{\phi} = \frac{M_x}{I_{xx}} = \delta_\theta \left[2 \frac{1}{I_{xx}} \frac{\partial L_t}{\partial \delta_t} h_t + 4 \frac{1}{I_{xx}} \frac{\partial L_b}{\partial \delta_b} h_b \cos \frac{\pi}{4} \right] - \frac{I_p w_p}{I_{xx}} q \quad (122)$$

$$\dot{q} = \ddot{\theta} = \frac{M_y}{I_{yy}} = \delta_\phi \left[-2 \frac{1}{I_{yy}} \frac{\partial L_t}{\partial \delta_t} h_t - 4 \frac{1}{I_{yy}} \frac{\partial L_b}{\partial \delta_b} h_b \cos \frac{\pi}{4} \right] + \frac{I_p w_p}{I_{yy}} p \quad (123)$$

$$\dot{r} = \ddot{\psi} = \frac{M_z}{I_{zz}} = \delta_\psi \left[4 \frac{1}{I_{zz}} \frac{\partial L_t}{\partial \delta_t} d_t + 4 \frac{1}{I_{zz}} \frac{\partial L_b}{\partial \delta_b} d_b \right] \quad (124)$$

The linearized equation of motion for ATLAS in term of state-space form becomes:

$$\begin{bmatrix} \dot{p} \\ \dot{q} \\ \dot{r} \\ \dot{u} \\ \dot{v} \\ \dot{\phi} \\ \dot{\theta} \\ \dot{\psi} \end{bmatrix} = \begin{bmatrix} 0 & -\frac{I_p w_p}{I_{xx}} & 0 & 0 & 0 & 0 & 0 & 0 \\ \frac{I_p w_p}{I_{yy}} & 0 & 0 & 0 & 0 & 0 & 0 & 0 \\ 0 & 0 & 0 & 0 & 0 & 0 & 0 & 0 \\ 0 & 0 & 0 & 0 & 0 & 0 & -g & 0 \\ 0 & 0 & 0 & 0 & 0 & g & 0 & 0 \\ 1 & 0 & 0 & 0 & 0 & 0 & 0 & 0 \\ 0 & 1 & 0 & 0 & 0 & 0 & 0 & 0 \\ 0 & 0 & 1 & 0 & 0 & 0 & 0 & 0 \end{bmatrix} \begin{bmatrix} p \\ q \\ r \\ u \\ v \\ \phi \\ \theta \\ \psi \end{bmatrix} + \begin{bmatrix} 0 & 2 \frac{1}{I_{xx}} \frac{\partial L_t}{\partial \delta_t} h_t + 4 \frac{1}{I_{xx}} \frac{\partial L_b}{\partial \delta_b} h_b \cos \frac{\pi}{4} & 0 & 0 & 0 & 0 & 0 & 0 \\ -2 \frac{1}{I_{yy}} \frac{\partial L_t}{\partial \delta_t} h_t - 4 \frac{1}{I_{yy}} \frac{\partial L_b}{\partial \delta_b} h_b \cos \frac{\pi}{4} & 0 & 0 & 0 & 0 & 0 & 0 & 0 \\ 0 & 0 & 4 \frac{1}{I_{zz}} \frac{\partial L_t}{\partial \delta_t} d_t + 4 \frac{1}{I_{zz}} \frac{\partial L_b}{\partial \delta_b} d_b & 0 & 0 & 0 & 0 & 0 \\ 0 & 2 \frac{1}{m} \frac{\partial L_t}{\partial \delta_t} + 4 \frac{1}{m} \frac{\partial L_b}{\partial \delta_b} \cos \frac{\pi}{4} & 0 & 0 & 0 & 0 & 0 & 0 \\ 2 \frac{1}{m} \frac{\partial L_t}{\partial \delta_t} + 4 \frac{1}{m} \frac{\partial L_b}{\partial \delta_b} \cos \frac{\pi}{4} & 0 & 0 & 0 & 0 & 0 & 0 & 0 \\ 0 & 0 & 0 & 0 & 0 & 0 & 0 & 0 \\ 0 & 0 & 0 & 0 & 0 & 0 & 0 & 0 \\ 0 & 0 & 0 & 0 & 0 & 0 & 0 & 0 \end{bmatrix} \begin{bmatrix} \delta_\phi \\ \delta_\theta \\ \delta_\psi \end{bmatrix}$$

(125)

5.7 Controllability and Observability

Controllability and observability represent two major concepts of modern control system theory. These concepts were introduced by R. Kalman in 1960. They can be roughly defined as follows. Controllability: in order to be able to do whatever we want with the given dynamic system under control input, the system must be controllable. Observability: in order to see what is going on inside the system under observation, the system must be observable. Observability and controllability tests will be connected to the rank tests of certain matrices. The state-space representation is

$$\begin{aligned} \dot{x} &= Ax + Bu \\ y &= Cx + Du \end{aligned} \tag{126}$$

where A = System matrix, X = State Vector, B = Control input matrix, u = input vector, C = Output matrix, Y = Output vector, and D = Direct Matrix. Therefore,

$$A = \begin{bmatrix} 0 & -\frac{I_p w_p}{I_{xx}} & 0 & 0 & 0 & 0 & 0 & 0 \\ \frac{I_p w_p}{I_{yy}} & 0 & 0 & 0 & 0 & 0 & 0 & 0 \\ 0 & 0 & 0 & 0 & 0 & 0 & 0 & 0 \\ 0 & 0 & 0 & 0 & 0 & 0 & -g & 0 \\ 0 & 0 & 0 & 0 & 0 & g & 0 & 0 \\ 1 & 0 & 0 & 0 & 0 & 0 & 0 & 0 \\ 0 & 1 & 0 & 0 & 0 & 0 & 0 & 0 \\ 0 & 0 & 1 & 0 & 0 & 0 & 0 & 0 \end{bmatrix} \tag{127}$$

$$B = \begin{bmatrix} 0 & 2\frac{1}{I_{xx}} \frac{\partial L_t}{\partial \delta_t} h_t + 4\frac{1}{I_{xx}} \frac{\partial L_b}{\partial \delta_b} h_b \cos \frac{\pi}{4} & 0 \\ -2\frac{1}{I_{yy}} \frac{\partial L_t}{\partial \delta_t} h_t - 4\frac{1}{I_{yy}} \frac{\partial L_b}{\partial \delta_b} h_b \cos \frac{\pi}{4} & 0 & 0 \\ 0 & 0 & 4\frac{1}{I_{zz}} \frac{\partial L_t}{\partial \delta_t} d_t + 4\frac{1}{I_{zz}} \frac{\partial L_b}{\partial \delta_b} d_b \\ 0 & 2\frac{1}{m} \frac{\partial L_t}{\partial \delta_t} + 4\frac{1}{m} \frac{\partial L_b}{\partial \delta_b} \cos \frac{\pi}{4} & 0 \\ 2\frac{1}{m} \frac{\partial L_t}{\partial \delta_t} + 4\frac{1}{m} \frac{\partial L_b}{\partial \delta_b} \cos \frac{\pi}{4} & 0 & 0 \\ 0 & 0 & 0 \\ 0 & 0 & 0 \\ 0 & 0 & 0 \end{bmatrix} \quad (128)$$

By using Matlab, the Observability function is $Ob = \text{obsv}(A, C)$ and the controllability function is $Co = \text{ctrb}(A, B)$. The model is observable if Ob has a full rank n . This resulted in Rank of 8. The number of Unobservable States is $unob = \text{length}(A) - \text{rank}(Ob) = 0$ and the Uncontrollable States is $uncon = \text{length}(A) - \text{rank}(ctrb(A, B)) = 0$. Therefore, the system using the coupled control vanes to control all three major axes is controllable and observable.

5.8 Preliminary Studies on the Dynamic for Hovering Stability

In order to hover in a static equilibrium condition, the thrust or lift of a vehicle must act through the center of gravity. If a hovering airplane or helicopter is tilted or banked from its hovering position, the lift vector tilts with the airplane, continuing acting through the center of gravity. Therefore, no restoring moment is generated and neutral static stability exists. In order to hover in a static equilibrium condition, the thrust or lift of a vehicle must act through the center of gravity. If a hovering hot air balloon is disturbed from its equilibrium attitude, and if the center of buoyancy is placed above the center of gravity, the buoyancy force continues to act in a vertical direction and thus generates a restoring moment about the center of gravity. This is called pendulum stability. Of even more interest than static stability is the question of dynamic stability. Is the ATLAS stable, unstable, or neutrally stable when one considers such occurrences as with or without gyroscopic precession effect? The following will analyze two special cases of hovering conditions using equation 128.

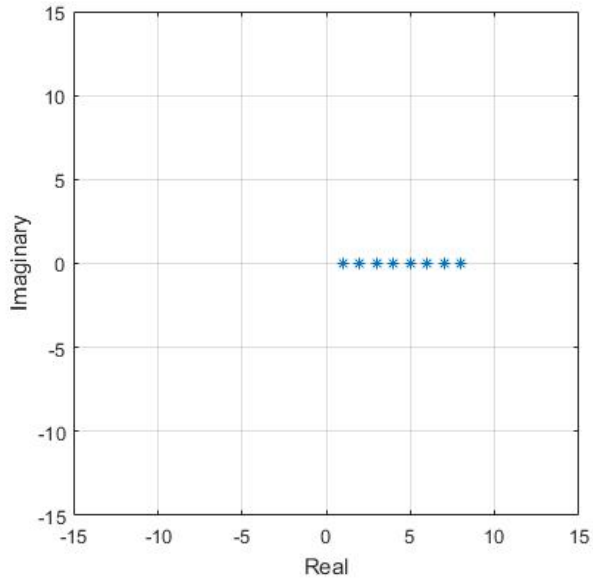


Figure 155: Instability without gyroscopic and aerodynamic terms exist.

No Gyroscopic Precession Terms or Aerodynamic Forces and Moments

Assuming U_1 is so small that aerodynamic forces and moments are negligible, even though U_1 and u cannot be neglected. Thrust perturbation are negligible, the equations then become

$$\begin{bmatrix} \dot{p} \\ \dot{q} \\ \dot{r} \\ \dot{u} \\ \dot{v} \\ \dot{\phi} \\ \dot{\theta} \\ \dot{\psi} \end{bmatrix} = \begin{bmatrix} 0 & 0 & 0 & 0 & 0 & 0 & 0 & 0 \\ 0 & 0 & 0 & 0 & 0 & 0 & 0 & 0 \\ 0 & 0 & 0 & 0 & 0 & 0 & 0 & 0 \\ 0 & 0 & 0 & 0 & 0 & 0 & -g & 0 \\ 0 & 0 & 0 & 0 & 0 & g & 0 & 0 \\ 1 & 0 & 0 & 0 & 0 & 0 & 0 & 0 \\ 0 & 1 & 0 & 0 & 0 & 0 & 0 & 0 \\ 0 & 0 & 1 & 0 & 0 & 0 & 0 & 0 \end{bmatrix} \begin{bmatrix} p \\ q \\ r \\ u \\ v \\ \phi \\ \theta \\ \psi \end{bmatrix} \tag{129}$$

Therefore, a hovering vehicle, without gyroscopic effect, is unstable.

Gyroscopic Precession Terms Exist, No Aerodynamic Forces and Moments

In this case, the single propeller produces nonnegligible angular momentum, but aerodynamic terms are negligible. The longitudinal and lateral-directional equations cannot be uncoupled. As the vehicle is axis-symmetric in both XZ and YZ plane, the model can be further simplified where $I_{yy} = I_{xx}$. This makes pitch and roll dynamics are described by similar equations. For this reason, a similar expression for the control of the roll axis can be directly deduced.

$$\begin{bmatrix} \dot{p} \\ \dot{q} \\ \dot{r} \\ \dot{u} \\ \dot{v} \\ \dot{\phi} \\ \dot{\theta} \\ \dot{\psi} \end{bmatrix} = \begin{bmatrix} 0 & -\frac{I_p w_p}{I_{xx}} & 0 & 0 & 0 & 0 & 0 & 0 \\ \frac{I_p w_p}{I_{yy}} & 0 & 0 & 0 & 0 & 0 & 0 & 0 \\ 0 & 0 & 0 & 0 & 0 & 0 & 0 & 0 \\ 0 & 0 & 0 & 0 & 0 & 0 & -g & 0 \\ 0 & 0 & 0 & 0 & 0 & g & 0 & 0 \\ 1 & 0 & 0 & 0 & 0 & 0 & 0 & 0 \\ 0 & 1 & 0 & 0 & 0 & 0 & 0 & 0 \\ 0 & 0 & 1 & 0 & 0 & 0 & 0 & 0 \end{bmatrix} \begin{bmatrix} p \\ q \\ r \\ u \\ v \\ \phi \\ \theta \\ \psi \end{bmatrix} \quad (130)$$

The existence of neutrally stable oscillation increase the probability of unstable pilot induced oscillations, PIO. One method of reducing the problem is to eliminate the induced torque or angular momentum terms with counter-rotating propellers or stators. However, these will make the hovering stability unstable, and the problem of precise control and PIO may still exist.

5.9 Control System Design

The ATLAS uses PD controller to achieve flight stability. A PD controller continuously calculates the error value $e(t)$ as the difference between a desired setpoint and measured process variables and applies a correction based on propotional and derivative terms. This can be written as follow:

$$\delta_{\phi, \theta, \psi} = K_p e(t) + K_d \frac{de(t)}{dt} \quad (131)$$

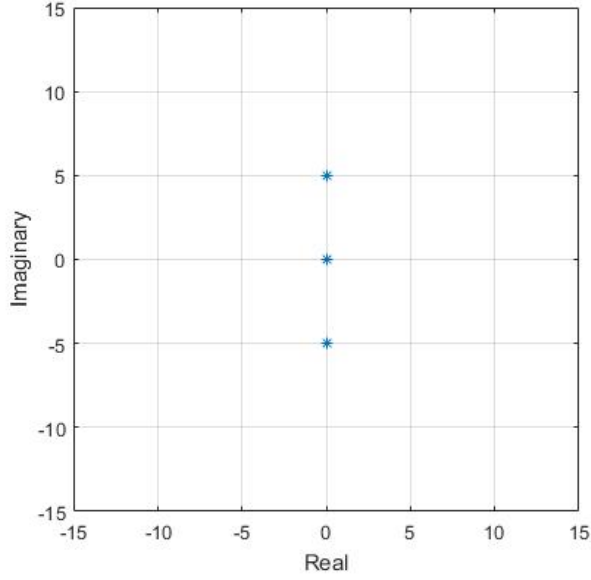


Figure 156: Neutral stability when gyroscopic term exists.

Where K_p and K_d represent the coefficients for the proportional, integral, and derivative terms, respectively. During the flight, two flight modes are being considered: rate mode and self-level mode. The self-level mode is an assisted flight mode that the flight controller would always attempt to put the vehicle in its neutral position when the pilot let go of the transmitter control sticks. On the other hand, rate-mode does not level the vehicle automatically and required manual control. The self-level mode uses both the gyro and accelerometer sensor, while rate-mode uses only the gyro.

In order to achieve rate-mode, the idea is first to control the vehicle's angular speed. The control command that combines the pitch, roll, and yaw is sent to the control surfaces as follows:

$$\delta_\phi = K_p(p_d - p) + K_d \frac{(p_d - p)}{dt} \quad (132)$$

$$\delta_\theta = K_p(q_d - q) + K_d \frac{(q_d - q)}{dt} \quad (133)$$

$$\delta_\psi = K_p(r_d - r) + K_d \frac{(r_d - r)}{dt} \quad (134)$$

where subscript d represents desirable setpoint or reference variable. With the pitch rate controller in place, angle controller was designed to regulate the vehicle's attitude. Thus the angle controller was of the form:

$$p_d = K_p(\phi_d - \phi) + K_d \frac{(\phi_d - \phi)}{dt} \quad (135)$$

$$q_d = K_p(\theta_d - \theta) + K_d \frac{(\theta_d - \theta)}{dt} \quad (136)$$

$$r_d = K_p(\psi_d - \psi) + K_d \frac{(\psi_d - \psi)}{dt} \quad (137)$$

The P and D gain value is tuned by trial and error between flight tests to get the optimum performance. Figure 158 shows the partial code to implement the PD controller for eight servos and a single motor.

5.10 Simulink Linearized Model for Hovering stability

A Simulink model was made based on the equation of the model presented in Chapter 5.4 for ATLAS. Due to the limited access to a proper wind tunnel for flight vehicle testing to some of the aerodynamic coefficients like vehicle drag due to the crosswind, this Simulink model can only be used for linearized conditions such as hovering with small perturbation and no external disturbance. The Simulink model shows in figure 161 represent the linearized dynamic model of ATLAS with the proposed 8+ (oppo) control scheme with the rate and angle PD controller. Figure 162 shows the virtual vanes implementation box that represents the control surfaces that respond to pitch, roll, and yaw as described in equation 104. This can be a future work to verify the model for a better controller other than a PID controller. For linearized condition, as step input was given and figure 163 shows that the vehicle can achieve the desired conditions with a PD controller.

Figure 160 show the CAD model from Solidwork and the design aerodynamic Parameter for ATLAS model is listed below :

5.11 Dimension measured by Solidwork

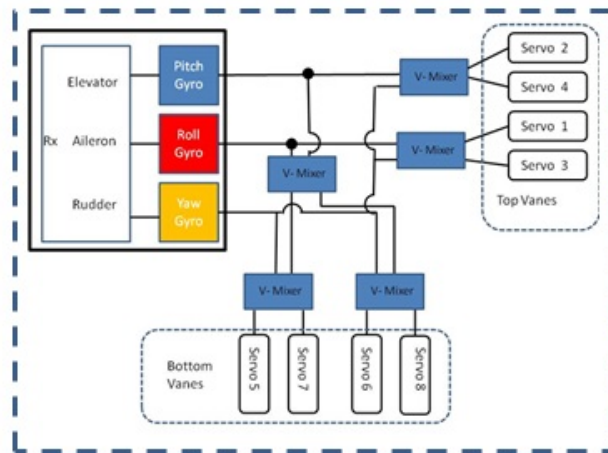
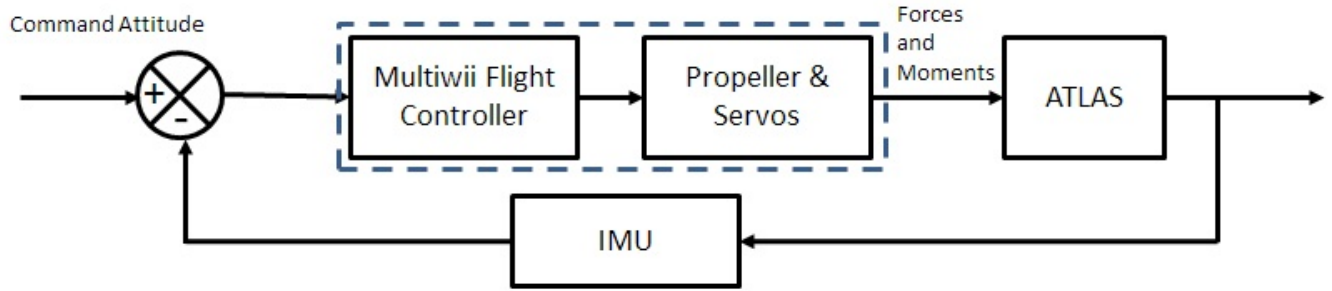


Figure 157: ATLAS's control schematic.

```

#elif defined(ATLAS){
servo[2] = get_middle(2) + (axisPID[YAW]*SERVODIR(2,2)) + (axisPID[ROLL]*SERVODIR(2,1));
servo[0] = get_middle(0) + (axisPID[YAW]*SERVODIR(0,2)) - (axisPID[PITCH]*SERVODIR(0,1));
servo[1] = get_middle(1) + (axisPID[YAW]*SERVODIR(1,2)) - (axisPID[ROLL]*SERVODIR(1,1));
servo[7] = get_middle(7) + (axisPID[YAW]*SERVODIR(7,2)) + (axisPID[PITCH]*SERVODIR(7,1));

servo[3] = get_middle(3) + (axisPID[YAW]*SERVODIR(3,2)) - (axisPID[PITCH]*SERVODIR(3,1)) - (axisPID[ROLL]*SERVODIR(3,1));
servo[6] = get_middle(6) + (axisPID[YAW]*SERVODIR(6,2)) + (axisPID[PITCH]*SERVODIR(6,1)) - (axisPID[ROLL]*SERVODIR(6,1));
servo[4] = get_middle(4) + (axisPID[YAW]*SERVODIR(4,2)) + (axisPID[PITCH]*SERVODIR(4,1)) + (axisPID[ROLL]*SERVODIR(4,1));
servo[5] = get_middle(5) + (axisPID[YAW]*SERVODIR(5,2)) - (axisPID[PITCH]*SERVODIR(5,1)) + (axisPID[ROLL]*SERVODIR(5,1));
}
motor[0] = rcCommand[THROTTLE];

```

Figure 158: Coding to implement PD controller to the microcontroller.

Table 5: Aerodynamic Parameters of ATLAS

Mass of the vehicle :	$m = 0.9 \text{ kg}$
Density of Air :	$\rho = 1.225 \text{ kg/m}^3$
Ambient Pressure :	1 atm
Center of Gravity of the vehicle:	$X_{c.g.} = 0, Y_{c.g.} = 0, Z_{c.g.} = 0$
Aerodynamic center of the top vanes :	$X_{a.c.t} = 0 \text{ m}$
	$Y_{a.c.t} = 0 \text{ m}$
	$Z_{a.c.t} = 0 \text{ m}$
Aerodynamic center of the bottom vanes :	$X_{a.c.b} = 0 \text{ m}$
	$Y_{a.c.b} = 0 \text{ m}$
	$Z_{a.c.b} = 0 \text{ m}$
Moment of Inertia :	$I_x = 0.01174 \text{ kg} - \text{m}^2$
	$I_y = 0.01171 \text{ kg} - \text{m}^2$
	$I_z = 0.00885 \text{ kg} - \text{m}^2$
Top Vane:	$S_t = 0.0048 \text{ m}^2$
Bottom Vane:	$S_b = 0.0046 \text{ m}^2$
Propeller:	Diameter = 0.2794 m
	Pitch = 7
	Weight = 0.01486 kg
	$I_{x_p} = 0.00004380 \text{ kg} - \text{m}^2$
	$I_{y_p} = 0.00003898 \text{ kg} - \text{m}^2$
	$I_{z_p} = 0.00008264 \text{ kg} - \text{m}^2$
Motor:	$K_m = 4.7e - 9$
	$K_t = 2.43e - 7$

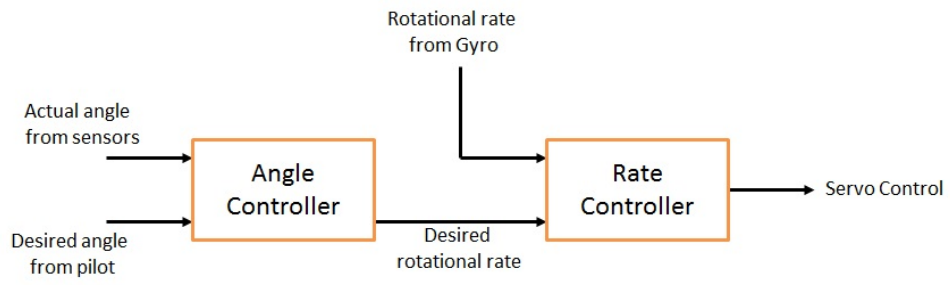


Figure 159: Per axis PD structure.

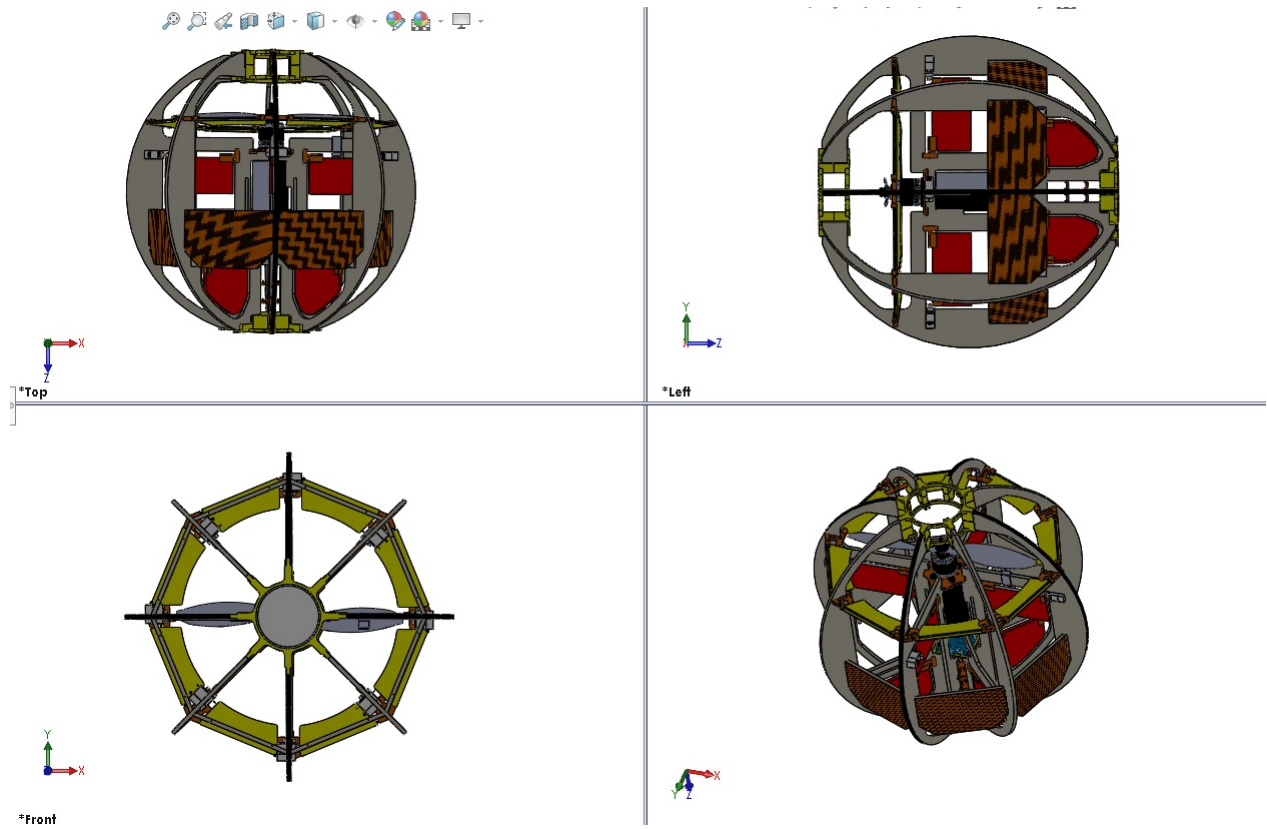


Figure 160: ATLAS

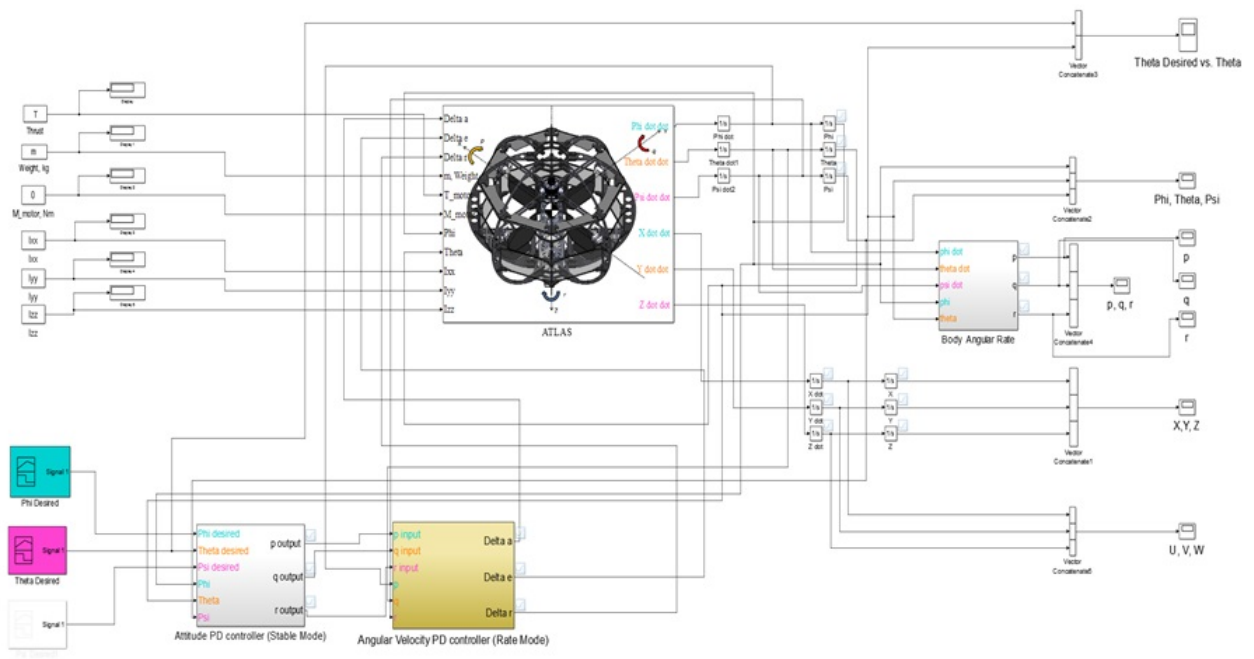


Figure 161: Linearized model using Simulink for pitching stability using PD controller.

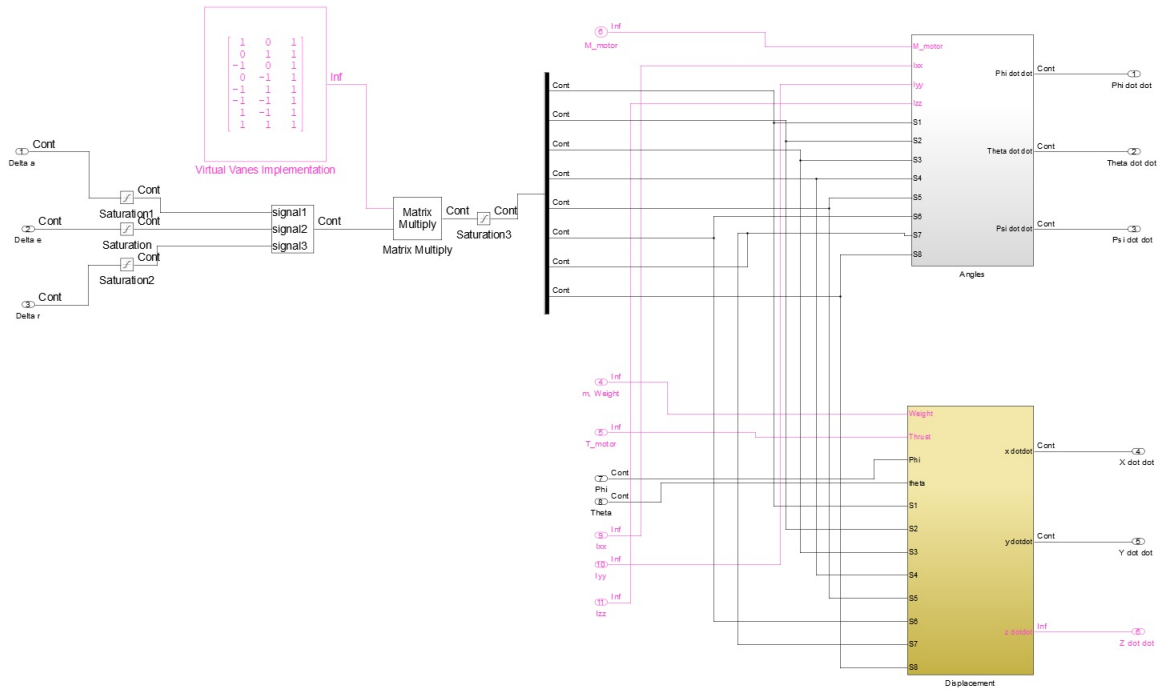


Figure 162: ATLAS System.

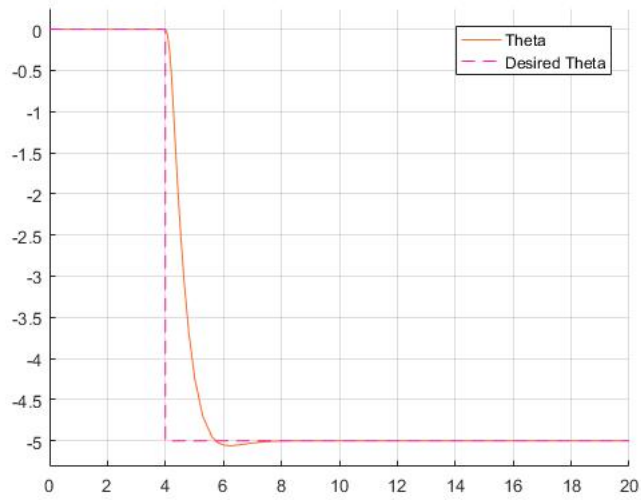


Figure 163: Respond with step input on to reach a desired theta using PD controller for both rate and angle controller in the linerized model.

CHAPTER VI

FLIGHT TESTING AND VALIDATION

The chapter presents the flight test results based on the proposed control scheme in Chapter 5 by using eight control vanes, eight movable vanes, and a single pitch propeller with the capability to perform upright maneuvering.

6.0 Flight Testing and Evaluations

The test flights will include the following to validate the stability and control of ATLAS:

- Take-off, hovering and translational flight.
- Heading Hold.
- Altitude Hold.
- Flight with Disturbances.
- Dynamic Upright Maneuvering.
- Sudden Descent Flight Test with Movable Vanes.

Take off and Hovering Stability

Fig. 164 shows the hovering stability indoor after ATLAS take off and hover for about 3.3 mins (200 seconds). The operator introduces minor aileron or elevator command inputs only when needed to keep the vehicle flying within the field of view of the Optitrack cameras. The roll and pitch of the vehicle achieve stability immediately after take-off and can well maintain a stable hovering flight within five degrees of rotational angle in both axes. The vehicle has no sensors for altitude control and position hold; therefore, the operator needs to manually control the throttle input when the vehicle is slowly descending as voltage gradually drops.

Figure 165 shows the hovering current is 24.5 A spinning with an average of rpm at 5769 and max rpm of 6831. The max power consumption is 300 Watt, with an average of 198 Watt.

Heading Hold

Heading hold was triggered after the vehicle has achieved stable hovering conditions. In this mode, the pilot provides throttle and translational input to maintain altitude while flying within the testing area. Figure 166 is multiple frames taken from a recorded flight video showing the vehicle can maintain the heading angle with a marker indicating the front of the vehicle during flight. Figure. 167 shows the change of elevation as recorded by the Optitrack that reflects the throttle changes. Increasing the throttle should increase the induced torque; however, the induced effect was significantly reduced with Heading Mode despite the rapid changes in the motor RPM. The surface area of the top and bottom control vanes is sufficient to provide stability and control to overcome induced yaw.

External Disturbance

The pilot induced the external disturbance by pushing the vehicle when ATLAS is maintaining a stable hovering flight. The IMU data shows the three disturbances that resulted in a maximum tilting angle of 75 degrees. The ATLAS can quickly return to hovering stability rapidly after each disturbance. Note that no position hold sensor was integrated. The vehicle drifts to a new position after any disturbances.

Upright maneuvering

Graph 169 shows the roll and pitch of the vehicle when performing the upright maneuver by manually adjusting the throttle when the ATLAS is on the ground. Note that the pilot is manually controlling the amount of throttle input. The second graph 170 shows that the upright maneuver consumes a maximum power of 40 Watt and 2.5 Amp. The multiple tests show that the maneuver is repeatable and reliable. Note that the eight control surfaces are not contributing to this maneuver like the lightweight JFS.

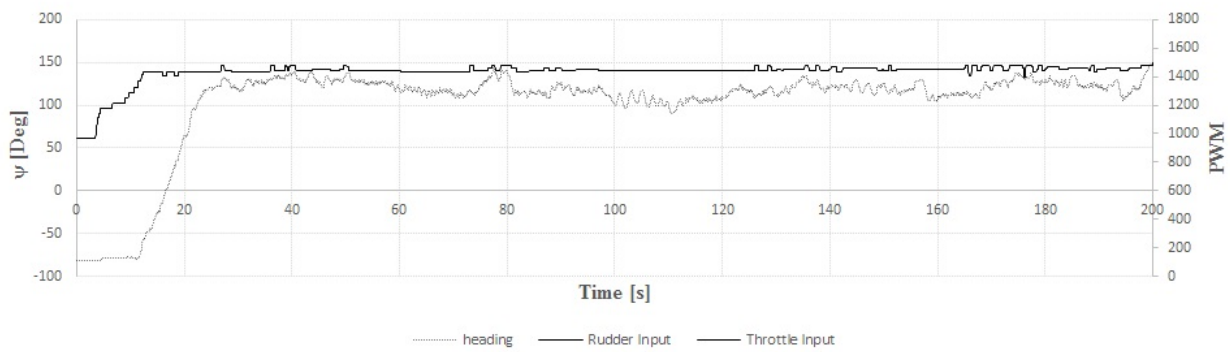
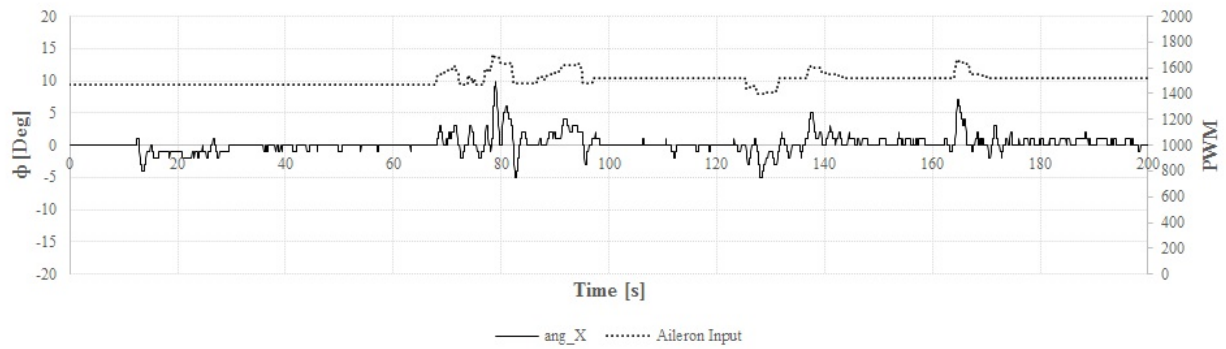
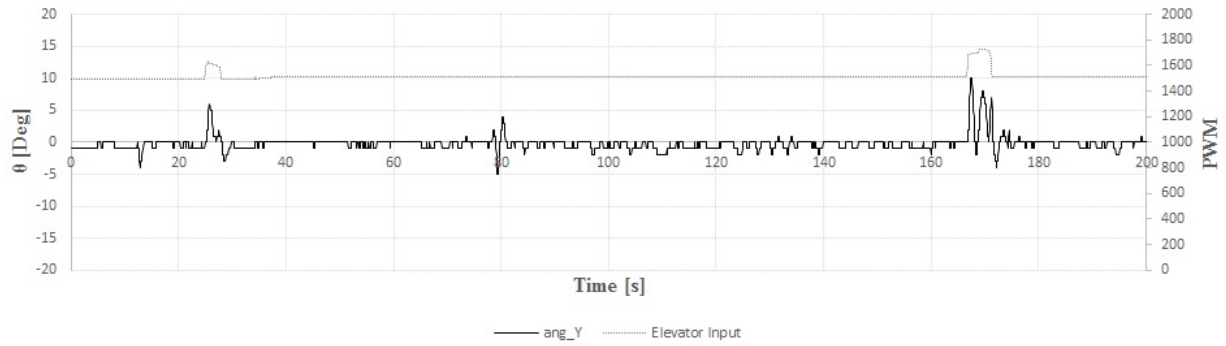


Figure 164: Hovering stability - 3 minutes flight with Heading Hold activated.



Figure 165: RPM, Watt and motor temperature at hovering flight.

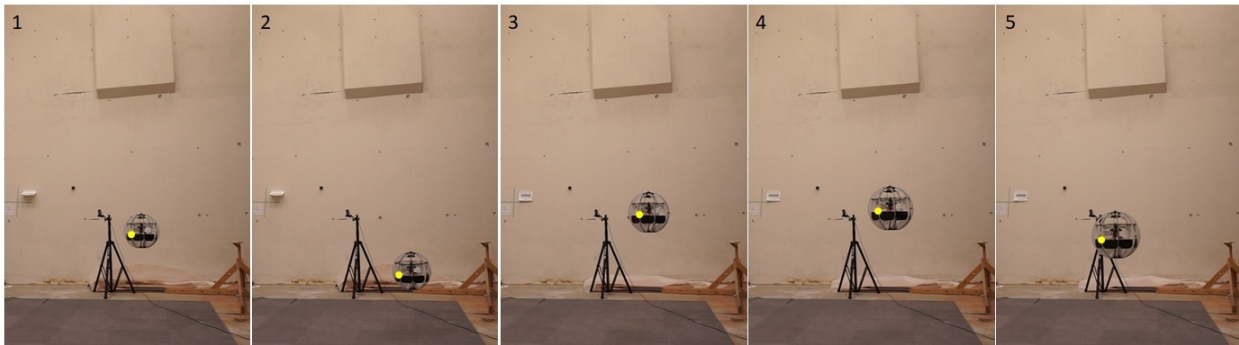


Figure 166: Heading Hold test.

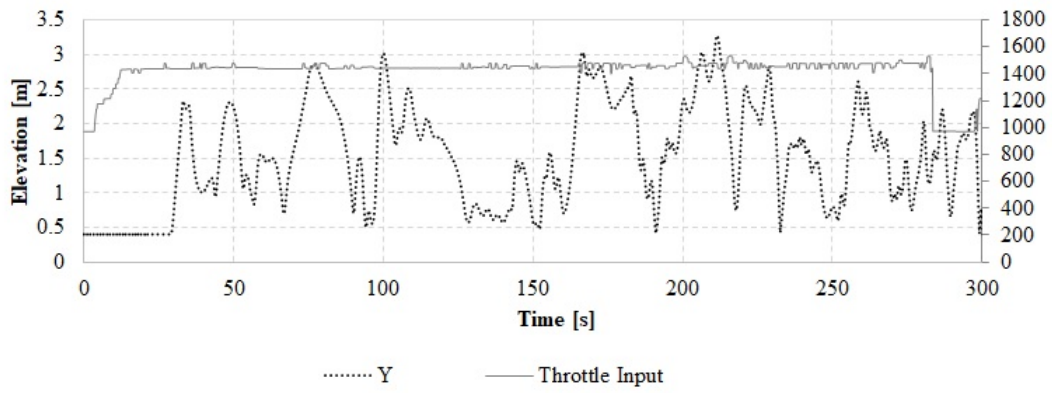


Figure 167: Throttle input to manually maintain the flight altitude.

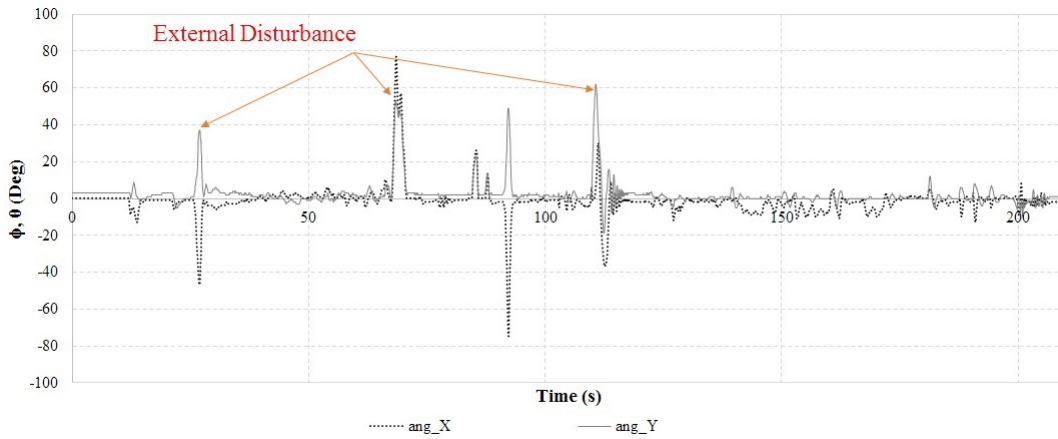


Figure 168: Flight recovery and stability after the pilot executed multiple disturbances.

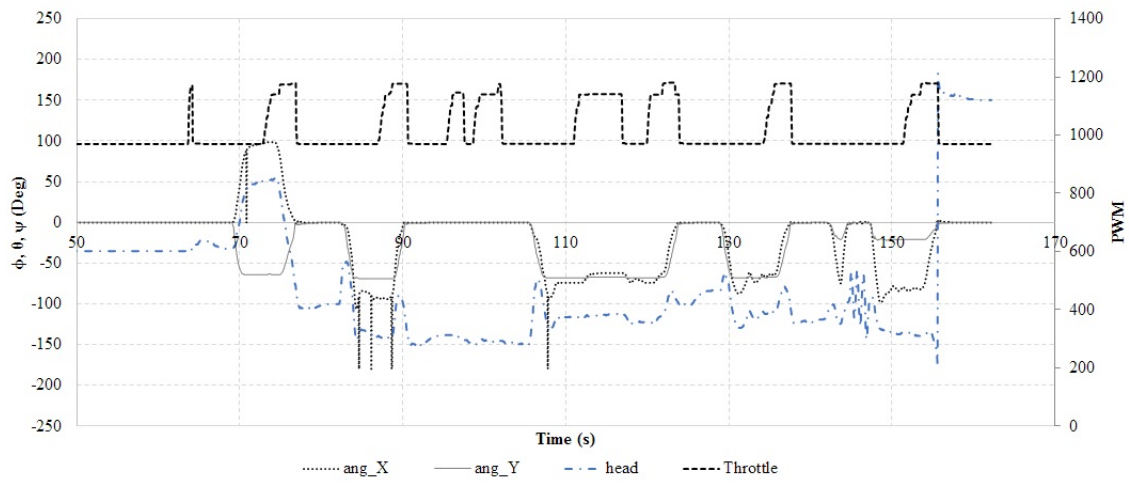


Figure 169: IMU data when performing upright maneuver.

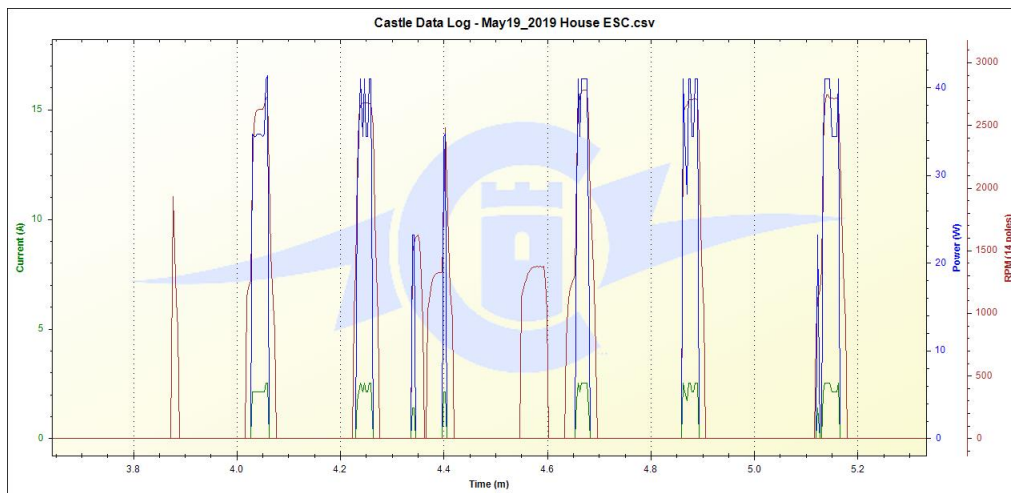


Figure 170: Recorded power and amperage consumption when performing upright maneuver.

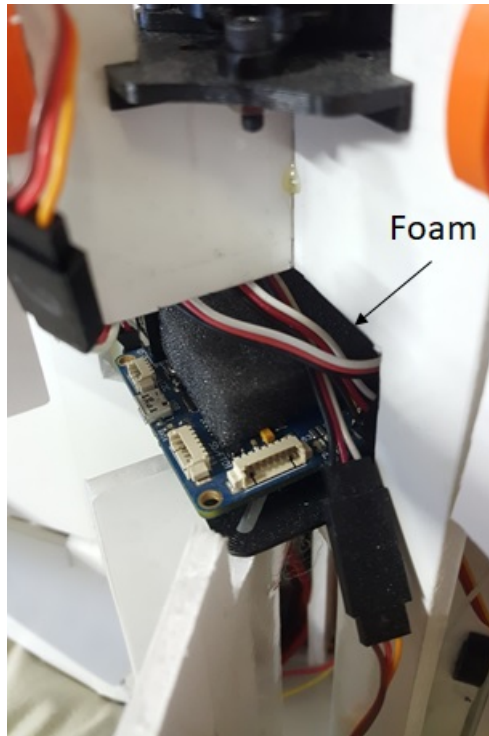


Figure 171: Foam on top of the board to protect the barometer from light and direct airflow.

Altitude Hold

Altitude sensing estimation is done by fusing Multiwii MS5611 Barometer with z Accelerometer for indoor flight. However, the integrated barometer on the Multiwii board is very sensitive to prop wash and light, so it must be covered with a small piece of open-cell foam to protect it, as shown in figure 171. Since the propeller is directly above the barometer, it is impossible to obtain a reliable altitude reading when the throttle is continuously changing the pressure or airflow within the spherical vehicle frame. Therefore, altitude hold throughout the flight is not possible yet. Figure ?? shows a result of a flight test with heading hold mode activated that lasted for only a few seconds with Heading Hold triggered. Figure 172 shows that no throttle input has been constant throughout the flight.

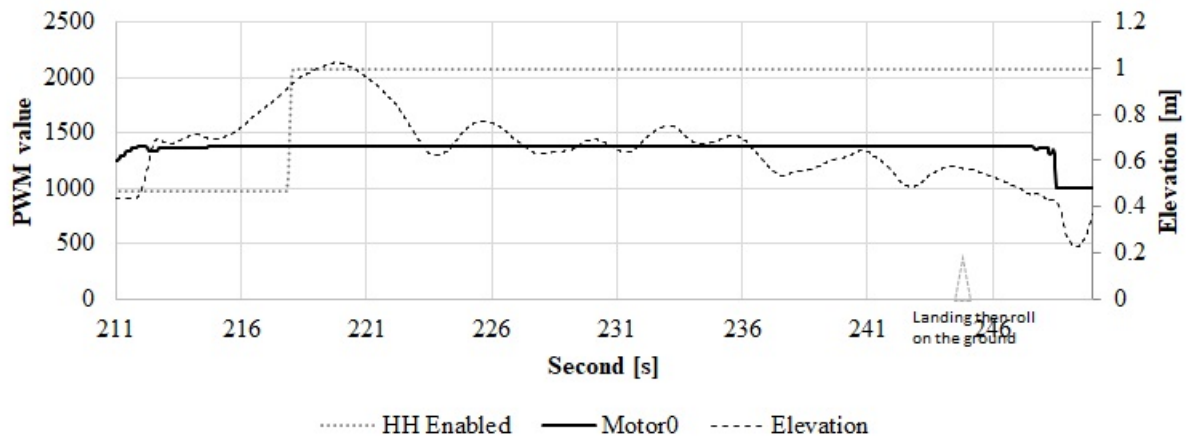


Figure 172: Change of elevation after altitude hold was enabled.

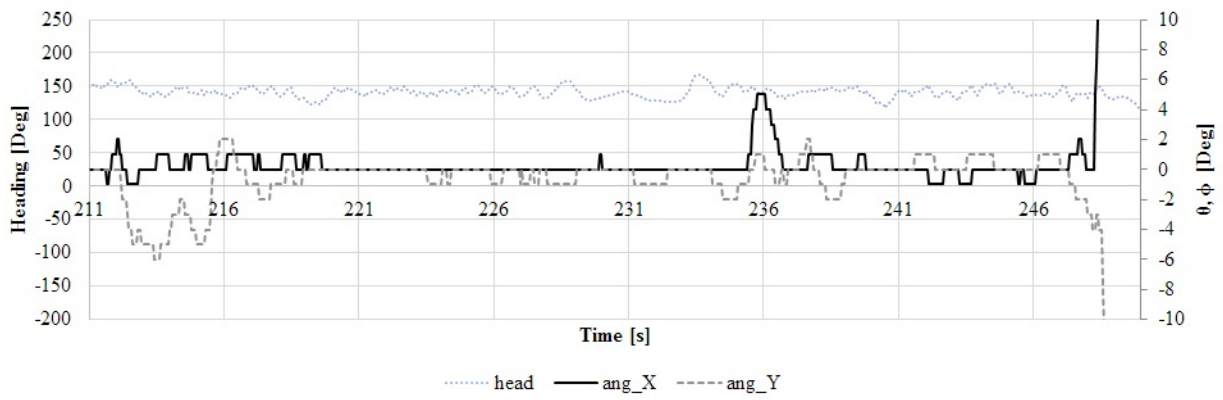


Figure 173: Vehicle's attitude after enabled altitude hold.

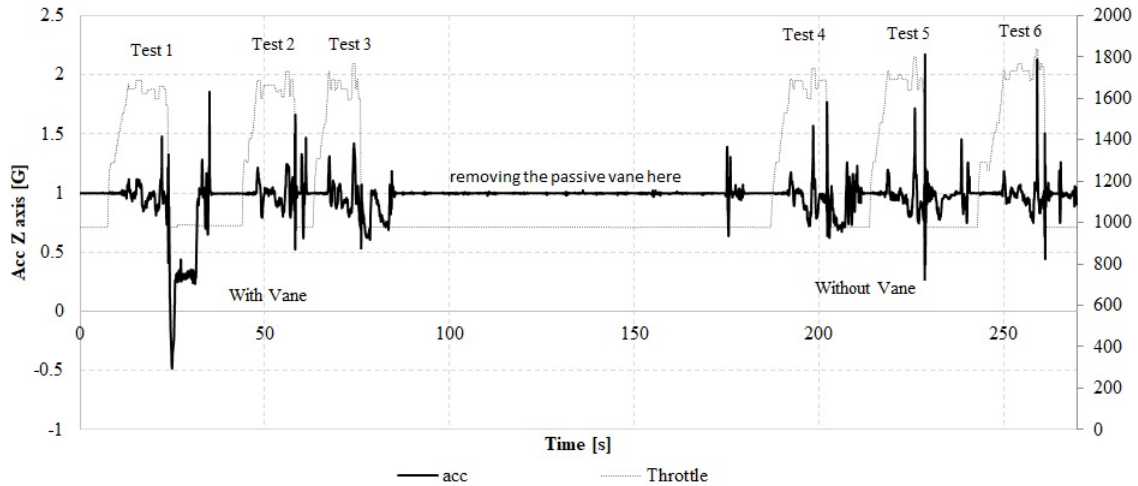


Figure 174: Recorded acceleration on the Z-axis with and without the movable vane.

Sudden Descent Flight Test with Movable Vanes

The goal of this flight test is to investigate the impact of the movable vane on descending flight by reducing the throttle input when the vehicle reaches a certain height in the flight test chamber. Note that all tests show that the vehicle has achieved hovering flight conditions before reducing the throttle to execute the descending test. The first three tests are with the passive vane installed on the vehicle and the last three tests with the passive vanes removed. Figure 174 is the recorded IMU data showing the acceleration in the Z-axis. To obtain the descending velocity, figure 175 measure the change of altitude for each test. Note that some data points are missing because the vehicle flew beyond and re-enter into the Optitrack camera field of view. Results in graph 176 show that passive vanes help reduce the descending rate. This flight also measured the impact load when the vehicle hit the ground when the pilot did not respond fast enough to increase the throttle before hitting the ground. Figure 175 shows that the highest measured g-force after landing is about 2.16 G when $t = 228$ s on test 5.



Figure 175: Recorded change of altitude from the OptiTrack cameras. Displacement vs. frame.

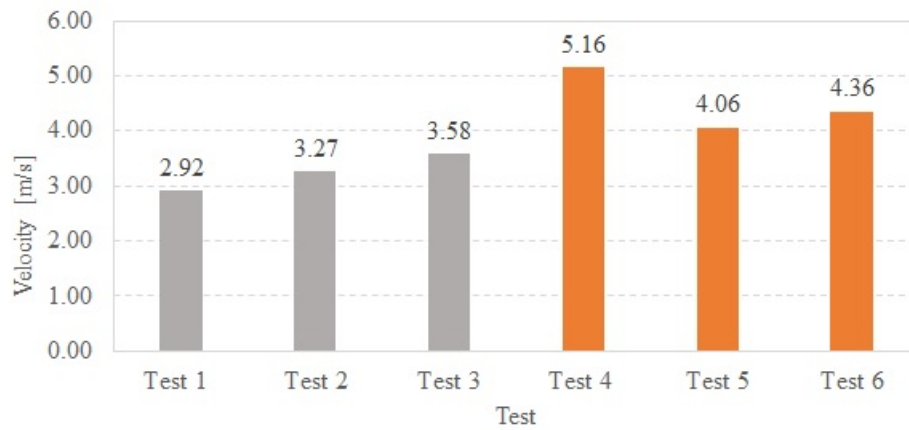


Figure 176: Descending velocity for each test.

CHAPTER VII

CONCLUSIONS AND FUTURE WORK

7.0 Conclusions

Dynamic Upright Maneuvering

The ability to recover to flight is a beneficial function for a UAV after accidental contact with objects or landing. The majority of the UAVs today, like the multirotor platform, are designed to continue flying, and only a few can have the upright capability if the vehicle loses its orientations on the ground. The operator needs to try their best to fly in contact with objects or people or to rely on sense and avoid sensors when operating in a cluttered or indoor environment. Among the UAVs with a spherical frame, both the ATLAS and JFS are the only two UAVs that can perform upright maneuver for flight recovery after landed on the ground. JFS is utilizing the propeller slipstream interacting with the control vanes. On the other hand, the ATLAS is reversing the propeller spinning direction to generate slipstream in the opposite direction to achieve upright maneuverability. The other research focused only focusing on in-flight dynamics and control. ATLAS has successfully demonstrated the dynamic upright maneuvering by mean of both servo actuation and electronic controller to change the polarity of the ESC to spin the propeller in dual directions. Combining with the unique spherical frame, the reversal of the propeller can generate sufficient thrust to tilt the vehicle upright for flight recovery.

Passive Control Movable Vanes

Table 178 also shows that other spherical frame UAVs like the SFV and NUS FS have passive vanes installed radially around the propeller; however, their research including the JFS has never presented the analysis of such passive vanes.

This research has conducted a series of bench tests to determine the characteristic of hinged passive vanes operating near the tip of a single rotating propeller. The force needed to deflect the vanes is dependent on the propeller pitch and RPM, and proximity of the propeller tip to the passive vane. The change of height of the propeller plane with respect to the movable vane can affect the direction of the force generated by these vanes. The maximum upward force in the thrust direction can be obtained by placing the vanes at $h = 0$, in which the chord length of the vanes needed to be in parallel with the propeller plane. Smoke visualization test shows that the high-speed airflow is coming in from the top of the vane is causing a low-pressure region. These phenomena provide the pressure differential needed to deflect the vane up and toward the propeller tip. Wind tunnel test has found the equivalent wind speed needed to make the vane fully deflected when the propeller is spinning at a constant RPM. This equivalent wind speed is considered the minimum velocity need to make sure the vane remains horizontal. The sudden loss of air pressure causes the vane to dropdown.

Indoor flight tests show that these passive movable vanes can help stabilize the in-flight stability and act as drag surfaces top stabilize the vehicle when descending rapidly. A bench test has shown that these passive vanes can help to damp the instability in roll or pitch when the vehicle is being perturbed or not having a balanced C.G. in the vehicle lateral direction. Seven types of vane designs were made and tested to investigate its drag characteristic in a range of Reynold numbers ranging from 4,000 to 70,0000. Most vanes design exhibits similar drag coefficient as the Reynold number increases. A chambered vane design can provide the higher drag coefficient, but flat plate vane has the simplicity for manufacturing and attachment onto the spherical frame of the vehicle. Such passive vane can be beneficial to be installed near a spinning propeller-like multicopter platform to generate additional lift and stability, assuming the overall weight is still favorable for the UAV after these passive vanes are added.

Coupled Active Control Configuration

Multiple control configurations were presented by using four or eight control surfaces, as shown in table 178. A coupled roll, pitch, and yaw control scheme using eight control surfaces can provide stability and control in flight. The control scheme through a series of indoor flight successfully overcome induced reactions by using a single pitch propeller like motor torque and gyroscopic precession. Induced yaw was significantly reduced in comparison to the spherical UAVs like NUS's Flying sphere and Korea's Uni-copter. This made



Figure 177: A GoPro session4 mounted on top of the ATLAS for ceiling inspection.

possible by coupling all active control vanes to respond to yaw input. Heading Hold is also achieved during the hovering flight with rapidly changing throttle while in-flight.

Endurance and Vehicle Weight

JFS and ATLAS are the only two spherical shape UAVs that have sufficient thrust to carry additional payloads. The ATLAS can operate around 10 mins and weight about 900 grams. Even though the weight of the ATLAS is 1.5 times heavier than JFS, it can perform stable flight and control with the payload capability up to 75 grams while JFS only carries a pin-hole camera. An example payload used by ATLAS was a GoPro Session 4 that weighs about 74 grams (2.61 oz) and still able to maintain a 7 min flight time by using a 4S Lipo 1500mAh battery. Figure 177 is showing the GoPro camera mounted on top of the ATLAS for indoor ceiling inspection. The lipo battery can be shifted along the bottom of the fuselage to make sure the center of gravity of the vehicle can remain at the center of the sphere when a payload is integrated on top of the ATLAS. Other UAVs do not allow adjustment of the center of gravity.

Figure 178 comparing the relevant spherical shape UAVs in term of size, passive vanes, center of gravity, endurance and etc.







	 JFS	 SFV	 NUS FS	 Contra-rotating	 Uni-Copter	 ATLAS
Country	Japan	Korea	Singapore	UK	Korea	US
Weight [g]	350	550	551	590	450	900
Diameter [cm]	42	44	42	23	48	40
Endurance [min]	8	6	7	~ 10 ? (claim)	8	10
Year	2011	2013	2013	2013	2018	2011 to present
# of Propeller	1	1	1	2	1	1
# of Control Vanes [Literature]	8 [No]	4 [Yes]	8 [Yes]	*4 [Yes]	*8 [Yes]	8 [Yes]
				*Stability & Control issue		
Passive Vane Installed [Literature]	Yes [No]	Yes [No]	Yes [No]	No [No]	No [No]	Yes [Yes]
Upright Maneuver [Method]	Yes [Slipstream and Control Vanes]	No	No	No	No	Yes [Thrust Reversal]
Center of Gravity [Method]	Center ? [Shift-able C.G??]	Top	Top	Top	Center	Center [Adjustable by shifting battery]

Figure 178: ATLAS in comparison with other spherical UAVs with control vanes and single or coaxial propeller.

7.1 Future Work

Alternative Flight Controller and Control Algorithm for Outdoor Navigation.

The existing COTS PID controller can provide stable indoor flight, but a more robust algorithm is needed to provide better stability and control to operate outdoor and overcome wind gust. The current ATLAS has no sensors to achieve a position controller like sonar or GPS to help fix the vehicle at a location. The spherical frame can protect the propeller and avionics from the environment, but sonic sensors can be equipped to detect obstacles and walls when flying indoor. GPS, for outdoor navigation, should help ATLAS to operate outdoor and provide position hold control in-flight. The current barometer sensor on the Multiwii board is directly exposed to the propeller slipstream and significantly impact the barometer reading to provide stable altitude hold mode. A barometer sensor needs to be mounted outside the propeller slipstream to avoid disturbance and false reading of the altitude.

Measurement of Aerodynamic Characteristic for Modeling Validation

A non-linear six degrees of freedom dynamic model for ATLAS is assembled due to the analysis of aerodynamic forces and moments combined with equations of motion and dynamic equations. However, the theoretical methods for calculation of aerodynamic parameters for a spherical shape are limited; hence, proper wind tunnel testing is needed to validate the Simulink model presented in the Dynamic and Control chapter. Modeling and simulation of flight dynamics of spherical shaped UAVs are necessary to develop a new control strategy.

ATLAS with Rover Mechanism

In order to differentiate ATLAS from the Japanese Flying Sphere design, other ATLAS variation was considered to enhance ground mobility. Current ATLAS design use the propeller slipstream to roll away from the obstacle and not designed for coordinated ground maneuvering. The separate ground system allows the vehicle to perform a surveillance mission, as shown in figure 180. Figure 180 shows the rover mechanisms concept integrated into the flying-only model. Two robotic motors govern the ground mobility and controlled

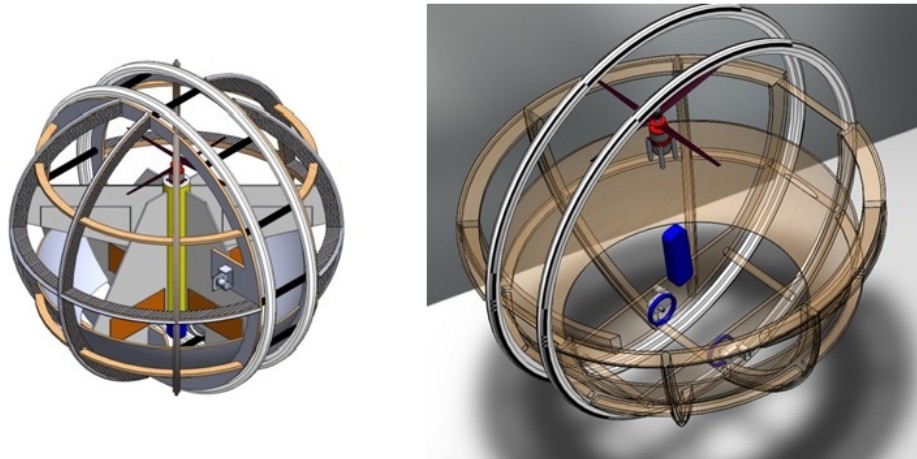
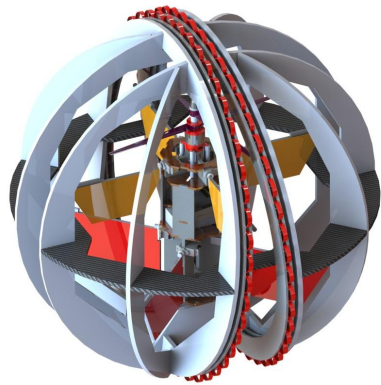


Figure 179: The overview of ATLAS concept with rover mechanism in 2011.

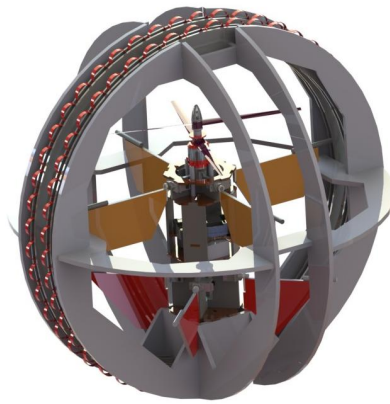
by a separate control system. Ground maneuverability can be achieved by using differential speed on each wheel. Each wheel is tilted inward to provide ground stability that allows the contra-rotating prop to point upright after landed on the ground. The US20170210468A1 patent for ATLAS included these rover concepts.

ATLAS with Foldable Frames

Another patented alternative ATLAS concept has a foldable spherical frame for ease of storage and transportation. Figure 182 and 183 shows the prototype of such a concept with eight pieces of panels with hinges installed at both top and bottom side of the vehicle. A removable fuselage with the avionic components that can be easily mounted at the center of the foldable frame for quick deployment.



Tilted Wheel



Straight Wheel

Figure 180: Straight wheel and tilted Wheel.



Figure 181: Rover design mockup.

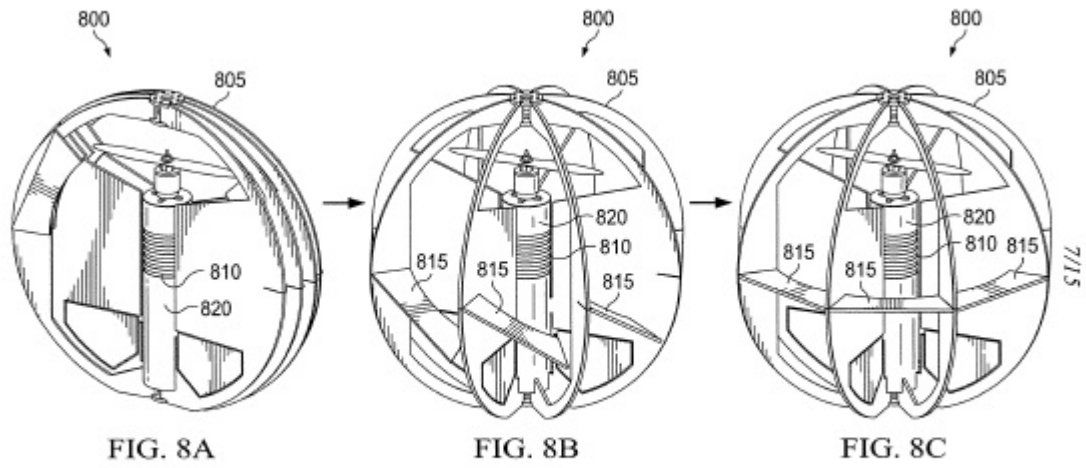


Figure 182: ATLAS with foldable frame.



Figure 183: Foldable frame prototype for compact ATLAS design.

Bibliography

- [1] Anderson, J.D. (2013) *Aircraft Performance and Design*, WCB McGraw-Hill.
- [2] Kohlman, D.L. (1982) *Introduction to V/STOL Airplanes*. Iowa State University Press.
- [3] Japanese Flying Sphere. (2011) Retrieved from <http://www.coolrobots.net/2011/06/amazing-japanese-robot-flying-ball.html>.
Last Accessed : 04/21/2019.
- [4] Japanese Flying Sphere. (2011) Retrieved from <http://www.youtube.com/watch?v=pF0uLnMoQZA>.
Last accessed on 4/21/2019.
- [5] Humiyuki, S. (2011) <http://www.ekouhou.net/>.
- [6] Chia, Y. H. (2013) *Spherical VTOL Unmanned Aerial Vehicle - Structural and Aerodynamics*. National University of Singapore. Department of Mechanical Engineering. Project AM31.
- [7] Hawk Eye. Video posted on November 2011. Video for Techfest 2-12, IITB. Retrieved from <https://www.youtube.com/watch?v=MfRA7ckEKeQ>. Last accessed on 4/21/2019.
- [8] Spherical Flight Vehicle. (2012) Korea Aerospace University, Flight Control LAB.
Retrieved from <https://think-tank.tistory.com/223>. Last accessed on 4/21/2019.
- [9] Moon, J.S., Kim, C.Y., Youm, Y.G., and Bae, J.B. (2017) *UNI-copter : A Portable Single-Motor-Powered Spherical Unmanned Aerial Vehicle (UAV) with an Easy-to-assembly and Flexible Structure*. *Journal of Mechanical and Science and Technology* 32 (5) 2018 2289-2298.
- [10] Spherical Flying Machine with No Control Surface. (2017) Retrieved from <http://www.instructables.com/id/A-Spherical-Flying-Machine-with-no-Control-Surface/>.

- [11] Fleye. (2013) Retrieved from <https://www.gofleye.com>. Last accessed on 4/21/2019.
- [12] Malandrakis, K., Dixon R., Savvaris, A., and A. Tsourdos. (2016) *Design and Development of a Novel Spherical UAV*, 20th IFAC Symposium on Automatic Control in Aerospace, ACA 2016, 21 -25 August 2016, Sherbrooke, Quebec, Canada. in IFAC-PapersOnLine, Vol 49, Issue 7, 2016, pp. 320 -325.
- [13] ELIOS. (2015) Retrieved from <https://www.flyability.com/elios/>. Last accessed on 4/25/2019.
- [14] ELIOS2. (2015) Retrieved from <https://www.theverge.com/2015/2/9/8006509/bouncy-ball-drone-flyability-gimball>. Last accessed on 4/25/2019.
- [15] Sun, H.X., Hou, K., and Jia, Q.X. (2013) *Development, Analysis and Control of a Spherical Aerial Vehicle*. . Vibroengineering. Journal of Vibroengineering. June 2013. Volume 15, Issue 2. ISSUE 2. ISSN 1392-8716. School of Automation, Beijing University of Posts and Telecommunications, 100876, Beijing, China.
- [16] Hytaq. (2012) Retrieved from <http://www.engadget.com/2012/11/28/hytaq-hybrid-quadmotor-robot-travels-by-air-and-land/>.
- [17] Airburr. (2013) Retrieved from <http://lis.epfl.ch/airburr>. Last accessed on 04/25/2019.
- [18] Kossett, A. and Papanikolopoulos, N. (2011) *A Robust Miniature Robot Design for Land/Air Hybrid Locomotion*, IEEE International Conference on Robotics and Automation. Shanghai International Conference Center, Shanghai, China, May 9 - 13, 2011.
- [19] Rolling robot. (2013) Retrieved from <http://www.ubergizmo.com/2011/05/rolling-robot-transforms-into-helicopter-applies-for-autobot-position/>. Last accessed on 05/05/2013.
- [20] Mielniczek,W. (2012) Retrieved from <http://www.kickstarter.com/projects/2017062404/b-go-beyond?ref=category>. Lasty accessed on 05/05/2012.
- [21] Fleming, J.E., Langford, M.D., and Goossen, E.R. (2012) *Development of an Air Data System for Ducted Fan Unmanned Aircraft*. 50th AIAA Aerospace Sciences Meeting including the New Horizons Forum and Aerospace Exposition, 2012.

- [22] Graf, W. (2005) *Effect of Duct Lip Shaping and Various Control Devices on the Hover and Forward Flight Performance of Ducted Fan UAVs*. Master Thesis, Virginia Tech, Blacksburg, VA, May 13, 2005.
- [23] T-Hawk UAV. (2011) Retrieved from <https://en.wikipedia.org/wiki/Honeywell-RQ-16-T-Hawk>. Last accessed on 05/05/2012.
- [24] McCormick, B.W. (1999) *Aerodynamics of V/STOL Flight*. Dover Publication, 1999.
- [25] istar ducted UAV. (2009) Retrieved from <https://www.fs.fed.us/t-d/programs/im/aerial/uav.shtml>. Last accessed on 04/11/2017.
- [26] Pflimlin, J., Binetti, P., Soueres, P., Hamel, T. and Trouchet, D. (2010) *Modeling and Attitude Control Analysis of a Ducted-Fan Micro Aerial Vehicle*. Control Engineering Practice 18, pp. 209-218., 2010.
- [27] Zhao, H. W. and Bil, C. *Aerodynamic Design and Analysis of a VTOL Ducted-Fan UAV*, 26th AIAA Applied Aerodynamics Conference, Honolulu, Hawaii. 18 - 21 August 2008.
- [28] Peddle, L., Jones, T., and Treunicht, J. *Practice Near Hover Flight Control of a Ducted Fan (SLDe)*, Control Engineering Practice 17, pp. 48 -58, 2010.
- [29] Naldi, R., Gentili, L, Marconi, L., and Sala, A. (2010) *Design and Experimental Validation of a Non-linear Control Law for a Ducted-Fan Miniature Aerial Vehicle*. Control Engineering Practice 18, 2010. Page 747 - 760.
- [30] Kruger, W. (1944) *On Wind Tunnel Tests and Computations Concerning the Problem of Shrouded Propellers*. NACA Technical Memorandum 1202, January 1944.
- [31] Felming, J., Jones, T., Ng, W., Gelhausen, P., and Enns, D. (2003) *Improving Control System Effectiveness For Ducted Fan VTOL UAVs Operating in Crosswinds*, AIAA Unmanned Unlimited System, Technologies and Operations, AIAA 2003-6514-2003, pp. 1-3.
- [32] Fleming, J., Jones, T., Lusardi, J., Gelhausen, P., and Enns, D. (2004) *Improved Control of Ducted Fan VTOL UAVs in Crosswind Turbulances*. AHS 4th Decennial Specialist's Conference on Aeromechanics. 2004.
- [33] Moller, P.S. (1989) *Robotic or Remotely Controlled Flying Platform*. U.S. Patent No: 4795111.

- [34] Harris, R. (2007) *Investigation of Control Effectors for Ducted Fan VTOL UAVs*. Master Thesis, VirginiaTech, Blacksburg, VA, June 27, 2007.
- [35] Shkarayev, S., Moschetta, J., and Bataille, B. (2008) *Aerodynamic Design of Micro Air Vehicle in Vertical Flight*. Journal of Aircraft, Vol, 45, No.5, September-October 2008.
- [36] TRACKER. (2014) Retrieved from <https://www.opensourcephysics.org>.
- [37] Yen, D. and Brauche, F. (2000) *Calibration and Uncertainty Analysis for the UC Davis Wind Tunnel Facility*. Retrieved from <https://research.engineering.ucdavis.edu/flight/wp-content/uploads/sites/33/2015/01/Calibration.pdf>. Last accessed on 2/21/2019.
- [38] Basic Propeller Principles. (n.a) [http : //www.flightlearnings.com/2009/08/24/basic – propeller – principles – part – four – %E2%80%93 – gyroscopic – action](http://www.flightlearnings.com/2009/08/24/basic-propeller-principles-part-four-%E2%80%93-gyroscopic-action). Last accessed on 3/21/2019.
- [39] Wang, Z. J., Liu, Z. J., Fan, N.J., and Guo, M.F. (2013) *Flight Dynamic Modeling of a Small Ducted Fan Aerial Vehicle based on Parameter Identification*. Chinese Journal of Aeronautics, 2013, 26(6); 1439 - 1448.
- [40] Shetty, O.R. and Selig, M.S. (2011) *Small-Scale Propeller Operating in the Vortex Ring State (VRS)*., 49th AIAA Aerospace Science Meeting, 4 - 7 January 2011, Orlando, FL.
- [41] Prouty, R.W. (1997) *Why Hovering Helicopters Are Unstable*. Rotor & Wing, April, Page 53.
- [42] Bristeu, P.J., Martin, P., Salaun, E., and Petit, N. (2009) *The Role of Propeller Aerodynamic in the Model of a Quadcopter UAV*. Proceeding of the European Control Conference 2009, Budapest, Hungary, August 23-26.

Appendix A: Patent Detail for ATLAS

Full 41 page link: <https://patentimages.storage.googleapis.com/9b/8c/56/c5760121619416/WO2015149000A1.pdf>

2014-03-27 Priority to US201461970954P

2014-03-27 Priority to US61/970,954

2015-03-27 Application filed by The Board Of Regents For Oklahoma State University

2015-10-01 Publication of WO2015149000A1

(12) INTERNATIONAL APPLICATION PUBLISHED UNDER THE PATENT COOPERATION TREATY (PCT)

(19) World Intellectual Property Organization
International Bureau



(10) International Publication Number
WO 2015/149000 A1

(43) International Publication Date
1 October 2015 (01.10.2015)

- (51) International Patent Classification:
B62D 57/00 (2006.01) *B64C 39/02* (2006.01)
- (21) International Application Number:
PCT/US20 15/023 134
- (22) International Filing Date:
27 March 2015 (27.03.2015)
- (25) Filing Language: English
- (26) Publication Language: English
- (30) Priority Data:
61/970,954 27 March 2014 (27.03.2014) US
- (71) Applicant: THE BOARD OF REGENTS FOR OKLAHOMA STATE UNIVERSITY [US/US]; Technology Development Center-OSU, 1201 S. Innovation Way Dr., Suite 210, Stillwater, OK 74074 (US).
- (72) Inventors: JACOB, Jamey, D.; 282 1 W. 25th Ave., Stillwater, OK 74074 (US). LOH, Weng, Kheong; 140 N. Duck, Apt. 29, Stillwater, OK 74075 (US).

- (74) Agent: WATT, Terry, L.; Fellers, Snider, Blankenship, Bailey &, Tippens, P.C., 321 South Boston, Suite 800, Tulsa, OK 74103-33 18 (US).
- (81) Designated States (unless otherwise indicated, for every kind of national protection available): AE, AG, AL, AM, AO, AT, AU, AZ, BA, BB, BG, BH, BN, BR, BW, BY, BZ, CA, CH, CL, CN, CO, CR, CU, CZ, DE, DK, DM, DO, DZ, EC, EE, EG, ES, FI, GB, GD, GE, GH, GM, GT, HN, HR, HU, ID, IL, IN, IR, IS, JP, KE, KG, KN, KP, KR, KZ, LA, LC, LK, LR, LS, LU, LY, MA, MD, ME, MG, MK, MN, MW, MX, MY, MZ, NA, NG, NI, NO, NZ, OM, PA, PE, PG, PH, PL, PT, QA, RO, RS, RU, RW, SA, SC, SD, SE, SG, SK, SL, SM, ST, SV, SY, TH, TJ, TM, TN, TR, TT, TZ, UA, UG, US, UZ, VC, VN, ZA, ZM, ZW.
- (84) Designated States (unless otherwise indicated, for every kind of regional protection available): ARIPO (BW, GH, GM, KE, LR, LS, MW, MZ, NA, RW, SD, SL, ST, SZ, TZ, UG, ZM, ZW), Eurasian (AM, AZ, BY, KG, KZ, RU, TJ, TM), European (AL, AT, BE, BG, CH, CY, CZ, DE, DK, EE, ES, FI, FR, GB, GR, HR, HU, IE, IS, IT, LT, LU, LV, MC, MK, MT, NL, NO, PL, PT, RO, RS, SE, SI, SK,

[Continued on nextpage]

(54) Title: SPHERICAL VTOL AERIAL VEHICLE

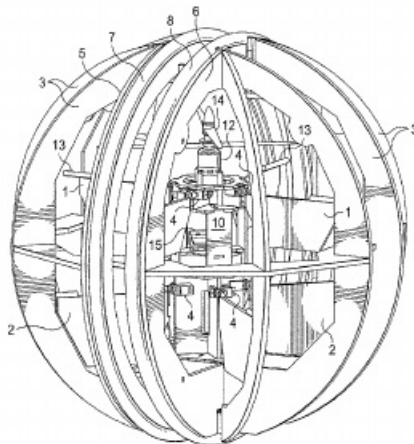


FIG. 1

(57) Abstract: An embodiment of the present disclosure relates to an unmanned flying robotic object that contains a wheeled mechanism that encircles its spherical exoskeleton. This feature allows the flying spherical vehicle to readily transform into a ground maneuverable vehicle. A robotic motor with differential speed capability is used to operate each wheel to provide effective ground maneuverability. There are examples provided herein of wheel configurations suitable for use with an embodiment. One is the straight- (or parallel) wheel design, and another is tilted-wheel design as are illustrated and discussed hereinafter. One embodiment of an unmanned flying robotic object taught herein is foldable.

WO 2015/149000 A1

Appendix B: ATLAS with Coaxial Contra-Rotating Motor

Earlier ATLAS prototypes have propulsion selection involves using a coaxial contra-rotating propeller that produces no torque or gyroscopic effect, as shown by a single propeller. Fig 185 indicates the type of COTS available counter-rotating motors with the thrust and weight ratio breakdown. Only a handful of the coaxial motor was available for radio-controlled airplanes since 2011. The AEO-RC CR28M had the highest thrust to weight ratio and was chosen for the earlier prototype. The thrust, torque, and RPM were obtained by varying the throttle setting on the motor from 10% to 100% throttle for every 10% interval. The static thrust and torque vs. rpm data were plotted. This test was conducted to verify that the induced gyroscopic effect can be canceled using a contra-rotating propeller. The motor includes 10x6 and 10x6R propeller. Two 35A rated ESCs were used to test the motor. The isolated lower motor in terms of the static thrust and torque is presented as a function of RPM. In figure 187, the variation of static thrust and torque is presented for the tractor configuration at 11 V.

The static thrust force increase linearly with the increase of RPM and reaches a maximum at 1.62 N and 5000 rpm. This thrust is 1.7 times greater than the thrust generated by a single-propeller motor under the same voltage. Note that the linear relationship simplifies thrust control in an automatic system. The maximum torque in this test was measured 0.01 lb-in, as shown in figure 187. In this test, negative torque associated with the bottom motor. As expected, this torque is 19 times less in comparison with the torque produced by a single-propeller. As evident from figure 187, the contra-rotational propellers reduce the gyroscopic torque, as seen on a single propeller. This feature significantly simplifies control for VTOL vehicle and provide more control authority for pitch and roll control vanes.

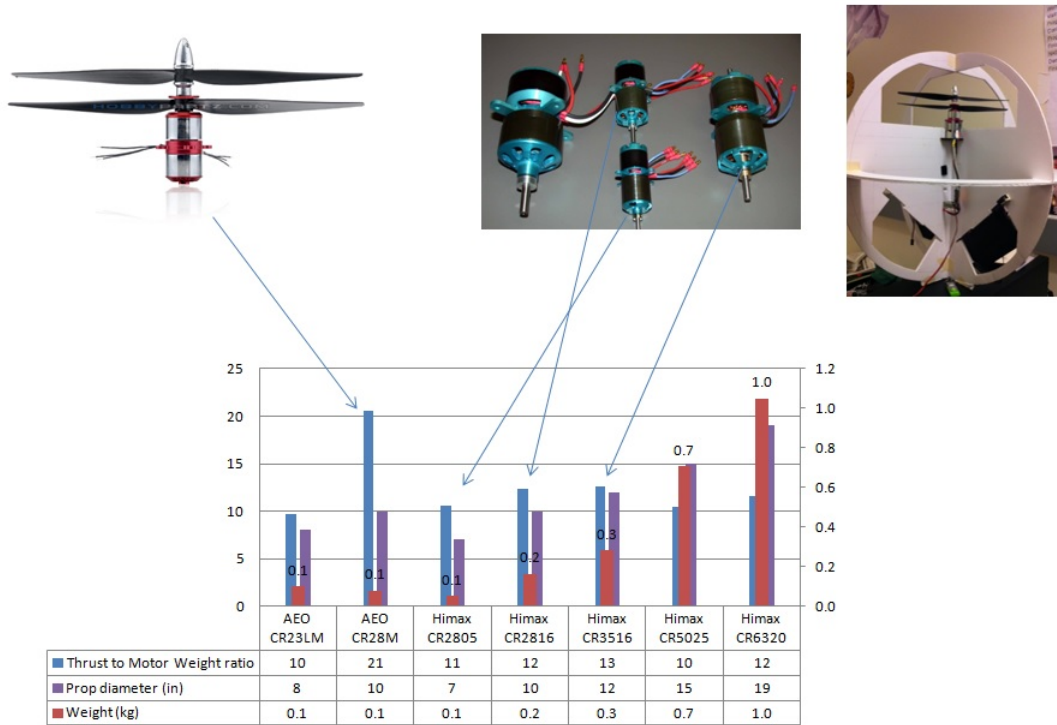


Figure 185: Types of COTS coaxial contra-rotating motor.

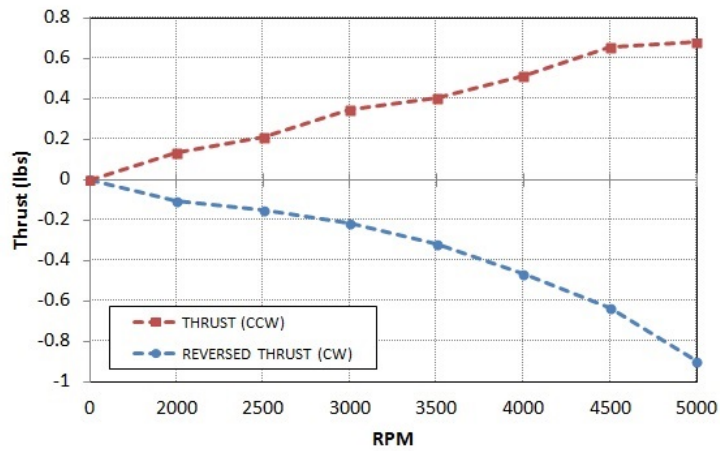


Figure 186: RPM vs. reversed thrust by reversing the motor spinning direction force using one of the single propeller of AEO-RC CR28M.

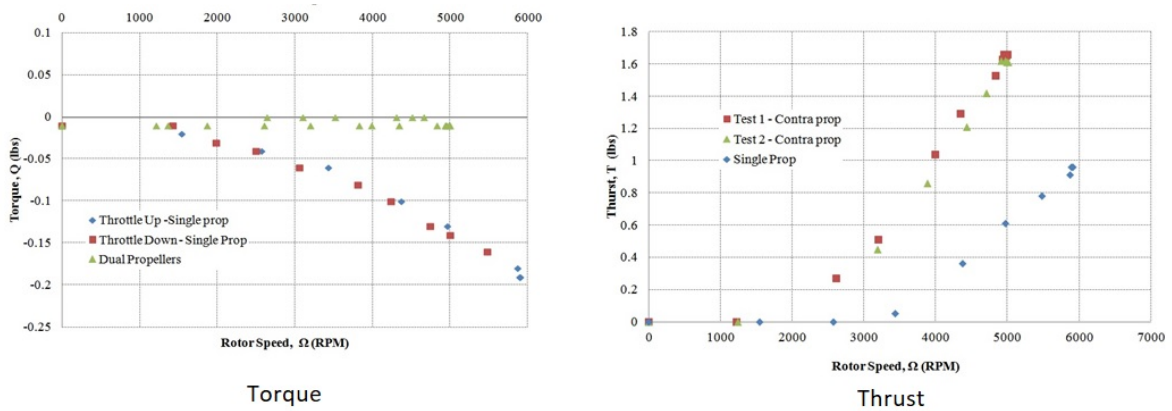


Figure 187: Thrust and torque measurement produced by AEO-RC CR28M.

VITA

(Ben) LOH WENG KHEONG

**Candidate for the Degree of
Doctor of Philosophy**

Dissertation: DESIGN AND CONTROL OF A SPHERICAL VTOL VEHICLE

Major Field: Mechanical and Aerospace Engineering, Unmanned Aerial System Option

Biographical: Education:

Completed the requirements for the Doctor of Philosophy in Mechanical and Aerospace Engineering at Oklahoma State University, Stillwater, Oklahoma in December 2019.

Completed the requirements for the Master of Science in Mechanical Engineering at Oklahoma State University, Stillwater, Oklahoma in December 2009.

Completed the requirements for the Bachelor of Science in Mechanical and Aerospace Engineering at Oklahoma State University, Stillwater, Oklahoma in May 2006.

Experience :

OSU Unmanned System Research Institute, Stillwater, OK
Research Engineer (December 2015 - Present)

Unmanned Cowboys, LLC, Stillwater, OK
Chief Technology Officer and Founder (October 2014 - December 2015)

ModernBlox, LLC, Tulsa, OK
President and Founder (May 2014 - Present)